



UNIVERSITÀ DI PISA
Dipartimento di Scienze della Terra

Dottorato di Ricerca in Scienze della Terra

Settore scientifico-disciplinare
GEO/03 – Geologia Strutturale

Ciclo 2003

**LATE-HERCYNIAN GRANITOID PLUTONS
EMPLACED ALONG A DEEP CRUSTAL SHEAR ZONE.
A CASE STUDY FROM THE S. LUCIA NAPPE
(ALPINE CORSICA, FRANCE)**

Candidato

Dr Ivan Zibra

Tutori

Prof J.H. Kruhl

(Technische Universität München)

Prof M. Marroni

(Università di Pisa)

Abstract

The S. Lucia Nappe (Alpine Corsica, France) is located in the Corte area. This tectonic unit recorded a polyphase Alpine evolution developed under lower greenschist facies conditions. In addition, the basement recorded an older (i.e. late-Paleozoic) tectono-metamorphic history, which mainly developed under granulite to amphibolite facies conditions. The S. Lucia basement represents an example of Ivrea-type lower crustal section, including a segment of a Km-scale granulite-facies shear zone made up of sheared Permian gabbros and enclosed metasediments. The occurrence of a thick (i.e. at least 1 Km-wide) high-grade shear zone indicates that the late-Palaeozoic deformation in the lower crust was homogeneously distributed on a large scale. The non-coaxial character of the deformation and the invariable sinistral shear sense, generalized along the whole section, recalls the models of uniform-sense, crustal-scale normal shear zones.

Two distinct granitoid plutons were emplaced at the margins of the S. Lucia shear zone. Field relations, microstructures, quartz LPO fabric and mineral chemistry data document the syntectonic emplacement respect to the shear zone. Indeed, both plutons experienced a nearly continuum down-temperature deformation, during emplacement and subsequent syndeformational cooling.

The observed structural style suggests that the granitoids probably accommodated large strains through magmatic to submagmatic flow. In both cases, the pattern of magmatic and subsequent solid-state fabric was strongly controlled by the stress field imposed by the S. Lucia shear zone. Moreover, the bulk composition of the two plutons likely played a fundamental role in the tectonic evolution, influencing the structural style and the spatial distribution of the solid-state overprint. Finally, the occurrence of magmas along the shear zone may have promoted strain partitioning within the melt-rich areas, allowing the exhumation and the preservation of granulite-facies rocks.

The Mesozoic syn-rift exhumation of the S. Lucia basement is suggested by the occurrence of undeformed MORB-type dolerites, by the Middle Jurassic thermal anomaly and by the Cretaceous sedimentary cover. However, although the P-T-t evolution of the S. Lucia section is only partly constrained, several lines of evidence suggest that the Permian granulites had already been incorporated into the upper crust prior to the Mesozoic.

Several paleogeographic reconstructions propose that, in the Alpine region, Permian granulites were intimately associated with the Mesozoic ophiolites at the ocean-continent transition. However, the case study proposed here points out that the occurrence of granulites alone cannot be taken as an indication of a syn-rift exhumation of the lower crust along the continental margin.

Contents

Abstract	3
Introduction	9
1. Geological background.....	10
1.1 Geology of Corsica-Sardinia “microplate”	10
1.1.1. Pre-carboniferous metamorphic belt.....	10
1.1.2. Corsica-Sardinia batholith	12
1.1.3. Overview on tectonic framework of Alpine Corsica	13
1.1.3.1 External units (Tenda complex, Corte Units, S. Lucia nappe).....	14
1.1.3.2 Schistes Lustrés Nappe (sensu lato)	14
1.1.3.3 Crystalline units with uncertain origin.....	14
1.1.3.4 Upper Nappe of “Ligurian affinity”	14
1.1.4 The Corte area: regional geological setting	15
1.2 The S. Lucia nappe: overview on existing literature.....	16
1.2.1 Sedimentary cover.....	16
1.2.2 Alpine tectonic evolution: a short outline	19
1.2.3 The basement	20
1.3 Evidences for primary contacts between basement and cover.....	22
1.4 Outline on meso- and microstructures of Alpine age: the main tectonic foliation in Tomboni Conglomerate.....	25
2 Mafic Complex.....	29
2.1 Mafic Complex: field relations and microstructures.....	29
2.1.1 Introduction	29
2.1.2 Mantle rocks.....	32
2.1.3 Gabbroic layered complex	34
2.1.3.1 Unit I: ultramafic rocks to layered gabbros	34
2.1.3.2 Unit II: coarse-grained gabbro and gabbro-norite.....	38
2.1.4 Grt-bearing paragneiss and quartzofeldspathic granulites	41
2.1.5 Evidences of synmagmatic deformation.....	47
2.1.6 Qtz LPO in the lower and intermediate part of MC	50

2.1.7	The roof of MC: the diorite-granite suite (DGS).....	55
2.1.7.1	Overview on different rock types.....	55
(a)	Enderbite to norite	55
(b)	Tonalite to diorite.....	57
(c)	Porphyritic rapakivi granite	60
(d)	Leucocratic dykes.....	60
2.1.7.2	Magmatic to submagmatic fabric (F ₀₋₁ fabric).....	62
(a)	Field relations and microstructures.....	62
(b)	Quartz LPO	65
2.1.7.3	High-temperature solid-state flow (F ₂ fabric).....	67
(a)	Meso- and microstructures	67
(b)	Quartz LPO	71
2.1.7.4	Moderate- to low-temperature solid-state flow (F ₃ fabric)	74
(a)	Meso- and microstructures	74
(b)	Quartz LPO	77
3	granitic complex.....	79
3.1	Outline on field relations and microstructures.....	79
3.1.1	Hornblende-bearing granitoid suite	79
3.1.1.1	Hornblendite to diorite	80
3.1.1.2	Tonalite	81
3.1.1.3	Granite to leucogranite.....	82
3.1.2	Two-mica microgranitoid suite.....	83
3.1.3	Mafic and felsic dykes	84
3.2	Synmagmatic fabric	85
3.2.1	Magmatic to submagmatic fabric	85
3.2.1.1	Magmatic fabric (f ₁)	87
3.2.1.2	Submagmatic fabric (f ₂).....	88
3.2.1.3	Fabric developed at low melt fraction (f ₃).....	94
3.2.2	Quartz LPO	99
3.2.2.1	F ₁ fabric	99
3.2.2.2	F ₂ fabric.....	99
3.2.2.3	F ₃ fabric.....	100

3.2.3	Dominant shear sense during magmatic to submagmatic flow.....	103
3.3	Solid-state fabric	106
3.3.1	Introduction	106
3.3.2	The main solid-state fabric.....	107
3.3.2.1	S tectonite	107
3.3.2.2	S-C tectonite	109
(a)	Moderately deformed S-C tectonite	109
(b)	Highly deformed S-C tectonite.....	109
3.3.2.3	C' tectonite.....	111
3.3.3	Quartz LPO	113
3.3.3.1	Evolution of quartz fabric through the “mylonitic rim”	113
3.3.3.2	Interpretation of the quartz fabric	114
(a)	Porphyroclasts	114
(b)	Recrystallized grains.....	114
3.3.4	Relicts of high-temperature solid-state fabric	118
3.3.5	Pre-Alpine low-temperature solid-state fabric	123
3.3.6	Some remarks on quartz and feldspars microstructures.....	124
3.3.6.1	Quartz	124
(a)	The main solid-state fabric.....	124
(b)	High-temperature solid-state fabric	125
(c)	Low-temperature solid-state fabric	125
3.3.6.2	Feldspars.....	125
(a)	The main solid-state fabric	125
(b)	High-temperature solid-state fabric.	127
3.4	The effect of superposed quartz fabrics: comparison with other case studies.....	127
4	Mineral chemistry and geochronology	129
	Mineral chemistry data.....	129
4.1.2	Mineral chemistry from S. Lucia basement; introduction.....	129
4.1.3	The lower part of MC: Grt-bearing gneisses	129
Biotite		130
Orthopyroxene.....		130
Plagioclase		130

Garnet	130
Hbl-bearing granitoids from DGS and GC	136
Amphibole.....	136
Plagioclase.....	145
Biotite	148
Pyroxenes	150
Ms-bearing granitoids	151
White mica and biotite	151
Feldspars	154
Pressure and temperature estimations	155
4.2.1 “Peak” conditions in Grt-bearing gneisses.....	155
4.2.2 Estimation of P-T conditions for the emplacements of Hbl-bearing granitoids (DGS and GC).....	156
4.2.3 Estimation of P-T conditions for the emplacements of Ms-bearing granitoids (GC) 157	
4.3 Geochemical investigation on dolerite dykes (MC).....	160
4.4 Geochronology	161
5 Synthesis, discussion and tectonic interpretation	164
5.1 The age of deformation through the S. Lucia deep crustal section	164
5.1.1 Mafic Complex	164
5.1.2 Granitic Complex	165
5.2 The restoration of Permian geometries.....	166
5.3 Tectonic interpretation	170
5.3.1 The S. Lucia section in the Late Paleozoic regional framework.....	170
5.3.2 Geodynamic implications for the Tethyan rifting.....	171
5.4 The emplacement of granitoid bodies along the shear zone	174
5.4.1 Some inferences concerning the emplacement model.....	179
5.5 Conclusions.....	181
Acknowledgments	182
References	183

Introduction

The overall structure and composition of the lower continental crust is still poorly understood, mainly because the rare exposed lower crustal fragments represent only small portions of the lower crust as a whole. The study of (originally deep-seated) crustal xenoliths and investigations by remote methods (i.e. seismic reflection, electrical conductivity measurements, etc.) provide little detailed information on structural style, three-dimensional relationships of any large-scale layering and lateral variations within the lowermost part of the crust. In alternative, one way to obtain information concerning the lower crust is to study the exposed geological regions interpreted as tectonically exhumed lower crustal portions. One of the few examples of nearly continuous, "regional" cross section through the lower and middle continental crust is exposed in the well-known Ivrea Zone of the Western Alps (e.g. Quick et al., 1994). Some other equivalent, late-Paleozoic lower crustal slices occur in the Alps-Northern Apennine system, as the Malenco Complex (Hermann & Müntener, 1996), the Sesia Zone (Lardeaux & Spalla, 1991) and Northern Apennines (Marroni et al., 1998). In these examples, deep-seated underplating of mafic plutons was associated with broadly coeval (~280Ma) and syndeformational granulite-facies metamorphism. The close connection between magmatism, deep-crustal shearing and late-Paleozoic crustal extension has been largely documented (see also Rutter et al., 1993; Snoke et al., 1999), including some evidences of synmagmatic deformation in gabbroic rocks (Quick et al., 1992).

This paper reports the results of structural mapping joined with microstructural study from the S. Lucia basement (S. Lucia nappe, Alpine Corsica), which represents another example of Ivrea-type lower crustal section (Libourel, 1988b).

The temperature conditions at which subsequent microfabrics developed are mainly estimated by the examination of microstructures and quartz LPO fabric. Here is assumed that stress and strain rate conditions during the development of S. Lucia shear zone fall in the common natural range usually estimated in natural shear zones (flow stress up to 200MPa; strain rates between 10^{-14} and 10^{-11} s⁻¹; see for example Zulauf, 2001).

1. GEOLOGICAL BACKGROUND

Chapter I is divided into two portions. The first section provides a brief overview on the regional geology of Corsica and Sardinia Island, dealing with both the Hercynian and the Alpine orogenic cycles. Special regard is dedicated to the S. Lucia unit, and a summary of previous works on this unit is provided. In the second part of the chapter, the main results of field and microstructural investigations on Alpine structures in the S. Lucia nappe are shown. This part of the work represents the essential background necessary to establish the effects of orogenic structures on pre-Alpine fabric preserved within the S. Lucia basement.

The micrographs proposed in this paper (if not otherwise indicated), derive from thin sections oriented normal to the foliation and parallel to the lineation.

1.1 Geology of Corsica-Sardinia “microplate”

Corsica and Sardinia are located in the northwestern Mediterranean. They are considered as part of the southern France and northern Iberia Variscan belt. The present-day position of the Corsica-Sardinia microplate is due to Oligo-Miocene $\sim 30^\circ$ counterclockwise rotation, related to the opening of the Liguro-Provencal Basin (Burrus, 1984). The microplate recorded a polyphase tectono-metamorphic history related to both Variscan and Alpine orogenesis.

1.1.1. Pre-carboniferous metamorphic belt

In Sardinia, a segment of the Variscan chain is preserved in the eastern and southwestern area. From south to north, three main tectonic regions are described (Arthaud & Matte, 1977). The southernmost part (“*external zone*”, i.e. *Iglesiente* area) is considered as an external orogenic domain, which recorded polyphase tectonic history associated with low-grade metamorphism. The central zone, or “*nappes zone*”, is characterized by a syn-metamorphic polyphase tectonic evolution, including three main tectonic phases, mainly developed under greenschist facies conditions (Franceschelli et al., 1982b). The NE sector, or “*axial zone*”, includes medium to high-grade rocks (i.e. amphibolites and migmatites containing relics of older eclogites). At the scale of the island, the metamorphic grade increases toward the NE (Franceschelli et al., 1982b). Recent investigations on metabasic eclogites suggest that a Paleozoic high-pressure metamorphic belt occurred from the axial zone of Sardinia to Corsica, Maures-Esterel and Alps (Giacomini et al., 2005).

In Corsica, a spatially continuous (pre-batholith) metamorphic belt is not preserved. Instead, some fragments of pre-carboniferous country rocks are isolated into middle- to late-Hercynian granitoids. These metamorphic fragments are classically divided into two families. The slices of *Belgodere*, *Solenzara*, *Porto Vecchio* and *Zicavo* recorded a polyphase metamorphic evolution, which is broadly comparable with those of the axial zone in Sardinia (Ricci and Sabatini, 1978).

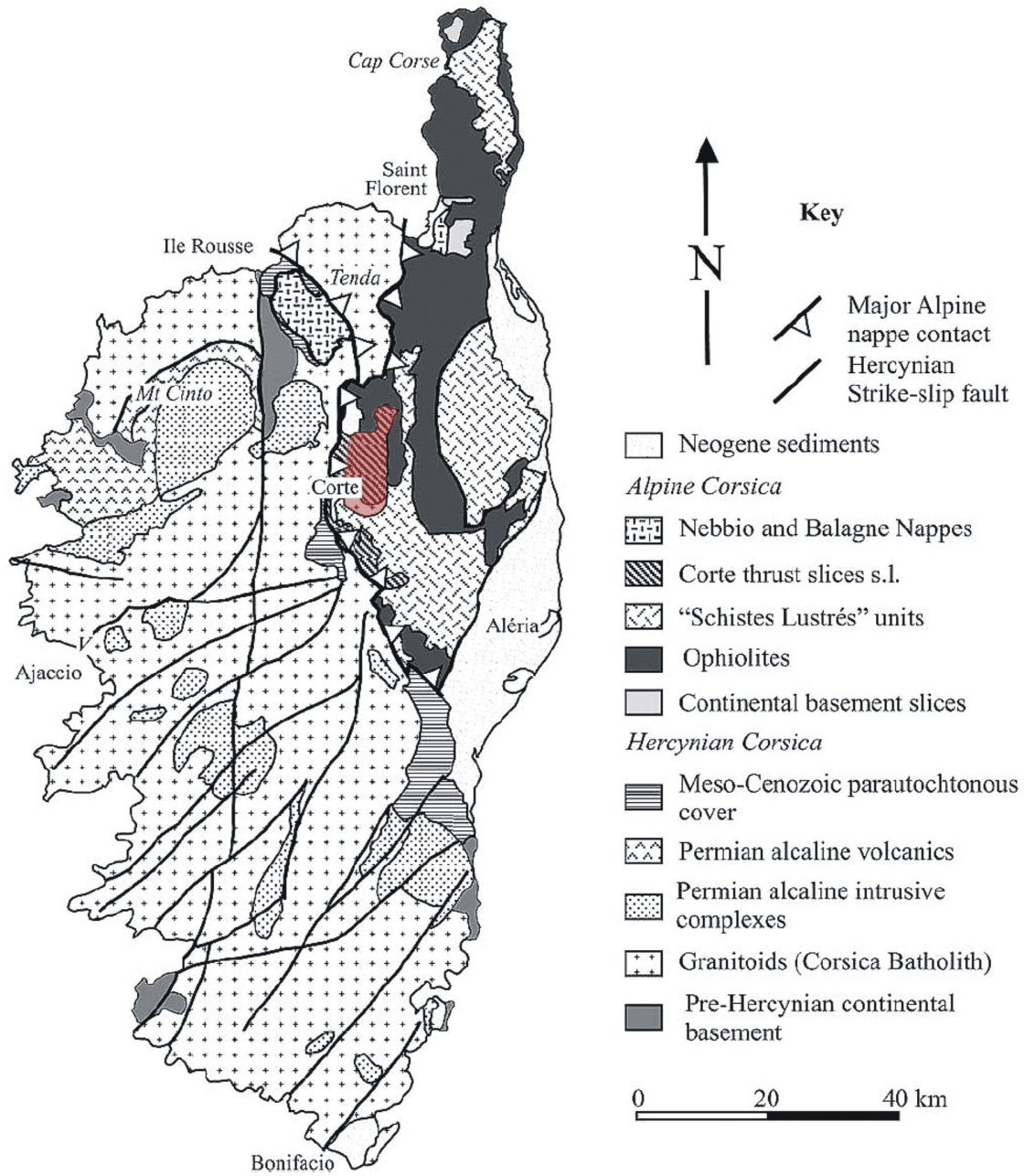


Fig. 1.1: Simplified tectonic map of Corsica. RED: S. Lucia Nappe. Slightly modified after Zarki-Jakni et al. (2004).

The Belgodere Complex mainly contains migmatitic gneisses, two-mica orthogneisses and amphibolites. The oldest part of the metamorphic evolution developed under eclogitic to granulitic conditions (likely during Devonian times, Palagi et al., 1985), followed by widespread syntectonic migmatitization, dated at ~350Ma (Rossi et al., 1988).

The metamorphic complex of Zicavo (central-southern Corsica) mainly contains a leptyno-amphibolitic complex associated with metapelites and Ms-Bt-Crd orthogneisses (mineral symbols from Kretz, 1983), which are locally associated with migmatites. Vezat (1988) proposed that the main metamorphic imprint developed under high-temperature, low-pressure conditions during Eo-Variscan to Variscan times, whereas the anatexis occurred during the emplacement of the surrounding calc-alkaline granitoids (300-280Ma, Paquette et al., 2003). These late orogenic leucocratic monzogranites intruded into the middle crust during active extensional shearing (Thévoux-Chabuel et al., 1995).

The Solenzara Complex from southern Corsica includes granulitic paragneisses, pyrigarnites and migmatites, interlayered with metabasic rocks (Arthaud & Matte, 1977). The older high-pressure assemblage (P=13-17Kb; T=800°C, Libourel, 1985) recorded isobaric cooling followed by decompression under amphibolite facies (in the andalousite stability field). This later evolution is associated to widespread migmatitization (Libourel & Vielzeuf, 1988).

The Porto Vecchio Complex (southern Corsica) is made up of pre-Variscan two-mica orthogneiss, associated with a leptyno-amphibolitic complex and migmatites (Ménot & Orsini, 1990).

The Vico-Cargese Complex (western Corsica) mainly contains some fragments of a Proterozoic magmatic layered complex intruded into Grt-Crd-bearing paragneisses (P=5.5Kb, T=700°C; Ferré, 1989). This complex is associated with amphibolite-facies metabasites and migmatitic gneisses dated at ~375Ma (Malusky, 1977).

The Argentella Complex (NW Corsica) includes a metamorphic basement (with micaschists, gneisses and metabasic rocks) and a Paleozoic sedimentary sequence, recording a Silurian tectonic history developed under low-grade conditions (Ménot & Orsini, 1990). It displays lithostratigraphic and metamorphic features comparable with those of the external zone of Sardinia (Baudelot et al., 1981).

1.1.2. Corsica-Sardinia batholith

The Corsica-Sardinia batholith is geochronologically subdivided into three main syn- to late orogenic magmatic suites (Cocherie et al., 2005). These different plutonic and volcanic rocks were emplaced from early Carboniferous to lower Triassic times.

The oldest magmatic suite occurs only in NW Corsica (i.e. between Ile-Rousse and Cargese, Fig.1.2), and mainly contains monzonites to syenites (commonly Bt-Hbl-Ttn-Cpx-bearing), associated with minor mafic rocks, which are mainly represented by diorites and cumulative gabbros. These mafic stocks derived from lamprophyric magmas from an enriched mantle source (Ferré and Leake, 2001). K- and Mg-rich granitoids were emplaced in a syn-orogenic context as vertical N-S trending sheet-like bodies (Laporte et al., 1991; Palagi et al., 1985). This suite is dated at ~338Ma, being preceded by slightly older peraluminous granites

(Paquette et al., 2003). High-K calc-alkaline plutons were exposed to erosion before 273Ma, as pebbles of them occur in a Westphalian conglomerate (Rossi et al., 1994).

The second suite includes plutonic and subordinate volcanic rocks, which make up most of the central and southern part of the Corsica-Sardinia batholith. Plutonic rocks exhibit clear calc-alkaline affinity, being mainly represented by Hbl-Bt-bearing tonalites to granodiorites, commonly associated with mafic microgranular enclaves and dioritic bodies of various sizes. The emplacement of calc-alkaline granitoids occurred at ~305Ma (Paquette et al., 2003), whereas most of the mafic counterpart took place around 285-280 Ma at mid to lower crustal levels (Paquette et al., 2003). The regional-scale foliation is mainly oriented NW-SE in central and southern Corsica. This main orientation is highlighted by the preferred elongation of mafic to intermediate coeval septa. The shallow-level intrusion of the Tenda massif (Rossi 1993) and deep-crustal mafic sequence of S. Lucia layered Complex (Libourel, 1985) represent roughly coeval complexes (~280Ma, Paquette et al., 2003), both belonging to calc-alkaline suite. Volcanites are mainly represented by andesitic and rhyolitic lavas and dykes, and crop out in the NW Corsica (Cabanis et al., 1990). They were mainly emplaced during lower Permian (Orsini et al., 1987).

The youngest plutonic suite is mainly composed by A-type granitoids and minor mafic rocks. Most common rocks are “hypersolvus” (perthite-bearing) granites, containing fayalite, aegerine, hedembergite and blue amphibole (Rossi & Cocherie, 1991). Combined crustal and mantle sources were likely involved in the genesis of alkaline suite (Cocherie et al., 1994).

In Sardinia, only the rocks belonging to second suite are present. They are mainly exposed in the NE part of the island, where granitoids transect both the *Nappes Zone* and the *axial Zone* of the Variscan belt. In detail, the northernmost sector is dominated by Bt-bearing leucogranites, Bt-monzogranites and Hbl-bearing granodiorites. A peculiar character of the Sardinian part of the batholith is represented by the presence of peraluminous granodiorites to granites (containing Bt, Ms \pm Grt \pm Crd as feric phases). Two-mica granitoids are dated at ~300Ma (Carmignani & Rossi, 1999) being spatially associated with broadly coeval Hbl-bearing tonalites to granodiorites and minor mafic rocks (Paquette et al., 2003).

1.1.3. Overview on tectonic framework of Alpine Corsica

Corsica and Sardinia Island recorded a partly different post-Paleozoic tectono-stratigraphic evolution. In eastern Corsica, the “Alpine domain” displays an “Eo-” to “Meso-Alpine” thrust and fold belt which is commonly interpreted as the southern prolongation of the Penninic belt from Western Alps. In contrast, Alpine structures in Sardinia (affecting the Hercynian basement) are mainly represented by Late-Alpine strike-slip faults, associated with minor local thrusts. These structures affect also subvolcanic to volcanic rocks of W Sardinia, emplaced during Oligo-Miocene times (likely during the rotation of the Corsica-Sardinia microplate; Speranza et al., 2002). In Corsica, the Alpine domain is located in the NW area, being represented by a complex stack of nappes, derived from both Mesozoic Liguro-Piemont oceanic basin and associated continental margins (Durand Delga, 1984). During late Cretaceous to Eocene times, Alpine nappes were thrust on the pre-Mesozoic

crystalline basement, represented by the Hercynian Corsica. From bottom to top, the Alpine Corsica nappe stack includes:

1.1.3.1 External units (*Tenda complex, Corte Units, S. Lucia nappe*)

Tenda massif from NE Corsica mainly consists of granitoids, gabbroic rocks and subvolcanic to volcanic rocks (Ohnenstetter & Rossi, 1985). In central Corsica, Corte units consist of slices of Hercynian basements with some remnants of Mesozoic to Eocene cover (Egal, 1992). S. Lucia Unit consists of pre-Alpine composite basement overlain by Cretaceous covers (Durand Delga, 1984).

These allocthonous units are commonly referred to the Corsican\European continental margin, recording polyphase Alpine history, partly related to a subduction event (Bézert & Caby, 1989; Molli & Tribuzio, 2004).

1.1.3.2 Schistes Lustrés Nappe (*sensu lato*)

This nappe contains several tectonic units deriving from both oceanic and continental domain (Caron, 1977). They commonly lie upon previous units, displaying Eclogite to blueschist "Eo-Alpine" assemblages, partly retrogressed under greenschist facies conditions (Pèquignot & Potdevin, 1984).

1.1.3.3 Crystalline units with uncertain origin

These units mainly consist of gneisses embedded in the Schistes Lustrés nappe, sharing with them the Alpine tectono-metamorphic evolution. Centuri Unit (from northernmost part of Corsica Island, "Cap Corse", Fig.1.1) mainly includes pre-Alpine amphibolite-facies paragneisses, associated with granitoids. The paleogeographic origin of this slice of continental crust is poorly constrained. Centuri Unit is compared to the Dent Blanche nappe from western Alps (Austroalpine domain, Caby et al., 1984) or is considered an intra-oceanic slice of continental crust (Dallan & Nardi, 1984). In contrast, according to Durand Delga (1984) it is comparable with pre-Carboniferous country rocks from western Corsica. Serra di Pigno Unit (from Bastia region, NE Corsica) includes some slices of eclogite-facies orthogneiss lying on (or is embedded in) the meta-ophiolitic units (GLOM, 1977). According to Caby et al. (1984), Serra di Pigno Unit is comparable with Centuri complex, both deriving from the Austroalpine domain. In contrast, according to, Mattauer & Proust (1975), Durand Delga (1978) and Lahondère (1988) these slices of orthogneisses are comparable to the Tenda Massif and, thus, are referred to the European continental margin ("Penninic domain").

1.1.3.4 Upper Nappe of "Ligurian affinity"

The uppermost tectonic complex comprises several tectonic slices (*Balagne nappe, Nebbio and Macinaggio Klippe*), mainly containing some remnants of Jurassic ophiolitic basement, overlain by Jurassic to Eocene sedimentary covers (Durand Delga, 1984). These units recorded polyphase deformation history (Egal & Caron, 1988), lacking any evidence of syn-deformational metamorphism.

The regional tectonic evolution of the whole Alpine domain of Corsica Island is examined in Durand Delga (1984), Caron (1994), Daniel et al. (1996), Malavieille et al. (1998), Molli & Tribuzio (2004), Lacombe & Jolivet (2005). According to these authors, in this area the main structures developed in a context of an Alpine-type subduction regime, which led to the emplacement of the main nappes, mainly during late Cretaceous to Eocene times. The subsequent Oligo-Miocene tectonic activity is dominated by transcurrent to extensional movements, leading to the exhumation of previously buried tectonic units (displaying HP-LT assemblages; Caron, 1994).

These evolutionary models are mainly based on investigations carried out in the northern portion of the Alpine nappe stack, where a regional E-W cross-section is well exposed (from Bastia to Balagne region, Fig. 1.1). In contrast, the bulk regional framework of central and southern portions of the Alpine domain is less constrained (partly owing to the less favourable outcrop situation). Caron (1994) pointed out that the regional evolution of the southern Alpine domain in Corsica could differ substantially from those of the northern domain.

1.1.4 The Corte area: regional geological setting

The Corte area represents a key-area for the comprehension of the tectono-metamorphic evolution of the Alpine Corsica. In this region is exposed a segment of the main boundary between Hercynian and Alpine domains (Fig.1). The Corte zone is separable into three distinct morpho-structural domains. Westward from Corte city, the steep and high-mountain landscape (i.e. Mt. Rotondo, 2622m) is dominated by the Permo-Carboniferous calc-alkaline granitoids and associated mafic rocks (U2 suite in Paquette et al., 2003), representing the easternmost part of the autochthon domain. On the contrary, the eastern sector (i.e. toward the Castagniccia region), which is dominated by supra-ophiolitic metasedimentary covers ("Schistes Lustrés"), commonly exhibits gentle and hilly morphology. In this sector, the north-south trending crest line of the "Castagniccia dome" (Durand Delga, 1984) corresponds to the presence of eclogite to blueschist-facies meta-ophiolitic basement (i.e. Mt. S. Petrone, 1767m; Pèquignot and Potdevin, 1984). Between these two domains, the Corte area (in the strict sense) corresponds to a N-S trending depressed area (Simi, 1980) centred between Corte and Ponte Leccia cities, and transected by the national road RN 193. In the Corte zone, we can observe a complex stack of tectonic units of Alpine age derived from both oceanic and continental domains.

The (W-directed?) final emplacement of the main tectonic units in the Corte Area took place during Middle Eocene, as attested by the implication of Eocene Flysch into the main syn-metamorphic tectonic structures (Bézert & Caby, 1989). This is the case for the emplacement of the Corte Units and Balagne nappe on the external portion of the Hercynian Corsica (Bézert & Caby, 1989; Egal & Caron, 1988), the emplacement of S. Lucia nappe on Caporalino unit (Rieuf, 1980). The emplacement of meta-ophiolitic units in the Corte area is considered as roughly contemporaneous with this main Eocene tectonic event (Durand Delga, 1984), though a late-Cretaceous emplacement was proposed by Caron (1977). On the other hand, blue amphiboles from a meta-ophiolite near to Corte provided an Ar/Ar age of 40 ± 2 Ma (Malusky, in A. Du Chaffaut & Saliot, 1979).

The main tectonic structures are affected by two generations of folds (mainly with axes E-W and N-S, respectively), which are largely developed in the whole Corte area (Caron, 1977; Rieuf, 1980). Youngest tectonic events include the development of the Central Corsica Fault Zone (likely active between late Eocene to early Miocene times, Waters, 1990), which in the Corte area is mainly represented by the S. Quilico fault (Malusky et al., 1973), and by sub-horizontal folds. These later events affect also the Miocene deposits of Francardo and Corte (Durand Delga, 1984).

1.2 The S. Lucia nappe: overview on existing literature

This section briefly describes the general framework of S. Lucia nappe, based on the literature. The Alpine tectono-metamorphic evolution is also discussed in the second part of this chapter, where new original data will be presented.

The S. Lucia Unit is located in the central part of Corsica, few kilometres eastward from Corte. The Alpine polyphase history recorded by the S. Lucia nappe mainly developed under lower greenschist facies conditions (Libourel, 1985). This is shown by the examination of successive generations of structures, which are preserved within the Mesozoic sedimentary sequence (Egal, 1992). In addition, the basement recorded an older (i.e. late-Paleozoic) tectono-metamorphic evolution, which mainly developed under granulite to amphibolite facies conditions (Libourel, 1985). Consequently, the comprehension of the Alpine evolution is a prerequisite in order to separate, in the basement, the pre-Alpine structures from the Alpine ones.

In the recent past, this unit was studied by several authors, who provided partly different interpretations. Ritsema (1952) outlined the structural framework of the nappe, which (according to this author) includes a Paleozoic basement overlain by Eocene sedimentary covers (Tomboni Conglomerate and Tralonca Flysch; Fig.1.2A).

1.2.1 Sedimentary cover

The sedimentary sequence is represented by the Tomboni Conglomerate and the Tralonca Flysch. Despite the traditional name, the Tomboni Conglomerate is rather classifiable as sedimentary breccia, owing to the widespread occurrence of angular fragments (few cm to several meters in size) of granitoids, schists, rhyolites, metabasites, dolerites and limestones. The latter locally contain fossil associations attributable to upper Jurassic (Rieuf, 1980). The Tomboni Conglomerate reaches a maximum thickness of ~500m. According to A. Du Chaffaut (1980), neither bedding surface nor other sedimentary features are detectable; however, Rieuf (1980) noted that the size and the proportion of pebbles roughly decrease upward, deducing that this formation exhibits normal polarity. In the uppermost part of the conglomerate, green sandstones (locally interlayered with pelites and micro-conglomerates) provide the stratigraphic transition to the Tralonca Flysch. This sedimentary contact is well visible along the road between S. Quilico and Tralonca localities, as described in Durand Delga et al. (1978).

The Tralonca Flysch (~250-300m of thickness) is dated at lower Senonian (Rieuf, 1980). Close to the base, the flysch exhibits microconglomeratic and pelitic layers, whereas the calcareous

content progressively increases upward. The Tomboni Conglomerate is not directly dated. However, a Cenomanian age was suggested by Durand Delga (1984), mainly on the basis of the stratigraphic relationship with The Tralonca Flysch and the occurrence of upper Jurassic pebbles.

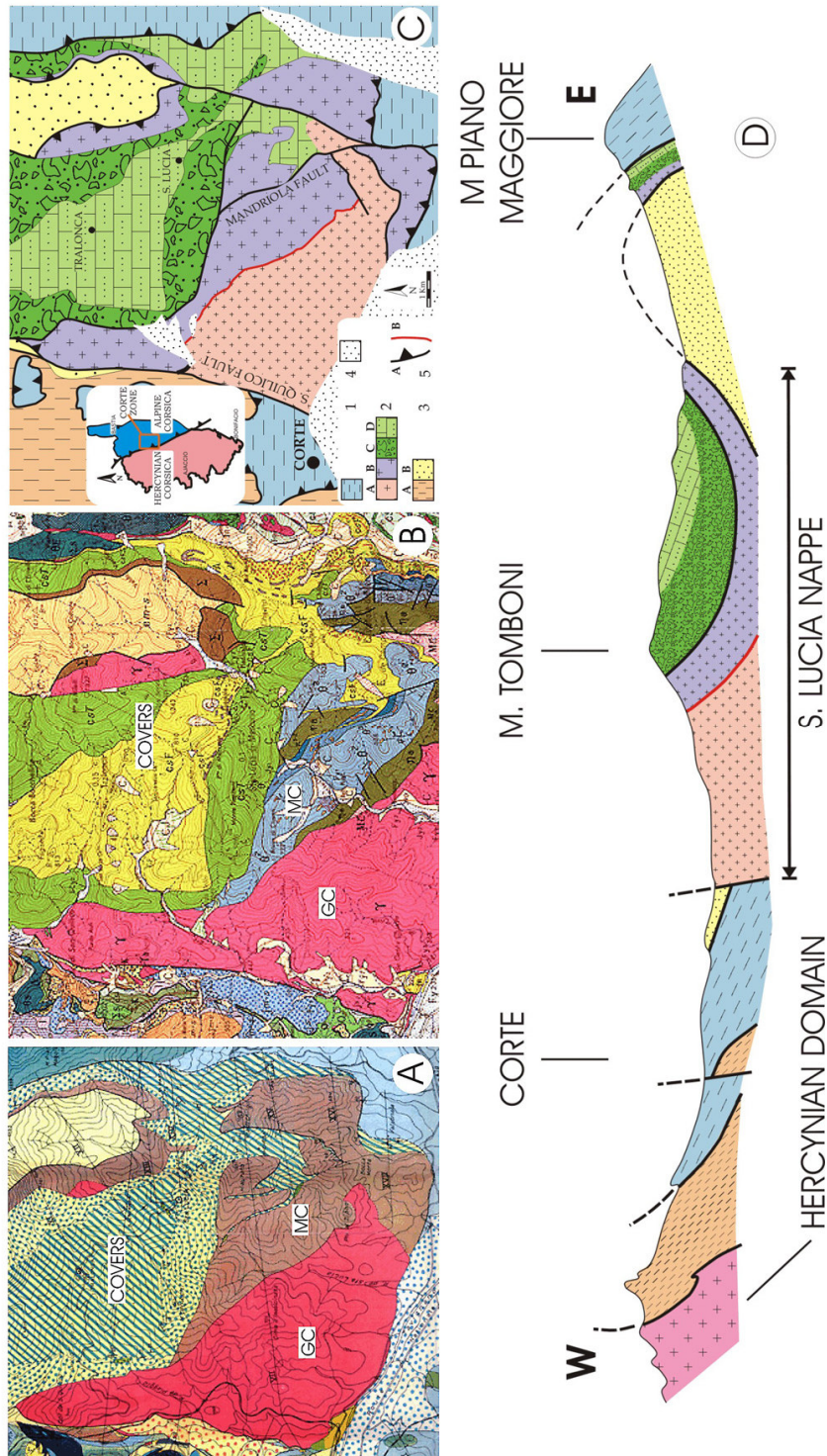


Fig. 1.2: Subsequent generations of geological maps of S. Lucia nappe. (A) Ritsema (1952); (B): Rossi et al (1994), after field and petrological investigation on MC (Libourel, 1985). (C): Tectonic scheme of the Corte area (Zibra, 2005; 1:metaophiolites; 2: S. Lucia Nappe [A: GC; B: MC; C: Tomboni Conglomerate; D: Tralonca Flysch]; 3: Corte nappes; 4: Neogene covers. Tectonic contacts: [A]: Alpine age; [B]: pre-Alpine age). (D) E-W schematic cross-section through the Corte area (same key of C); modified after A. Du Chaffaut and Salot (1979).

1.2.2 Alpine tectonic evolution: a short outline

According to Rieuf (1980) and Egal (1992), the cover series recorded four (five?) main deformation phases. The sequence of superposed folds is well detectable in the Tralonca Flysch; the main foliation (S_2) is represented by a crenulation cleavage, associated with sub-metric to cartographic isoclinal and strongly non-cylindrical recumbent folds. The main tectonic foliation and the basement-cover contacts are largely verticalized during D_3 event, which is associated with upright N-trending folds (Rieuf, 1980) and N-trending mainly transcurrent shear zones. Latest phases are mainly related to vertical shortening, with local development of S_4 sub-horizontal cleavage. Interference pattern between P_2 and P_3 folds is well visible at map scale, producing type 2 fold interference pattern (Ramsay & Huber, 1987). This sequence of superposed folds (from P_2 to P_4) is also detectable (with the same orientation) in the adjacent meta-ophiolitic units (Caron, 1977; A. Du Chaffaut, 1980).

In the northern sector, S. Lucia nappe is thrust onto Eocene cover (Corte nappes). The western nappe boundary is marked by the S. Quilico Fault, which belongs to the Central Corsica Fault Zone (CCFZ, Malusky et al., 1973; Waters, 1990). Along the Tavignano valley (southern nappe boundary), this unit is thrust onto meta-sedimentary ophiolitic covers (Caron, 1977; Fig.1.2C), whereas in the Mt. Piano Maggiore area (eastern sector) this tectonic contact exhibits the opposite polarity.

The paleogeographic origin of S. Lucia nappe is still not clear: according to Rieuf (1980), and Durand Delga (1984), this unit derives from the Corsican/European Mesozoic continental margin. Du Chaffaut (1980) divided the S. Lucia nappe into two independent tectonic units; the "lower unit" (which should include the basement and Tomboni Conglomerate) might belong to the European continental margin, but an Austroalpine ("ultra-Ligure") origin is not excluded. In contrast, the "upper unit" (i.e. the Tralonca Flysch) is compared to the Balagne nappe and with similar Mesozoic formations of western Alps and Northern Apennine. However, the occurrence of two distinct "sub-units" was contradicted by subsequent works (i.e. Durand Delga, 1984).

For Warburton (1986), S. Lucia nappe represents a part of the Corte nappe, which was emplaced eastward upon the meta-ophiolitic units, and subsequently affected by metre to kilometre scale N-trending upright folds. In contrast, Cabry & Jacob highlighted the similarities existing between S. Lucia unit and the upper Austroalpine units from central Alps.

In conclusion, the paleogeographic origin of S. Lucia nappe is uncertain. This is mainly because: (i) both the pre-Alpine basement (see below) and sedimentary covers are hardly comparable with Paleozoic and Mesozoic formations of Corsica island; (ii) tectonic and geometrical relationships between S. Lucia nappe and meta-ophiolitic units are still not clear.

1.2.3 The basement

After the pioneering work of Ritsema (1952), the S. Lucia pre-Alpine basement is clearly separated into two complexes (Fig.1.2A). The easternmost part of the basement includes Grt-bearing gneisses “interlayered” with different kind of flaser gabbros (“*gabbro rubanés*”, Ritsema, 1952). In contrast, the westernmost portion of the basement consists of a “*granite-diorite association*”. The NW area is dominated by amphibole-rich “*massif gabbros*”, displaying a gradual transition toward the “*melanocratic granite*”. Porphyritic and Ms-bearing leucogranites are also present in the central portion of the complex. Several types of leucogranitic veins are injected into both “*massif gabbro*” and “*granite*”. The author concluded that leucogranites are younger than the “*massif gabbros*” and “*melanocratic granite*”. Field relations between the “*granite-diorite association*” and flaser gabbros/Grt-bearing gneisses remained unknown at that time. Within his geological map (Fig.1.2A), Ritsema showed the outline of the two main complexes, but he did not provide the spatial distribution of different lithologies.

In the northern part of the basement, Rieuf (1980) described the magmatic association of melanocratic granodiorite and Hbl-rich gabbros. The latter term crops out as plurimetric pockets, showing a gradual transition to the surrounding melagranite. The author considered these different rocks as coeval magmatites. They are thought as intrusive into Grt-bearing gneisses, owing to the presence (in the NE sector of the nappe) of “leucogranitic veins” into leucocratic granulites. The author concluded that the granitoids belonging to the S. Lucia basement differs from the typical leucogranite of the adjacent “para-autochton” domain. Based on field observation on the SW portion of the basement, Du Chaffaut (1980) confirmed the general framework proposed by Ritsema (1952). At that time, field relations between the two major complexes were still unclear, as the occurrence of granitic dykes intruded into granulites (Rieuf, 1980) were not confirmed by the subsequent workers (e.g. A. Du Chaffaut, 1980).

Libourel (1985) focussed his studies on the “S. Lucia Complex” (here referred as Mafic Complex, MC), i.e. the granulitic complex including Grt-bearing gneisses and “gabbros rubanés” of Ritsema (1952). This author carried out detailed field and petrological investigations, comparing the S. Lucia complex with the well-known lower crustal section exposed in the Ivrea Zone (western Alps; Libourel, 1988b).

The MC consists of a typical deep-crustal association, where gabbroic layered intrusions, granulitic paragneiss and mantle rocks are closely associated. Within the gabbroic series, granulite-facies, Grt-bearing paragneiss (regarded as country rocks respect to the mafic intrusion), occurs as metric to decametric lenses, embedded at various levels within the mafic series (Fig.2.1).

The lower portion of MC displays a pervasive syntectonic recrystallization under granulite facies conditions (Libourel, 1985), as testified by “peak” metamorphic assemblage (Grt-Sill-Kfs-Qtz-Rt ± Opx; $P=7\pm 1\text{Kb}$; $T\sim 800^\circ\text{C}$; Libourel, 1985) recorded by the country rocks. These are considered as the conditions prevailing during the intrusion of the mafic magma. The retrograde synkinematic assemblage ($P=4.5\text{-}6\text{Kb}$; $T=750\text{-}800^\circ\text{C}$) occurred during the exhumation of the complex (Libourel, 1988a), and includes Crd, Bt, Opx and Qtz. Mantle rocks are composed by (largely serpentized) spinel- to plagioclase-bearing lherzolites and

websterites. These rocks recorded a deformation/recrystallization event developed into the lithospheric mantle ($P=12-16\text{Kb}$; $T\geq 1200^\circ\text{C}$; Libourel, 1985), which is strongly retrogressed in the lower crustal environment.

The mafic series exhibits a well-defined 'stratigraphy' (see geological map in Libourel, 1988a) from ultramafic rocks at the east (i.e. the former base of the complex; Libourel, 1985) to more differentiated rocks in the western area. Because of the pervasive deformation, relics of magmatic structures are rarely observable (Libourel, 1985). The layered body displays a clear calc-alkaline affinity, and cumulitic features are locally preserved in all magmatic sub-units (Libourel, 1985). The intrusion of the gabbroic series (and the coeval "peak" assemblage in country rocks) was recently dated at $286\pm 1\text{Ma}$, whereas the roof of the complex provided a slightly younger age ($280\pm 1.4\text{Ma}$; Paquette et al., 2003).

In summary, recent investigations were concentrated upon the MC, whereas the knowledge on the Granitic Complex was never actually updated, after the very preliminary observations carried out by Ritsema (1952).

Libourel (1985) considered the S. Lucia granodiorites as part of the calc-alkaline series from Central Corsica (300-330Ma). Ms-bearing facies crops out in the proximity of the "Mafic Complex". Contacts between the two main complexes are still interpreted as intrusive. This opinion is also shared by Caby & Jakob (2000).

According to Rossi (1993), the Granitic Complex belongs to the Corsican calc-alkaline suite (referred as "U2 suite" in the recent French literature). This author proposed that the granitoids intruded the Mafic Complex around 300-310Ma. An Upper Carboniferous emplacement age was proposed by Carmignani and Rossi (1999). This age is broadly in agreement with the $\sim 278\text{Ma}$ Ar/Ar Ms cooling age obtained from Ms-bearing granite pegmatite (this work).

1.3 Evidences for primary contacts between basement and cover

Rieuf (1980) described that, even if the basement-cover boundary was largely tectonically reworked during the Alpine orogeny, primary relationships between Granitic Complex and Tomboni Conglomerate were locally preserved (in the NE portion of the unit). On the other hand, A. Du Chaffaut (1980) and Libourel (1985) described, in the Tomboni Conglomerate, the occurrence of pebbles deriving from the Mafic Complex. Thus, both authors provided additional (even if indirect) evidences on the existence of a sedimentary contact between S. Lucia basement and the cover.

Another local example of preserved sedimentary contact (between the Mafic Complex and Tralonca Flysch) was found during this work, in the SW sector of the nappe. The example proposed here comes from the sector between *Mandriola* and *P.ta di Chilgo* localities.

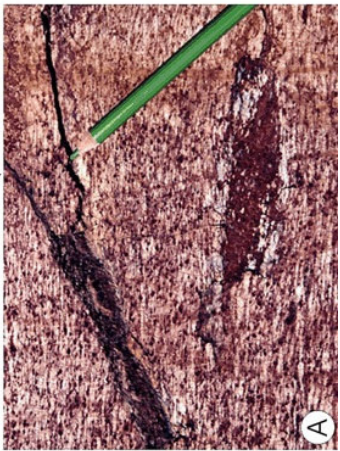
In this area, the basement is mainly represented by flaser gabbros belonging to Unit II (Mafic Complex), displaying well-preserved (pre-Alpine) high-temperature fabric (chapter II and Fig.1.3a). Toward the contact with sedimentary cover, flaser gabbro are progressively affected by cataclastic shear zones, being gradually replaced by chaotic and nearly monogenic breccia, mainly made up of angular fragments (displaying large range in size, from few cm to few dm; Fig.1.3b) deriving from adjacent flaser gabbros. The metagabbro-derived breccia displays irregular thickness (~1-10m), highlighting (even though in a discontinuous manner) the basement-cover boundary in all the *Mandriola-P.ta di Chilgo* area.

The exact basement-cover boundary is locally exposed, as in the example proposed here, where the cataclastic anorthosite lies in direct contact with dark, layered sandstone, containing angular fragments from the same crystalline basement (Fig.1.3c). Thin section examination (Fig.1.3d) indicates that the (altered) anorthosite display a pre-Alpine fabric comparable with those commonly preserved within the western portion of Mafic Complex (chapter II). Moreover, the quartz-rich matrix from dark sandstone seems weakly or not deformed at all (e.g. undulose extinction in quartz is nearly absent in this sample). These data indicate that the pervasive low-temperature (mainly brittle) deformation (documented by the occurrence of metagabbro-derived breccia) predate the deposition of the sedimentary covers.

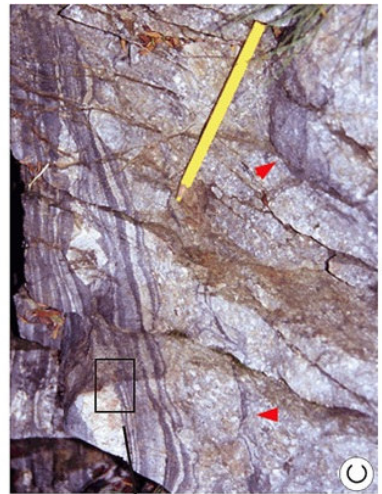
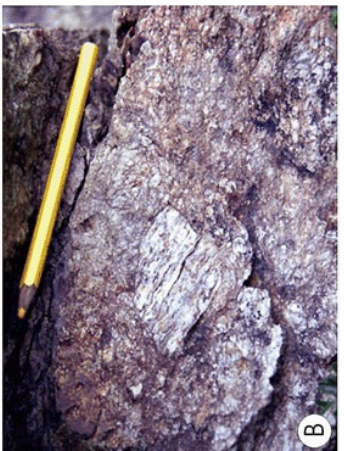
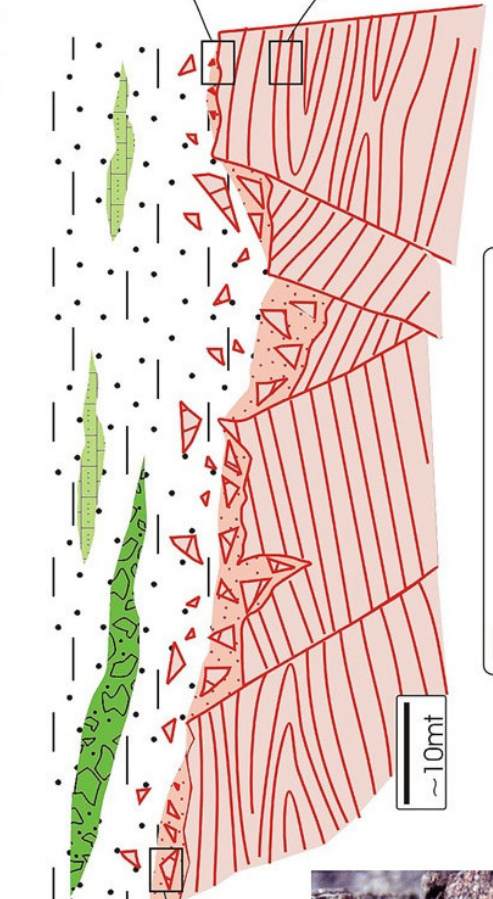
The examination of adjacent outcrop allowed the local restoration of the original architecture of the Cretaceous erosion surface, where dark sandstone are followed by ~20cm-thick calcareous strata (enriched in detritus of crystalline nature, mainly deriving from granitoids and rhyolites), alternating with ~1m-thick lenses of breccias and conglomerates (Fig.1.3e) and thin quartzite layers.

In summary, both the main complexes from pre-Alpine crystalline basement contain some remnants of primary (sedimentary) contacts with detritic covers of lower Senonian age. The punctual observations from the available rock exposition are too discontinuous to allow the comprehension of the geometrical relations between the main pre-Alpine fabric (in the basement) and the erosion surface. On the other hand, the uppermost portion of the basement (exposed during Cretaceous times), where likely represented by a network of tilted blocks of various size (Fig.3.1), as suggested by the (even localized) occurrence of brittle structures of pre-Senonian age (red arrowheads in Fig.3.1c).

Fig. 1.3 (next page): sketch summarizing the primary relationships between Mafic Complex and Cretaceous sedimentary cover, as reconstructed through observations in adjacent outcrops, in the surroundings of Mandriola locality. **[A]**: flaser gabbro preserving “primary” pre-Alpine (granulite-facies) fabric: weakly deformed noritic lens with Opx megacrysts in strongly foliated coarse-grained norite, close to the roof of unit II. Sinistral shear sense. **[B]**: metagabbro-derived sedimentary breccia; **[C]**: primary contact between metagabbro-derived breccia (mainly containing anorthosite blocks) and layered sandstone belonging to Tralonca Flysch. Red arrowheads point to pre-Alpine cataclasites, which do not propagate through the flysch; **[D]**: micrograph from thin section prepared at the interface between anorthosite clast (with pre-Alpine high-temperature microfabric) and weakly deformed sandstone (crossed polars, base of photo: 3mm). **[E]**: detail from nearly undeformed conglomerate lenses, which commonly occur at the base of the flysch in the SE area (base of photo ~1mt).



- CONGLOMERATE LENSES
- CALCAREOUS LENSES
- TRALONCA FLYSCH
- METAGABBRO-DERIVED BRECCIA
- METAGABBRO WITH PRE-ALPINE FABRIC



1.4 Outline on meso- and microstructures of Alpine age: the main tectonic foliation in Tomboni Conglomerate

The rheology of Tomboni Conglomerate is approximately comparable with that of crystalline basement, because this deposit mainly contains granitic and mafic pebbles, embedded in quartzofeldspathic (detritic) matrix. Consequently, the examination of microstructures of the main tectonic foliation in the conglomerate provides useful indications in order to estimate the effects of Alpine tectonics on pre-Alpine structures in the basement. Analogous investigations were carried out along some portions of crystalline basement involved into main nappe basal contacts (e.g. the southern boundary against meta-ophiolitic covers). However, in these cases, owing to the problem of inherited pre-Alpine structures, microstructural observations are more ambiguous.

The most deformed portions within Tomboni Conglomerate are commonly located near the basement-covers boundaries (Fig. 1.4 to 1.8). In fact, this interface was largely reworked during Alpine time, as the present-day contact is commonly marked by mylonitic foliation. In these cases, the strain gradient from undeformed (or weakly-deformed) conglomerate toward spectacular layered mylonite is commonly detectable in the proximity of the boundary. The high-strain zone at this interface commonly exceeds ~10mt in thickness. In these cases, the aspect ratio of sheared pebbles is commonly >10:1 (Fig. 1.4 and 1.5).

In the western sector, the sheared basement-covers boundary is nearly continuously exposed from the surroundings of P.ta Auli locality (NW nappe boundary) to S. Lucia Valley, at the intersection with Mandriola fault. At outcrop scale these mylonites appears as medium to fine-grained LS tectonites, where stretching lineation is marked by long axis of quartz-feldspatic polycrystalline aggregates.

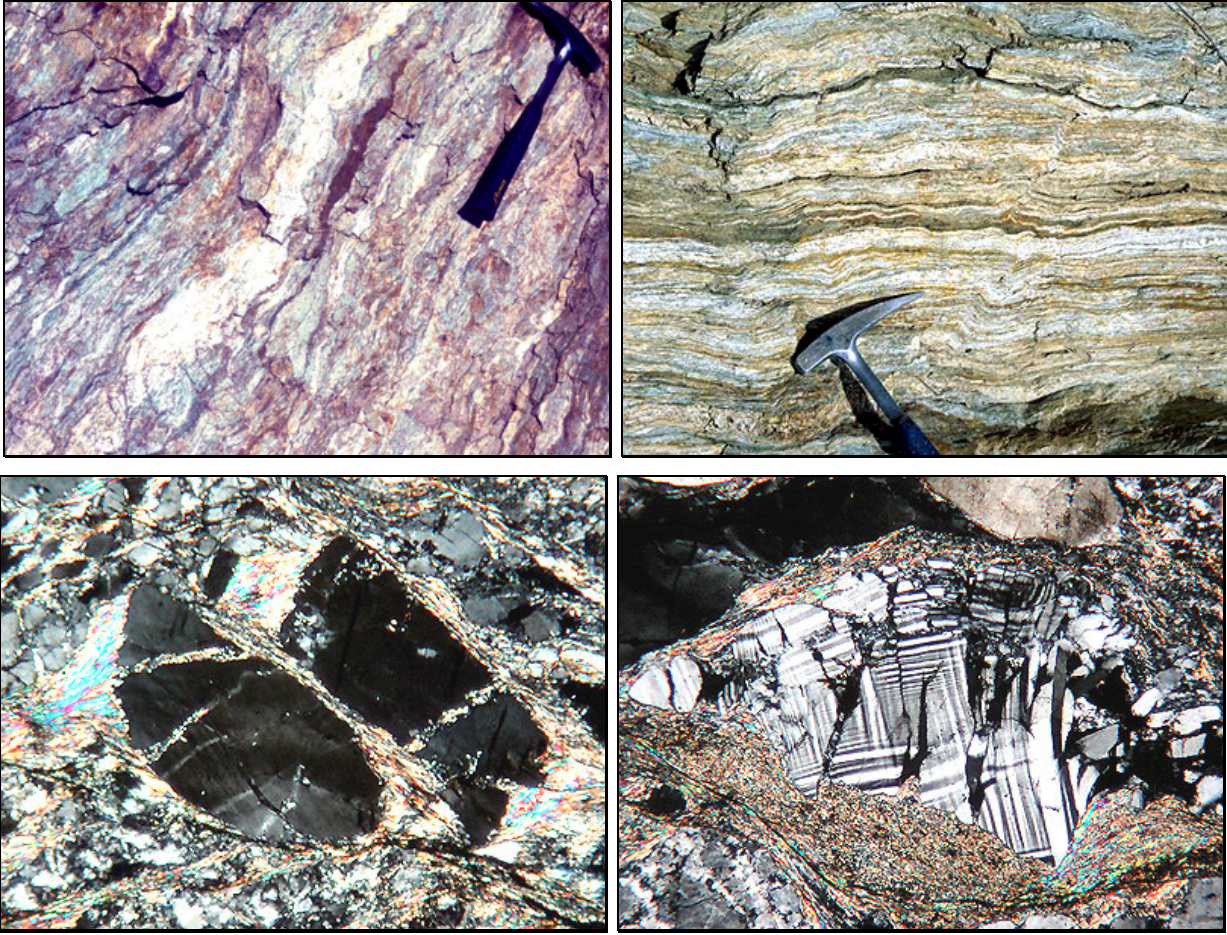


Fig. 1.4 (upper left): sheared conglomerate at ~10mt from mylonitized contact with granitic basement, near *P.ta di Milelli* locality (NE sector); mafic and felsic pebbles are still detectable. **Fig. 1.5** (upper right): the main alpine foliation at ~1mt from the basement-covers boundary, from the same area of Fig.1.14. The layered appearance derives from extremely sheared mafic and felsic pebbles. **Fig. 1.6** (lower left): detail from F₂ Alpine microfabric in Tomboni Conglomerate, basement-covers boundary, near S. Rocco locality. Brittle deformation in Qtz porphyroclasts, showing antithetic microfault and patchy undulose extinction (crossed polars, base of photo: 4mm). **Fig. 1.7** (lower right): another example from D₂ Alpine microfabric: brittle deformation in microcline, largely replaced by syntectonic sericite (crossed polars, base of photo: 4mm).

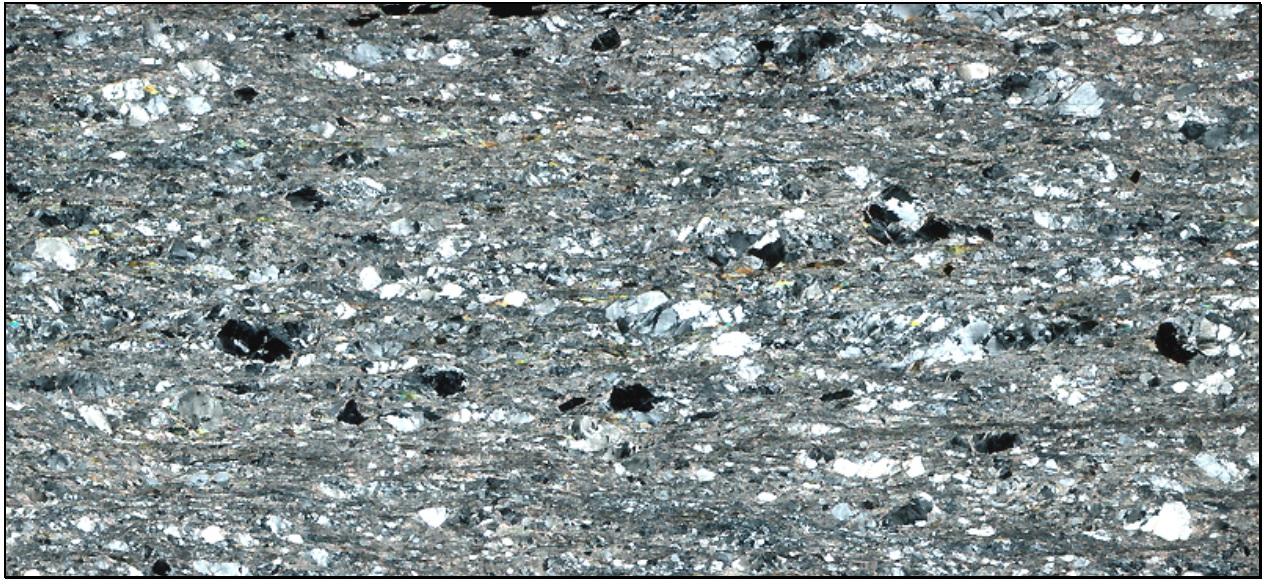


Fig. 1.8: enlarged micrograph from sample SL2, showing the main (Alpine) F_2 microfabric near the basement-covers boundary. "Rigid" Qtz and feldspars porphyroclasts are mainly deformed by brittle processes; they are embedded in a sericite-chlorite-rich ductile matrix. Sinistral shear sense is defined by C' shear bands (crossed polars; base of photo: 2cm).

During this work, several samples of quartzofeldspathic matrix of Tomboni Conglomerate were collected from high-strain domains, in both eastern and western sector of S. Lucia Unit. At grain scale this mylonites exhibit well-developed S/C to C' microfabric, where discontinuous C' shear planes developed at $\sim 20-25^\circ$ from the C surfaces (Fig.1.8). Mono- and polycrystalline porphyroclasts are commonly represented by quartz, plagioclase, K-feldspar, muscovite, biotite and epidote. The main mylonitic foliation contains relics of an older tectonic foliation, which are locally preserved within (mica-rich) strain shadow near larger porphyroclasts. Moreover, in the central portion of the unit, the main foliation is inhomogeneously folded by post-metamorphic, N-S trending upright folds, which are not associated with any visible axial plane foliation. Consequently, the main mylonitic (Alpine) foliation in the sheared conglomerate is comparable with S_2 foliation in the Tralunca Flysch, which represent the most penetrative tectonic fabric recorded by this deposit (Rieuf, 1980). Grain size reduction within D_2 mylonites is mainly achieved by fracturing, affecting both quartz and feldspar porphyroclasts (Fig.1.6 and 1.7). Quartz commonly exhibits undulose and patchy extinction, irregularly shaped subgrains, (low angle) synthetic and (high angle) antithetic microfaults, microboudinage and kink bands. Deformation lamellae are common. Some grains show incipient fine-grained ($10-20\mu$) dynamic recrystallization, which mainly occur along grain boundaries at high angle from the main foliation, or along fractures and near crack tips. Microstructures suggest that quartz recrystallization mainly took place through bulging recrystallization (Drury & Urai, 1990). The proportion of recrystallized quartz is about 10%. Quartz porphyroclasts parallel to foliation frequently exhibit straight boundaries, and most of them appear as truncated grains, suggesting that diffusive mass transfer (e.g. pressure solution) occurred during shearing. Feldspar porphyroclasts commonly exhibit both synthetic and antithetic microfaults, being commonly mantled by fine-grained sericite tails. Deformation twins are locally developed. Muscovite is mainly deformed by slip along basal (001) plane, by microfolding and kinking. Marginal recrystallization into fine-grained sericite is locally developed. Biotite is

pseudomorphosed by chlorite. Quartz lattice preferred orientation (LPO) was investigated (by conventional U-stage measurement) in two samples from both eastern and western domain. Owing to the very small grain size of recrystallized grains, only quartz fabric from porphyroclasts was investigated. In both samples, quartz fabric is ill defined, showing some maxima scattered along the periphery in the [c]-axis pole figures (Fig.1.9). Main maxima are preferentially located close to Z-axis (sample SL3), or defining small circle around Z-axis (sample z3). In both samples, external monoclinic symmetry suggests dominant non-coaxial deformation and sinistral shear sense, being in agreement with the commonly observed microstructural criteria (e.g. Fig.1.6 and 1.7). The observed quartz fabric suggests that basal $\langle a \rangle$ slip was prevailing during D₂ Alpine shearing, possibly with minor contribution of rhomb slip (Schmid & Casey, 1986). The observed poorly defined C-axis pattern is likely partly related to widespread cataclasis affecting quartz porphyroclasts. The opening angle (measured across z axis, i.e. the foliation pole) is $\sim 50^\circ$ (sample z3), suggesting deformation in the temperature range of 300-400°C (Kruhl, 1998). Quartz microstructures suggest that D₂ mylonites developed in the lower part of the bulging recrystallization (BLG) regime, where intracrystalline plasticity is very limited, and brittle deformation dominates in quartz. Consequently, the temperature range can be constrained between 300° and 350°C (Stipp et al., 2002). The proposed temperature range is in agreement with the microstructures in feldspars, and with the observed comparable strength between quartz and feldspars porphyroclasts (Passchier and Trouw, 1996). The occurrence of high-pressure-low temperature assemblages within the Alpine mylonites from the eastern sector (A. Du Chaffaut & Saliot, 1979) was not confirmed by subsequent investigations (Libourel, 1985; Caby & Jacob, 2000). During this work, mafic to intermediate rocks sheared at basement-cover interface were sampled in several localities, such as in the surroundings of the *Olivetta* syncline (SE area, Ritsema, 1952) or near Mount Piano Maggiore. Microstructures from retrogressed mafic rocks are comparable to those described for Tomboni Conglomerate. In particular, within the amphibole-rich Qtz-diorite to melagabbros, hornblende recorded widespread cataclasis, but no evidences of high-pressure assemblages (i.e. development of blue amphibole and/or lawsonite) were found. From the data presented in this paper and from Libourel (1985), we can infer that the main Alpine tectonic foliation in S. Lucia nappe developed at T \sim 300-350°C, likely under normal geobarometric gradient.

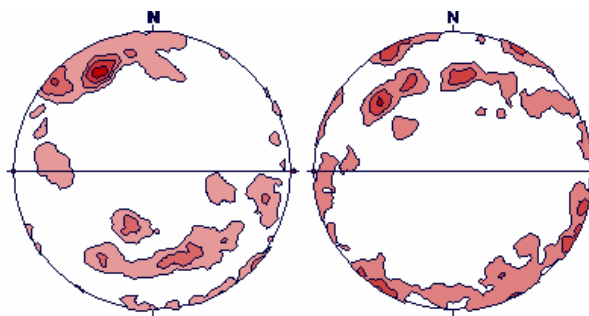


Fig. 1.9: CPO quartz porphyroclasts in S₂ Alpine mylonites in Tomboni Conglomerate. Sample SL3 (left) from *S. Rocco* locality (western sector); sample z3 (right) from *Borsolacce* locality (eastern sector). N=308 and n=304 respectively.

2 MAFIC COMPLEX

This chapter presents the results of field and microstructural investigations carried out in the western portion of the Mafic Complex (MC). This part of the work was mainly focussed on the roof of the complex, which had not been studied before. Moreover, systematic quartz LPO investigations were carried out in order to emphasize structural variations from the base to the roof of the MC.

2.1 Mafic Complex: field relations and microstructures

2.1.1 Introduction

In the western basement portion (i.e. westward from Mandriola Fault, Fig.2.1), the consistent orientation of fabric elements (foliation and lineation, see also Fig.3.11) demonstrate that the Alpine tectonic overprint did not modified both map-scale framework and mesoscopic pre-orogenic structures. However, a detailed microstructural analysis on basement rocks is difficult, due to widespread mineral alteration. Plagioclase is commonly transformed into fine-grained aggregate of albite, muscovite, calcite, epidote and quartz ('saussuritisation', Bard, 1980). Moreover, widespread serpentinization occurs within mantle rocks, and partly affects Opx-bearing metagabbros and meta-granitoids. Despite these problems, a restricted number of relatively 'fresh' thin sections were obtained for each representative rock type, allowing the description of the main (pre-Alpine) microstructural features in the whole MC.

In the lower and central portion, the MC is homogeneously deformed, displaying a steep, NW-SE trending, mylonitic foliation acquired at high temperature (Caby & Jacob, 2000). The pervasive main foliation exhibits a similar orientation in all units, being also concordant with the compositional layering in the meta-gabbroic series and with the long axis of felsic septa (Fig.2.1). The main foliation bears a pronounced stretching and mineral lineation, marked by the long axis of pyroxene, amphibole and feldspars porphyroclasts, and the long axes of recrystallized aggregates of the same minerals. Dominant sinistral shear sense is detectable from outcrop to thin section scale. This main fabric is locally overprinted by a second generation of more localized, discrete shear zones, which preferentially nucleated along Bt-rich layers in metasedimentary septa. These younger mylonites are usually geometrically and kinematically coherent with previous structures. Boudinaged layering, isoclinal and rootless folds, strongly flattened magmatic contacts, deformed veins and xenoliths represent common features within this highly deformed complex.

In contrast, the roof of MC (referred here as "diorite to granite suite", DGS) exhibits some compositional and structural peculiarities, which are summarized as follows:

- (i) DGS includes more differentiated rocks, where granitoids are largely prevailing on gabbroic rocks;
- (ii) No Grt-bearing septa occur in the granitoid-dominated DG suite;

- (iii) As a whole, this upper MC portion is more heterogeneously deformed, where some late-magmatic structures are preserved within restricted low-strain domains. This is markedly in contrast with what observed in the lower and central portion of MC where, owing to the nearly homogeneous high-temperature shearing, magmatic structures rarely escaped the solid-state overprint.

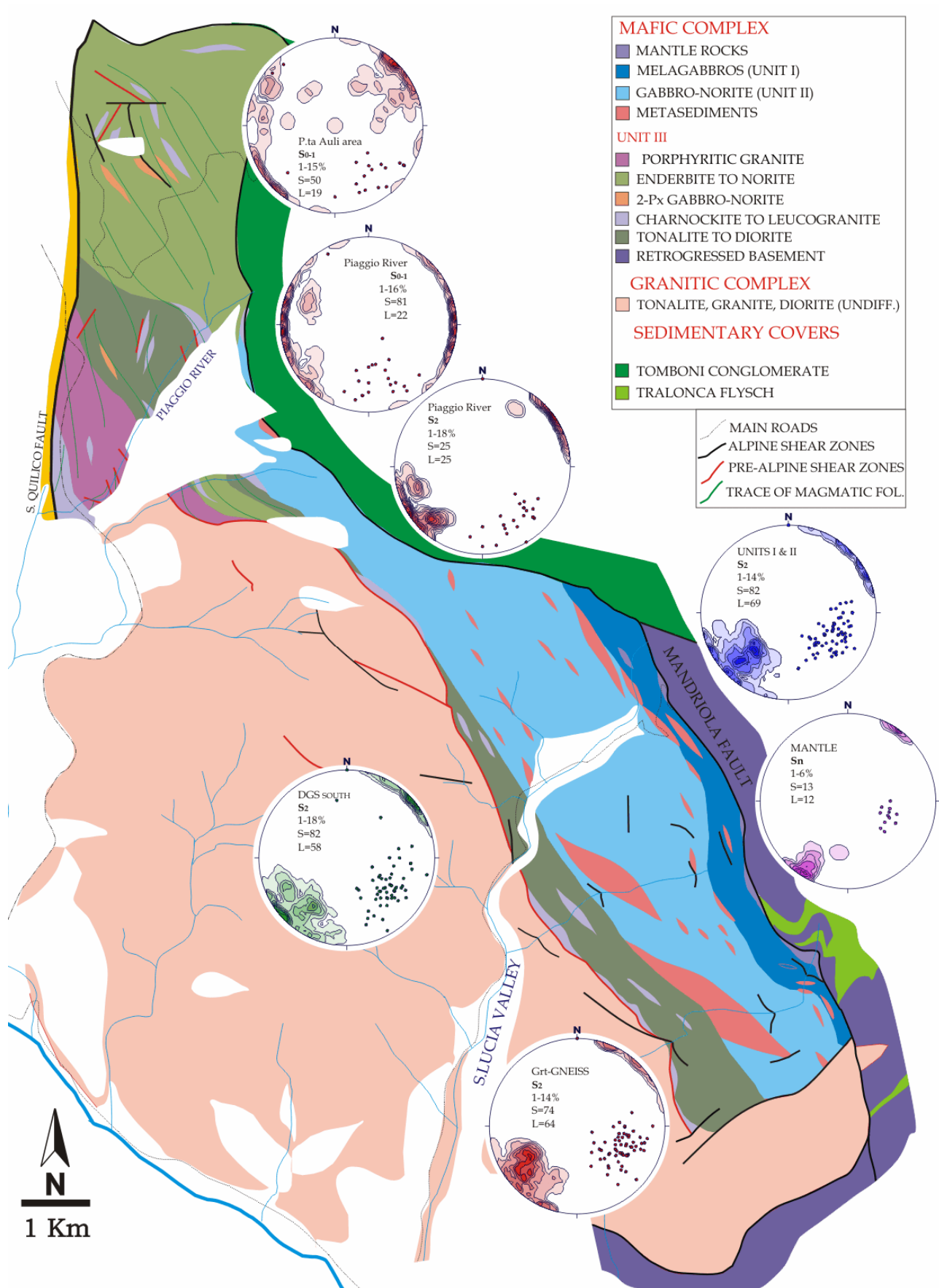


Fig. 2.1: Geological map of the western portion of the Mafic Complex. The foliation poles and the magmatic/solid-state lineation are plotted in each pole figure. Labels indicate (from top): (i) rock type\analyzed sub-area; (ii) type of foliation; (iii) contour interval; (iv) number of foliation poles data; (v) number of lineation data. The trace of the steeply inclined S₀₋₁ foliation is indicated for the northern portion of unit III, where it can be traced with continuity.

2.1.2 Mantle rocks

West of the Mandriola Fault, the present base of the MC is represented by thin (up to 50 mt-thick) slices of mantle rocks. The largest mantle slice (~50mt thick) crops out in the surroundings of *Mandriola*. It is the only mantle slice that escaped complete serpentinization.

At outcrop scale, Spinel-bearing lherzolites appear as brownish and massive LS tectonites, associated with mm to cm-thick Spl-bearing websteritic layers. Both rocks display mylonitic to ultramylonitic foliation, defined by the alignment of coarse Opx porphyroclasts (up to 2cm, Fig.2.6 and 2.7), and by disposition of websteritic layers, which are usually sub-parallel to the main foliation. These layers are locally isoclinally folded (Fig.2.4), displaying a well-developed axial-plane foliation and stretching lineation sub-parallel to the fold hinge (Fig.2.2 and 2.3). Contacts between lherzolite and websterite are usually sharp, even at thin section scale.

The main fabric in mantle rocks is roughly concordant with solid-state fabric in adjacent metagabbros (Fig.2.1). The shear sense is constantly sinistral, as revealed by the monoclinic symmetry of mantled porphyroclasts (e.g. this is partly visible in Fig.2.7). The rims of mantle bodies are usually largely serpentinized; therefore, the relationships with layered magmatites and Grt-bearing gneisses are virtually unknown. On the other hand, no gabbroic dykes are visible within the mantle body.

Olivine, Opx, Cpx and brown spinel are the main phases in the lherzolite. Brown Hbl and plagioclase represent accessory phases. Fresh olivine is hardly observable. Opx occurs as large and plastically deformed porphyroclasts, showing Cpx exsolution lamellae and Opx^{II} recrystallized grains. Because of the widespread serpentinization, detailed microstructural study was avoided here.

According to Libourel (1985), the older assemblage (equilibrated in the upper mantle, within the spinel facies; $T > \sim 1200^{\circ}\text{C}$; $P = 14 \pm 2 \text{ Kb}$) was strongly retrogressed during shearing from lower to mid crustal environment (final reequilibration at $T \sim 700^{\circ}\text{C}$; $P = 5 \pm 1 \text{ Kb}$).

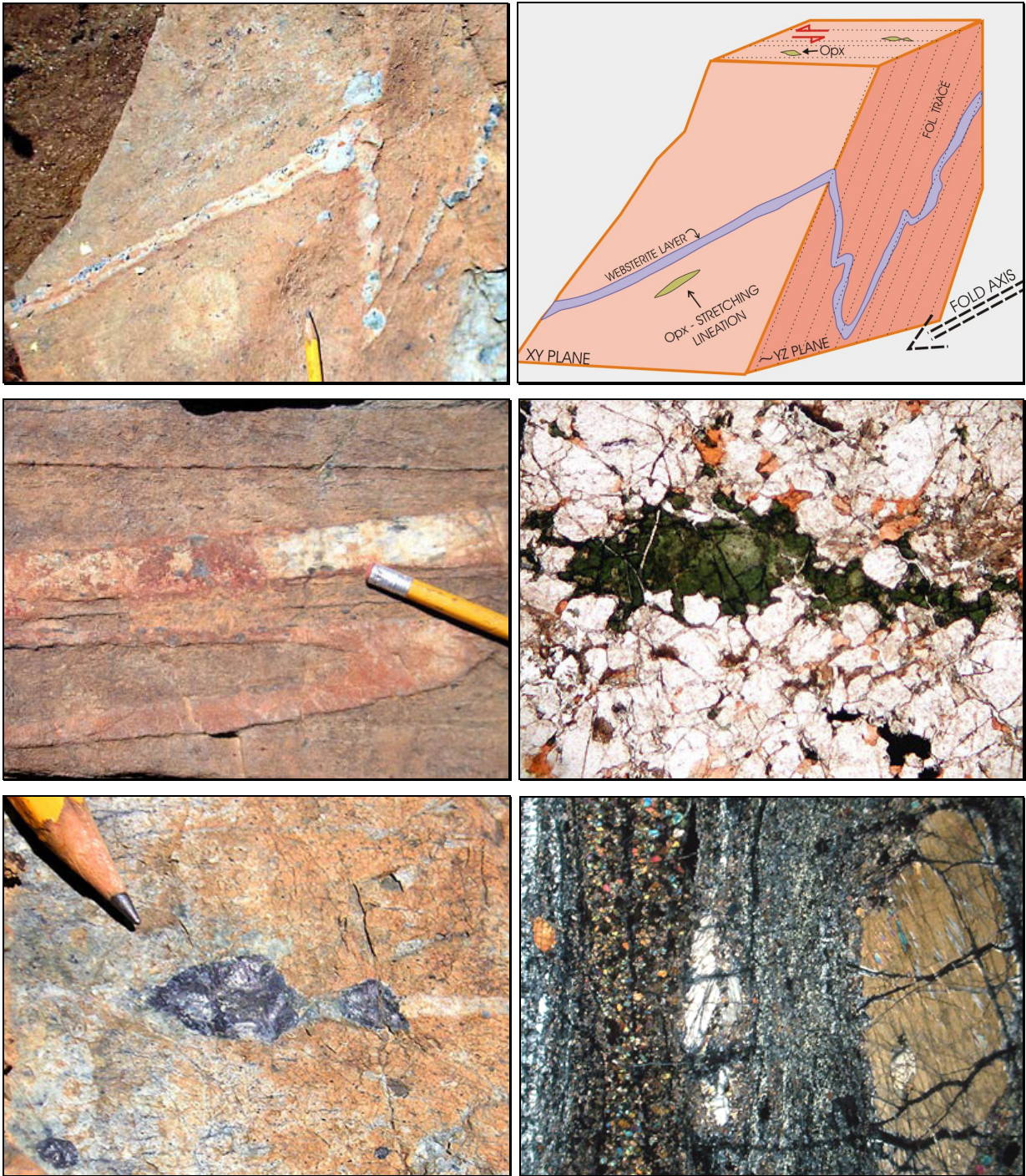


Fig. 2.2 (upper left) and **Fig. 2.3** (upper right): three-dimensional view of folded websterite layer in a mylonitic lherzolite. **Fig. 2.4** (centre left): another example of isoclinal fold, in a section nearly normal to the foliation and parallel to the stretching lineation. **Fig. 2.5** (centre right): detail of a 2-Px websteritic layer, with interstitial neoblasts of brown Hbl and green Spl (plane polarizer light; base of photo: 0.4 cm). **Fig. 2.6** (lower left): boudinaged Opx porphyroclast (serpentinized) in ultramylonitic lherzolite. **Fig. 2.7** (lower right): typical microfabric from porphyroclastic lherzolite, showing thin websterite layer (left hand side) and Opx porphyroclasts with Cpx exsolution lamellae (sinistral sense of shear; crossed polars; base of photo: 1 cm).

2.1.3 Gabbroic layered complex

The six magmatic units defined by Libourel (1985) are simplified here into three main units, identified on the basis of compositional and structural features.

Unit I includes (generally fine-grained) ultramafites to melagabbros; Unit II contains meso- to leucocratic coarse-grained gabbros. Both units are associated with Grt-bearing gneisses. Finally, in Unit III (which is treated separately, section 2.1.7), granitoids are prevailing and Grt-bearing gneisses are absent.

The various magmatic rocks could be described using the terminology of mafic granulites (because of the strong and pervasive HT tectonic overprint). Nevertheless, in agreement with previous workers, the igneous terminology will be used here, in order to underline the plutonic origin of mafic granulites.

2.1.3.1 Unit I: ultramafic rocks to layered gabbros

The striking feature of metagabbros from Unit I is represented by high-hornblende contents, associated with minor Cpx and plagioclase; large Opx phenocrysts may sporadically occur (Fig.2.12). The (present-day) base of the layered sequence is represented by medium- to fine-grained (from ~200 μ to ~3mm in grain size) hornblendite with cm-thick pyroxenite layers. Ultramafic rocks crop out discontinuously at the base of the layered pile (together with mantle rocks), reaching a maximum thickness of ~15-20mt. Owing to the high content in dark Hbl (60-90%) and dark green Cpx, ultramafites appear as medium grained, dark and massive SL tectonites. The alignment of these main phases underlines a well-defined planar and linear fabric. Transition to melagabbros takes place through gradual increase of Pl content. Here, mesoscopic magmatic layering is more evident, marked by variation in Pl content (from ~20 to 50%). Despite to the massive aspect of these melanocratic rocks, some local structures are indicative of the large amount of finite strain recorded by the base of MC. Metasedimentary xenoliths are locally boudinaged (Fig. 2.8) and igneous layering is commonly isoclinally folded (sheath folds are locally detected on the field).

In melagabbro, the compositional layering becomes progressively more evident upward, providing the gradual transition toward the layered gabbro subunit. This term is characterized by rhythmic magmatic compositional layering. Hbl represents the main phases, associated with Cpx and Pl. Different proportions of these minerals typify different layers: darker ones are Hbl-rich, whereas light layers are usually anorthositic to leucogabbroic (Hbl-free) in composition. Isolated Opx phenocrysts (now porphyroclasts) may locally occur within darker layers (Fig.2.12). The transition between different layers is commonly sharp, even at thin section scale (fig 2.13). According to Libourel (1985), the compositional layering is due to 'oscillatory in situ crystallization', joined with synmagmatic diffusional processes. Near contacts with granulitic metasediments, large and isolated garnet grains locally occur in the gabbroic rocks, testifying the gabbro-granulite transition (Libourel, 1985).

Pegmatoid norite to enderbite veins and minor anorthosite dykes locally occur within unit I. Depending on their original orientation, these dykes were severely boudinaged

(Fig.2.15) or folded (Fig.2.9). Therefore, these intrusions predate (or are contemporaneous with) the development of the main mylonitic fabric. Isoclinal (commonly rootless) and nearly similar folds commonly display manifest axial plane foliation, which is well evident in the hinge zone (Fig.2.9).

Despite the massive appearance at outcrop scale, a well-defined foliation is present in hornblende at thin section scale, marked by well-defined alignment of Hbl grains. This alignment might partly represent a primary feature related to magmatic flow, as suggested by the presence of large and subhedral brownish amphibole grains displaying primary features such as Ap and Zrn inclusions and partly preserved magmatic grain boundaries. Larger Hbl grains (up to 0.5cm in length) form a load-bearing framework (in the sense of Handy, 1990), where interstitial space is filled by smaller Hbl and minor Cpx grains (Fig.2.11). This matrix shows an average grain size of about ~50-100 μ . Deformation features are rarely detectable at grain scale: undulose extinction, subgrains, microfaults and clearly visible recrystallized grains are uncommon within these Hbl-rich domains. Consequently, the observed seriate distribution of grain size could be partly related to magmatic processes. These microstructures were defined as 'adcumultic' to 'mesocumultic' by Libourel (1985), implying that the frequently observed subhedral to anhedral shape of Hbl grains might partly represent a primary feature of melagabbroic rocks. Grain scale deformation features are much more evident in layered gabbros. Within leucocratic layers, Cpx and Pl polygonal grains develop monomineralic ribbons, defining a tectonic foliation concordant or at low-angle (~10°-20°) with magmatic layering (Fig. 2.13). Within the aggregates, Cpx is locally arranged with triple junction contacts and interfacial angle of about 120°. Cpx porphyroclasts exhibit a well defined SPO and aspect ratio up to 3:1. Larger grains are surrounded by smaller grains in pressure shadow positions, suggesting syntectonic recrystallization. Both Cpx-Pl and Pl-Pl grain boundaries are gently curved to interlobate, suggesting the occurrence of grain-boundary reworking (by diffusional processes?). Within Pl-Hbl layers, Hbl shows some deformation features such as undulose extinction, subgrain formation and core and mantle structure (Fig. 2.14). The surrounding feldspar grains exhibit well-rounded and flattened shape, suggesting plastic deformation. Strain partitioning between different but spatially associated rocks might occur within the lower part of MC: Hbl-rich ultramafites and melagabbros, which dominate at the base of the complex, seems less deformed at grain scale. In contrast, more felsic rocks such as layered gabbros and felsic granulites (section 2.1.4) exhibit well-defined mylonitic foliation. These observations suggest that hornblende behaved as the strongest mineral phase, during the development of the main solid-state fabric.

Deformation behaviour of amphiboles is still poorly understood, and it is usually difficult to determine the dominant deformation mechanisms (Berger & Stünitz, 1996; Kruse & Stünitz, 1999). Cataclasis at grain scale, with slip along cleavage planes may produce 'false' subgrain and core and mantle structure (Nyman et al., 1992). This seems the case of Fig. 2.14, where subgrain boundaries are represented by the traces of cleavage planes. Crystal plasticity is difficult in hornblende (Berger & Stünitz, 1996), and amphibole is inferred to be stronger in ductile deformation than pyroxene and plagioclase, even at high-grade conditions (Lafrance & Vernon, 1993; Passchier & Trouw, 1996). Moreover, a greater strength is expected for rocks where Hbl forms a load-bearing framework (Brodie & Rutter, 1985).

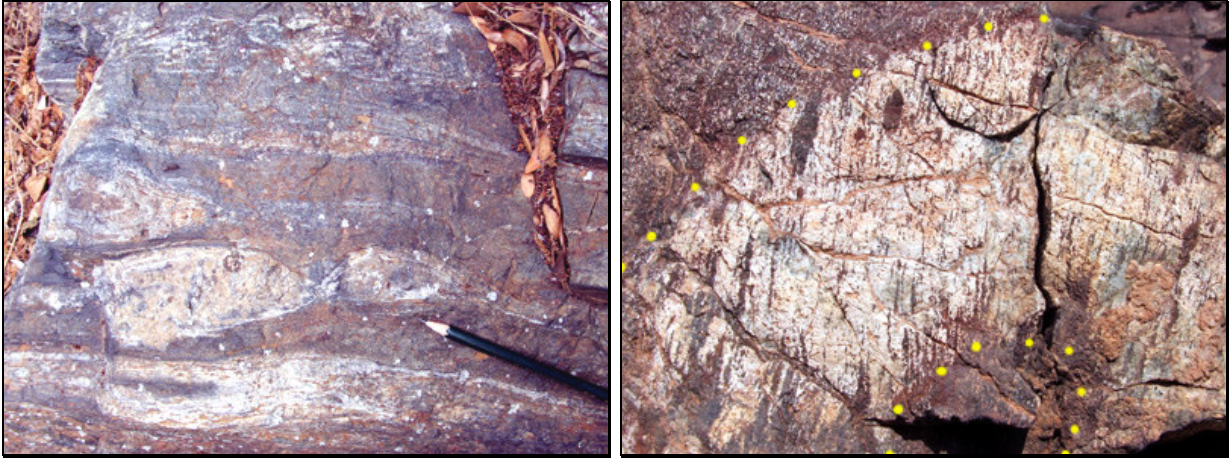


Fig. 2.8 (left): boudinaged biotite-rich (metasedimentary?) xenoliths in mylonitic melagabbro. **Fig. 2.9** (right): detail from the hinge zone of a folded coarse-grained norite dyke, injected into host melagabbro. The outline of the fold hinge is dotted. Note the strong axial plane foliation, highlighted by stretched Opx porphyroclasts.

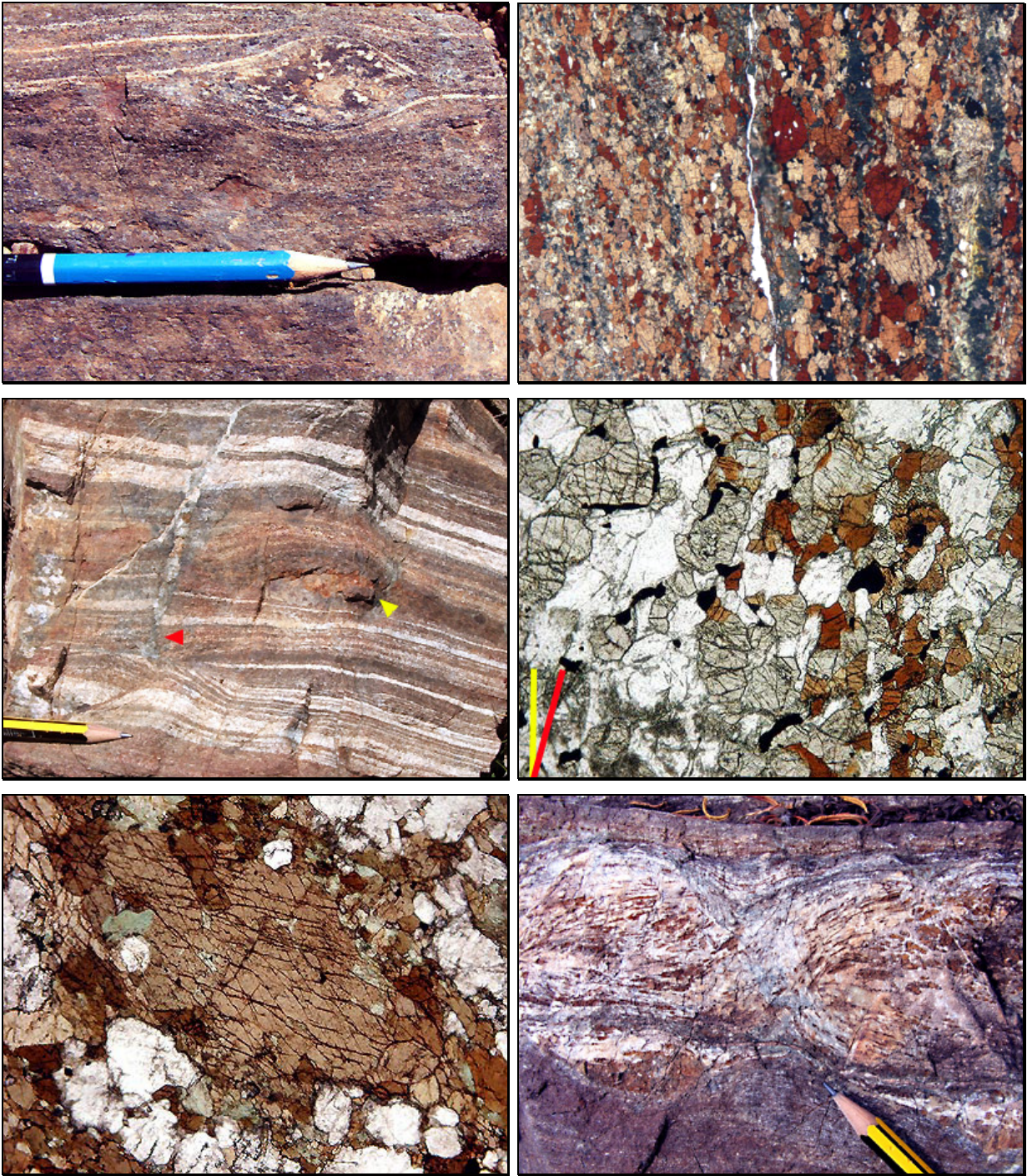


Fig. 2.10 (upper left): detail of augen-shaped coarse-grained gabbro relict within a strongly foliated melagabbro. **Fig. 2.11** (upper right): microstructure from the homogeneously foliated portion of outcrop shown in Fig. 2.12: the alignment of larger Hbl grain was likely achieved during magmatic flow. Note the compositional layering due to different proportions of Hbl and Pl (plane polarized light; base of photo: 1cm). **Fig. 2.12** (centre left): boudinaged layering (parallel to mylonitic foliation) in a layered gabbro. Red arrowhead point to a minor high-angle fault sealed by undeformed gabbroic magmas. Yellow arrowhead indicates the occurrence of large Opx porphyroclasts. **Fig. 2.13** (centre right): sharp transition between melagabbro and leucogabbro layers in layered gabbro. Yellow and red lines indicate the trace of compositional layering and the superimposed solid-state fabric, respectively (plane polarized light; base of photo: 4mm). **Fig. 2.14** (lower left): detail of Hbl-Pl layer in melagabbro showing core and mantle microstructure in nearly euhedral Hbl porphyroclast. Note that in some cases SGBs coincide with cleavage plains (section normal to both foliation and mineral lineation; plane polarized light; base of photo: 1.8mm). **Fig. 2.15** (lower right): boudinaged enderbite (Opx-bearing tonalite) vein injected into mylonitized melagabbro. Note the extreme and inhomogeneous stretching of Opx porphyroclast.

2.1.3.2 Unit II: coarse-grained gabbro and gabbro-norite

This is the main term of the complex, reaching an average thickness of ~600-700m. Discontinuous septa of Grt-bearing gneiss (up to 100 m-thick) separate this unit from adjacent layered gabbro. Near the base, the gabbro is usually fine-grained and fairly melanocratic; dark and fine-grained (Hbl-rich) layers are quite common at this pluton level. The gabbro gradually becomes coarse-grained and more leucocratic upwards. Moreover, the gradual decrease in Cpx content is mirrored by the increase in Opx content. As a whole, this unit is much more homogeneous than Unit I.

Several mesoscopic structures occur, highlighting the extreme deformation recorded by this complex. Dark and fine-grained Hbl-rich layers, pegmatoid norite-enderbite and leucocratic (Cpx-rich) layers are frequently boudinaged and folded within the main foliation. Commonly the solid-state foliation lies in the axial plane of these similar folds (fig.2.16 and 2.17), whereas the stretching lineation is approximately parallel to the fold hinge. Boudin necks are locally filled by granitoid to gabbroic melt patches (section 2.2.4). Here, the extension direction within boudins is commonly parallel with the local trend of stretching and mineral lineation. Coarse-grained norite to websterite lenses are locally preserved within the intensely sheared metagabbro (Fig.1.3A).

Because of the increased grain size, the solid-state foliation is more evident in unit II, as defined by alternation of polycrystalline Pl and Cpx-Opx recrystallized trails (Fig.2.18). Well-defined stretching and mineral lineation are usually present, underlined by recrystallized aggregates of pyroxene and plagioclase.

One of the rare examples of partly preserved magmatic structures is shown in figure 2.20a, where fine-grained noritic enclave is aligned in the magmatic foliation of the host two-Px gabbro. At thin section scale, Opx magmatic phenocrysts are surrounded by fine-grained Opx-Pl-Bt granoblastic tails (Fig.2.20b), whereas Cpx exhibit incipient core and mantle microstructure (Fig.2.20c). Consequently, this weakly deformed gabbro displays a moderate high-temperature solid-state overprint, which developed sub-parallel to pre-existing magmatic anisotropy. This fabric is sharply truncated by nearly ultramylonitic shear zone, which likely nucleated along the boundary with metasedimentary septa. Here, Opx porphyroclasts are partly replaced by biotite and quartz (Fig.2.20e). This reaction ($\text{Opx} + \text{Kfs} \rightarrow \text{Bt} + \text{Qtz}$; described by Libourel, 1985) highlights the syndeformational retrogression from granulite to amphibolite assemblages. Within more strained domains, scattered Opx porphyroclasts are surrounded by a very fine-grained mylonitic matrix (~1-10 μ), composed by nearly equidimensional biotite, plagioclase, cordierite and quartz grains (Fig.2.20d). Moreover, quartz grains exhibit a weak LPO, as qualitatively checked with the gypsum plate. These microstructures suggest that diffusion-assisted grain boundary sliding might contribute to deformation ("SP mylonites"; Boullier & Gueguen, 1975) within these fine-grained domains.

In the coarse-grained, upper part of the unit II, Opx ribbon grains occur (~0.2-0.5 cm in length, with aspect ratio up to 5:1), exhibiting sweeping undulose extinction, which is indicative of plastic deformation at high temperature (e.g. Suhr, 1993). Recrystallization process in pyroxene commonly led to complete replacement of former porphyroclasts (Fig.2.39). Pyroxene syntectonic aggregates display an average grain size of about 200 μ . Microprobe analysis (chapter IV) reveals that Opx newgrains exhibit comparable

composition to those of host porphyroclasts. Plastic deformation in Opx is locally overprinted by microboudinage, with serpentine-filled necks suggesting that, at least locally, deformation continued under retrograde conditions.

Plagioclase occurs as large porphyroclasts (up to 1cm in length) with strong SPO and aspect ratio between ~3:1 and 5:1. Core and mantle structure is commonly visible. Recrystallized plagioclase occurs as granoblastic aggregates with an average grain size of ~100-200 μ , commonly with strongly serrate grain boundaries, suggesting extensive recrystallization.

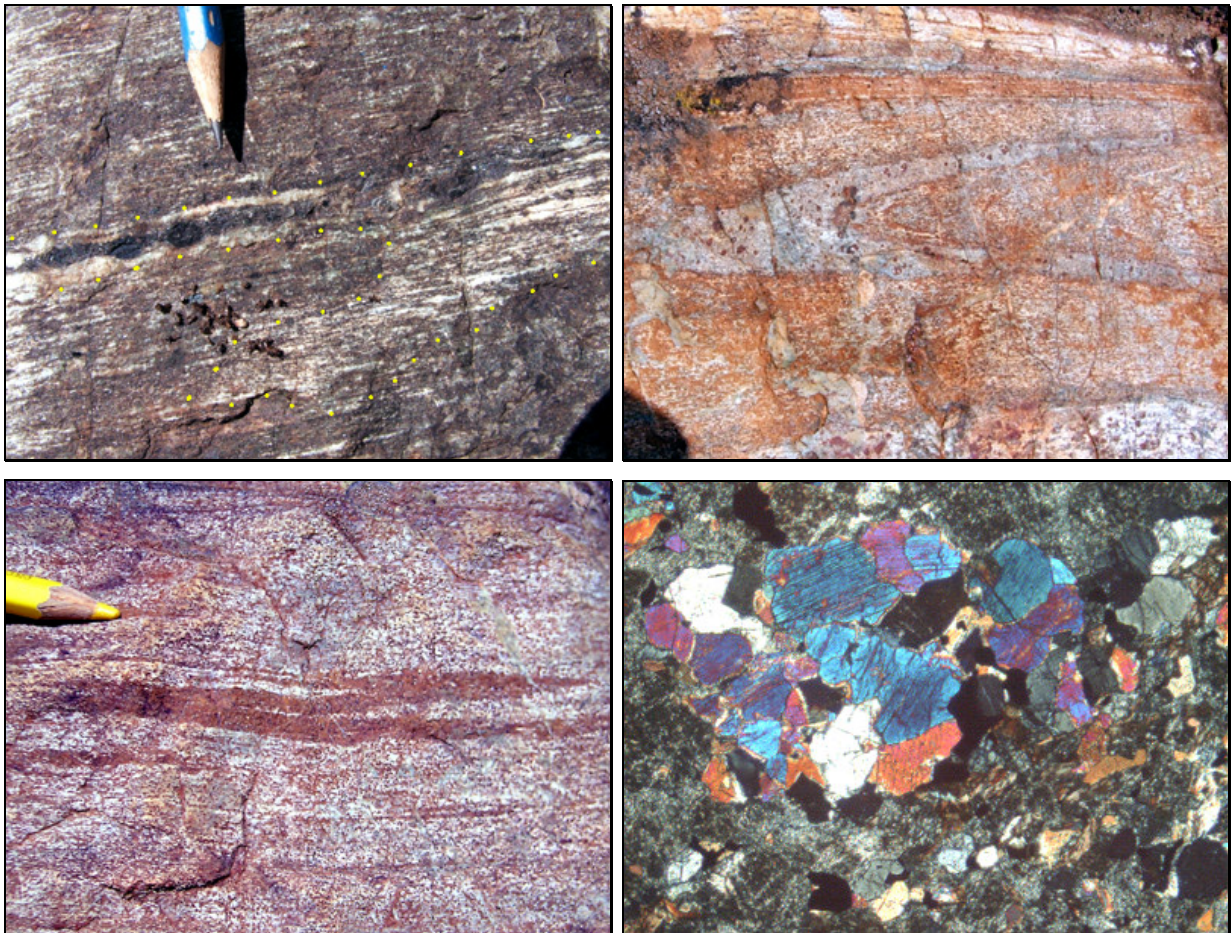


Fig. 2.16 (upper left): folded and sheared gabbroic pegmatite intruded into host 2-Px gabbro. The fold outline is dotted. The more competent (dark) Hbl porphyroclasts are weakly deformed respect to Px and Pl. **Fig. 2.17** (upper right): isoclinally folded Grt-bearing quartzofeldspathic layer in fine-grained gabbro-norite. Note the nearly perfect similar geometry and the strong axial plane foliation (base of photo: 10cm). **Fig. 2.18** (centre left): boudinaged isoclinal (rootless) fold from Hbl-rich layer within host fine-grained two-Px gabbro-norite, at the base of unit II. **Fig. 2.19** (centre right): typical microfabric from two-Px gabbro, showing augen-shaped recrystallized Cpx aggregate, likely replacing former Cpx phenocryst, in a groundmass of completely altered, An-rich plagioclase. Brown grains are Hbl and Bt (crossed polars; base of photo: 3mm).

In the uppermost portion of MC, dark and fine-grained dioritic dykes conformably intrude the gabbro-norite unit (see detail from the sheared magmatic contact, Fig.2.21). The occurrence of these Hbl-rich layers marks the transition zone toward the Unit III (diorite-granite suite, DGS). As observed within previous units, the transition takes place gradually; gabbro-norite and diorite are interlayered over a few tens of meters. This transition apparently takes place without discordant crosscutting relations. As described by Libourel (1985), diorite unit represents the uppermost and younger unit in the gabbroic layered sequence. The magmatic relationship between gabbroic rocks and diorites is strongly suggested by field relations, where magmatic contacts predate the main deformation event.

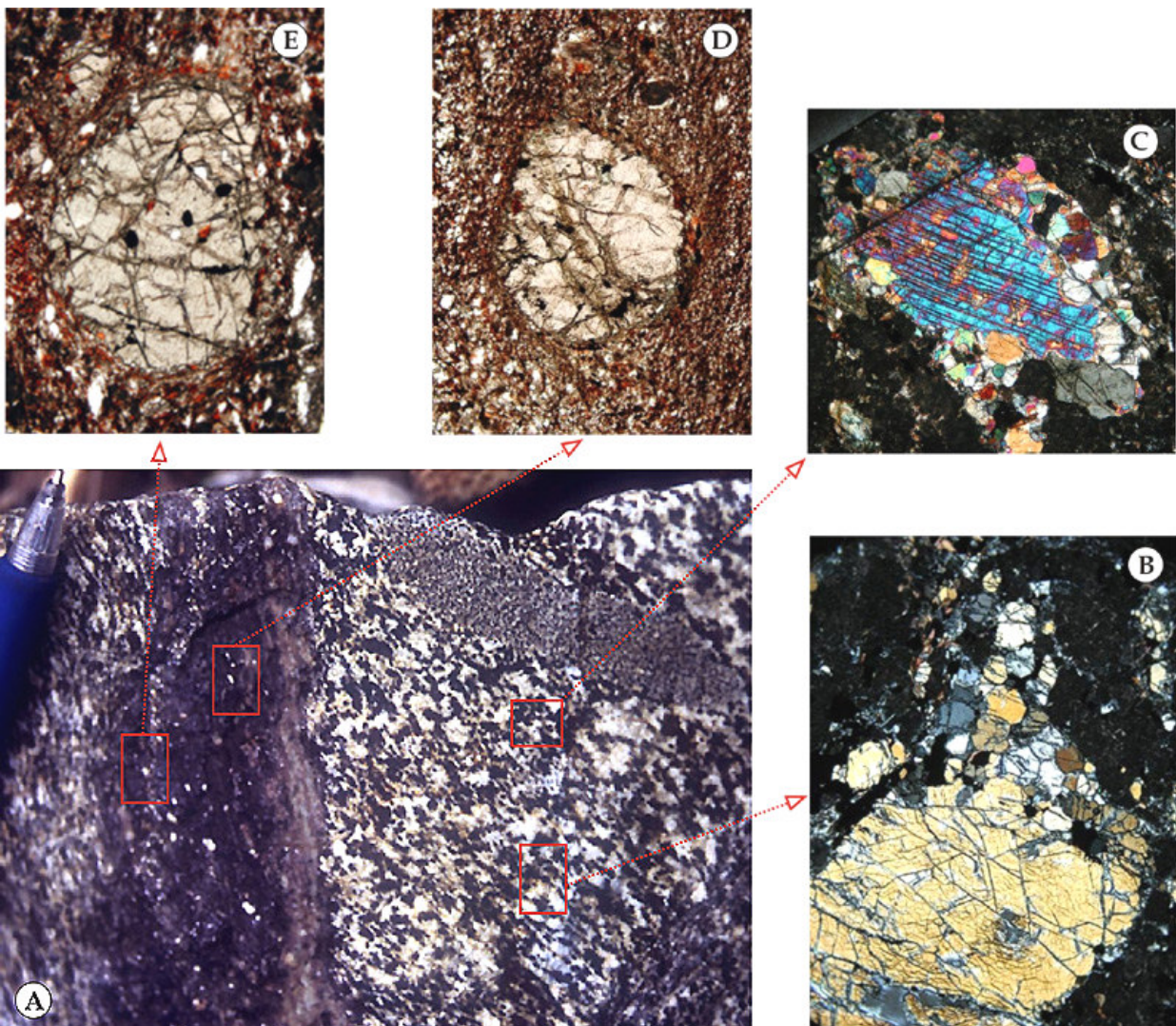


Fig. 2.20 [A]: polyphase deformation in a rare example of moderately deformed gabbro-norite with norite enclave. [B]: detail of gabbro-norite with Opx porphyroclast and syntectonic tail made up of Opx, Bt and Pl (crossed polars; long side of photo: 4mm). [C]: Detail on core and mantle microstructure in Cpx (crossed polars; base of photo: 2mm). [D] and [E]: microstructures from the localized shear zone, showing the destabilization of Opx porphyroclasts, with the syntectonic development of Bt, Pl and Qtz (plane polarized light; long side of photo: 0.7mm for D and 1.8mm for E).

2.1.4 Grt-bearing paragneiss and quartzofeldspathic granulites

This group of rocks includes Grt-bearing mylonitic gneisses, which are embedded within the meta-gabbroic series. These rocks crop out as lenticular and elongate bodies (“septa”), which rarely exceed few tens of meters in thickness. The interlaying of metagabbros and Grt-bearing gneisses occurs from map- to centimetre scale (Fig.2.26). Contacts against metagabbros are usually sharp (Fig.2.22). Grt-bearing rocks are characterized by the alternation of cm- to dm-thick quartzo-feldspatic and ferromagnesian layers (Fig.2.21). The irregular and discontinuous compositional layering is concordant with the mylonitic fabric in both metasediments and adjacent mafic granulites (i.e. metagabbros). Two end-member layers are detectable (Fig.2.21):

- (i) Medium- to fine-grained (white-weathered) quartzofeldspathic layers, which contain $Qtz + Pl \pm Kfs \pm Grt \pm Rt$;
- (ii) Fine-grained, dark and massive, ferromagnesian (“restitic”) layers, where Grt, Opx, Sill and Pl porphyroclasts are scattered within the $Bt + Pl + Qtz \pm Crd$ matrix (Libourel, 1985; Caby and Jacob, 2000). The transition between these end member layers is achieved through the gradual increase in femic content, mirrored by a decrease in quartz and K-feldspar content.

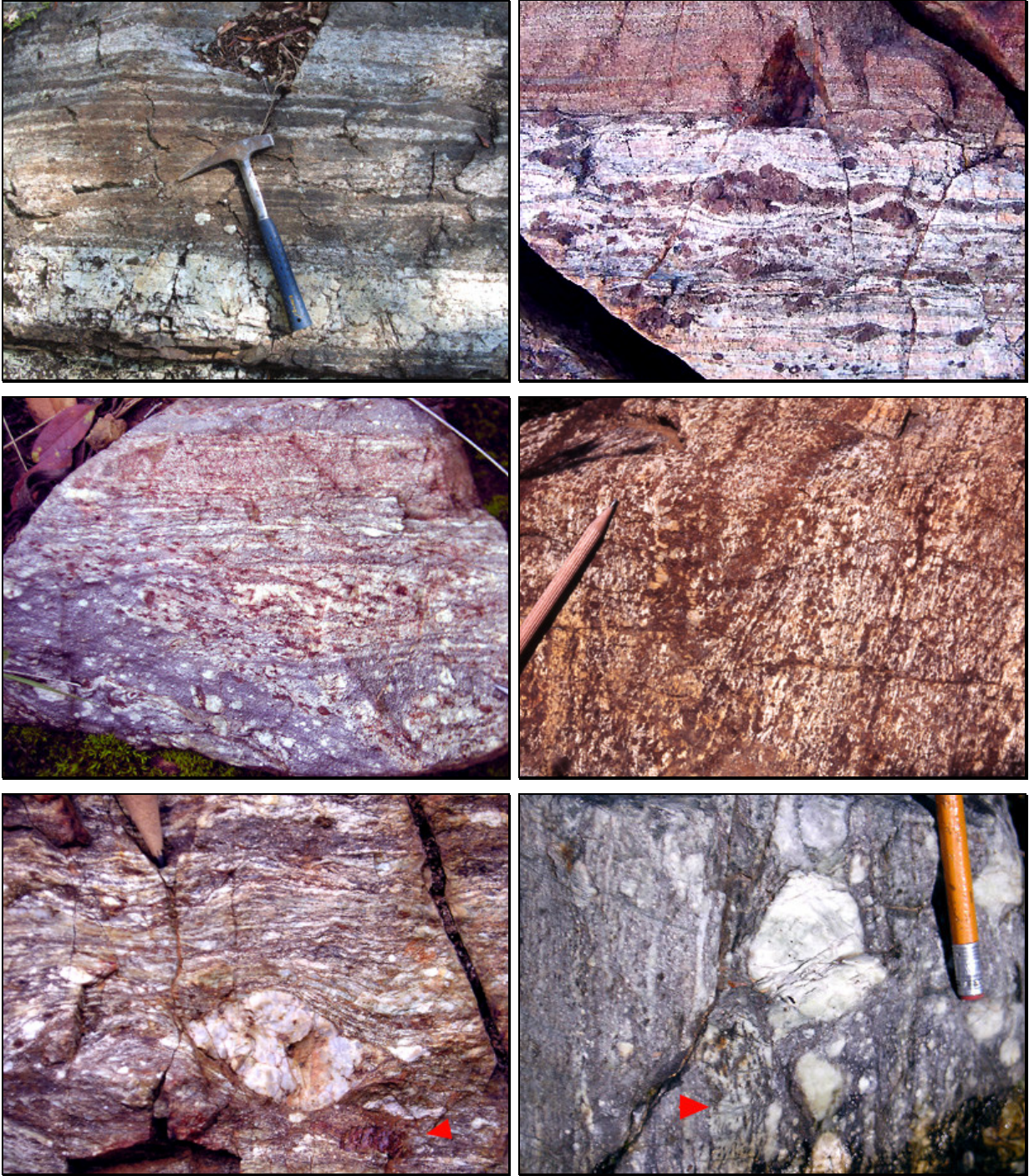
Close to the roof of unit II, some pegmatoid layers contain plagioclase megacrysts (up to 6cm in diameter) embedded in a fine-grained and Bt-Pl rich matrix (Fig.2.27 and 29).

According to Libourel (1985), the geochemical signature of ferromagnesian septa suggests that these layers represent restitic paragneiss deriving from a pelitic protholith. Thus, the compositional layering within Grt-bearing septa might represent the sheared end product obtained from pervasive solid-state overprint superimposed on a former migmatite (for example, a former leucosome/melanosome stromatic sequence). Indeed, the occurrence of deformed (i.e. folded and boudinaged) quartzofeldspathic layers, isolated within orthogneisses, might represent sheared leucosome dykes injected into metagabbroic rocks. In the deepest portion of the Ivrea crustal section, analogous anhydrous granitoids ($Qtz + felds \pm Grt \pm Opx$) are named ‘leucocratic charnockites’ (Sinigoi et al., 1994). These authors documented that the anhydrous granitic melt was extracted from granulite-facies metapelites. In our case, because no primary meso- and microstructures are clearly identifiable, the purely descriptive terminology of “quartzofeldspathic” and “ferromagnesian” end-members is adopted here.

At grain scale, quartzofeldspathic granulites are classifiable as striped gneisses, where coarse-grained monomineralic quartz layers are alternate with fine-grained plagioclase (and, less commonly, K-feldspar) layers.

Within quartz-rich layers, single quartz grains locally exhibits exaggerated grain growth. As an example, in the 5mm-thick ribbon shown in Fig.2.28, the four interfingered quartz grains (“island grains”, or “dissection microstructure”; Urai et al., 1986), occupy ~30% of the thin section surface. In contrast, where non-quartz material is more abundant (e.g. Fig.2.31), quartz ribbons are commonly 1 grain-thick, developing Qtz-Qtz grain boundaries at high-angle from the foliation trace (type 3 ribbons of Boullier & Bouchez, 1978). Ribbons boundaries parallel to the foliation are commonly sharp and smooth against feldspar layers. Single ribbon-forming grains usually display very irregular

outline, and mosaic-like pattern (Gapais and Barbarin, 1986) is commonly present (Fig. 2.28 and 2.29). This morphology of grain boundaries is probably due to high crystallographic control (Lister & Dornsiepen, 1980), being the typical microfabric in rocks equilibrated at high-temperature (Kruhl & Peternell, 2002).



Some mesoscopic features from Grt-bearing gneisses. **Fig. 2.21** (upper left): typical outcrop-scale appearance of layered Grt-bearing gneiss, displaying irregular alternation of quartzofeldspathic and ferromagnesian layers. **Fig. 2.22** (upper right): Mylonitized contact between felsic granulite and meta-gabbro-norite. Sinistral shear sense defined by monoclinic symmetry of deformed Grt porphyroclasts and C' shear bands. **Fig. 2.23** (centre left): coarse-grained fabric within Grt-bearing gneiss truncated by nearly ultramylonitic Pl-Bt-Qtz shear zone (base of photo: 10cm). **Fig. 2.24** (centre right): tight mylonitic fold within Grt-rich gneiss, displaying axial plane foliation and fold axis nearly parallel to stretching lineation. **Fig. 2.25** (lower left): mylonitic gneiss with coarse-grained Pl and Grt porphyroclasts (arrowhead). The foliation is defined by the alternation of Pl-rich (white) and Bt-rich (dark) layers. Sinistral shear sense. **Fig. 2.26** (lower right): detail from biotite-rich pegmatoid septa (with deformed plagioclase megacrysts) including boudinaged layer of metagabbro (red arrowhead).

Few intracrystalline deformation features are visible in quartz, where only ~20-30% of grains exhibit well-developed SGBs, displaying both prismatic and basal orientation. This might indicate that most of the intracrystalline strain energy was stored within Qtz-Qtz grain boundaries. Undulose extinction is present in some sample, being probably related to weak low-temperature overprint.

Kfs is commonly completely recrystallized, but strongly deformed mesoperthite clasts may locally occur, showing serrate grain boundaries, undulose extinction, core and mantle structure and gradual transition between subgrains and newgrains. Strain-induced myrmekite (Simpson, 1985; Simpson and Wintsch, 1989) are uncommon within Kfs porphyroclasts. Subgrains occur in the outer rim of porphyroclasts (with an average grain size of ~30-50 μ), providing the gradual transition toward the neoblasts in the mantle, which show comparable grain size. Fine-grained Kfs-layers display equigranular and interlobate aggregates. Grain boundaries are commonly serrate and interlobate. Plagioclase exhibits comparable microstructures: the rare porphyroclasts (which escaped from complete recrystallization) are plastically deformed (Fig.2.28). Plagioclase recrystallization likely occurs mainly by SGR recrystallization (Fig.2.27). However, owing to the occurrence of lobate and serrate Pl-Pl grain boundaries, a contribution from diffusional processes (Rosenberg & Stünitz, 2003) and/or grain boundary migration (Lafrance et al., 1995) cannot be completely ruled out. The grain size of neoblasts is commonly ~30-50 μ , for both plagioclase and K-feldspar. As qualitatively checked (in several thin sections) with the gypsum plate, recrystallized feldspars grains exhibit (at least locally) a remarkable LPO.

Garnet is usually euhedral to subhedral within monomineralic quartz layers (Fig.2.28), behaving as rigid (more competent) objects respect to the quartzofeldspathic matrix. Grt porphyroclasts are affected by a dense network of grain-scale fractures, which usually do not produce relative displacement of fragments (e.g. Fig.2.32).

In rare cases, garnet exhibits some clues of plastic deformation, as suggested by the occurrence of pinch and swell microstructure and sigmoidal shape (Fig.2.29). These microstructures are only present where Grt grains are enclosed within Qtz layers. In contrast, Grt within feldspar or mixed matrix are commonly deformed by brittle processes alone (Fig.2.31 and 2.32). These observations fit the findings of Kleinschrodt and McGrew (2000); these authors described that brittle and plastic deformation processes cooperate during garnet deformation under granulite-facies conditions.

In summary, quartzofeldspathic septa exhibit a relatively simple microstructure, where nearly totally recrystallized quartz and feldspars are associated with weakly deformed garnet porphyroclasts. Usually these domains do not exhibit any sign of retrogression.

Instead, microstructures from ferromagnesian layers offer more opportunities to unravel the subsequent steps of the tectono-metamorphic evolution. These rocks contains a restitic assemblage, with Pl, Kfs, Bt, Grt, Opx, Qtz, Crd. Mylonitic foliation is widespread developed, and two main metamorphic assemblages are present (Libourel, 1985; Cabyl & Jacob, 2000):

- (i) D_1 : Grt-Kfs-Qtz-Bt-Pl-Rt \pm Opx \pm Sill \pm Spl
- (ii) D_2 : Opx-Bt-Crd-Qtz-Pl

D₁ assemblage (P=7±1 Kb; T~800°C, Libourel, 1985) is largely destabilized: Grt is commonly anhedral, with amoeboid shape and strongly curved grain boundaries. The final shape of Grt is probably the effect of deformation during mylonitization, joined with corrosion by D₂ assemblages. Kfs is generally totally consumed. Opx is rarely present within D₁ assemblage (Libourel, 1985). In contrast, it commonly develops secondary aggregates with Crd, derived from Grt destabilization (Grt+Qtz+H₂O → Crd + Opx). Voids in Grt (due to embayment) are commonly filled by Opx, Bt, Crd, Pl and Qtz. This younger assemblage marks the final steps of retrograde evolution (P=4.5-6 Kb; T=700°-800°C, Libourel, 1985). An example of the syndeformational retrograde reaction is shown in Fig.2.30.

Within intermediate rocks, Grt voids are commonly filled by quartz alone (Fig.2.33). Incipient embayment produces a peculiar microstructure, which superficially could evocate the occurrence of pre-tectonic porphyroblasts (Fig.2.32). In fact, in two-dimensional sections garnet shows well-rounded (apparently undeformed) quartz inclusions. However, these “internal” quartz grains are often in optical continuity with the ribbon-forming grains in the mylonitic matrix, suggesting that “internal” quartz blebs derive from syndeformational infilling, which likely took place during the development of the main fabric. The interpretation of quartz blebs as “false inclusions” is also corroborated by quartz LPO investigations.

Owing to the absence of *true* inclusion in garnet (with the exception of rare biotite flakes), the relative timing relationship between the development of D₁ assemblage and the main mylonitic fabric is not well constrained. On the other hand, D₂ assemblage is clearly syntectonic respect to the main solid-state fabric (Fig.2.30). As the widespread feldspar alteration largely prevents detailed microstructural investigations within ferromagnesian layers, here is assumed that D₁ and D₂ assemblages developed subsequently during the main deformation event (i.e. garnet might represent early syntectonic porphyroblasts). This is indirectly confirmed by the geometrically homogeneous retrograde evolution preserved in the roof of the MC (section 2.2.7.3).

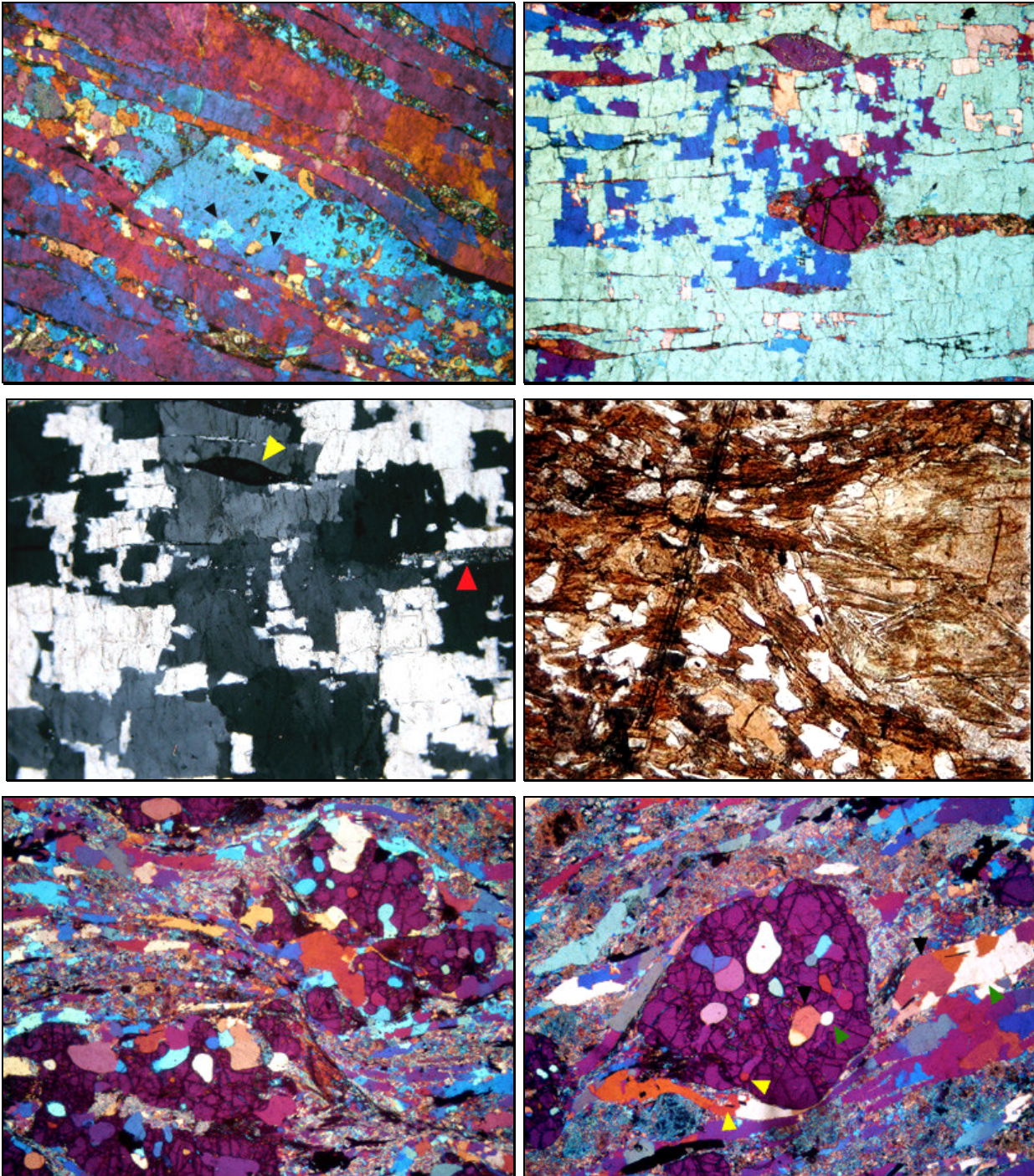


Fig. 2.27 (upper left): microstructures from quartzofeldspathic granulite. These striped gneisses are composed of alternating layers of nearly completely recrystallized Qtz and feldspars (mainly Pl). Plagioclase porphyroclasts exhibit a gradual transition between subgrains (arrowheads) and recrystallized grains in the mantle (crossed polars; gypsum plate inserted; base of photo: 1.8 mm). **Fig. 2.28** (upper right): detail of a 5mm-thick nearly monomineralic quartz layer displaying mosaic-like pattern, enclosing sigmoidal plagioclase porphyroblast and recrystallized aggregates. In contrast, garnet is nearly euhedral (crossed polars; gypsum plate inserted; base of photo: 4mm). **Fig. 2.29**: (centre left): another example of mosaic-like Qtz aggregate enclosing sigmoidal Gtr (yellow arrowhead) and thin trail of recrystallized plagioclase (red arrowhead; crossed polars; base of photo: 4mm). **Fig. 2.30** (centre right): mylonitic foliation in ferromagnesian septa, where the syntectonic Bt- Qtz- Pl (D_2) assemblage largely replaced Opx porphyroclasts. This sample derived from the outcrop shown in Fig.2.36 (plane polarized light; base of photo: ~1.8mm). **Fig. 2.31** (lower left): intermediate gneiss showing widespread embayment in Grt, where voids are filled by quartz alone (crossed polars; gypsum plate inserted; base of photo: 4mm). **Fig. 2.32** (lower right): detail from an apparent pre-tectonic Grt porphyroblast. Pairs of arrowheads with the same colour indicate different grain portions in optical continuity (crossed polars; gypsum plate inserted; base of photo: 4mm).

2.1.5 Evidences of synmagmatic deformation

The preservation of syn-magmatic microstructures and fabrics depends on several factors, and it is expected to be uncommon in deep-crustal plutons, where they are usually severely overprinted by subsequent solid-state fabric (e.g. see discussion in Miller & Paterson, 1994).

Within units I & II, despite the widespread mylonitization, field evidences suggest that some former melt was still present (at least locally) during the development of the main fabric. In fact, undeformed (or weakly deformed) gabbroic and granitoid material (inferred to represent former melt) occur in two distinct settings.

Medium-grained gabbroic pockets occur as boudin neck-infill or along small shear zones. In Fig.2.33, the amphibole-rich layer is boudinaged within the less competent two-Px metagabbro, near the base of unit II. Here, the boudin neck is filled by undeformed gabbro, made up of euhedral amphibole phenocrysts within a plagioclase matrix. Analogous gabbroic material also occurs within small shear zones, which transect the main foliation in the layered gabbros (Fig.2.34, red arrowhead in Fig.2.12).

Moreover, medium- to coarse-grained leucotonalite material occurs as small veins or shear zone infill (e.g. Fig.2.35 to 2.37); the granitoid material was only detected in the surroundings of the interfaces between Grt-bearing gneiss and host metagabbros. Leucotonalite material contains plagioclase, quartz, minor biotite, apatite and zircon. Fig.2.35 shows a detail from the boundary between leucotonalite vein and host layered metagabbro. This orthogneiss crops out near the roof of unit II, exhibiting an alternation of coarse-grained norite and fine-grained diorite layers. Leucotonalite is nearly undeformed at grain scale, containing tabular plagioclase grains surrounded by anhedral and weakly deformed quartz (the only visible deformation feature in quartz is represented by local chessboard SGBs pattern, Kruhl, 1996).

Comparable leucotonalite material occurs also within the sinistral ("top to SW") shear zone shown in Fig.2.36, which nucleated at the boundary between ferromagnesian septa and host gabbro-norite. Some fragments from the host mylonitic metagabbro were incorporated within the leucotonalite material (this is well visible in the detail from the photo on the right hand side of Fig.2.36). This melt-sealed shear zone postdates the development of the synkinematic retrograde (D₂) assemblage within the meta-sedimentary septum (Fig.2.30).

Fig.2.37 illustrates a detail from the boundary between quartzofeldspathic gneiss and host mylonitic metagabbro. A thin plagioclase-quartz (leucotonalite) vein, which likely originated in the strain shadow of the large garnet porphyroclast, was injected through the mylonitic foliation of the leucocratic striped gneiss.

It is commonly thought that, where partial melting occurs during deformation, melt migrates toward low stress sites, such as tension gashes boudin necks (Passchier et al., 1990b). In addition, Rosenberg & Handy (2000) shown that, during melt-bearing deformation, strain tends to localize within the melt-rich domains or, in contrast, it could migrate toward low-strain sites generated by the opening of short-lived spaces.

Thus, in our case, gabbroic and leucotonalitic melt pockets shown here might have originated during latest stage of the development of the main mylonitic fabric (as this former magma completely escaped the high temperature solid-state overprint).



Fig. 2.33: boudinaged melagabbroic layer within two-Px gabbro-norite. The photo on the right hand side shows the irregularly shaped gabbroic pocket, containing undeformed amphibole phenocrysts (2-5mm-long).



Fig. 2.34 (left): small sinistral shear zone transecting the main foliation in layered gabbro, associated with gabbroic undeformed material. **Fig. 2.35** (right): detail from one branch of leucotonalite vein transecting the solid-state foliation in a diorite-norite sequence, at the transition between Units II and III. Red arrowheads point to euhedral plagioclase grains (base of photo: 20cm).

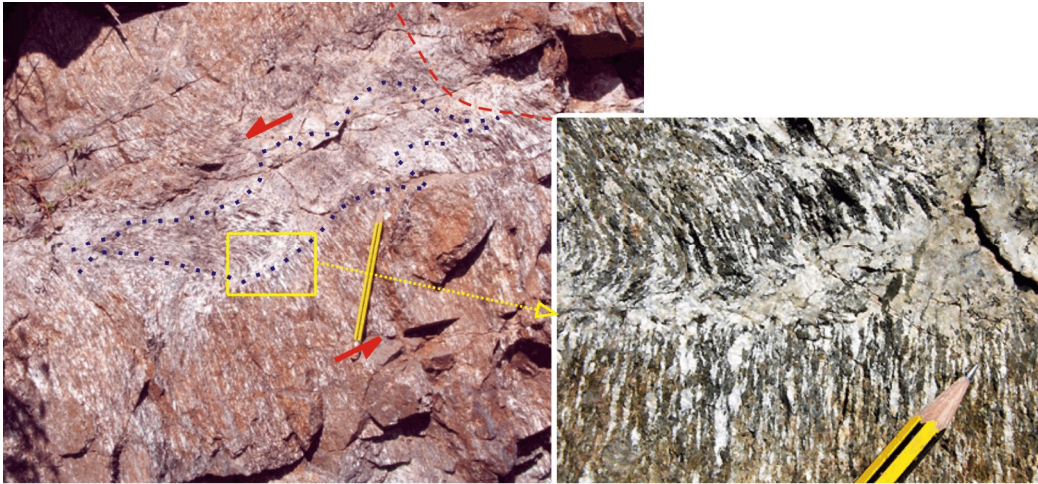


Fig. 2.36: irregular shear zone near the boundary between norite and Grt-bearing gneiss (indicated by the red broken line). The shear zone is injected by leucotonalite melt.

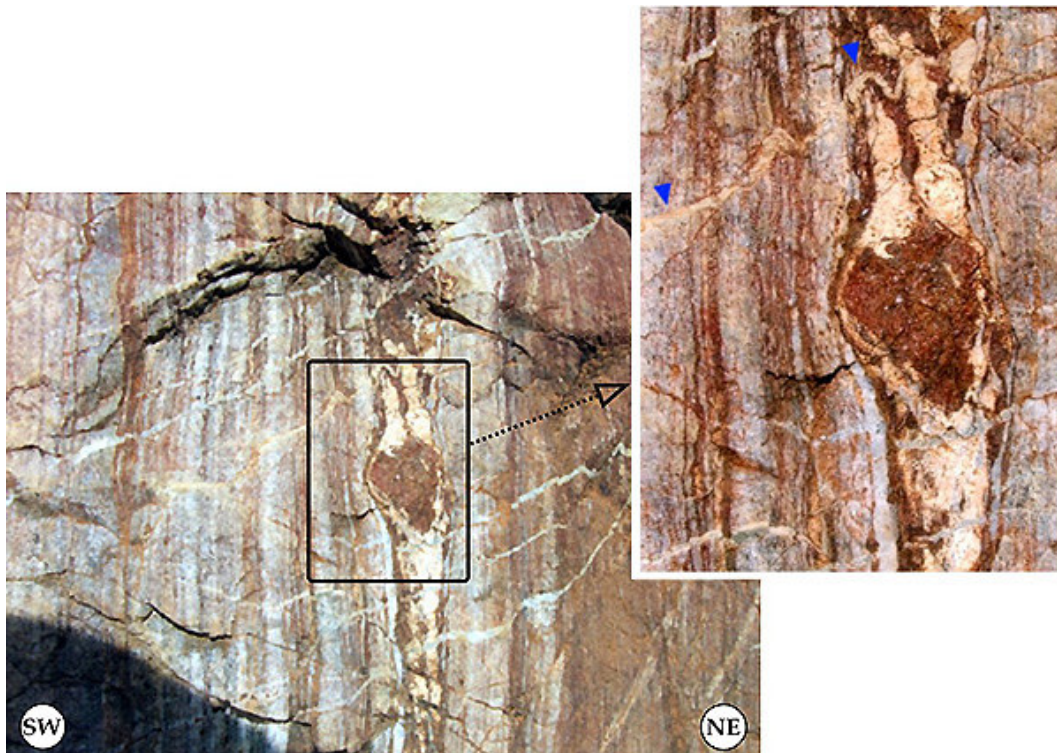


Fig. 2.37: boundary between Grt-bearing quartzofeldspathic granulite and meta-melagabbro (right). The photo in the right hand side shows a detail from the thin plagioclase-quartz vein (pale yellow, indicated by blue arrowheads). It likely originated from the leucosome (interpreted to be former melt) in the strain shadow of the large garnet porphyroclast. In contrast, white thin veins are quartz veins, which are likely younger than leucotonalite vein. The base of the larger photo is ~20cm.

2.1.6 Qtz LPO in the lower and intermediate part of MC

Quartz fabrics have been measured in twelve samples collected at different structural levels within the lower portion of the layered mafic complex (Fig.2.40). Samples representative of Grt-bearing quartzofeldspathic septa (Fig.2.27 to 2.28) are shown with red pole figures; blue-coloured pole figures correspond to samples from Bt-rich ferromagnesian (Fig.2.30) and intermediate septa (Fig.2.31 and 2.32). Finally, quartz fabric from Qtz-norite (sampled near the roof of unit II) has been investigated (Fig.2.38 and 2.39).

Quartz fabric is strong in quartzofeldspathic gneisses; in general, within quartz-rich rocks deformed at high-grade conditions, quartz fabric might be in part artificially strengthened by measuring different portions of the same grains. This problem is due to the exaggerated grain growth (in the sense of Wilson, 1973) and complex three-dimensional interfingering, which produce "island grains" (or dissection microstructure, Urai et al., 1986) where these microstructures are viewed in two-dimensional sections (e.g. Fig.2.28). Relatively large quartz grain size is likely achieved within feldspar-rich domains also, as not-impurity-controlled grain boundary migration may occur during recrystallization within the high-quartz field (Stipp et al., 2002).

The five investigated samples of quartzofeldspathic granulites were collected along a short and continuous section (~100m in length) along the S. Lucia River, at the transition between Units I and II. All samples belong to the same septum, recording negligible low-temperature overprint (i.e. undulose extinction is usually absent or scarce). Within these Qtz-rich adjacent samples, three mutually perpendicular prominent maxima are located near the main three axes. As a whole, this type of quartz fabric is similar to those described for the *Saxony granulites* (Lister & Dornsiepen, 1982) and, more in general, it represents the typical c-axis fabric for rocks deformed in the high-quartz field (GBM II regime, Fig.14b in Stipp et al., 2002). In both cases, the observed Qtz-fabric is explained in the scenario of simultaneous slip on basal $\langle a \rangle$ plane and prism plane (along both $\langle a \rangle$ and $[c]$ directions). Nevertheless, in our case, some samples show Y maxima alone (i.e. sample SL11b), others show combined X and Y maxima (with X stronger, samples SL13 and SL14), whereas sample SL9 displays combined X and Z maxima. Only in one case (sample SL13a), the three mutually orthogonal maxima occur within the same thin section, being the X maxima the strongest. In all cases, Qtz pattern exhibit monoclinic external symmetry (namely the maxima near the periphery of pole figures are rotated ~10-35° counter clockwise respect to X and Z axes; see Fig.2.40), which is consistent with the overall sinistral sense of shear deducible at outcrop (Fig.2.25) and thin section scale (Fig.2.28).

These data suggest that domainal quartz fabric likely developed on a scale overtaking the common thin section dimension (which is generally $<10\text{cm}^2$). The occurrence of domainal quartz fabric is described by several authors (among others: Garcia Celma, 1982; Burg, 1986; Pauli et al., 1996). In these cases, however, the described fabric domains are markedly smaller than those described here. On the other hand, wider quartz fabric domains within high-grade gneisses were reported by Feuten et al. (1991). These authors described that fabric domains are pronounced within quartz-rich domains, whereas isolated grains (in quartz-poor layers) tend to behave independently.

Grains deformed by multiple slip systems build up higher internal strain energy than those with only one prevailing slip system (Law et al., 1990). Thus, in our case, some strain softening is expected to occur within domains where only one or two slip systems are prevailing (respect to the three available slip system within the high-quartz field), where fast GBM (thus, widespread diffusional mass transfer) may help to ensure strain compatibility. Moreover, GBM recrystallization might contribute to strengthen the fabric within a single domain, by the selective removal of grains with unsuitable crystallographic orientation (Knipe & Law, 1987).

Within ferromagnesian and intermediate Grt-bearing gneisses, quartz fabric is generally weaker, being qualitatively analogous to quartz fabric in Qtz-rich domains. In contrast with quartzofeldspathic rocks, Y maxima are commonly prevailing (i.e. samples SL15, z43, DSL89, DSL68a). Samples with prominent X maxima are compositionally the closest to quartzofeldspathic rocks.

Within sample SL15, the severe syndeformational retrogression is accompanied by dramatic grain size reduction (Fig.2.32), indicating that this domain is representative or progressive strain localization during retrograde shearing (Fig.2.23). Here, the observed quartz fabric exhibit Y maxima, with a tendency to type I crossed girdle (in the sense of Lister, 1977). Lister & Dornsiepen (1982) shown that this kind of fabric (with opening angle of $\sim 50^\circ$) might be achieved through prism [c] slip deactivation, during syndeformational retrogression from granulite to amphibolite facies.

C-axis fabric from quartz included within garnet (sample SL13) is qualitatively comparable with those obtained from the matrix quartz, showing some prominent maxima around the main three axes (Fig.2.40). This data corroborate the hypothesis of the "quartz false inclusions" (Fig.2.31 and 2.32), as discussed previously. In this case, the observed weaker pattern could be partly related to the high strength contrast between quartz and garnet (Lister & Price, 1978).

Quartz fabric in (meta-) Qtz-norite has been investigated in both XZ and YZ sections of the finite strain ellipsoid (Fig.2.38). XZ section exhibits markedly layered fabric, highlighted by elongate ribbons made up of completely recrystallized plagioclase (left in Fig.2.38). During the development of the main fabric, orthopyroxene porphyroclasts were likely stronger than plagioclase; however, they recorded some plastic deformation (showing incipient development of ribbon grains) being surrounded by a mantle of recrystallized Opx^{II} (Fig.2.39).

As evident by comparing the green pole figures in Fig.2.40, fabric measured in XZ section is markedly different from those exhibited by YZ section (in the latter case, all the data are rotated toward the conventional XZ orientation). In YZ section, some strong maxima cluster around the X-axis, whereas some minor maxima are scattered at low angle from the foliation plane. In contrast, quartz fabric from XZ section is strikingly weaker, with dominant maxima near Y and Z-axes, and minor X maxima. The weak fabric along the XZ section might be partly related to the low quartz content (Starkey & Cutforth, 1978). In fact, in this sample non-interconnected quartz ribbons are isolate within the plagioclase-rich matrix.

When observed along XZ sections, ribbon-forming quartz grains exhibit various aspect ratios, generally ranging between 1:1 and $\sim 1:5$. Therefore, on a statistical basis, any YZ section will contain a higher proportion of grains with high aspect ratio, respect to the XZ

section, as described in Culshaw & Fyson (1984). Thus, the discrepancy between XZ and YZ quartz fabric suggest that a correlation exist between the aspect ratio of quartz grains (as visible in XZ sections) and their crystallographic orientation. In fact, the c-axis of the longest grains clusters around the stretching lineation, whereas the quartz fabric from the whole quartz population (as measurable along any XZ section) is markedly weaker and ill defined. These data suggest that oriented grain growth occurred during (and after?) the development of the main fabric: the longest quartz grains (i.e. the grains which grew faster) are those oriented in a favourable direction for [c] slip. Analogous conclusions were reported by Gapais & Barbarin (1986), and by Urai & Humphreys (1981).

Most of the measured opening angles lie in the range 75-100°, being the typical values for quartz fabric developed under upper amphibolite to granulite facies (Kruhl, 1998). Smaller opening angles (~50-60°) typify ferromagnesian septa subjected to pervasive retrograde overprint, likely developed at middle to lower amphibolite facies.

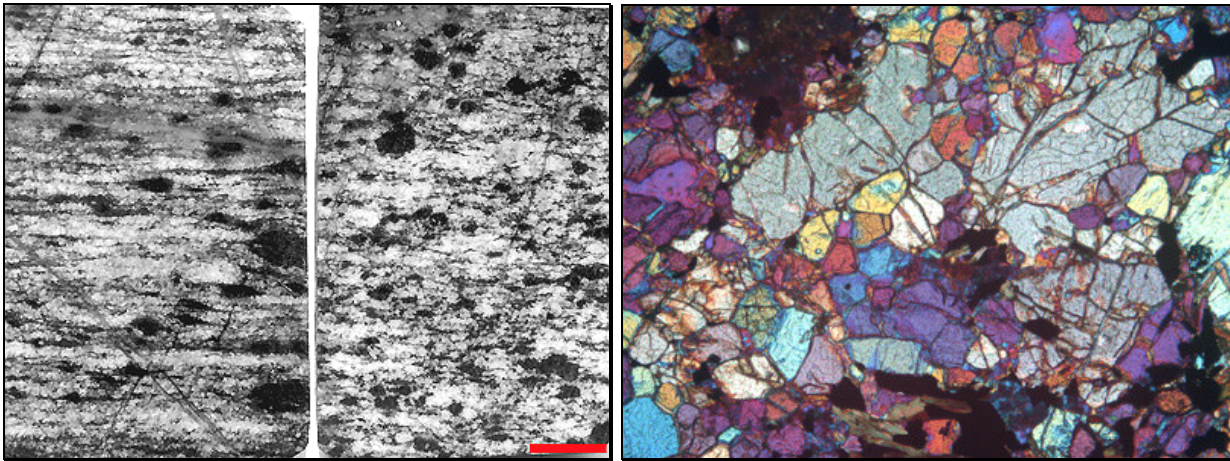


Fig. 2.38 (left): XZ (left) and YZ polished sections from quartz-norite (samples DSL64.2 and DSL64.1, respectively). Scale bar is 0.5cm. Fig. 2.39 (right): detail from quartz-norite, showing Opx porphyroclasts (grey) largely replaced by syntectonic Opx^{II} granoblastic aggregates. High-angle microfractures likely postdate the development of the main fabric, because they affect the recrystallized grains also (crossed polars; gypsum plate inserted; base of photo: 4mm).

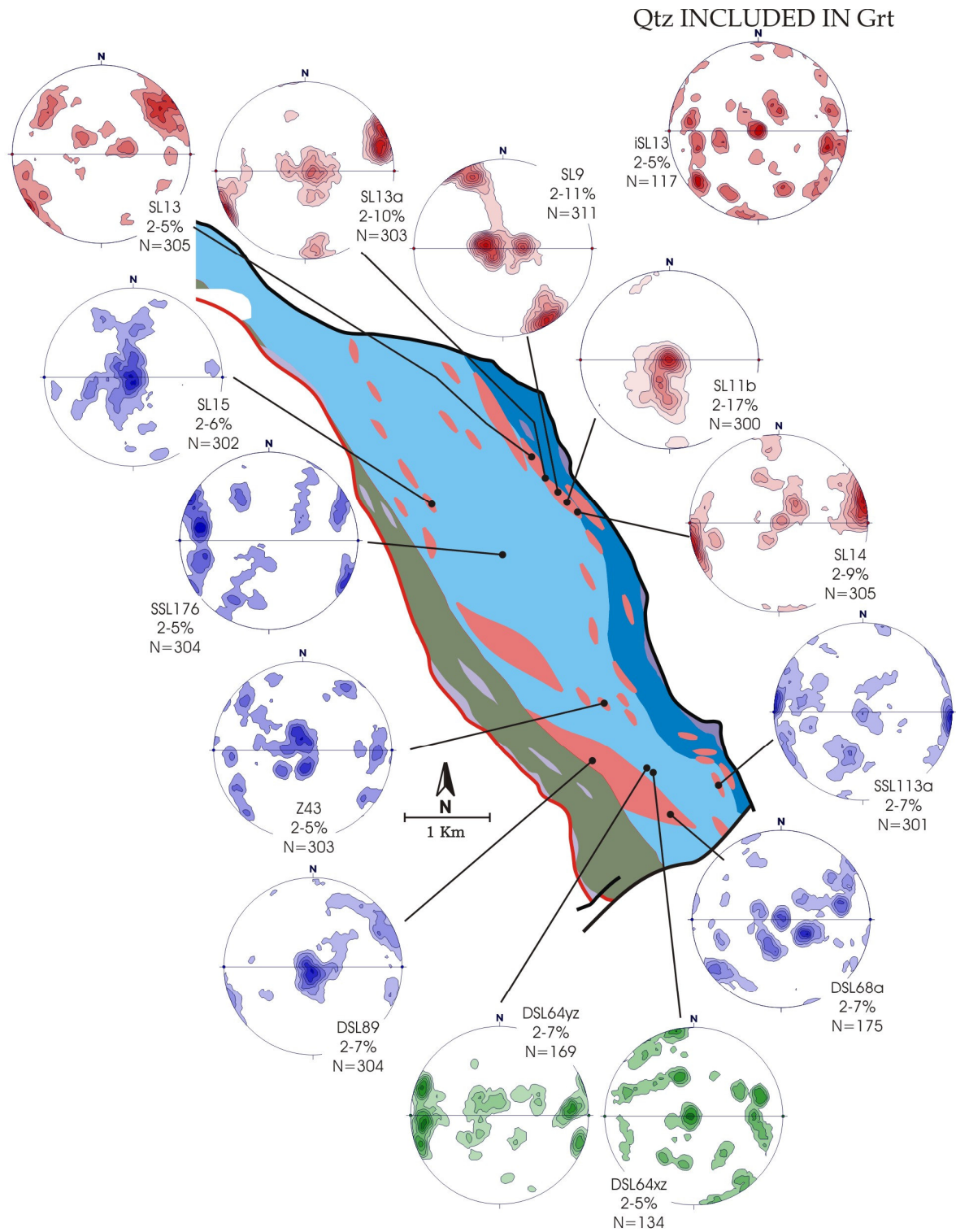


Fig. 2.40: map summarizing quartz c-axis fabric from garnet-bearing mylonitic gneisses included within Unit I and II. For each equal area stereographic projection (lower hemisphere, 1% of search area), the labels are (from the top): sample name, contour interval, number of measurements. Red pole figures indicate quartzofeldspathic gneiss, whereas blue pole figures correspond to ferromagnesian and intermediate gneisses. Finally, green pole figures are from the two orthogonal sections in quartz-norite. In this case, data collected from YZ section were rotated toward the conventional XZ orientation.

Tab. 2-1: table summarizing the main features of the investigated samples. “X” symbols indicate the frequency of the occurrence of a certain microstructural feature (i.e. quartz subgrain boundaries), as approximately estimated in a relative range (from zero, indicated with “\”) to three.

	Rock type	assemblage	LT Overprint.	Opening angle	F.intensity (%)	Qtz SGBs	Chessboard SGBs	Qtz content (%, ±10%)
iSL 13	Qtz-feld septa	Grt,Pl,Qtz ±Bt±Opx	\	55°	5,13	X	\	40
DSL642 (XZ)	Qtz-norite	Pl,Opx,Qtz±Bt	\	140°	5,22	X	X	25
SL 13	Qtz-feld septa	Grt,Pl,Qtz ±Bt±Opx	\	105°	5,25	XX	X	40
Z 43	Fe-magn septa	Grt, Opx,Bt, Crd,Pl,Qtz	\	60°, 95°	5,28	X	X	30
SSL176	Qtz-feld septa	Qtz,Pl,Kfs, Grt±Bt	X	90°	5,92	X	X	35
SL15	Fe-magn septa	Grt, Opx,Bt, Crd,Pl,Qtz	\	\	6,29	X	X	25
DSL 89	interm septa	Opx,Bt,Pl,Qtz	\	135°	6,91	XX	\	30
SSL11,3a	Fe-magn septa	Grt,Pl,Qtz±Bt	X	95°	7,31	X	X	30
DSL 68a	interm septa	Opx,Bt,Pl,Qtz	\	75°	7,43	X	\	30
DSL641 (YZ)	Qtz-norite	Pl,Opx,Qtz±Bt	\	90°	8,28	X	\	25
SL14	Qtz-feld septa	Qtz,Pl±Grt	X	85°	9,84	X	X	25
SL13a	Qtz-feld septa	Grt,Pl,Qtz ±Bt±Opx	\	75°	10,89	X	X	45
SL9	Qtz-feld septa	Qtz,Pl±Grt	X	\	11,58	X	\	70
SL11b	Qtz-feld septa	Qtz,Pl±Grt	\	\	17,67	X	\	70

2.1.7 The roof of MC: the diorite-granite suite (DGS)

According to Libourel (1985), the uppermost part of the gabbroic-layered sequence is represented by diorite unit. Instead, detailed field investigations reveal that this portion of the complex is very heterogeneous, containing a composite magmatic suite where melagranitoids, mafic rocks and minor leucogranitoids are intimately associated.

The striking feature of DGS is represented by the occurrence of igneous charnockites. In the recent past, the term "*charnockite*" has been used (incorrectly) as a synonym of granulite. Instead, Opx-bearing granitoids were already described in the beginning of the last century (Holland, 1900), representing granitoid rocks that have crystallized under low water activity (Frost et al., 2000). The terminology proposed by Le Maitre et al. (1989) is adopted here for pyroxene-bearing granitoids.

The transition between melagranitoids and mafic rocks is commonly gradual and imperceptible in nature. In contrast, leucogranite appears as dykes intruded into previous rocks, commonly displaying sharp boundaries against host rocks. In the sector comprises between *P.ta Auli* locality and the *Piaggio* River, "primary" late-magmatic features are partly preserved. Common macroscopic igneous features include the occurrence of (sub-) magmatic foliations, compositional layering, mafic microgranular enclaves (MME), porphyritic fabric and dykes displaying various compositions. As most of the granitoids exhibit tonalite-dioritic compositions, ~50% of thin section surface is commonly occupied by altered (An-rich) plagioclase. Consequently, detailed microstructural investigations were mostly restricted to leucocratic rocks.

2.1.7.1 Overview on different rock types

(a) Enderbite to norite

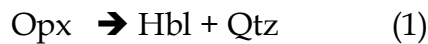
In the northern area, around *P.ta Auli* locality, the prevalent rock type is represented by enderbite. Within the coarse-grained hypersthene-bearing tonalite, plagioclase content is ~50%; femic phases are represented by brownish-weathered pyroxene, black amphibole and biotite. Magmatic foliation and lineation are well defined by alignment of idiomorphic feldspars, oriented trail of Hbl and Bt (which, however, may develop during solid-state flow also, Paterson et al, 1989) and by the elongation of Hbl-rich microgranular enclaves.

Quartz is unevenly distributed within enderbite. Commonly, the greater is the amount of femic minerals, the lower is the quartz content. Therefore, leucocratic enderbite contain pyroxene crystals isolated in a quartz-feldspatic matrix, whereas 'mafic' end-member contains large amounts of Hbl and Bt, and rare Px rimmed (and partly replaced, Fig.2.43 and 2.44) by Hbl. Consequently, colour index of enderbite is various, due to different Qtz / femics ratio. Dioritic MME are quite common in mafic enderbite, whereas are rarely observed in leucocratic term. Enclaves exhibit variable aspect ratio and size, ranging from several decimetres to few millimetres in length.

Leucocratic enderbite display a quite homogeneous grain size. On the contrary, a closer observation reveals that mafic enderbite show a very heterogeneous magmatic fabric: coarse-grained Pl, Opx and Hbl are surrounded by a fine-grained dioritic matrix. Gradual transition between pluridecimeteric enclaves and the 'dioritic matrix' exist, suggesting that mingling between leucocratic enderbite and coeval dioritic magma might occurred during magmatic evolution. Moreover, magma hybridism is evidenced by the occurrence of large and scattered Qtz ocelli (Vernon, 1984). Leucocratic and mafic enderbite are closely associated and interlayered from outcrop to thin section scale. The alternation of these enderbite varieties roughly defines a compositional layering concordantly with magmatic foliation. Transition between these end-members is gradational and usually imperceptible in nature. Moreover, the mafic variety exhibits a gradual transition toward gabbro-dioritic rocks.

Locally, leucocratic enderbite exhibit pegmatoid texture, with brownish Opx phenocrysts surrounded by plagioclase-rich matrix. In these cases, the transition from leuco-enderbite to norite takes place by a gradual decrease in quartz. Enderbite is locally intruded by charnockite pegmatite (i.e. hypersthene-bearing granite; Fig.2.41), exhibiting irregular and finely lobate boundaries (syn-plutonic dykes?).

Leuco-enderbitites differ from norite essentially by their quartz content. Both rocks contain anhydrous assemblages (Pl + Opx ± Qtz), where Opx is stable or just locally consumed by the reactions:



These reactions produce embayment in Opx and Cpx, which are generally filled by magmatic quartz, which is optically continuous with the matrix quartz. Hbl and Bt are uncommon within these rocks. In contrast, mafic enderbites display high Bt-Hbl content, whereas Opx (± Cpx) is nearly completely consumed by reaction (1) and (2). Opx may be partially replaced by Hbl-Qtz simplectites, which are usually oriented parallel to the main F₀₋₁ fabric (Fig. 2.43; section 2.2.7.2). This reaction may continue up to nearly total disappearance of Opx, as shown in Fig. 2.49 and 2.50. Hbl-Qtz and Bt-Qtz simplectites commonly contain apatite and zircon inclusions. Quartz from these intergrowths is frequently optically continuous with the matrix quartz.

In summary, leuco-enderbite to norite display well preserved anhydrous assemblages, being rather similar to the igneous protholith of gabbro-norites from Unit II. In contrast, within the mafic enderbite the anhydrous assemblage was largely destabilized by interaction with Hbl- and Bt-rich (hydrous) melt. The preservation of these microstructures within samples devoid of any important solid-state overprint suggests that reactions (1) and (2) likely occurred in the presence of melt (i.e. during magmatic to submagmatic flow, section 2.1.7.1).

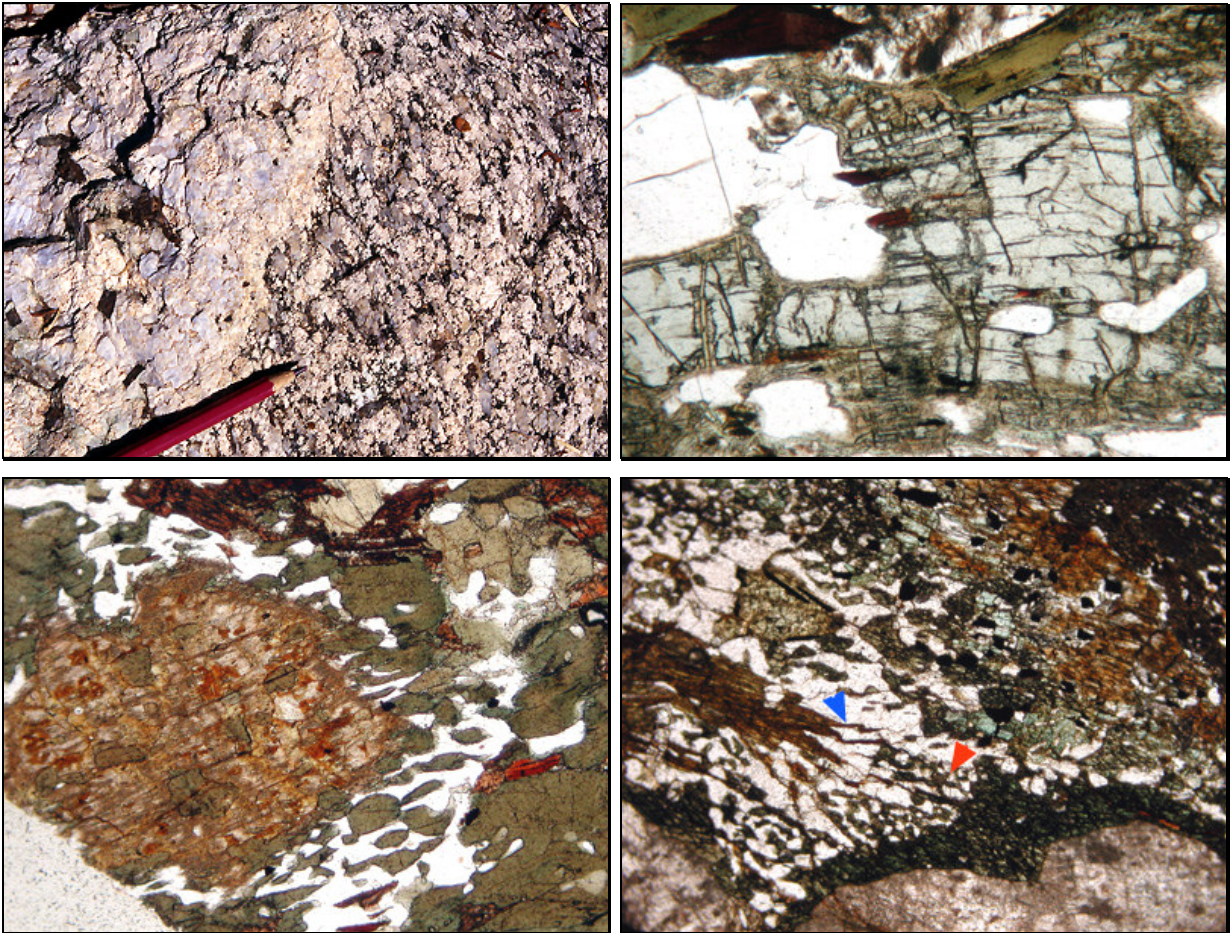


Fig. 2.41 (upper left): enderbite with well-defined sub-magmatic fabric. Note the irregular magmatic contact with charnockite pegmatite (hypersthene-bearing granite). In the next pictures: pyroxene destabilization within two-pyroxene mafic enderbite: **Fig. 2.42** (upper right): magmatic Opx (see euhedral Ap inclusions) partially embayed and replaced by magmatic quartz and biotite (plane polarized light; base of photo: 4mm). **Fig. 2.43** (lower left): detail from mafic enderbite, where magmatic Opx displays Hbl-Qtz corona. Amphibole partly grew also in the interior of pyroxene (plane polarized light; base of photo: 4mm). **Fig. 2.44** (lower right): complex microstructure around some remnants of Opx grains (brown): Qtz-Bt (blue arrowhead) and Qtz-Hbl intergrowth (red arrowhead) are rimmed by Qtz-free amphibole, mainly developed against (altered) plagioclase (plane polarized light; base of photo: 4mm).

(b) Tonalite to diorite

The gradual transition from enderbite to tonalite is exposed along the *Piaggio River*, where it takes place by gradual vanishing of pyroxene and without visible crosscutting relations between the two end members. Tonalite is usually coarse-grained with medium to high colour index, related to high content of Hbl and Bt. At the macroscopic scale, these rocks are very similar to the femic variety of enderbite, and the above-described mingling-related fabric is also detectable (Fig.2.45). Besides the absence of pyroxene, the tonalite also differs by the common occurrence of granitic pockets with porphyritic fabric (described in the next section).

At outcrop scale, the tonalite displays a gradual transition toward the diorite, which is detectable by distinctive high colour index (~50-60, related to high content of black-weathering amphibole). Scattered Opx phenocrysts are locally present; moreover, biotite and quartz represent common accessory phases. Diorite is usually layered at the centimetre to meter scale. The layering is mainly due to grain size variation (Fig. 2.45 and 2.48), being parallel with magmatic foliation. As described for enderbite, the sporadic Opx phenocrysts in diorite are commonly rimmed and \ or partially destabilized by Hbl

aggregates. A striking feature of diorite is the variability in grain size and the heterogeneity of magmatic fabric. Large dioritic bodies are usually medium- to coarse-grained (sporadic pegmatoid texture may occur), whereas MME and dykes are fine-grained. These mafic dykes are intruded in coarse diorite, enderbite and tonalite. Both dyke boundaries and internal magmatic foliation are roughly concordant with magmatic foliation in host rocks. The gradual transition between partially disaggregated dykes and enclaves is locally observable. Field relations suggest that synplutonic mafic dykes were intruded into unconsolidated host rocks, and were probably the source of dioritic enclaves and of the above described mingling fabric.

Hornblende-quartz simplectites are common in tonalite and Qtz-diorite, especially close to the enderbite sub-unit. In Fig.2.49, the inferred magmatic origin of the simplectite is suggested by optical continuity in Qtz (blue arrows) and by apatite inclusions (despite the occurrence of apatite inclusion is not a strong single criterion for magmatic origin). In analogy with what observed within the enderbite (Fig.2.44), quartz-free amphibole rims developed between the simplectite and the plagioclase. Thus, the transition between enderbite and Px-free tonalite could be partly related to the complete replacement of orthopyroxene by hornblende and biotite.

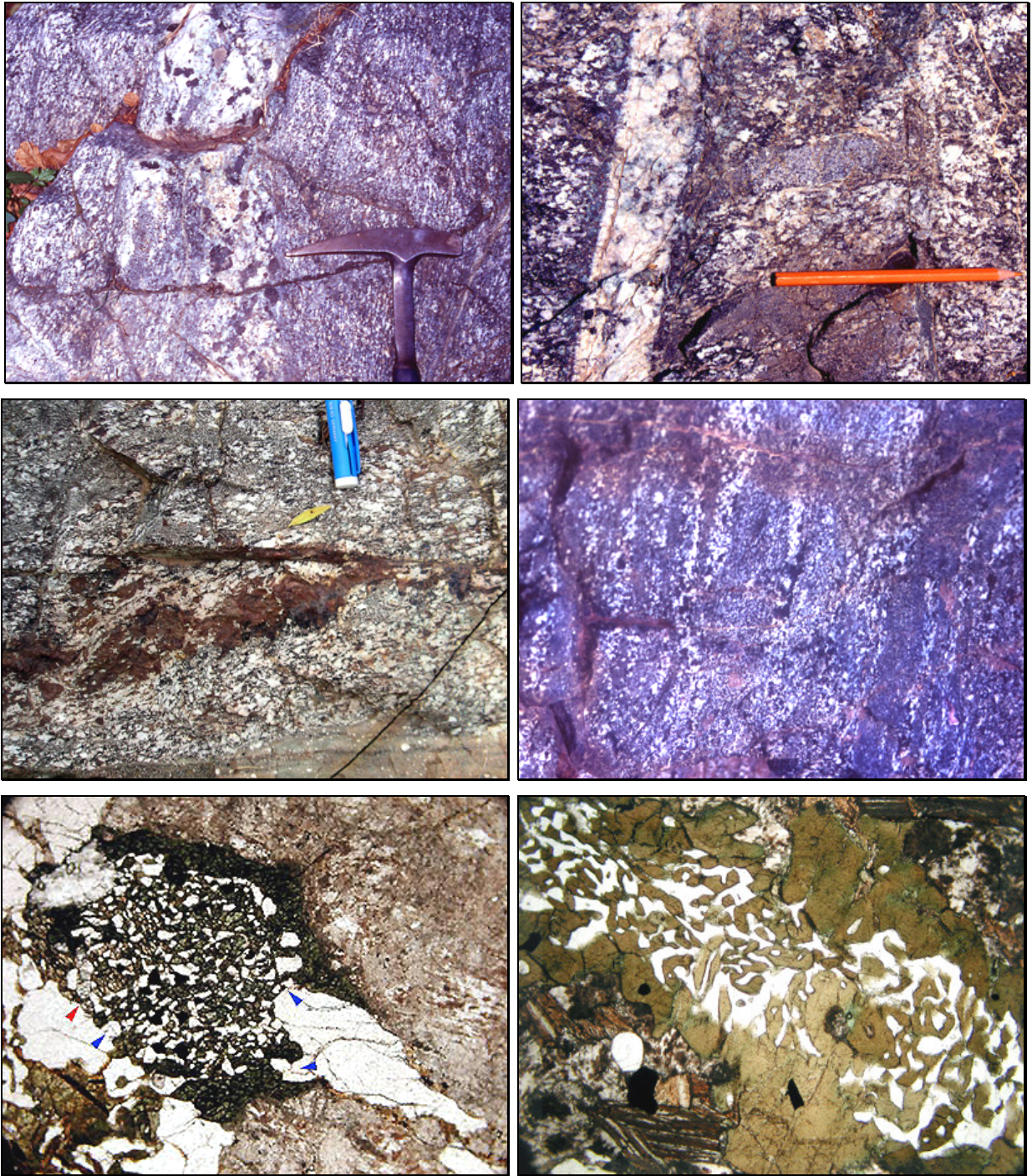


Fig. 2.45 (upper left): detail of diffuse contact between tonalite and Hbl-bearing pegmatite. Note the extreme variety in grain size of tonalite, and the schlieren-like fabric due to strong elongation of dioritic microgranular enclaves. **Fig. 2.46** (upper right): moderately deformed magmatic fabric in Qtz-diorite (sub-horizontal) highlighted by SPO of plagioclase, feldspar minerals (Hbl + Bt ± Opx) and MME. This primary fabric is transected by Bt-bearing pegmatite. **Fig. 2.47** (centre left): heterogeneous magmatic fabric in diorite, containing pegmatoid norite pocket (brown). Note irregular contacts between coarse Qtz-diorite and fine-grained diorite. Magmatic fabric is sharply transected by D₃ ultramylonite (bottom). **Fig. 2.48** (centre right): magmatic fabric in diorite. The centimetric layering is mainly due to grain size variation, where coarser layers are slightly enriched in brownish Opx respect to medium- and fine-grained diorite. **Fig. 2.49** (lower left): Hbl-Qtz simplectite surrounded by Hbl subhedral rim. Blue arrows indicate bulging of magmatic quartz into simplectite. Red arrow indicates Ap grains included into simplectite (plane polarized light; base of photo: 1.8mm). **Fig. 2.50** (lower right): spectacular Hbl-Qtz intergrowth within a melanocratic tonalite. Small Hbl portions from the simplectite are optically continuous with the outer Hbl rim. This complex microstructure is surrounded by Ap + Bt + Pl magmatic assemblage (plane polarized light; base of photo: 4mm).

(c) *Porphyritic rapakivi granite*

Porphyritic granite mainly crops out along the NW nappe boundary, and it is well exposed along the natural section provided by the *Piaggio River*. At the outcrop scale, this term appears as medium-grained melanocratic granite, containing scattered K-feldspar phenocrysts (Fig.2.51). These centimetric crystals commonly exhibit *rapakivi texture*, which consists of salmon-coloured K-feldspars cores, with irregular embayed margins, overgrown by a thin (white) plagioclase mantle (Fig.2.52). The high colour index is related to high content in black-weathered amphibole and biotite. Dioritic MME are common, as described for tonalite and enderbite. The porphyritic granite is frequently intruded by K-feldspar-rich pegmatites (Fig.2.53). These veins locally show diffuse boundaries and gradual disaggregation against the host granite. The sporadic occurrence of Kfs phenocrysts within the MME (Fig.2.54) suggests that magma hybridism occurred, incorporating Kfs grains from host granite (Paterson et al., 2004).

(d) *Leucocratic dykes*

Besides the above-described dioritic veins (which represent the oldest visible dykes within DGS), several kinds of slightly younger leucocratic veins can be detected in the field. They are distinguished on the basis on the main assemblage, crosscutting relations and type of contact with host rock. Precocious veins are represented by charnockite pegmatites (Fig.2.41), Hbl-bearing pegmatite (Fig.2.45), Kfs-rich pegmatite (Fig.2.53), and Bt-rich (red-weathered) microgranite (Fig.2.55 and 2.56). All the cited dykes are (slightly?) younger respect to dioritic veins, exhibiting very irregular and diffusive contacts against host rock.

The term charnockite includes a group of leucogranitic pegmatites with abundant Kfs megacrysts, where sporadic femic phases are represented by orthopyroxene and hornblende. Charnockites usually occur as decimetre to metre- thick dykes, intruded in all the rocks described previously.

Microgranite veins are locally boudinaged within host melanocratic granitoid, displaying irregular to crenulate boundaries (Fig.2.55). Field and microstructural observations (Fig. 2.56 and 2.57) suggest that deformation occurred entirely in the magmatic state. These fine-grained (locally Bt-rich) veins in some cases display pegmatitic rim, indicating that large volumes of water-rich fluids occurred during pluton crystallization (Blumenfeld et al., 1986). Youngest dykes are represented by Bt-bearing pegmatites and aplites. These veins commonly exhibit sharp and planar boundaries against host rocks (note the difference in vein boundary morphology between Fig.2.45 and 2.46).

Precocious veins commonly took place sub-parallel (or at moderate angle) from magmatic fabric in host granitoid. In contrast, younger dykes (which display sharp boundaries against host rocks) are commonly oriented at high angle from magmatic foliation and lineation. Similar geometric relationships are observed in the Granitic Complex also (chapter III).

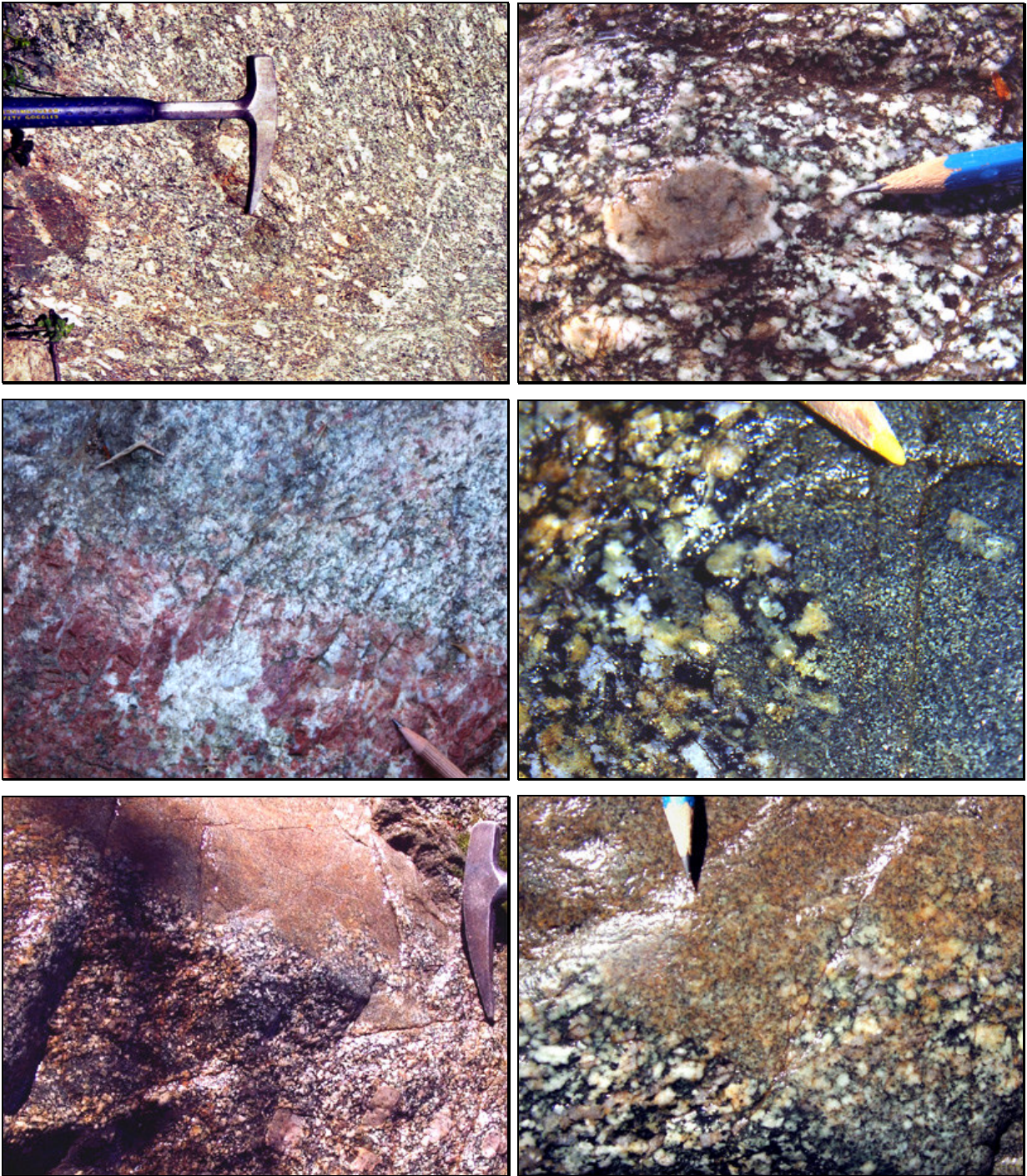


Fig. 2.51 (upper left): outcrop-scale appearance of porphyritic granite: magmatic foliation (steeply dipping toward the right) is highlighted by the alignment of Kfs megacrysts and dioritic MME. The primary fabric is transected by shear zone with diffuse boundaries (horizontal, at bottom). **Fig. 2.52** (upper right): detail of the magmatic fabric in porphyritic granite, showing rapakivi texture and high contents of Hbl and Bt. **Fig. 2.53** (lower left): detail from the boundary between Kfs-rich pegmatite and host granite. Note the (sub) magmatic foliation, which overprints the magmatic contact. **Fig. 2.54** (lower right): detail of the irregular magmatic contact between dioritic enclave (containing Kfs crystals) and host porphyritic granite. **Fig. 2.55** (left): crenulate contact between red-weathered microgranite vein and host rapakivi granite. Some Kfs phenocrysts (displaying rapakivi texture) are visible in the lower part of the photo. **Fig. 2.56** (right): detail from the crenulate contact, showing the magmatic foliation (gently dipping toward the left) that overprints the igneous contact. Note the gradual transition from melagranite to diorite enclave (lower right corner).

2.1.7.2 Magmatic to submagmatic fabric (F_{0-1} fabric)

(a) Field relations and microstructures

The above-described rocks belonging to DG suite share both late-magmatic and subsequent solid-state evolution. The magmatic origin of the main foliation is suggested by the alignment of MME (Fig.2.45 and 2.46), tabular feldspars (Fig.2.51 and 2.53), subhedral to euhedral amphibole (Fig.2.58) and pyroxene (Fig.2.41 and 2.42), in the absence of any important deformation at grain scale. However, magmatic fabric in the strict sense is rarely preserved at thin section scale. One of these rare examples is provided by microgranite vein (with pegmatitic rim) shown in Fig.2.57 (the corresponding outcrop is shown in Fig.2.55 and 2.56). Here, aligned euhedral feldspars are surrounded by interstitial quartz grains, which do exhibit neither shape fabric nor recrystallization. However, most of the quartz grains exhibit chessboard SGB pattern (Kruhl, 1996) and some feldspar grains are affected by submagmatic microfractures (Bouchez et al., 1992). These features suggest that, even the less deformed portion of the DG suite recorded some deformation at temperature close to the granite solidus, likely in a melt-bearing environment.

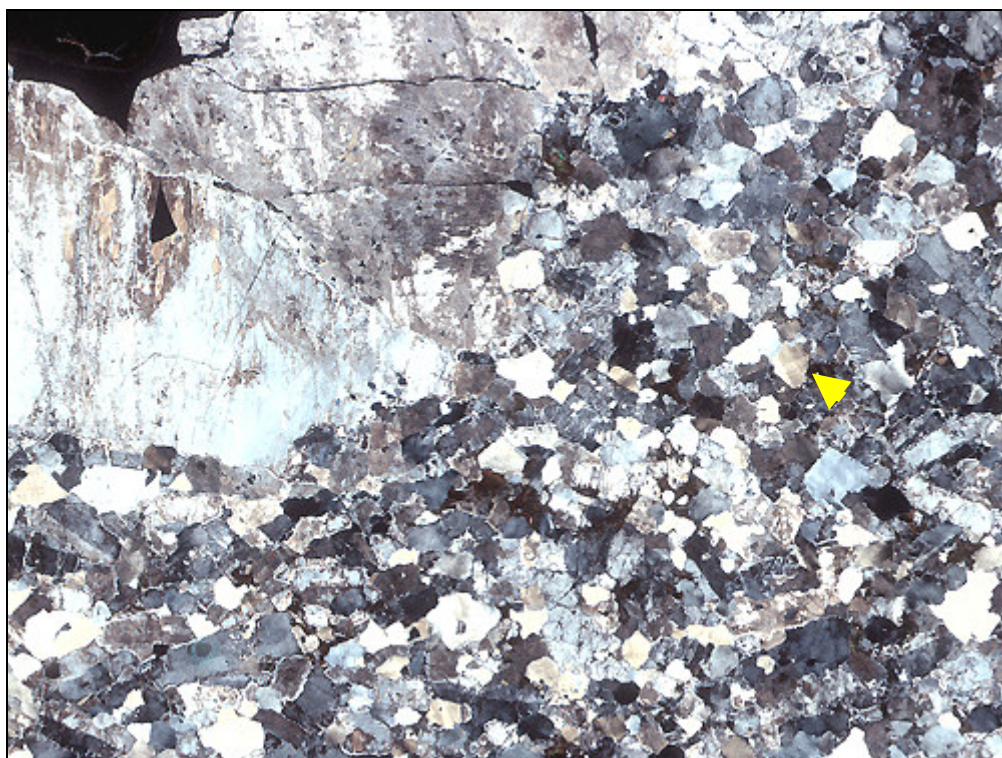


Fig. 2.57: enlarged micrograph from microgranite vein with pegmatitic rim, showing well defined magmatic foliation (sub-horizontal), underlined by alignment of tabular Kfs and Pl. Interstitial quartz do not shows any visible shape fabric, but it commonly exhibit chessboard SGB pattern (yellow arrowhead; sample DSL60; crossed polars; base of photo: 3cm).

Besides these (uncommon) weakly deformed domains, all rocks are much more deformed. In fact, a closer observation to mesoscopic fabric of granitoids evidences that quartz commonly shows evident SPO (shape preferred orientation) parallel to magmatic anisotropy, displaying aspect ratio up to 5:1 (Fig. 2.41 and 2.49).

At grain scale, coarse monocrystalline quartz ribbons usually show evidences of dynamic recrystallization, where lensoid and coarse Qtz grains are partially replaced by polycrystalline aggregates displaying mosaic-like aggregates (Gapais and Barbarin, 1986). New grains exhibit strongly lobate and irregular Qtz-Qtz grain boundaries and wide range of grain size (50-300 μ), suggesting that grain boundary migration recrystallization (GBM) was the dominant recrystallization mechanism (Stipp et al, 2002). Old porphyroclasts commonly show strong internal deformation, where both basal and prismatic SGBs may occur (Fig.2.59). Prism-parallel SGBs are commonly planar, transecting all the grain. In contrast, base-parallel SGBs are generally discontinuous, showing finely lobate outlines. Prismatic SGBs are generally more common within F₀₋₁ fabric; nevertheless, within some domains, basal SGBs are prevailing (Fig.2.59).

In plagioclase, some grains preserve tabular shape with igneous planar surfaces, whereas most of the grains exhibit incipient to widespread ribboning (Fig.2.60). This indicates that, along the main foliation, igneous feldspars were affected by crystal plastic deformation and they were partly replaced by granoblastic aggregates. Moreover, the common occurrence of aligned biotite-hornblende aggregates point out the superimposed solid-state overprint (Paterson et al., 1989).

Plagioclase and K-feldspar exhibit incipient recrystallization, displaying core and mantle microstructure. Recrystallized feldspars exhibit a grain size of ~50-100 μ . K-feldspars are affected by submagmatic microfractures (Bouchez et al., 1992). Here, intragranular fractures commonly affect a single grain; they are sealed by quartz material, which is in optical continuity with adjacent magmatic quartz from the matrix. Composite plagioclase-quartz infill may also locally occur (Fig.2.63). In this case, the albite-rich plagioclase (An~10%, as estimated by conventional optical methods) suggests that these fractures were sealed by a melt that gradually evolved toward a residual melt composition. Orthopyroxene, hornblende and feldspar porphyroclasts commonly displays sweeping undulose extinction, reflecting plastic deformation at relatively high-temperature (Van Roermund, 1983; Tullis & Yund, 1987).

Locally quartz-feldspar phase boundaries are coarsely lobate, where grain boundary cusps consistently point along the foliation trace (Fig.2.61 and 2.62). Cuspate to lobate quartz-feldspar grain boundaries reflect solid-state diffusion creep at high temperature ($T > 650^\circ$, Gower and Simpson, 1992). However, this deformation mechanism is inferred to contribute to deformation under melt-bearing conditions also ("melt-assisted diffusion creep", Dell'Angelo & Tullis, 1988; Rosenberg & Berger, 2001). This topic is treated with more detail in chapter III (section 3.2.1).

In summary, within the "low-strain" domains of DG suite, the preserved microstructures suggest that a transition from nearly undeformed magmatic fabric (i.e. Fig.2.57) toward gneissic fabric (acquired at high-temperature, in the solid state or at low melt fraction, Fig.2.61 to 2.63) occurred during pluton crystallization. The field observation that this composite F₀₋₁ fabric commonly overprints igneous contacts (also within domains containing weakly deformed quartz, Fig.2.55 to 2.57; see also Fig.2.53) suggests that the main (sub-) magmatic fabric developed after the juxtaposition of most of the granitoid\mafic rocks, but before the full crystallization of the pluton (owing to the occurrence of submagmatic microstructures; see also Paterson et al., 1998). This conclusion, is limited to the roof of Mafic Complex (namely DG suite), as primary features are nearly totally transposed in units I and II.

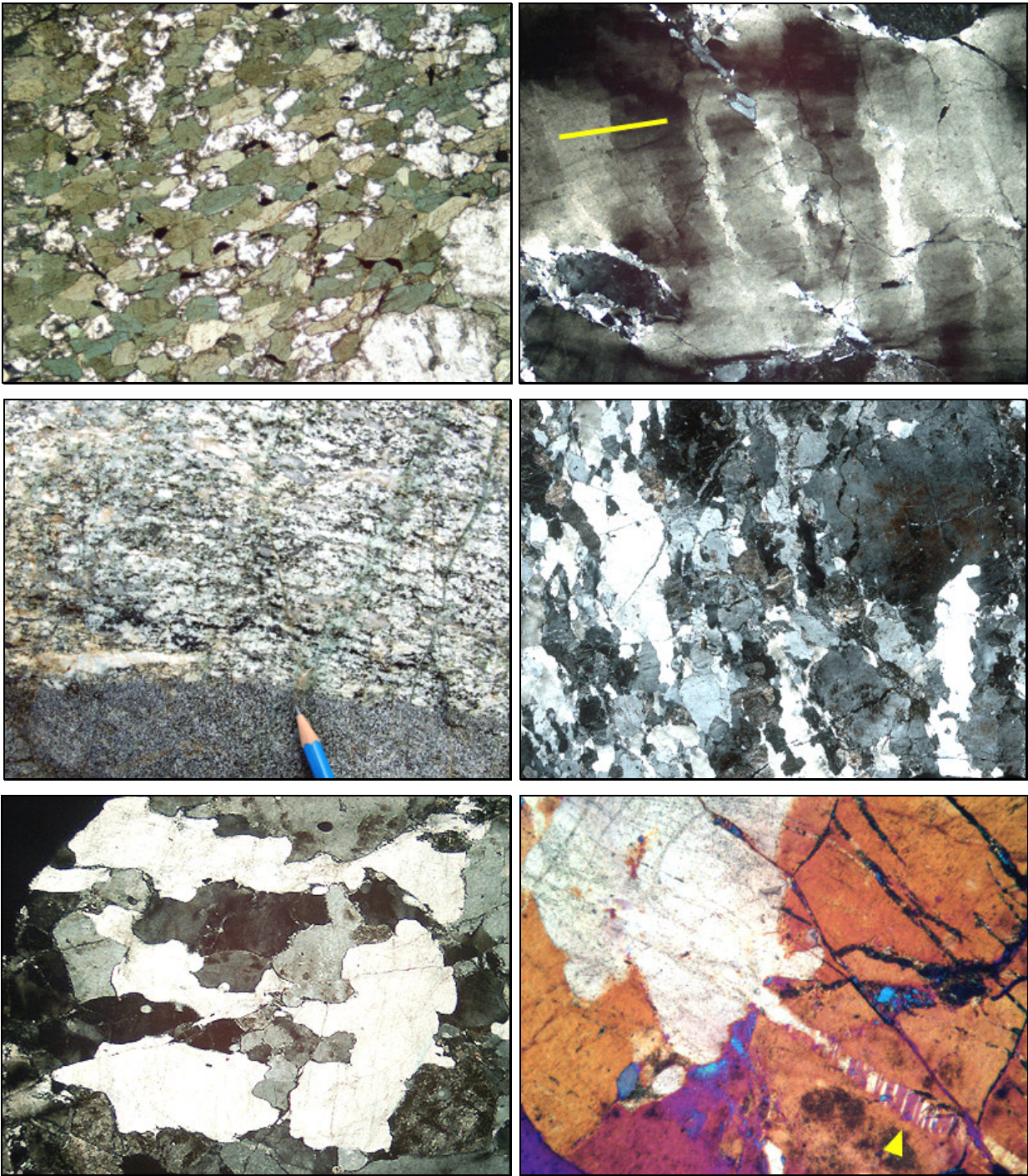


Fig. 2.58 (upper left): magmatic foliation in diorite (marked by aligned euhedral plagioclase and green hornblende), at the transition between fine-grained and coarse-grained layers (at bottom right). This sample was collected from the outcrop shown in Fig.2.52 (plane polarized light; base of photo: 4mm). **Fig. 2.59** (upper right): detail of magmatic quartz grain from melanocratic tonalite with F_{0-1} fabric. Unusual strong base-parallel SGB is largely prevailing on prism-parallel SGB (yellow line indicates the c-axis trace; crossed polars; base of photo: 4mm). **Fig. 2.60** (centre left): detail of the boundary between MME and host quartz-diorite. Note stretched plagioclase aggregates with aspect ratio 1:10 concordant with magmatic foliation. **Fig. 2.61** (centre right): enlarged micrograph from leucogranite vein injected into host porphyritic granite. Note the evident quartz SPO and high aspect ratio (sample z5, crossed polars; base of photo: 3cm). **Fig. 2.62** (lower left): detail from sample z5, showing cusped and lobate Qtz-Kfs grain boundaries, where cusp point along the foliation trace (horizontal; crossed polars; base of photo: 4mm). **Fig. 2.63** (lower right): detail from the same sample, showing submagmatic microfracture in Kfs. The infill is represented by quartz and sodic plagioclase, showing albite growth twins (yellow arrowhead; crossed polars; gypsum plate inserted base of photo: 4mm).

(b) *Quartz LPO*

Quartz lattice preferred orientation has been measured in seven samples collected in the northern area (Fig.2.64), where primary magmatic to submagmatic features are better preserved. According to the mean grains size and quartz content, the number of c-axis measurements varies between 60 and ~300.

In the less deformed sample (DSL60, Fig.2.57), c-axis pattern tends to develop a diffuse girdle around the (XY) foliation plane, displaying some prominent maxima close to the magmatic lineation. Here, quartz lacks any evident SPO, but intracrystalline strain features are partly developed. Thus, the rather strong quartz fabric could reflect synmagmatic quartz oriented grain growth, as described by Gapais & Barbarin (1986).

Within the other six samples, despite the difference in primary assemblage and quartz content, the typical microstructure is comparable to that preserved in the "gneissic" leucogranite (sample z5, Fig.2.61 to 2.63). In these cases, monocrystalline quartz ribbons display strong internal strain features, where chessboard SGB pattern is very common. The resulting c-axis fabric is qualitatively comparable: each sample exhibits some evident maxima close to the mineral lineation. X maximum is rather strong in Qtz-rich leucogranite, whereas the fabric within quartz-poor melanocratic enderbite is markedly weaker and more diffuse, being likely partly related to the low quartz content (Starkey & Cutforth, 1978; Lisle, 1985), and partly influenced by the subsequent lower temperature overprint. In fact, samples z26 and z57 recorded moderate solid-state overprint, mainly developed in the regime of subgrain rotation recrystallization (section 2.2.6.4), which may produce the observed secondary maxima around the foliation poles (Fig.2.64). The other samples recorded lower temperature overprint (likely during Alpine tectonic evolution), as revealed by the common occurrence of diffuse undulose and patchy extinction.

In summary, quartz fabric data suggest that oriented grain growth and slip, both along prism [c] direction were prevailing during magmatic to submagmatic flow (Blumenfeld et al., 1986). This hypothesis is in agreement with the common occurrence of chessboard SGB pattern, which indicate that quartz was mainly deformed through dislocation creep, in the high quartz field (Kruhl, 1996).

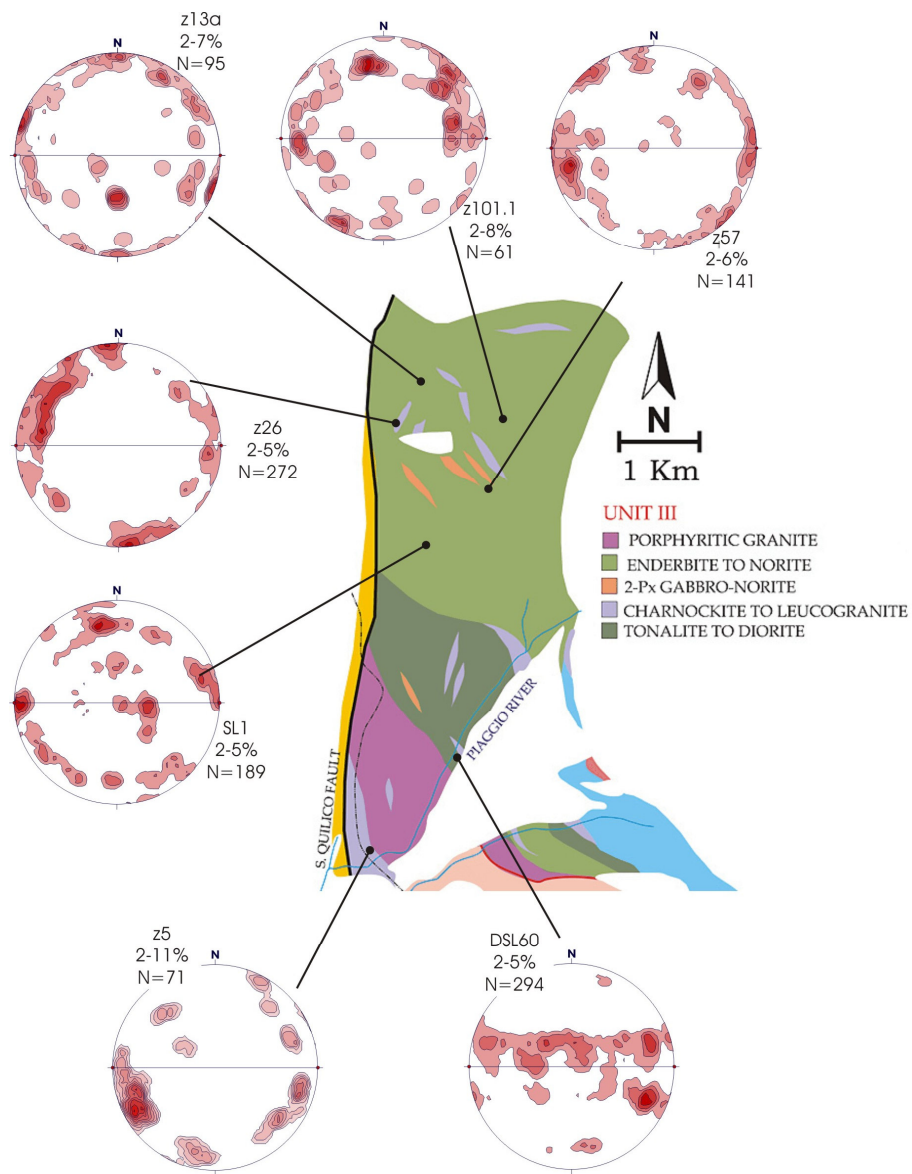


Fig. 2.64: map summarizing quartz c-axis from samples with magmatic to high-temperature solid-state fabric (F_{0-1} fabric), from the roof of mafic complex (NW area). For each equal area stereographic projection (lower hemisphere, 1% of search area), the labels are (from the top): sample name, contour interval, number of measurements.

Tab. 2-2: table summarizing the main features of the investigated samples. “X” symbols indicate the frequency of the occurrence of a certain microstructural feature (i.e. quartz subgrain boundaries), as approximately estimated in a relative range (from zero, indicated with “\”) to three.

	rock type	assemblage	LT overprint.	Opening angle	Fabric intensity (%)	Qtz SGBs	Chessboard SGBs	Lob. Q-F GBs	Qtz content (%; ±10%)
DSL60	granite vein	Kfs,Pl,Qtz,Bt	\	130°	5,44	XX	XX	XX	40
SL1	leuco-enderbite	Opx,Pl,Qtz ±Hbl±Bt	X	90°	5,82	XXX	XX	\	35
z26	charnockite	Kfs,Pl,Qtz, Bt±Opx	XX	75°	5,88	X	X	XX	30
z57	mela-enderbite	Opx,Cpx,Hbl, Bt,Pl,Qtz	X	50°, 94°	6,38	XXX	XX	XX	30
z13a	mela-enderbite	Opx,Cpx,Hbl, Bt,Pl,Qtz	XX	\	7,37	XXX	XX	XXX	25
z1011	enderbite	Opx, Hbl, Bt, Pl, Qtz	XX	60°	8,2	X	X	\	25
Z6	leucogranite	Kfs,Pl,Qtz	X	\	12,68	XXX	XX	XXX	40

2.1.7.3 High-temperature solid-state flow (F_2 fabric)

(a) Meso- and microstructures

The striking feature of S_{0-1} fabric is represented by the presence of a rather homogeneous foliation, where igneous fabric displays evidence of various degree of deformation, which was likely acquired during the transition from submagmatic to high-temperature solid-state flow. In these cases, the transition between heterogeneously deformed domains is commonly gradational. In contrast, F_{0-1} fabric is transected at various angles by discrete high-strain zones, displaying sharp to diffusive boundaries against wallrocks (Fig.2.65). These localized shear zones range from few cm to few mt in thickness, and usually they can be traced for just few tens of meters. They are developed in all the rocks described previously (Fig.2.65 to 2.70). Mylonitic folds are common, showing fold hinges roughly concordant with the stretching lineation. In Fig.2.67, asymmetric fold (reflecting sinistral shear sense) is bounded (at the base) by narrow D_2 shear zone. The fold shape is outlined by the folded magmatic layering in the mingled diorite (compare with Fig.2.48). Leucogranite to charnockite veins are commonly folded and boudinaged along D_2 shear zones. Some details from sheared charnockite pegmatites are shown in Fig.2.68 to 2.70.

D_2 mylonites represent a 100-200 mt. spaced network displaying quite homogeneous and coherent kinematics (this is well exposed along the *Piaggio River*), approximately exhibiting the same kinematic typifying the main fabric in Units I and II (Fig.2.1). Locally D_2 shear zone nucleate along pre-existing pegmatite boundaries, as suggested by felsic assemblage respect to the host Qtz-diorite, and by the presence of deformed Kfs porphyroclasts (up to 5 cm in length).

As a whole, D_2 microfabric in quartzofeldspathic rocks does not differ substantially from those typical of the main solid-state fabric in adjacent Units I and II. Within the more strained domains, quartz occurs as elongate polycrystalline ribbons, made up of completely recrystallized coarse grains, displaying lobate grain boundaries and mosaic-like pattern (in the sense of Gapais & Barbarin, 1986; Fig.2.71).

Kfs porphyroclasts display sweeping undulose extinction and widespread recrystallization. In the border of larger Kfs clasts, gradual transition between subgrains and newgrains is visible (Fig.2.74), suggesting that SR recrystallization was the dominant

recrystallization mechanism. Deformation-induced myrmekites are locally observable within these high-strain zones, but they are not common. The size of Kfs newgrains is ~200-300 μ in pressure shadows around larger porphyroclasts, grading toward a mean grain size of ~30-50 μ in the matrix (Fig.2.73 and 2.74). Brittle deformation is not evident at light microscope scale. These microstructural features suggest that K-feldspar was deformed in the dislocation creep regime, i.e. at temperature $>\sim 550^{\circ}\text{C}$ (Tullis & Yund, 1987).

In adjacent mafic layers (with noritic assemblage), Opx porphyroclasts (with apatite inclusions, likely representing old phenocrysts, Fig. 2.72) show syntectonic tails made up of green Hbl. This microfabric is markedly in contrast with those observed few hundreds of meters eastward, in the adjacent gabbro-norite associated with Grt-bearing gneisses (Fig.2.39).

In the less deformed domains, strongly deformed quartz porphyroclasts (displaying chessboard SGB pattern) are surrounded by relatively coarse-grained newgrains (0.1-1mm), showing lobate grain boundaries (Fig.2.75). Quartz aggregates display elongate shape with axial ratio up to ~5:1, but are not interconnected. These micro-domains locally contain large and poikilitic hornblende crystals, which partly include the recrystallized quartzofeldspathic mylonitic matrix. Thus, these amphibole grains are likely interpretable as D₂ syntectonic porphyroblasts.

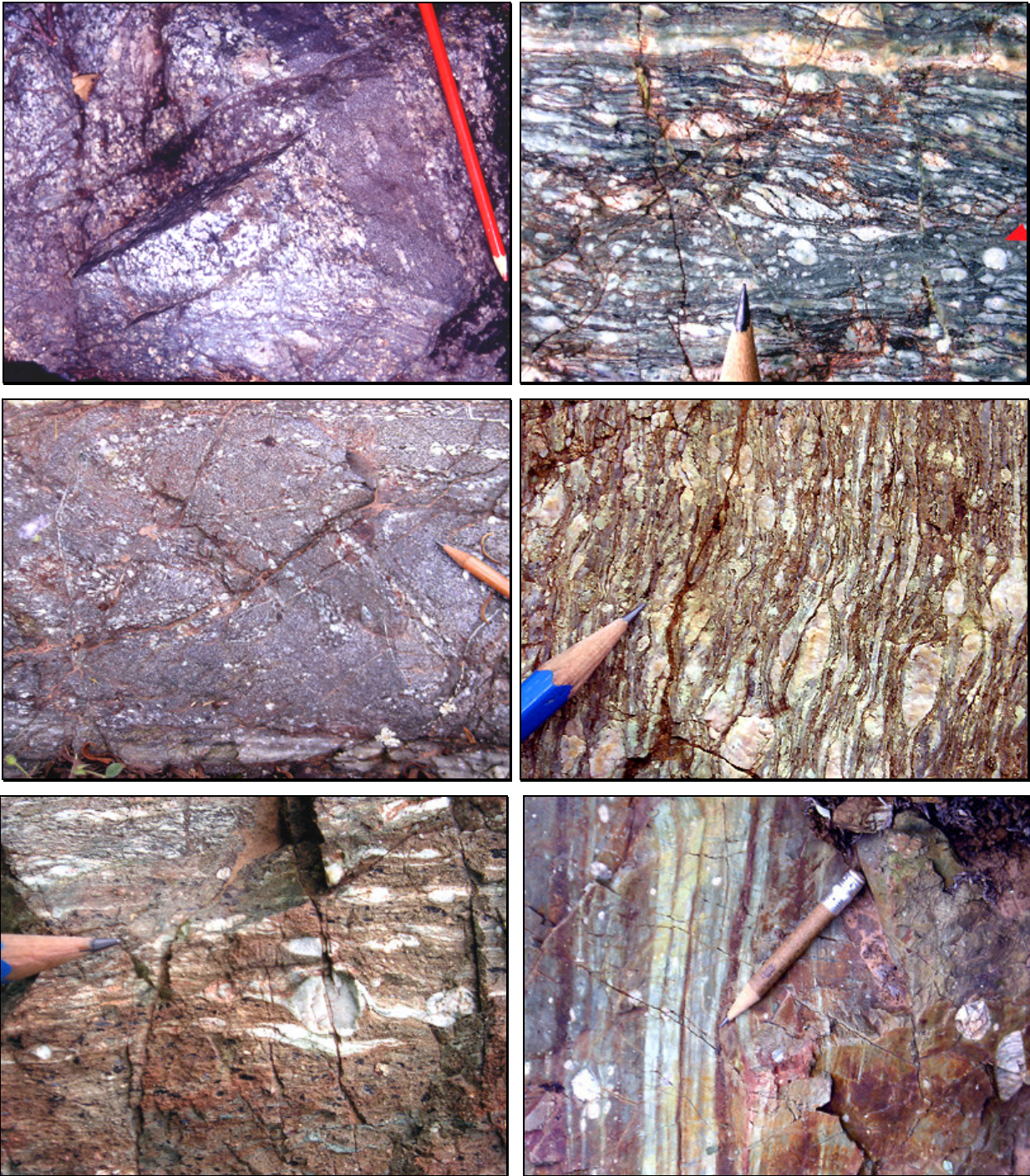


Fig. 2.65 (upper left): sharp boundary between sinistral D_2 shear zone and F_{0-1} fabric in tonalite, highlighted by aligned feldspars and MME. **Fig. 2.66** (upper right): detail from D_2 shear zone within Hbl-bearing tonalite intruded by thin leucogranite vein (at top). Sinistral shear sense is indicated by (flattened) S-C fabric and C' type, nearly ultramylonitic, shear bands (red arrowhead). **Fig. 2.67** (centre left): asymmetrically folded magmatic layering in diorite. Note brownish-weathered OPX crystals within coarser layers, as visible in undeformed domains (Fig.2.52). The mylonite nucleated along fold limb (visible at bottom), indicating shear parallel to the axial plane. **Fig. 2.68** (centre right): detail from D_2 mylonite developed within charnockite dyke. **Fig. 2.69** (lower left): detail from δ -type mantled K-feldspar porphyroclast indicating sinistral shear sense. These large clasts are arranged as elongate trails scattered within the mylonitic diorite, representing the remnants of a boudinaged pegmatite. **Fig. 2.70** (lower right): layered ultramylonite from sheared granite pegmatite. Note the occurrence of large K-feldspar porphyroclasts.

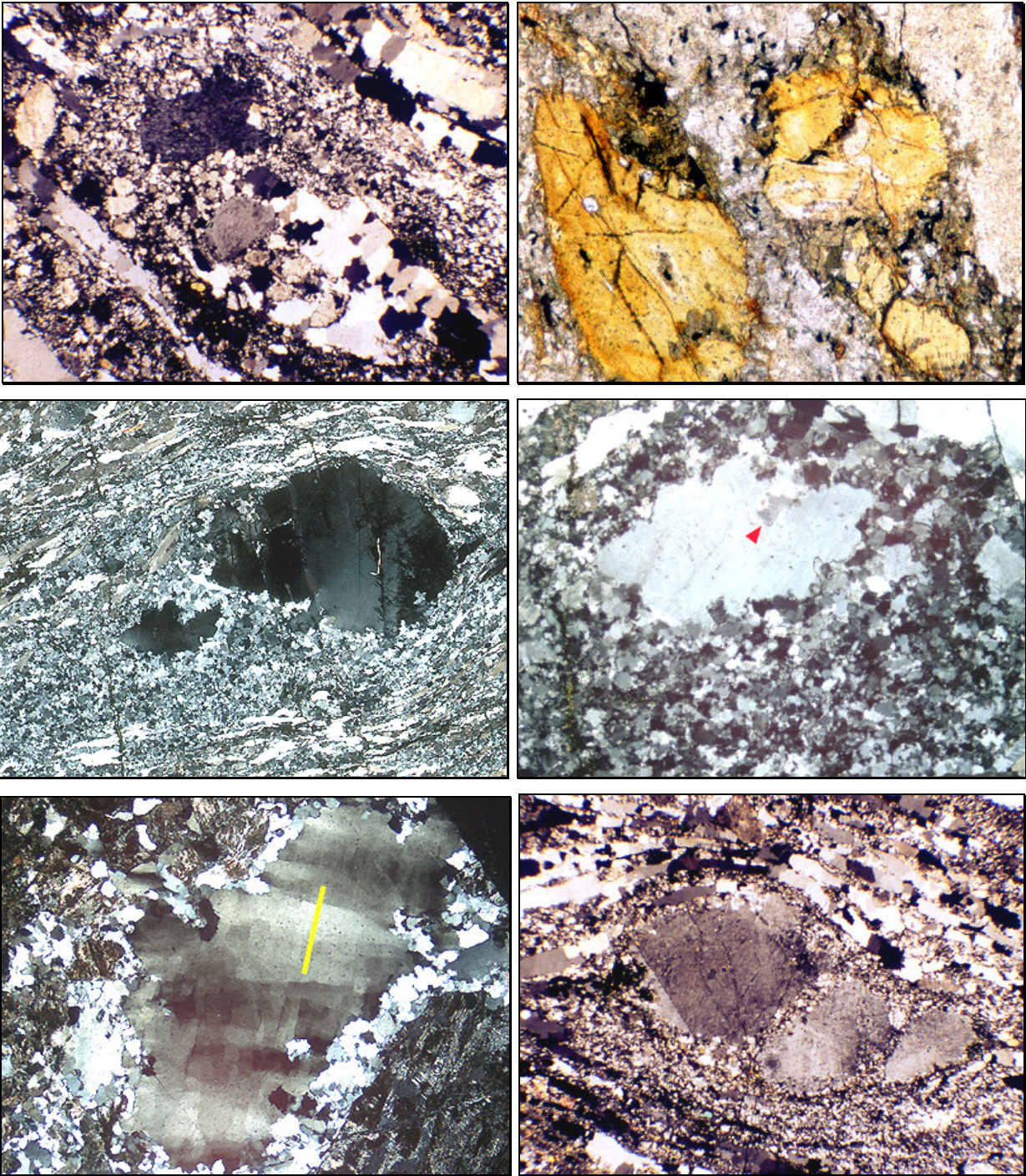


Fig. 2.71 (upper left): D₂ mylonite microfabric within leucogranite vein. Quartz ribbons display coarse-grained recrystallized grains and mosaic-like pattern. Kfs porphyroclasts are largely replaced by recrystallized Kfs, which develops fine-grained ribbons alternate with quartz ribbons (crossed polars; base of photo: 4mm). **Fig. 2.72** (upper right): detail from sheared norite, showing (altered) Opx porphyroclasts displaying syntectonic tails made up of secondary green hornblende. The white matrix is composed by completely recrystallized (and altered) plagioclase (plane polarized light; base of photo: 3mm). **Fig. 2.73** (centre left): enlarged micrograph showing typical D₂ microfabric within sheared granite pegmatite (sample v129a; section perpendicular to both foliation and stretching lineation; crossed polars; base of photo: 1.6cm). **Fig. 2.74** (centre right): detail from the central portion of Fig.2.79, showing Kfs recrystallization by progressive subgrain rotation: red arrowhead indicates some subgrains at the periphery of the host Kfs (section normal to both foliation and stretching lineation; crossed polars; base of photo: 4mm). **Fig. 2.75** (lower left): microfabric from D₂ shear zone shown in Fig.2.67. Strongly deformed quartz porphyroclasts (displaying chessboard SGB pattern; yellow line indicates the c-axis trace) are marginally replaced by recrystallized grains (sample DSL40a; crossed polars; base of photo: 4mm). **Fig. 2.76** (lower right): mylonite showing intermediate microstructures between F₂ and F₃ microfabric: GBM recrystallization for Qtz, patchy undulose extinction, microfaults and fine-grained (~10µ) recrystallization for Kfs (crossed polars; base of photo: 4mm).

(b) *Quartz LPO*

Quartz LPO has been investigated within thirteen samples corrected from D₂ shear zones, in both northern and southern domains (Fig.2.77). All mylonites exhibit comparable geometry (Fig.2.1) and qualitatively analogous microfabric. The low-temperature overprint is negligible at grain scale. By comparing the same “starting material” (i.e. leucogranite dykes), the main difference in the examined samples is related to the amount of the accumulated finite strain. In fact, quartz and feldspar porphyroclast are commonly preserved in the northernmost shear zones, being just marginally replaced by recrystallized grain. Here, most of quartz porphyroclasts exhibit chessboard SGB pattern (Fig.2.75). Quartz fabric from the northern “moderate-strain” shear zones differs substantially from that documented in the southern area, being strikingly similar to quartz fabric from F₀₋₁ (sub-) magmatic fabric (e.g. compare sample DSL60, from Fig.2.64, with sample DSL40a, from Fig.2.77). In fact, within all the five examined shear zones, the quartz fabric shows some prominent maxima around the stretching lineation, joined with minor maxima near Y and Z-axis.

In one case (sample v149a), quartz fabric has been investigated in both porphyroclasts and recrystallized grains, showing qualitatively equivalent patterns, with main maxima around X and Y-axes. Nevertheless, the prominent X maxima from the porphyroclasts is mirrored by prevailing Y maximum in the pattern of recrystallized grains (Fig.2.77). The comparison of these two quartz patterns might highlight the progressive syndeformational cooling during D₂ shearing.

In contrast, the more strained domains of the southern area, where quartz and feldspars are nearly totally recrystallized (Fig.2.73 and 2.76) exhibit strong (and commonly single) Y maxima, being the typical quartz fabric acquired at middle amphibolite facies condition (Schmid & Casey, 1986). In some samples, the Y maxima is very strong (i.e. v129a), whereas in others it is more diffuse (v34), likely owing to the local strain heterogeneities due to competence contrast between quartz and large feldspar porphyroclasts (as discussed in section 3.3.4). Some samples show intermediate pattern with the northern mylonites (i.e. samples z29, Z33 and z77), showing an additional maxima around the stretching lineation. Samples collected at few meters from the tectonic contact with the granitic complex (GC) exhibit Y maxima, but with a tendency toward the single girdle orthogonal to the mylonitic foliation (samples z37 and z83). The latter is the typical quartz LPO pattern recorded during D₃ shearing (section 2.2.7.4) and within the adjacent mylonites deriving from two-mica granitoids (GC, chapter III).

In summary, quartz LPO from D₂ mylonites suggests that fabric transition occurred during the D₂ shearing. In the northern area, the deformation was likely “frozen in” at an incipient stage of shearing, allowing the preservation of microstructures which are indicative of deformation in the high-quartz field. Assuming that of D₂ shearing started approximately at the crystallization level of the DGS (~5Kbar), the occurrence of prismatic [c] slip in quartz suggest a minimum temperature of ~700°C. These data fit the findings of Libourel (1985), who estimated comparable conditions (P=4.5-6Kb; T=750-800°C) for D₂ shearing within adjacent Units I & II.

In granitoid magma, some solid-state microstructures may develop when some melt is still present (see review in Vernon 2000a). Thus, D₂ shear zones might reflect the transition from “low-melt-fraction” to high-temperature solid-state-flow, as also

suggested by the occurrence of poikilitic hornblende (although poikilitic, nearly euhedral amphibole might grow during solid-state flow also). No clear microstructural criteria were found in order to testify the presence of residual melt during D₂ shearing. On the other hand, microstructures developed during flow at “low-melt-fraction” are hardly separable from those developed during high-temperature solid-state flow (Rosenberg, 2001).

D₂ shearing likely continued during cooling, as testified by the dominant quartz fabric for the southern area, where prismatic <a> slip were prevailing, and prismatic [c] slip were nearly totally deactivated. The tendency toward the single girdle quartz fabric (evidenced by some samples close to the GC; e.g. z37 and z83) provides the transition to the typical F₃ microfabric, as discussed in the next section. The transitional character of these mylonites is reflected by microstructures also, where quartz is recrystallized mainly by GBM, whereas K-feldspar exhibits low-temperature plasticity (Fig.2.76).

Tab. 2-3: table summarizing the main features of the investigated samples. “X” symbols indicate the frequency of the occurrence of a certain microstructural feature (i.e. quartz subgrain boundaries), as approximately estimated in a relative range (from zero, indicated with “\”) to three.

	rock type	assemblage	LT overprint.	Opening angle	F.intensity (%)	Qtz SGBs	Chessboard SGBs	Qtz content (% ±10%)	
	z1012	enderbite	Opx,Hbl,Bt,Pl,Qtz	XX	85°	4,94	XX	XX	30
	DSL40a	granodiorite	Hbl, Bt,Pl,Kfs,Qtz	X	86°	5,23	XXX	XX	35
	v34	tonalite	Hbl, Bt,Pl, Qtz	\	70°	5,25	X	\	30
	v149a	leucotonalite	Pl, Qtz, Bt	X	70°	5,26	XXX	XX	40
	DSL64p	tonalite	Hbl, Bt,Pl, Qtz	X	75°, 65°	5,3	XX	X	30
	DSL1102	granodiorite	Hbl, Bt,Pl,Kfs Qtz	XX	120°	5,63	XXX	X	40
	z33	leucogranite	mesopert.,Qtz ± Bt	\	120°	5,93	X	\	40
	z77	tonalite	Hbl, Bt,Pl, Qtz	\	80°	7,24	X	\	25
	z83	tonalite	Hbl, Bt,Pl, Qtz	X	45°	7,54	X	\	35
	z29	leucogranite	mesopert.,Qtz ± Bt	\	65°	7,57	X	\	40
	v143	charnockite	Opx, Hbl,Kfs,Pl,Qtz	\	55°	9,18	X	\	35
	v149ac	leucotonalite	Pl, Qtz, Bt	X	85°	9,35	XXX	\	40
	z37	leucogranite	Hbl, Bt,Pl,Kfs Qtz	X	\	9,51	X	XX	35
	DSL45	leucogranite	mesopert.,Qtz ± Bt	X	\	12,91	X	\	40
	v129a	leucogranite	Kfs,Pl,Qtz	\	\	14,14	X	\	40

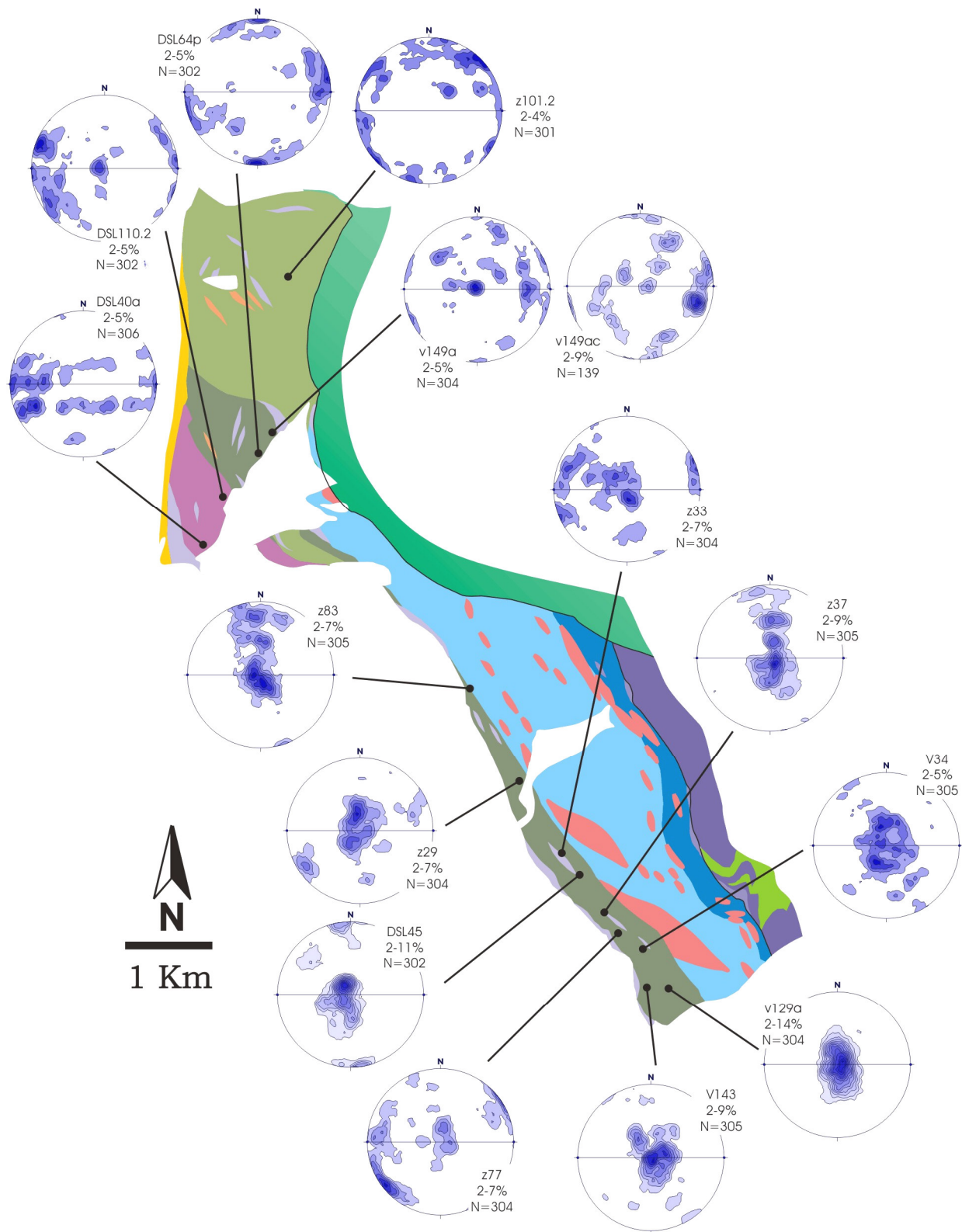


Fig. 2.77: map summarizing quartz c-axis fabric in D₂ shear zones, from the roof of mafic complex. For each equal area stereographic projection (lower hemisphere, 1% of search area), the labels are (from the top): sample name, contour interval, number of measurements.

2.1.7.4 *Moderate- to low-temperature solid-state flow (F₃ fabric)*

(a) Meso- and microstructures

S₀₋₁ and S₂ foliation are locally overprinted by D₃ shear zones, which are mainly detected by the extreme grain size reduction (being mostly thin ultramylonites) and by sharp boundaries against wallrocks (Fig.2.78). In the NW area, these younger mylonites commonly display sub-vertical foliation, which mainly cluster around two main orientations: N045° (dextral shear sense) and N120° (sinistral). In the central and southern portions of DGS, the progressive and concordant D₃ overprint is mainly detectable at the extreme margins of the complex, along the boundary with the adjacent GC. In this area, the geometry and kinematic of D₃ shear zones is comparable to those from the “mylonitic rim” of GC (chapter III). Within the low-strain domains, at margins of D₃ shear zones, partially overprinted (sub-) magmatic fabric is commonly detectable (Fig.2.83). Here, quartz recrystallization is mainly achieved through dominant SGR, suggesting that D₃ shear zones developed in the temperature range of ~400-500°C (assuming that deformation occurred strain rates; Stipp et al., 2002).

Within the high-strain domains, strongly layered microstructure occurs, as provided by alternation of quartz-rich and feldspar-rich polycrystalline ribbons (Fig.2.80). Here, quartz aggregates are made up of polygonal grains with nearly homogeneous grain size (~20-50μ), displaying the so-called “foam texture”. Recrystallized feldspar develops fine-grained (~5-10μ) aggregates, mainly containing albitic plagioclase and K-feldspar. Recrystallized feldspar aggregates exhibit strong LPO, as qualitatively checked with the gypsum plate (Fig.2.81). Feldspar (Fig.2.80) and amphibole porphyroclasts (Fig.2.82) behaved as rigid objects, within the ductile quartz-rich matrix; they commonly display microfaults and low-temperature plasticity (i.e. patchy undulose extinction). In the sheared quartz-diorite shown in Fig.2.79 and 2.82, hornblende porphyroclasts locally display syntectonic tails, made up of actinolite (see chapter IV for mineral chemistry details). Twin gliding and flame perthite are frequently developed within plagioclase and K-feldspar, respectively, being typical of deformed granites at greenschist facies conditions (Pryer, 1993). In contrast, strain-induced myrmekites are uncommon.

As a whole, D₃ microstructures are very similar to those typifying the main solid-state fabric along the “mylonitic rim” of the Granitic Complex. Consequently, these microstructures are treated with more detail in chapter III.

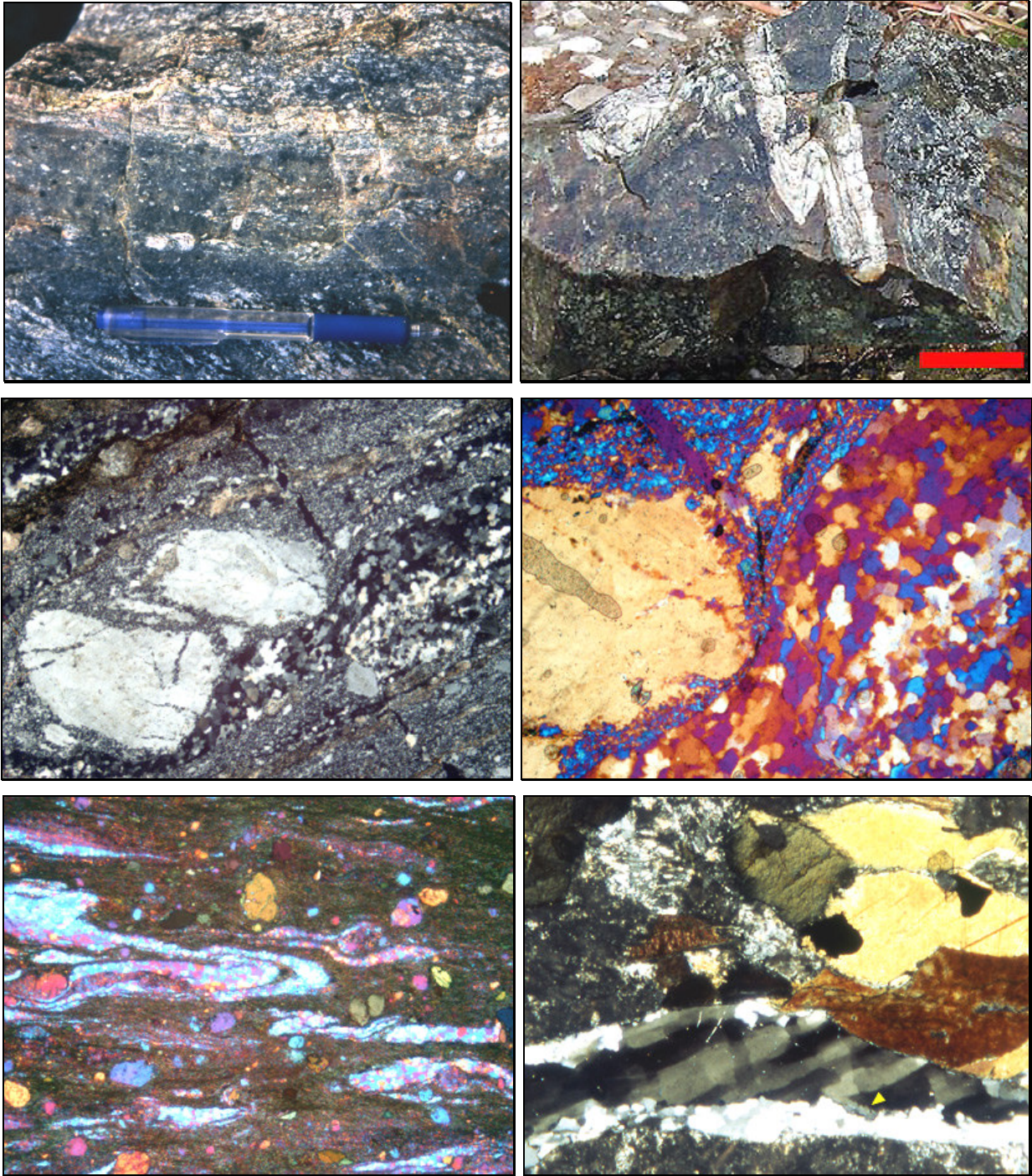


Fig. 2.78 (upper left): outcrop scale appearance of D₃ shear zone, developed within melanocratic (Hbl-rich) Qtz-diorite. This ultramylonite display leucogranitic assemblage and contains scattered Kfs large porphyroclasts. Thus, it likely nucleated along the boundaries between leucogranite vein and host Qtz-diorite. **Fig. 2.79** (upper right): detail of tubular (sheath) fold, highlighted by sheared aplite vein, from D₃ shear zone developed into quartz-diorite near the tectonic contact with GC (scale bar: 3cm). **Fig. 2.80** (centre left): typical microfabric within layered D₃ ultramylonite, showing antithetic microfault in Kfs porphyroclast (sinistral shear sense; sample DSL109a; crossed polars; base of photo: 4 mm). **Fig. 2.81** (centre right): detail from the same sample of previous photo, showing the strong LPO in both feldspars and quartz recrystallized grains (compare with analogous microfabric in section 3.3.2.3; crossed polars; gypsum plate inserted; base of photo: 1.8 mm). **Fig. 2.82** (lower left): example from the same D₃ ultramylonite shown in Fig.2.82 and 2.83, but within the host Qtz-diorite, showing mylonitic folds highlighted by quartz ribbon (with foam texture). The very fine-grained matrix (~<10μ) is mainly composed by Bt, albitic Pl and Qtz (sample DSL109b, crossed polars; gypsum plate inserted; base of photo: 4 mm). **Fig. 2.83** (lower right): microstructure from 2-Px enderbite sampled along the margins of a D₃ shear zone. Strong chessboard SGB pattern in the ribbon grain is partly overprinted by progressive SGR recrystallization (arrowhead: polygonal subgrains; crossed polars; base of photo: 3 mm).

There are some indications that deformation continued at lower temperature also. In some deformed leucogranite samples, large quartz porphyroclasts are inhomogeneously deformed (Fig.2.84), exhibiting dense network of kink bands. This intracrystalline strain feature, reflecting deformation at low-temperature or high strain rates, is overprinted (in the periphery of the grains) by a mantle of (strain-free) recrystallized grains (see detail in Fig.2.85), which were likely produced through dominant bulging recrystallization (BLG, grain size: ~10-20 μ ; see also Fig.2.86). This microstructure might reflect flow instabilities (i.e. subsequent cycles of work hardening, due to low recovery rates, and strain softening, owing to the production of new, strain-free, bulged grains) during deformation in the low-temperature plasticity field, in the manner reproduced by Gleason et al. (1993). Other common features of quartz porphyroclasts are represented by deformation lamellae and patchy undulose extinction. In these cases, feldspars are mainly deformed by brittle processes. This low-temperature microfabric is indicative of deformation in the temperature range of 350-400° (the absence of brittle deformation in quartz suggest $T > \sim 350^{\circ}\text{C}$; "regime 1" of Hirth & Tullis, 1992, BLG field of Stipp et al., 2002). This microfabric is thus well distinct from typical Alpine microfabric within the "main" S_2 foliation, which is marked by widespread brittle deformation of both quartz and feldspars (section 1.4).



Fig. 2.84: enlarged micrograph from sample z22 (granodiorite), showing heterogeneously deformed quartz porphyroclasts, wrapping around ("rigid") fragmented feldspars grains (crossed polars; base of photo: 1cm).

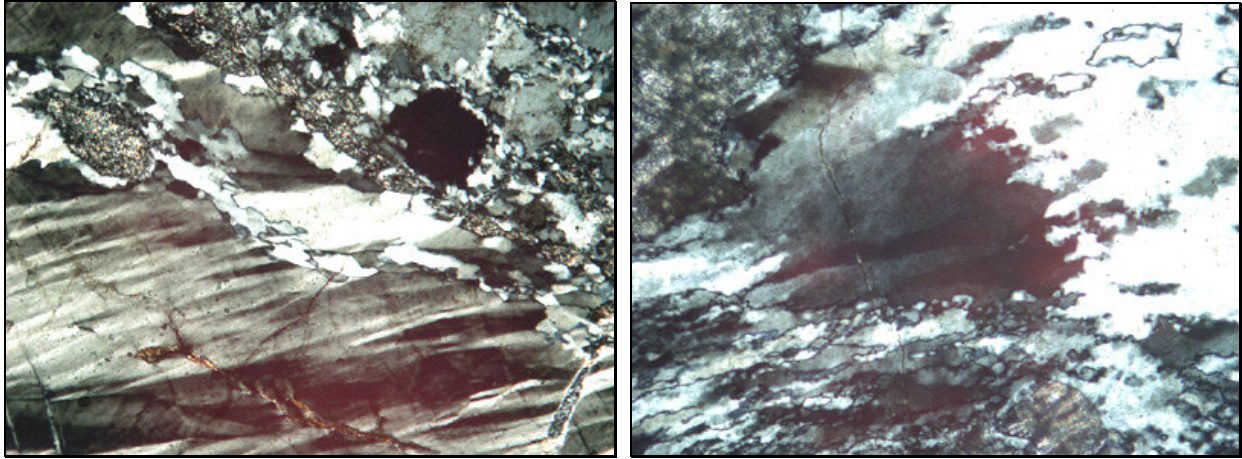


Fig. 2.85 (left): detail of Qtz porphyroclast from sample z22, showing kink bands overprinted by dynamic recrystallization along the periphery of the host grain (crossed polars; base of photo: 1.8mm). **Fig. 2.86** (right): detail of Qtz porphyroclast largely replaced by recrystallized grains, mainly produced through BLG recrystallization (crossed polars; base of photo: 0.7mm).

(b) Quartz LPO

Quartz LPO has been investigated in four D₃ mylonites mainly collected in the northern area (Fig.2.87). With the exception of sample z22 (Fig.2.84), the investigated samples represent sheared leucogranite veins, injected into host enderbite (sample DSL3), tonalite (sample z3) and rapakivi granite (sample DSL109). The resulting quartz fabrics vary from single (strong) Y maximum (Z3) to well-developed single girdle, displaying weak tendency toward type I crossed girdle (samples DSL3 and DSL109). Monoclinic (external) symmetry of quartz pattern is in agreement with the commonly used microstructural criteria, indicating dextral shear sense for sample DSL3 and sinistral shear sense for z3 and z22. Despite the unambiguous non-coaxial character of D₃ mylonite in sample DSL110 (Fig.2.79 to 2.81), the corresponding quartz fabric exhibits external orthorhombic symmetry. This could be related by the high finite strain recorded by this ultramylonite (Garcia Celma, 1982; Schmid & Casey, 1986), including the occurrence of (“tubular”) sheath folds (Fig2.79; Lacassin & Mattauer, 1985), displaying fold axis parallel to the stretching lineation.

Tab. 2-4: table summarizing the main features of the investigated samples. “X” symbols indicate the frequency of the occurrence of a certain microstructural feature (i.e. quartz subgrain boundaries), as approximately estimated in a relative range (from zero, indicated with “\”) to three.

	rock type	assemblage	LT overprint.	Opening angle	F.intensity (%)	Qtz SGBs	Qtz content (%; ±10%)
z22	granodiorite	Opx,Kfs,Pl,Qtz	\	\	5,26	XXX	35
DSL3	leucogranite	Kfs,Pl,Qtz	\	30°	6,6	XXX	35
DSL109	Qtz-diorite	Hbl,Bt,Pl,Qtz	\	35°	8,22	X	30
z 3	granodiorite	Pl,Kfs,Qtz	\	\	12,58	X	30

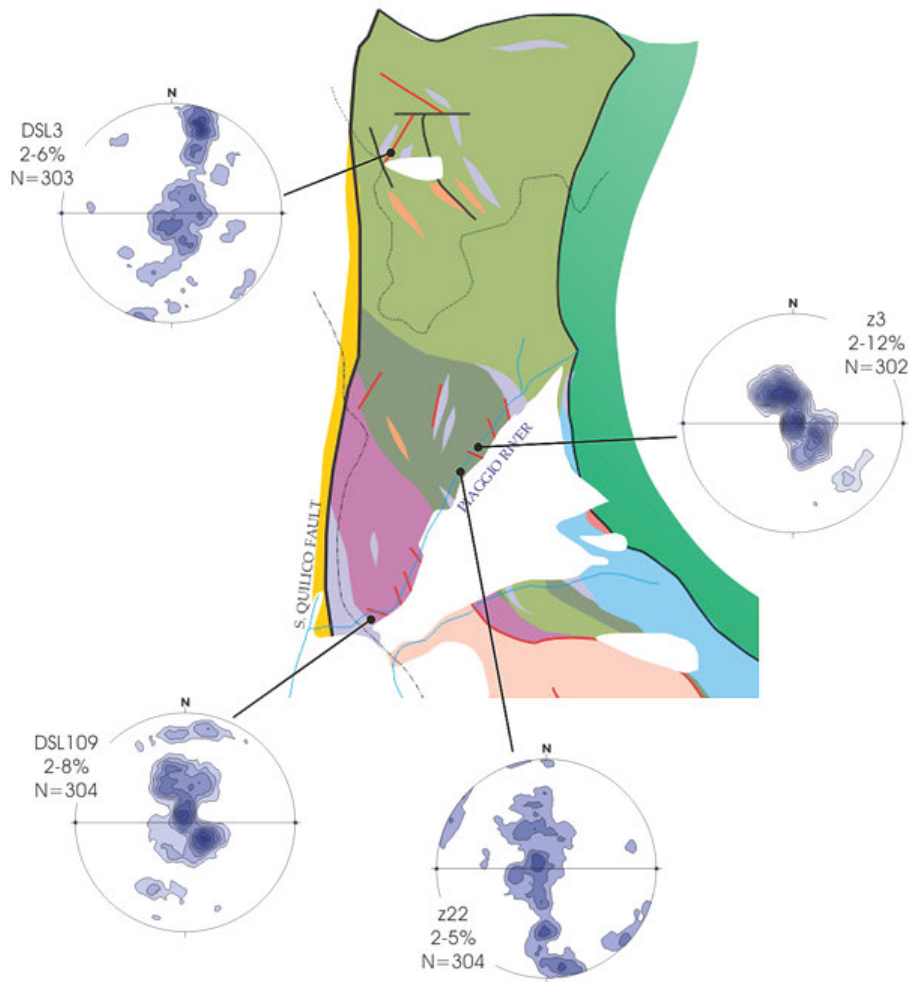


Fig. 2.87: map summarizing quartz c-axis fabric in D_3 shear zones, from the northern portion of roof of mafic complex. For each equal area stereographic projection (lower hemisphere, 1% of search area), the labels are (from the top): sample name, contour interval, number of measurements.

3 GRANITIC COMPLEX

This chapter is divided into three main parts. In section 3.1, the general framework of the different rocks composing GC is briefly presented. This part provides the essential background to illustrate and discuss the main topics of this chapter: the description of the main structural features related to the progressive fabric development during syndeformational emplacement (section 3.2) and subsequent syntectonic cooling (section 3.3).

3.1 Outline on field relations and microstructures

The GC is located in the SW sector of the basement (Fig.3.1). Its eastern and northern limits are represented by the NW-SE-trending tectonic contact with the roof of the Mafic Complex. Only these boundaries preserve the original pre-Alpine architecture, being roughly concordant with the internal pluton foliation. The southern and western boundaries of the GC are represented by Alpine faults, whereas the southwestern limit is covered by Quaternary deposits belonging to Tavignano River. The GC is compositionally separable into two main magmatic suites (Fig.3.1): (i) a medium to coarse-grained Hbl-bearing suite; (ii) medium to fine-grained, Ms-bearing suite. Both suites are largely heterogeneous and contain several magmatic rocks. From a structural viewpoint, two distinct domains are detectable: (i) the inner part of the pluton, which is nearly unaffected by solid-state deformation, displays a well preserved magmatic to late-magmatic fabric; (ii) the “mylonitic rim” (along the NE pluton margin), where all granitoids belonging to the GC are transformed into orthogneiss displaying S-C fabric.

3.1.1 Hornblende-bearing granitoid suite

The Hbl-bearing suite takes up about two thirds of the complex. It includes several rocks, ranging from leucogranites to ultramafites. Besides the different end-member rocks described here (and shown in the map), a nearly complete range of intermediate rocks are present in between.

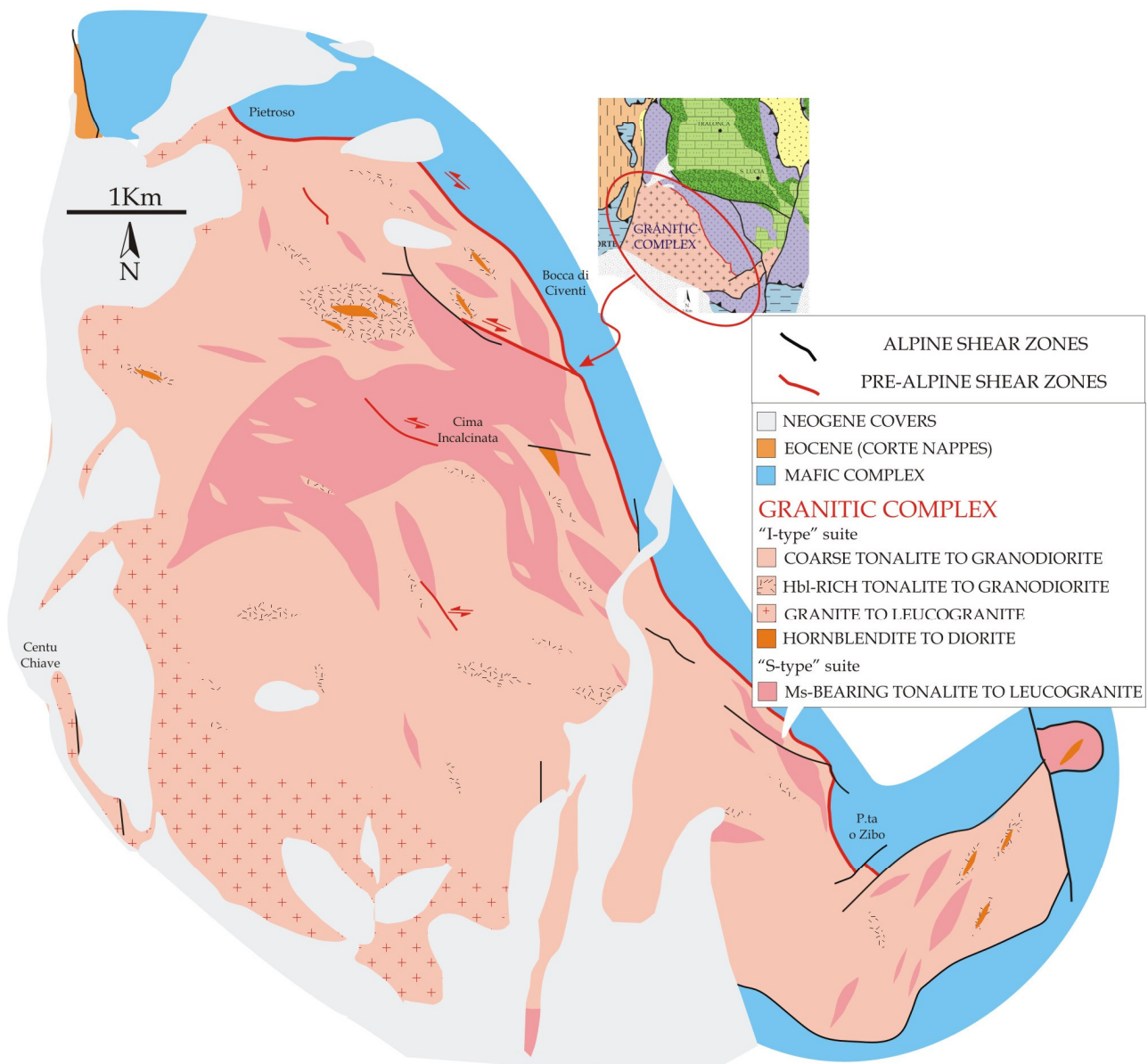


Fig. 3.1: Geological map of S. Lucia Granitic Complex, showing the distribution of different magmatic rocks (this work). Compare with pre-existing maps (Fig.1.2).

3.1.1.1 *Hornblendite to diorite*

This group of mafic rocks likely corresponds to the “massive gabbro” shortly described by Ritsema (1952). The largest mafic-ultramafic body crops out in the central part of the complex, few hundreds of meters westward from “Bocca di Civalenti” locality (Fig.3.1).

Mafic to ultramafic bodies appear as lenses (ranging from few meters to few hundreds of meters in length), completely enclosed into coarse granitoids. Mafic lenses are commonly roughly zoned, displaying hornblendite cores surrounded by dioritic to granodioritic rims (Fig.3.2). In some outcrops, hornblendite contains ~50cm-thick pegmatoid diorite layers,

displaying sharp to gradational boundaries against host hornblendite. Both rocks contain Hbl + Pl + Bt. In hornblendite, Hbl may reach up to ~90% in modal abundance, whereas the typical diorite is commonly rather leucocratic (Pl content ~50-60%). At both outcrop and grain scale, magmatic fabric is well preserved and no (pre-Alpine) solid-state overprint is generally visible.

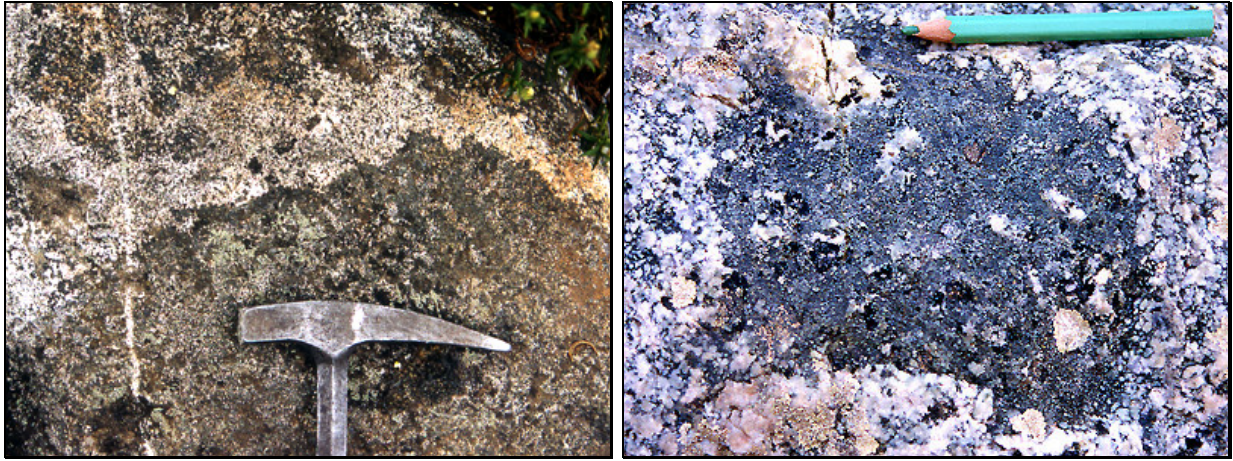


Fig. 3.2 (left): detail from crenulate boundary between dioritic corona enclosing metric hornblendite body. Fig. 3.3 (right): detail of a MME from “mingled granodiorite” containing Kfs and Hbl phenocrysts.

Larger mafic-ultramafic bodies are surrounded by a peculiar granitoid, distinctly enriched in Hbl and Bt. Here, relationships between mafic rocks and host granitoid are complex, where mingling relations (Vernon et al., 1988) are locally evident. Here, brecciid facies is commonly observable, producing heterogeneous magmatites with an overall granodioritic composition and presence of Kfs and Hbl megacrysts (Fig.3.3).

In this area, the “mingled granodiorite” is commonly injected by Hbl-bearing to Bt-bearing pegmatites and contains abundant MME (mafic microgranitoid enclaves, Didier & Barbarin, 1991). Contacts between these different magmatites are lobate and very irregular in detail (Fig.3.2). Besides mingling, some mineralogical evidences of magma hybridism include the local occurrence of Kfs phenocrysts within MME (Didier & Barbarin, 1991; Paterson et al., 2004), quartz grains with fine-grained mafic rims (“Qtz ocelli”, Vernon, 1984), and rapakivi structure (Vernon, 1984).

3.1.1.2 Tonalite

Few tens of meters away from the mafic/ultramafic bodies, the “mingled granodiorite” progressively grades into tonalite, which represents the dominant rock type in the Hbl-bearing suite. Tonalite displays a primary assemblage containing Pl + Qtz + Bt ± Hbl ± Kfs ± Ttn. Tonalite is rather heterogeneous in detail, where the (Hbl-rich) mafic end-member (Fig.3.4) grades into leucocratic (Hbl-free) tonalite. This transition commonly takes place over few meters, without crosscutting relations and with intermediate compositions in between. Dioritic MME are commonly fine-grained, they are moderately elongate (aspect ratio between 2:1 and 5:1), and exhibit rounded shapes. The grain size is uniform, in contrast with MME contained into the “mingled granodiorite”. Contacts with host diorite are commonly sharp, but they are finely lobate to crenulate in detail. The distribution of MME is very irregular at pluton scale, being very common in mafic tonalite, and nearly absent in leucocratic end member. The main magmatic fabric is concordant between MME

and host tonalite: no foliation deflection occurs along the boundaries, suggesting low competence contrast during foliation development.

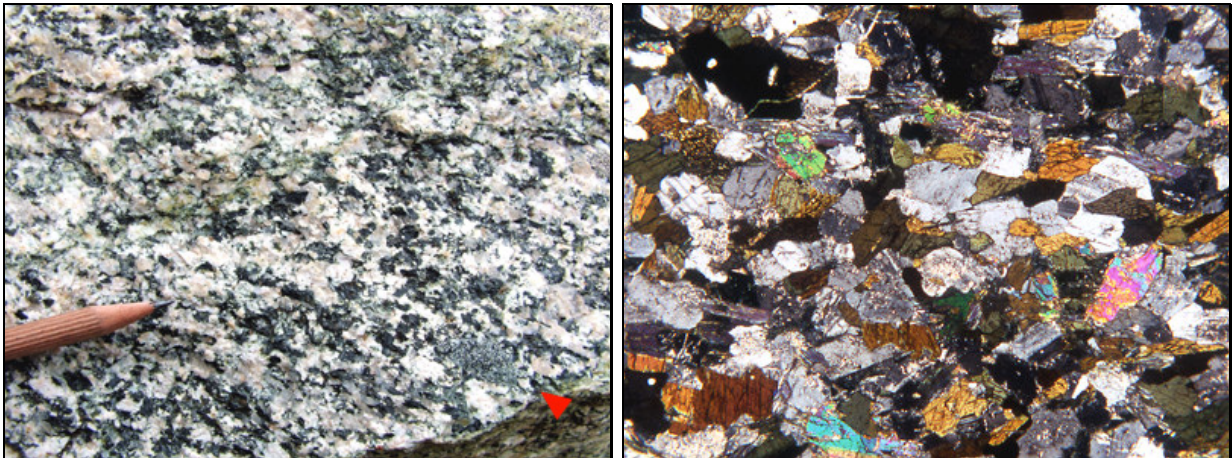


Fig. 3.4 (left): typical mafic tonalite, which is strongly enriched in Hbl and Bt. Arrowhead point to small dioritic MME scattered along the main fabric. **Fig. 3.5** (right): Dioritic MME with horizontal magmatic foliation, defined by alignment of main magmatic phases: Hbl, Pl and Bt (sample Z92a; crossed polars; base of photo: ~ 5 mm).

3.1.1.3 Granite to leucogranite

This facies crops out along the westernmost part of the complex (Fig.3.1), being characterized by the occurrence of pink Kfs phenocrysts (up to ~ 2cm in length) associated with Pl, Qtz \pm Bt \pm Aln \pm Hbl. As observed for tonalite, also granite exhibits several facies, ranging from (Hbl-rich) melagranite (Fig.3.6) to the more common leucogranite, which commonly contain sporadic mica flakes (Fig.3.7). Along *Tavignano Valley*, leucogranite commonly grades into leucotonalite, and sharp boundaries between these rocks are generally lacking.

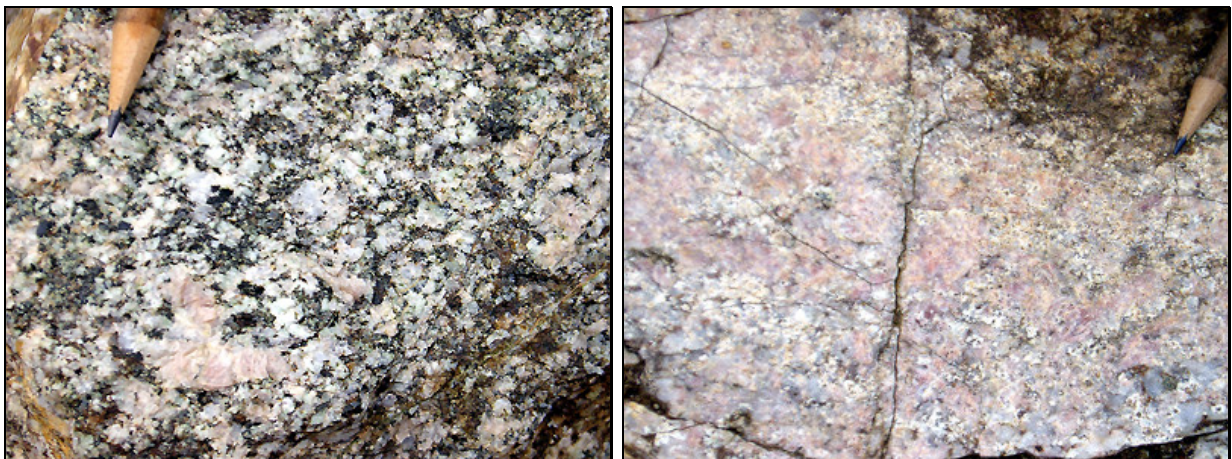


Fig. 3.6(left): Mafic granite displaying high femic content (Hbl + Bt \pm Aln). Aligned feldspars and amphibole highlight horizontal magmatic foliation. **Fig. 3.7** (right): typical leucogranite, displaying high Kfs-content and rare Bt flakes.

3.1.2 Two-mica microgranitoid suite

Two-mica microgranitoids belong to a compositionally heterogeneous suite, which is intrusive into both coarse-grained granitoids and associated mafic rocks. This is indicated by the widespread occurrence of microgranitic dykes (which are usually one to several meters in thickness) injected into host Hbl-bearing rocks. As visible at map scale, Ms-bearing rocks crop out into two distinct settings; in the central part of the complex, microgranitoids occur as a Km-scale continuous body, with an irregular and approximately sigmoidal outline, broadly oriented along a NNE-SSW direction. Here, the main microgranitoid body frequently includes small lenses of host coarse-grained granitoids and mafic rocks. Elsewhere microgranitoids crop out as lenticular bodies with the long axis (~50-500m in length) nearly oriented along the main magmatic foliation of the pluton (see below).

Magmatic contacts between microgranites and host I-type granitoids are frequently amoeboid and lobate at outcrop scale (Fig.3.9), implying that microgranites were intruded into low-viscosity (i.e. partially molten) host rocks.

Microgranitoids are typically fine-grained, displaying various colour index: mafic end member is tonalitic to granodioritic in composition, displaying high content of Bt and Ms (Fig.3.8, left). In contrast, in the leucocratic end member (represented by Kfs-rich microleucogranite), Ms is rather abundant, whereas Bt is absent or scarce (Fig. 3.8, right).

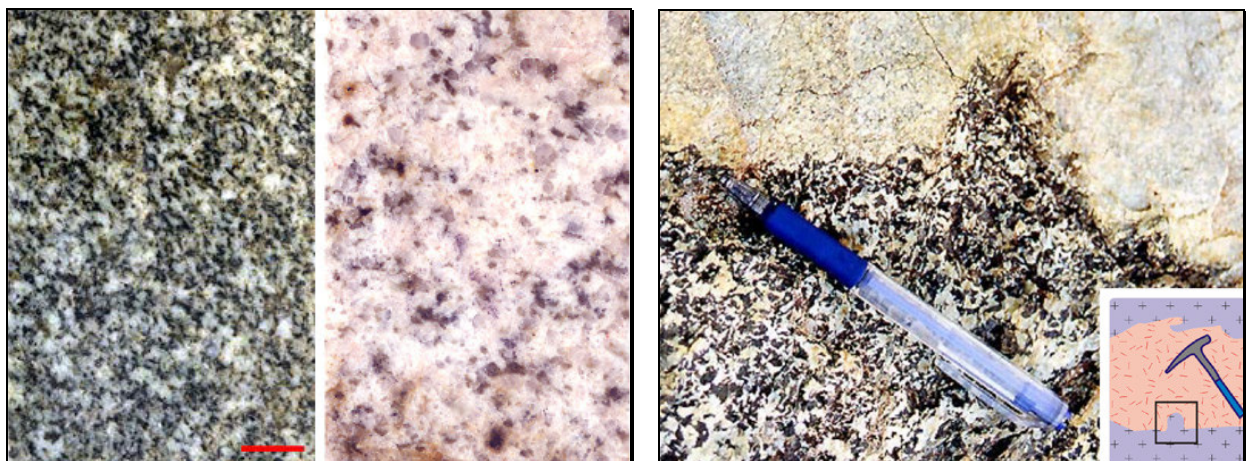


Fig.3.8 (left): polished samples from end-member lithotypes belonging to the microgranitoid suite. Tonalite/granodiorite (left, sample DSL88) displays relatively high colour index, due to high content of Bt. Note the well-defined magmatic alignment of tabular Pl grains and Bt flakes. Leucogranite (right, sample DSL72) shows high content of Kfs and Ms (grey; Scale bar is 0.5 cm). **Fig. 3.9** (right): detail of lobate contact with Qtz-diorite 'bulging' into microgranite dyke. The sketch on lower right corner highlights the morphology of dyke boundaries.

3.1.3 Mafic and felsic dykes

Both previously described suites are intruded by mafic dykes and Ms-bearing pegmatites to aplites. Crosscutting relations indicate that felsic dykes are younger.

Mafic dykes are dark and fine-grained, displaying dioritic assemblage (comparable to those of MME). Felsic veins contain albitic plagioclase (An ~10-20%), K-feldspar, quartz and muscovite. Hbl and Bt-bearing pegmatites are associated with the “mingled granodiorite”, whereas they are commonly absent elsewhere. Coarse-grained quartz veins represent the youngest magmatic product visible in the field.

As described before, also this vein network commonly display lobate and crenulate contacts with host rocks (i.e. Fig. 3.10), suggesting that dykes are just slightly younger than host rocks. In addition, these irregular contacts between dykes and all host rock types indirectly suggest that coarse granitoids, mafic rocks and two-mica microgranitoids are roughly coeval.



Fig. 3.10: irregular and crenulate contact between thin Ms-bearing pegmatite and host microgranite with magmatic foliation (sub-vertical, but not well visible here).

3.2 Synmagmatic fabric

3.2.1 Magmatic to submagmatic fabric

In the domain with preserved magmatic fabric (*lato sensu*), three end-member microfabrics are detected. F_1 microfabric is defined by aligned crystals (feldspars, hornblende) surrounded by anhedral and non-deformed quartz. F_2 fabric is defined by the coexistence of quartz ribbons and nearly idiomorphic (and non-deformed) magmatic crystals. Finally, within F_3 microfabric, all mineral phases exhibit evidences of deformation at high-temperature. S_2 and S_3 foliations are not geometrically distinguishable from S_1 . Thus, classical crosscutting relations between subsequent generations of structures are not visible in this complex. Indeed, the spatial transition from F_1 to F_3 fabric is rather vague; the fabric distribution seems irregular and “patchy” at pluton scale. Consequently, owing to the difficulty to separate F_1 to F_2 and F_3 fabric in the field, the foliation pattern and the fabric orientation in Fig. 3.11 deals only with magmatic and solid-state fabric, where magmatic fabric is a composite fabric ranging, through the space, from F_1 to F_3 .

From a purely geometrical viewpoint, both magmatic and solid-state fabrics exhibit an orientation that is largely comparable with those of the solid-state fabric (S_2 to S_3 foliation, sections 2.1.7.3 and 2.1.7.4) in the adjacent roof of MC (Fig.3.11). The correspondence concerns the orientation of foliation, lineation, and the sinistral sense of shear, as observable from outcrop to thin section scale. At pluton scale, the magmatic foliation pattern defines large-amplitude, “knee-shaped” folds, along which the foliation is progressively deflected from N-S toward E-W orientation. This fabric pattern is evidenced by the foliation trace shown in the map (Fig.3.11), and by the more scattered foliation poles orientation (compare with foliation poles of adjacent solid-state fabric). The significance of this pattern will be discussed later in the text.

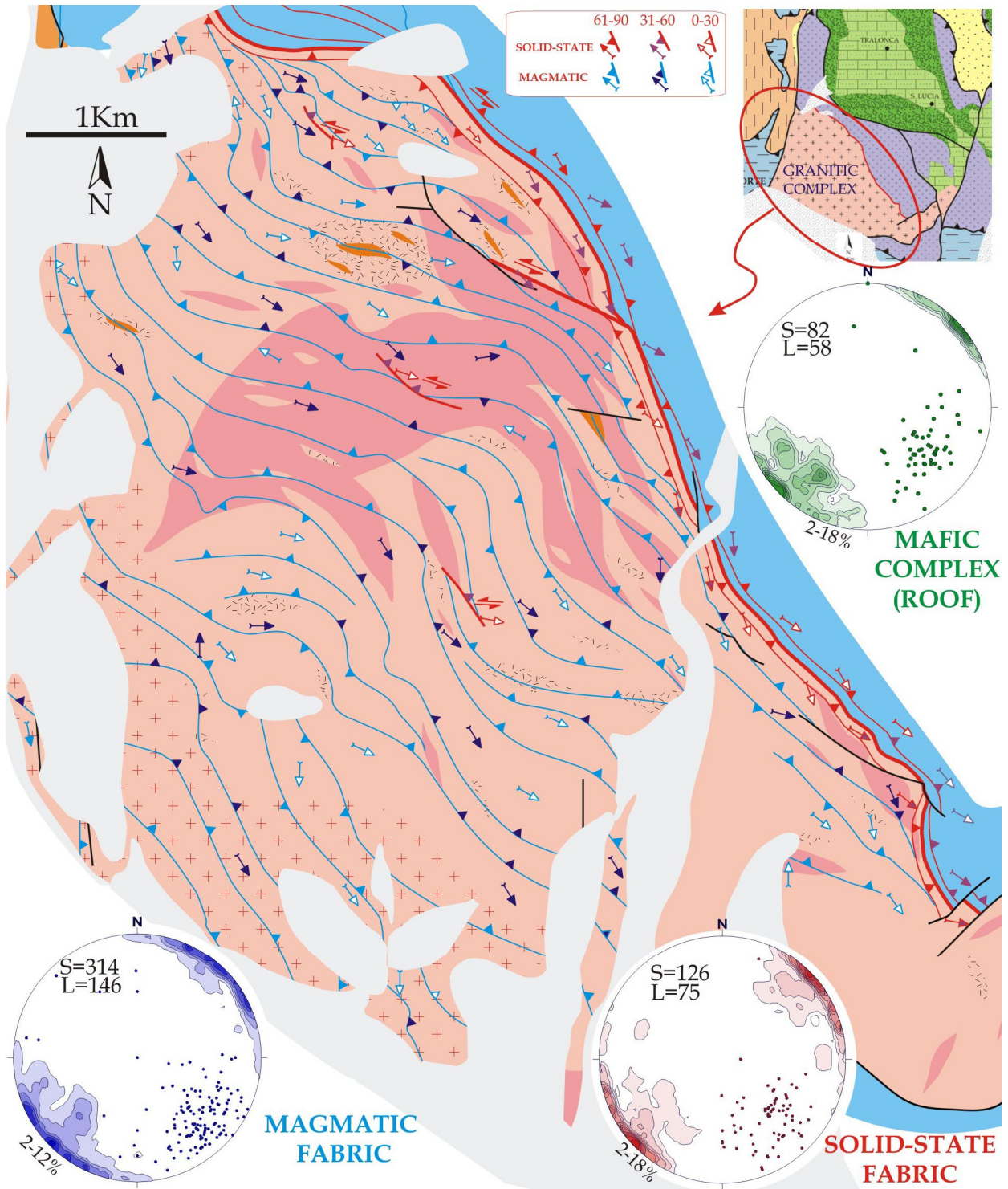


Fig. 3.11: structural map of Granitic Complex. Foliation pattern and main structural elements in GC and in the adjacent roof of Mafic Complex are indicated. In the pole figures, the countering of foliation poles and lineation are provided (S and L indicate the number of foliation and lineation measurements, respectively. Each measurement represents one outcrop. The range of countered density lines is also indicated).

3.2.1.1 Magmatic fabric (f_1)

The presence of well-defined magmatic foliation and lineation is evident in all magmatites belonging to GC, except for hornblendites (where the foliation is absent or weak; Fig. 3.2). At outcrop scale, I-type rocks exhibit a well-defined alignment of nearly euhedral feldspars and Hbl, which provides the best evidence for the magmatic origin of the main foliation (Figs. 3.12). The magmatic lineation is commonly well defined; in particular, this is evident in coarse-grained (Hbl-bearing) diorite and tonalite, where it is highlighted by strong plagioclase and amphibole alignment.

Quartz occurs as large, patchy grains with irregular outline; it lacks any shape fabric, being generally weakly deformed: magmatic Qtz-Qtz and Qtz-feldspars grain boundaries are usually preserved and internal deformation features are nearly absent (3.13). Prism- and (less frequently) base-parallel subgrain boundaries (SGBs) may locally occur in these cases, but they are uncommon.

Within microgranitoids, magmatic foliation is well evident at grain scale, marked by strong alignment of nearly euhedral plagioclase and orthoclase grains (the latter is partly inverted into microcline) and mica flakes (Fig.3.13).



Fig. 3.12: strong magmatic foliation in melanocratic (Hbl-rich) tonalite intruded by two-mica leucogranite vein. Note the irregular dyke boundaries and the continuity of the foliation across the vein.

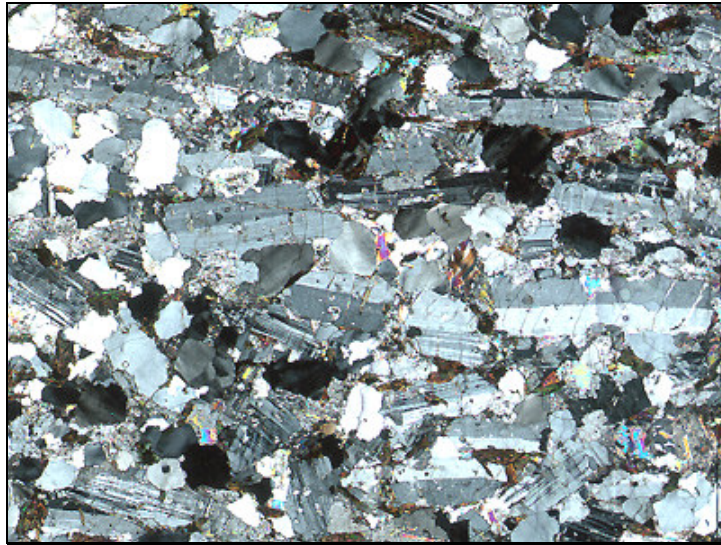


Fig. 3.13: F_1 fabric at grain scale: the strong magmatic foliation is highlighted by tabular Kfs grains; note the well-rounded and unstrained quartz blebs, which lack any quartz shape fabric (sample DSL71; crossed polars; base of photo: 4mm).

3.2.1.2 *Submagmatic fabric (f_2)*

Within coarse granitoids, there are some mesoscopic indications that flow locally continued under submagmatic conditions. On XZ sections from outcrops with macroscopically “magmatic-looking” fabric, the coexistence of aligned idiomorphic phases (i.e. feldspars, amphibole and micas) with elongate quartz ribbons represents a striking feature of F_2 fabric (Fig. 3.14). Here, quartz develops mono- to polycrystalline ribbons, commonly containing few grains. Qtz ribbons exhibit strong SPO parallel to the main orientation of tabular magmatic feldspars, showing aspect ratio between 1:2 and 1:8. In theory, should be possible to map, into coarse granitoids, distinct domains exhibiting this evident F_2 fabric. During this work, however, the attempt to get a coherent (map-scale) fabric distribution failed, mainly because of the very patchy F_2 spatial distribution, joined with an insufficient continuity of outcrop exposition.

Two end-member types of quartz ribbons occur within F_2 fabric: (i) Type 1: monocrystalline (or rarely polycrystalline) ribbons devoid of any internal strain feature; (ii) Type 2: polycrystalline ribbons displaying strong internal strain, testified by the presence of a dense network of SGBs (Fig.3.16). Most of quartz SGBs are parallel to the prismatic plane; they are generally straight, transecting all of the grain. In contrast, basis-parallel SGBs occur less frequently, exhibiting more irregular and discontinuous walls (Fig. 3.16). Fig. 3.15 shows a detail of the central portion of a type 2 Qtz-ribbon from coarse-grained F_2 Bt-granodiorite, exhibiting coarsely sutured grain boundaries, which is indicative of dynamic recrystallization. Analogous feature is commonly detected within microgranitoids also (Fig.3.17), where quartz grain boundaries exhibit nearly squared outline, (developing the so-called “mosaic-like pattern”), suggesting high crystallographic control on grain boundary orientation (compare with Fig.4b in Gapais & Barbarin, 1986).

The magmatic assemblage surrounding Qtz-ribbons commonly lacks strong evidences of pervasive plastic deformation. However, magmatic feldspars and (rarely) hornblende are affected by grain-scale fractures, which most likely developed in a melt-bearing environment. In order to verify the presence of submagmatic microfractures, the microstructural constrains proposed by Bouchez et al. (1992) are adopted here. The

microfractures are detected within domains where quartz lacks any evidence of recrystallization, grain boundary migration or strong internal deformation. These fractures are also preserved within more deformed domains (i.e. where quartz is deformed). Here, however, is more difficult to avoid ambiguous interpretations.

In our case, submagmatic fractures are commonly sealed by quartz alone, which is optically continuous with the matrix quartz. In the best cases, quartz grains are rather large, lacking evidences of strong internal deformation and recrystallization (Fig. 3.18). These fractures commonly affect a single grain; few adjacent grains may record brittle deformation, but only when they are into direct contact. This is an argument in favour of submagmatic cataclasis, as discussed by Vernon et al. (2004). K-feldspar infill may also locally occur, as shown in Fig. 3.19. In this example, the thin section comes from coarse-grained Hbl-bearing granodiorite, where K-feldspar typically occurs as large poikilitic anhedral grains, enclosing the large and euhedral plagioclase grains. Near the lower tip of the fracture, secondary overgrowths of more sodic (fresh) plagioclase occur as fringe, displaying optical continuity with host Pl fragments (yellow arrow in Fig.3.19). This microstructure reflects the infilling of fracture by melt which gradually evolves toward a minimum composition (Bouchez et al., 1992; Vernon et al., 2004).

F₂ submagmatic fabric is concordant between different magmatites (except for youngest pegmatites and aplites, Fig. 3.23), and commonly overprints igneous contacts (this fact is also evidenced by map-view observation, Fig.3.11). As stated by Paterson et al. (1998) this implies that the development of the main fabric postdates the juxtaposition of different magmatic rocks, and it must be formed over a relatively short time span: after emplacement but before final crystallization of the pluton.

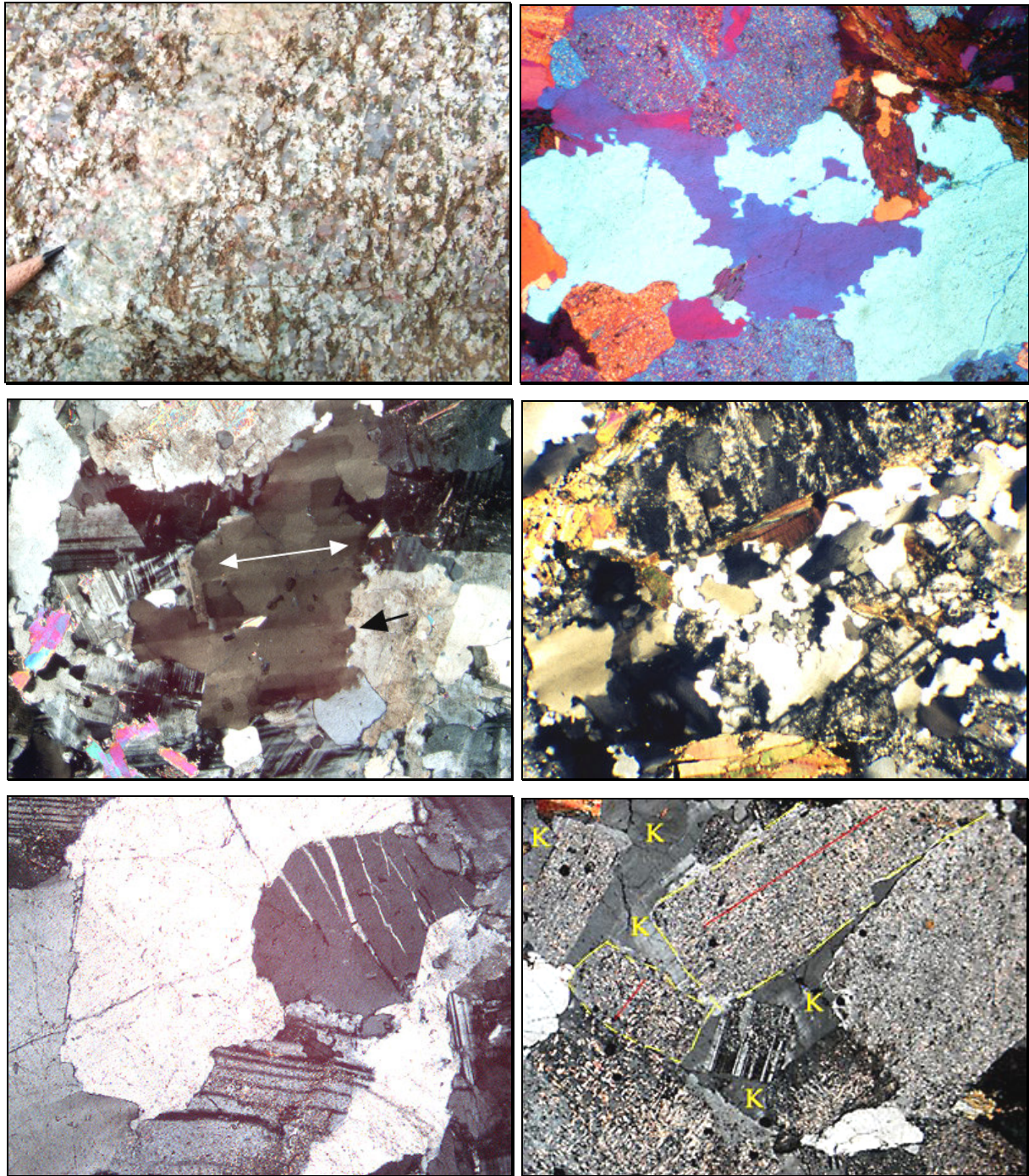


Fig. 3.14 (upper left): Ms-bearing aplite injected into coarse-grained Bt-Ep tonalite, displaying F_2 submagmatic fabric. Natural section nearly normal to the foliation and parallel to the lineation. **Fig. 3.15** (upper right): coarsely sutured Qtz-Qtz grain boundaries, suggesting GBM recrystallization at HT (sample Z72.2; crossed polars; gypsum plate inserted; base of photo: 4mm). **Fig. 3.16** (centre left): detail of a Qtz single grain within Ms-bearing microgranite. Double arrow indicates the trace of c-axis. Black arrow point to lobate Qtz-Pl grain boundary (sample DSL72; crossed polars, base of photo: 4mm). **Fig. 3.17** (centre right): Qtz aggregate with mosaic-like pattern, two-mica microtonalite (sample DSL88; crossed polars, base of photo: 2mm). **Fig. 3.18** (lower left): Qtz-filled submagmatic microfractures in Kfs, from coarse-grained leucogranite (sample DSL30; crossed polars; base of photo: 4mm). **Fig. 3.19** (lower right): coarse-grained Hbl-bearing granodiorite, with poikilitic Kfs (indicated with "k") infilling microfracture in magmatic Pl (partly altered into sericite). The yellow lines highlight the contour of the two portions of the fragmented grain, red lines mark the trace of polysynthetic albite (growth) twins (sample V15; crossed polars; base of photo: 1cm).

Fig. 3.20 shows the coarse-grained tonalite, intruded by a microgranite vein. F_2 fabric (sub-vertical in Fig. 3.20b) is continuous across the contact, as testified by observations at thin section scale (Fig. 3.21A). The polished hand sample (Fig. 3.20b) highlights the strong fabric in tonalite, which is marked by alignment of tabular plagioclase, undeformed Bt flakes and quartz ribbons.

The enlarged micrograph (Fig. 3.21A) shows the whole microfabric across the dyke margin. Here, quartz ribbons display aspect ratio up to $\sim 1:6$; ribbon-forming grains recorded strong internal strain, developing chessboard SGB pattern and coarsely lobate Qtz-Qtz grain boundaries (in both dyke and host tonalite; Fig. 3.21C and 3.21B, respectively; within the vein, this is well visible close to the boundary with the wallrock).

By following the same dyke through distinct but adjacent outcrops, the angle between dyke boundaries and S_2 foliation change from $\sim 90^\circ$ (as in Fig. 3.20 and 3.21) to $\sim 0-20^\circ$ at the nearby outcrop (Fig. 3.22 and 3.24). These adjacent dykes exhibit comparable thickness, assemblage and orientation of F_2 fabric. Moreover, the slight discrepancy in quartz aspect ratio between vein and wallrock is strikingly similar to those described previously (i.e. compare Fig. 3.21A and 3.24), suggesting similar timing relations between fabric development vs. vein emplacement.

Consequently, these observations suggest that two different portion of the same dyke are likely exposed here. These geometrical relationships suggest that microgranite dykes developed plurimetric folds (i.e. with a minimum wavelength larger than the available outcrop continuity), with S_2 foliation lying along the axial plane of these folds. Thus, the dyke portions exposed in Fig. 3.20 and 3.22 might represent (respectively) the fold hinge and the limb zone of a plurimetric, late magmatic fold. This is confirmed by the observation that the intersection lineation (i.e. the line obtained from the intersection between dyke boundaries and foliation plane) is approximately concordant with the local trend of magmatic lineation. Analogous geometrical relations between fold hinge and lineation are described by Miller & Paterson (1994). Fig. 3.25 summarize the inferred geometric reconstruction of late-magmatic folds.

Fig. 3.24 shows the enlarged micrograph from a thin section in the limb zone. Even though largely altered, the tabular outlines of aligned euhedral Pl grains are still easily detectable. Together with quartz ribbons, plagioclase defines the submagmatic fabric in tonalite (indicated by the red line), which is oriented at a low angle with respect to the vein boundary (marked by a red arrowhead). Pl and Kfs in the vein exhibit comparable orientation, although the alignment in the dyke is slightly weaker.

In both the investigated dykes, the morphology of vein boundaries is irregular, crenulate and gradational, even at light microscope scale. In addition, no truncated crystals occur along vein boundaries, and some grains may lie across the contact. According to Hibbard & Watters (1985), these microstructural relations between dykes and wallrock suggest that the veins were injected into a host rock containing $\sim 30\%$ of melt.

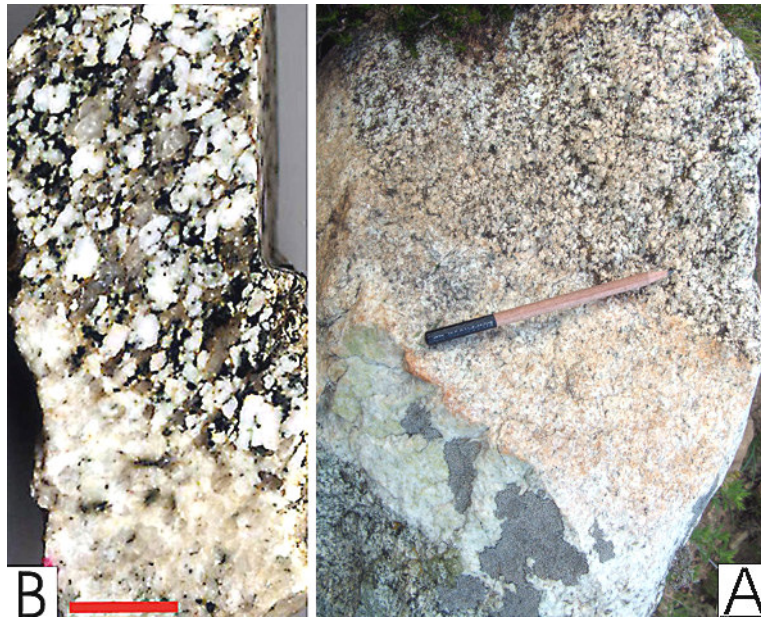


Fig. 3.20: [A] microgranite vein intruded into I-type tonalite. Magmatic boundary (gently dipping toward the right) is transected at high angle by the main submagmatic fabric (sub-vertical). [B] Polished hand sample from upper magmatic boundary of Fig.38a, showing the strong alignment of tabular Pl grains and Bt flakes (scale bar is 1cm).

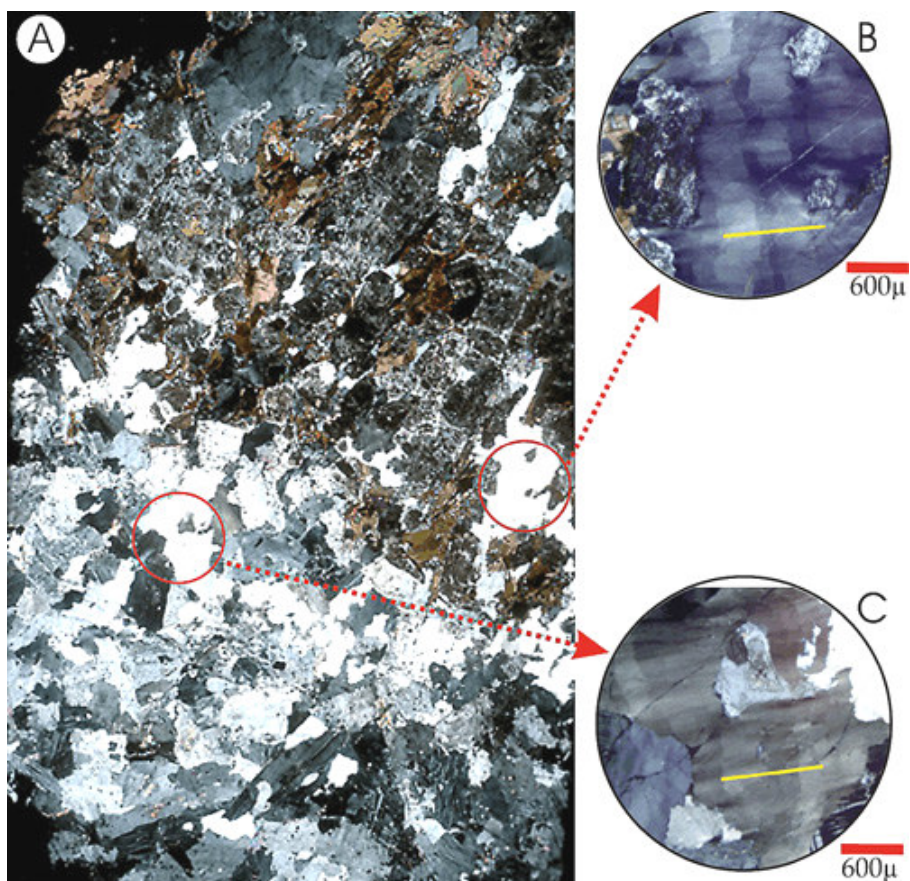


Fig. 3.21: [A] F_2 submagmatic fabric overprinting magmatic contacts, shown by the enlarged photo from sample DSL119. Photo [B] and [C] display a slightly different extinction position in Qtz, showing strong internal strain. Yellow lines indicate c-axis traces in Qtz grains with chessboard SGB pattern (crossed polars; base of photo: 2.5 cm).



Fig. 3.22 (left): microgranite dyke injected at low angle from S_2 foliation within host tonalite. This outcrop is located ~5mt from outcrop shown in Fig.3.21 and 3.22, by moving along S_2 foliation **Fig. 3.23** (right): detail of the contact between Hbl-bearing tonalite and one of the youngest Ms-bearing aplite. The latter displays a magmatic foliation parallel to vein boundaries, transected F_2 fabric in host tonalite (horizontal).

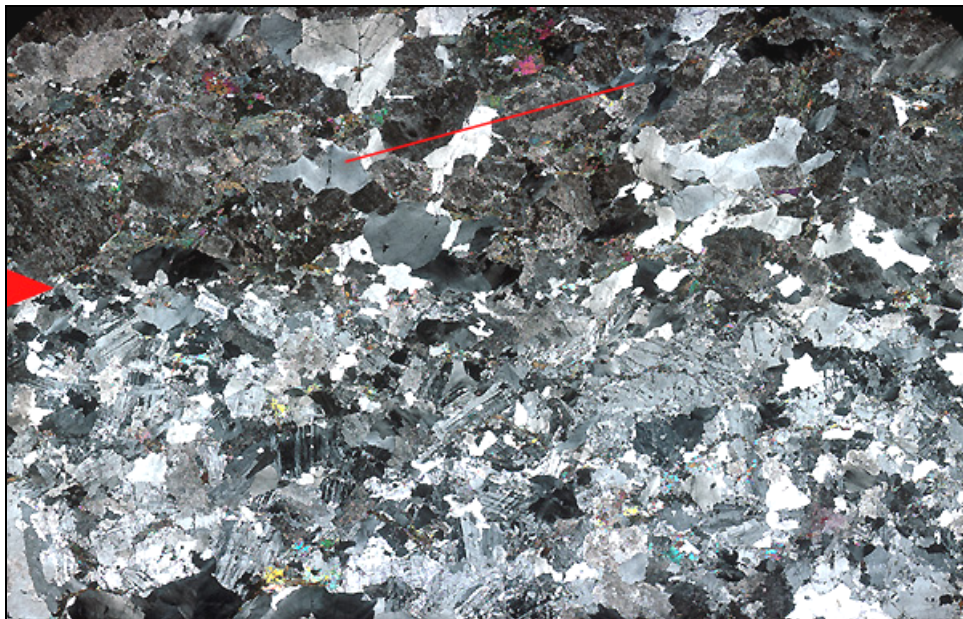


Fig. 3.24: enlarged photo showing a detail from dyke boundary shown in Fig. 3.22. Red arrowhead approximately indicates the vein boundary (horizontal), whereas the red line marks the foliation trace (crossed polars; base of photo: 2.5cm).

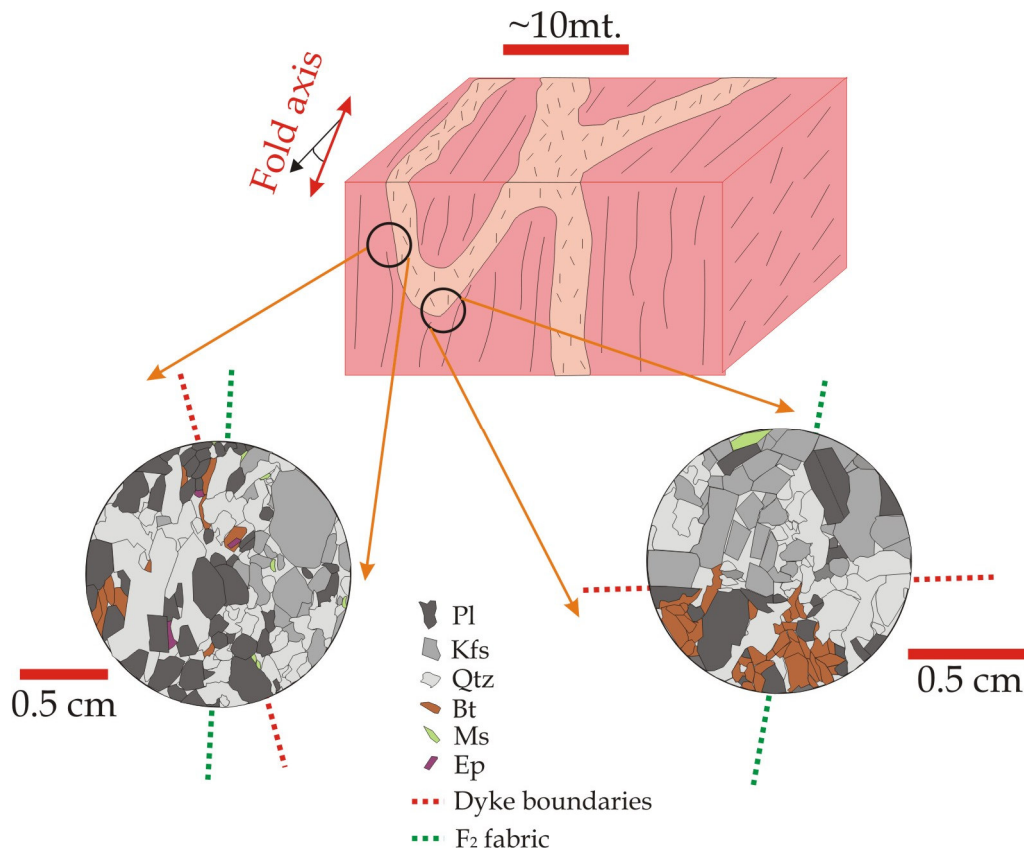


Fig. 3.25: sketch summarizing field and microstructural relations of adjacent outcrops providing some evidences of the occurrence of late-magmatic folding. The two microstructural sketches represent line drawings from thin sections shown in Fig.3.22A and 3.25. These sketches emphasize the crystal shapes of magmatic grains. Further explanations in the text.

3.2.1.3 Fabric developed at low melt fraction (f_3)

In contrast with F_2 microfabric, F_3 microfabric is characterized by the onset of widespread feldspar deformation. The microstructures in microgranitoids partly differ from those of coarse-grained (Hbl-bearing) rocks. In both cases, plagioclase and K-feldspar exhibit common adjustment of grain boundaries, which are generally very irregular to lobate. Anhedral feldspars commonly display aspect ratio between 2:1 and 3:1. In microgranitoids, strain features are nearly absent in feldspars (some grains exhibits weak to moderate sweeping undulose extinction). In contrast, within coarse granite, feldspar grains exhibit widespread sweeping undulose extinction, subgrain development and marginal recrystallization (Fig. 3.31). In microgranitoids, quartz exhibits moderate internal deformation (chessboard SGB pattern locally occurs, Fig. 3.29), and coarsely sutured Qtz-Qtz GBs may occur. In coarse granitoids, quartz is more deformed, commonly showing a dense network of SGBs (chessboard SGB pattern, Fig. 3.31) and deeply sutured Qtz-Qtz grain boundaries. Both kinds of samples exhibit widespread feldspars brittle deformation, commonly displaying quartz-filled submagmatic microfractures. Different stages of late-magmatic feldspar embrittlement are visible at thin section scale, from incipient fracturing in Kfs (blue arrowheads in Fig. 3.27 and 3.30) to total separation of distinct Kfs fragments (red arrowhead in Fig. 3.30; in these cases, the identity of single fragments was tested with the gypsum plate). However, microstructures shown in Fig.3.30 could also be obtained in the absence of brittle deformation, through

progressive pinch-and-swell to boudinage of a feldspar grain, due to diffusion creep processes (Gower & Simpson, 1992).

Analogous fractures were found in plagioclase (Fig. 3.29); in this case, the two fragments can still be matched by the visible trace of the Carlsbad twin plane and by the outline of fracture walls. Quartz infill exhibits chessboard SGB pattern, with the *c* axis oriented along the local stretching direction (i.e. normal to the fracture walls). The same crystallographic relation is present in the cases of Qtz crystallized in shadow zone around Kfs (Fig. 3.26 and 3.27). Analogous crystallographic relation was described by Gapais & Barbarin (1986), being interpreted as an evidence of (late-magmatic) Qtz oriented grain growth in a direction favourable for prism $\langle c \rangle$ glide. Quartz-feldspar grain boundaries are finely cusped and lobate. In detail, Qtz-Kfs phase boundaries are characterized by the common occurrence of feldspar cusps or “promontories”, which are ~10 to ~200 μ in length (Fig. 3.28). When observed in sections normal to the foliation and parallel to the lineation, cusps preferentially point along the foliation trace. In some samples, this grain boundary adjustment affects about 50% of quartz-feldspar interfaces.

In quartzo-feldspathic rocks, cusped and lobate Qtz-feldspar phase boundaries are generally referred to diffusion creep at high-temperature, under both melt-bearing and melt-free conditions. Phase and grain boundary geometry from F_3 microfabric resembles those typical of high-grade (melt-free) gneiss terrains (i.e. the low strain fabric [“Type1”] of Martelat et al., 1999, Fig.3a and b). Analogous microfabric was described for granitoids deformed (under solid-state conditions) at $T \sim 650^\circ\text{C}$, being ascribed to large-scale (up to 300 μ) grain (and phase) boundary migration due to diffusion processes (Rosenberg & Stünitz, 2003).

Diffusion creep is inferred to contribute to deformation also under melt-bearing conditions (“melt-assisted diffusion creep”, Dell’Angelo & Tullis, 1988). However, in the experiments of Dell’Angelo et al. (1987) and Dell’Angelo & Tullis (1988), this mechanism was dominant only in aplite with very small grain size (~10 μ). In contrast, Rosenberg & Berger (2001) described that a melt-induced transition in the dominant deformation mechanism (from dislocation creep to diffusion creep) may occur under natural conditions even with grain size of about 500 μ . In summary, after Rosenberg (2001), the term “flow at low melt fraction” is adopted here for those cases where microstructures typical of high-temperature solid-state flow are accompanied by microstructures diagnostic of synmagmatic deformation.

In fact, in our case, several microstructural criteria suggest that S_3 foliation developed in a melt-bearing environment: (i) feldspar grains preserve evidences of microfractures, which are inferred to occur during submagmatic flow (see Fig. 3.29 and 3.30). (ii) Primary quartz locally crystallized within low-strain zones (i.e. in pressure shadows around larger feldspars, Fig. 3.26 and 3.27, or inside fractures, Fig. 3.29), which is a good indication of submagmatic flow (Gapais & Barbarin, 1986; Hibbard, 1987; Vernon, 2004); (iii) S_3 foliation is transected by microaplite, which were injected into partially molten host microgranite (see below).

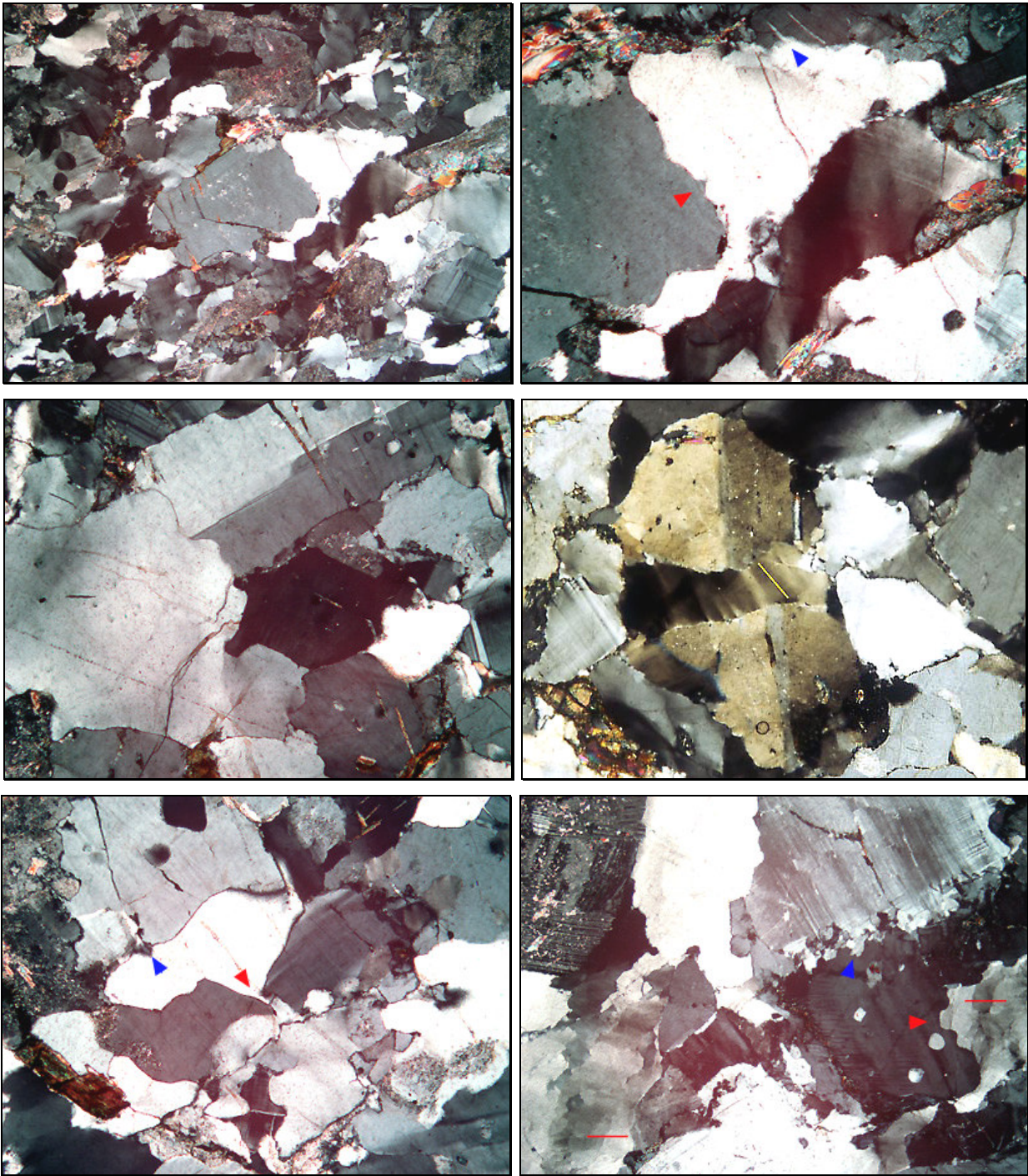


Fig. 3.26 (upper left): general aspect of F_3 microfabric: some feldspar grains preserve the original magmatic shape, whereas most of them are largely modified (further explanations in the text). Qtz exhibits elongate grains/aggregates, with coarsely sutured grain boundaries (crossed polars, base of photo: 4mm). **Fig. 3.27** (upper right): detail from the central portion of Fig.3.26, showing Kfs cusp pointing along the foliation (red arrowhead) and Qtz-sealed microfractures (blue arrowhead). Crossed polars; base of photo: 1.8mm. **Fig. 3.28** (centre left): strongly lobate Qtz-Kfs GBs, with Kfs cusps pointing to foliation trace (crossed polars; base of photo: 1.8mm). **Fig. 3.29** (centre right): Qtz-filled fracture in a Pl grain within microleucogranite with F_3 microfabric. Qtz displays weak chessboard SGB pattern (sample SSL27.1; yellow line indicates the trace of c axis). Crossed polars; base of photo: 1.8mm). **Fig. 3.30** (lower left): two different stages of submagmatic microfractures in Kfs (crossed polars; base of photo: 1.8mm). **Fig. 3.31** (lower right): F_3 fabric in coarse-grained granite: chessboard SGB pattern and coarsely sutured grain boundaries in Qtz (red lines: c-axis trace). Lobate GBs (red arrowhead) and marginal recrystallization (blue arrowhead) in Kfs (crossed polars; base of photo: 4mm).

The S_3 foliation in microgranite is locally transected by 300 μ to 1mm wide microaplite, mainly containing quartz and sodic plagioclase. The veins propagated through a framework of sub-parallel localized brittle microfaults (Fig.3.32), which overtake (in length) the thin section scale. Microaplite exhibits sharp walls against host granite, where all crystals appear as truncated grains (i.e. micrograph A to D in Fig.3.32). However, in some micro-domains, the vein boundaries are sealed by large and undeformed quartz grains (A and B in Fig.3.32). The observed microstructures suggest that during (or immediately after) vein injection, quartz-rich material spread from the host to the microaplite and vice versa. The grain size of magmatic Qtz is 100-200 μ in the vein, whereas it reaches ~1mm in the host granite. The very brittle character of the deformation is highlighted by micrographs C and D (Fig.3.32); here a network of micro-scale en-echelon slices (i.e. fragments), are detached from the host K-feldspar grain, being progressively incorporated into the vein. In the micrograph E (Fig.3.32), two sets of orthogonal microfractures in Kfs are sealed by a coarse and unstrained magmatic quartz grain.

The observed microstructural relations between vein and wallrock could represent an intermediate situation between the cases A (all crystals are truncated) and B (some grains are truncated, some lie across the boundary) proposed by Hibbard & Watters (1985). In these cases, the authors estimated (for the wallrock) a melt content of 1-2% and ~10-15%, respectively. These end member values fit the observed F_3 microfabric, which is indicative of flow at low melt fraction (melt fraction $< \sim 0.2$; Rosenberg, 2001). During the experiments carried out by Rutter & Neumann (1995), in the 0.1-0.4 melt fraction range melt propagated by through-going brittle shear zones, whereas brittle deformation was absent at a melt fraction greater than 0.4. However, the final microstructure likely depends also by the strain rate.

In summary, the observed microstructures within F_3 microfabric are likely influenced by the grain size, as dislocation creep was likely prevailing in coarse granitoids, whereas diffusion creep was possibly dominant within microgranitoids. In both cases, submagmatic microfractures contributed to accommodate the deformation. Dell'Angelo & Tullis (1988) reported that, during experimental deformation of coarse-grained (~150 μ) aplite, these three deformation mechanisms cooperated; the dominance of one mechanism over another should be a function of melt content and strain rate. In the following section, we will see how the quartz LPO pattern may help to obtain information about the role of different deformations mechanisms during fabric development.

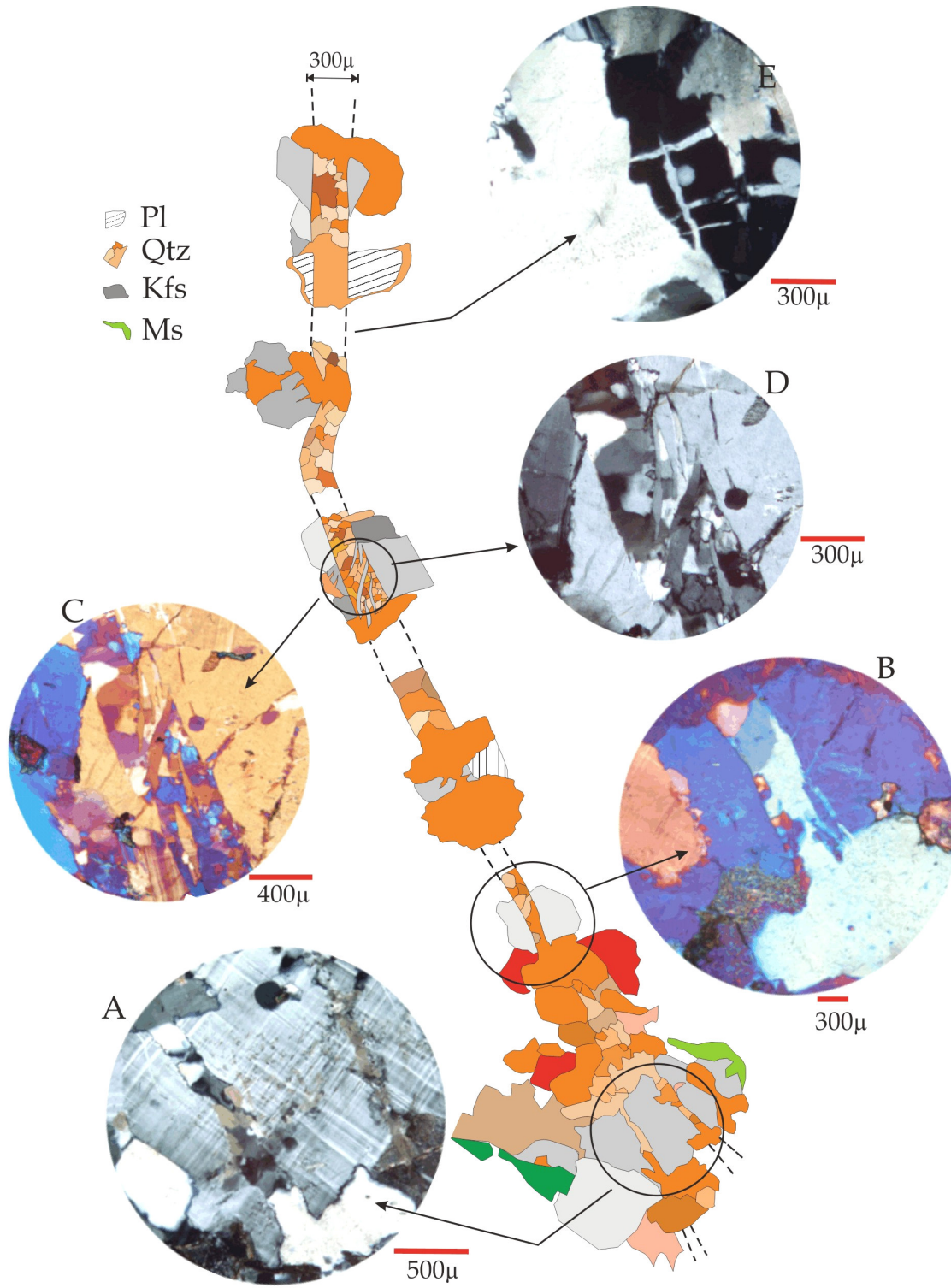


Fig. 3.32: sketch summarizing microstructural relations between microaplite and host microgranite, displaying F₃ fabric. Different tonalities of brown and orange indicate distinct quartz grains.

3.2.2 Quartz LPO

Quartz LPO has been measured in 13 samples deriving from both I-type and S-type granitoids. They are representative of all types of magmatic fabric described previously. As visible in Tab.1 (which summarizes the microstructural features of the analyzed thin sections), almost ~50% of samples lack any evidence of low-temperature overprint. In the pole figures assembled in the map (Fig.3.33), the inferred shear plane is drawn according to the “easy glide” hypothesis (Etchecopar, 1977), which predicts a strain-dependent rotation of the active glide system to an orientation approaching the shearing direction in the deformed rock.

3.2.2.1 F_1 fabric

Among the five (Ms-bearing) analyzed samples, two are from microtonalites and three are from microgranites. With the exception of sample DSL70, which exhibits a strong LPO (in the absence of evident Qtz SPO), the fabric is rather weak, as commonly observed in relation to magmatic foliation (i.e. Blumenfeld et al, 1986). On the other hand, one or few clear maxima close to the X position occur in each sample. Moreover, DSL70 and DSL71 exhibit an additional unambiguous maximum close to the Y-axis. Samples V26 and Z93a contain some secondary maxima close to the Z position, or along a discontinuous girdle normal to the foliation plane. These samples are those where the low-temperature overprint is more developed (widespread undulatory extinction). Monoclinic external symmetry provides sinistral shear sense in two samples (DSL70 and V26), whereas the others samples show nearly orthorhombic symmetry.

As described in chapter two, the opening angle (measured across the Z axis) may provide some indications about the temperature of fabric development (Kruhl, 1998). In our case, if we exclude angles of ~50°, which are compatible with the low-temperature overprint (possibly of Alpine age, section 1.5) detectable at thin section scale (namely, in samples Z93, DSL 71 and DSL107), all samples display opening angles of about 90-130°, providing temperature of about ~650-800°C (Kruhl, 1998). Opening angles larger than 90° are typically developed under granulite facies conditions (Lister & Dornsiepen, 1982) or in syntectonic granitoids (Gapais & Barbarin, 1986).

In summary, although some complications related to partial solid-state overprint, unambiguous quartz LPO developed during D_1 magmatic stage, despite the absence of clear Qtz SPO and Qtz strain features. These data fit the findings of Gapais & Barbarin (1986), who explained the Qtz LPO close to the bulk extension direction in rocks of Qtz oriented grain growth during pluton crystallization. The additional Y maximum shown by some samples is likely related to incipient overprint by F_2 fabric, as discussed in the next session.

3.2.2.2 F_2 fabric

Five samples from Ms-bearing microgranitoids have been analyzed (two tonalites, two granodiorite and one alkaligranite). Samples DSL72, DSL81 and Z31a exhibit a relatively strong fabric, with prominent maxima close to the mineral lineation and secondary maxima close to the Y position (the latter is dominant in sample DSL81). The effects of low-temperature overprint on pre-Alpine Qtz LPO are detectable by comparing samples

DSL81 and DSL88 (Fig.3.33). Both samples are tonalites displaying very similar microstructures, commonly displaying mosaic-like pattern (Fig. 3.17). Nevertheless, DSL88 recorded some later overprint, as revealed by widespread quartz undulose extinction. Even though a clear superimposed fabric is not developed, the quartz fabric is weaker, because a large number of c axes is scattered through the diagram (contour line with 1% are not plotted). The same considerations are valid for sample SSL26.1 too. By comparing samples devoid of pervasive LT overprint (i.e. samples z72.3, DSL70, z31a), quartz fabric is qualitatively analogous to those of F₁ fabric, but it is clearly stronger. Moreover, opening angle is slightly larger (namely between 105° and 135°). As quartz shows clear evidences of strong internal deformation (section 3.2.1.2), the observed LPO should be primarily due to dislocation creep processes. In quartz, multiple slip activation (basal and prismatic <a> glide and prismatic [c] glide), characterizes the GBM II field (Stipp et al., 2002), where the increased grain boundary mobility allows Qtz grains to store larger amounts of internal strain energy. Thus, in our case, F₂ microstructures (where no solid-state overprint is detectable at grain scale) suggest that the observed X and Y maxima in Qtz LPO are likely due to multiple (and simultaneous) slip activation in the high-quartz field, rather than high-temperature solid-state overprint superimposed on pre-existing magmatic LPO (Blumenfeld et al., 1986).

3.2.2.3 F₃ fabric

Three samples displaying F₃ fabric have been analyzed (one coarse-grained, I-type, granite; one Ms-bearing microgranodiorite, one Ms-bearing microleucogranite). All samples exhibit a relatively strong maximum close to the mineral lineation. The sample Z72.3 displays the strongest maximum, in agreement with the common occurrence of basis-parallel SGBs. This strong fabric supports the suggestion that coarse-grained granites accommodated deformation mainly by dislocation creep processes. In contrast, the weaker X maxima shown by microgranites might implies a larger contribute of diffusion creep (in agreement with the common occurrence of cusped-lobate Qtz-felds grain boundaries). In addition, sample DSL80 is also partly affected by low-temperature overprint, which might explain the presence of some sub-maxima close to the foliation poles.

As a whole, the intensity of the main maxima around X-axis is progressively strengthened from F₁ to F₃ fabric. This fabric evolution is interpretable in the viewpoint of different fabric contribute during subsequent magmatic stages. Fabric developed mainly by oriented grain growth during D₁ stage, whereas combined <a> and [c] slip (both on prismatic plane) was prevailing during D₂ and D₃ stages. During flow at low melt fraction (namely D₃ stage) dislocation creep was likely associated with diffusion creep processes. The influence of the latter process on Qtz LPO is difficult to predict, as Gower & Simpson (1992) shown that, in the same area, samples exhibiting strong maxima close to the X-axis were associated with others with a dispersed c-axis distribution.

F1	Rock type and Orientation	LT over print.	Opening angle	LPO shear sense	Tiling shear sense	Qtz SGBs	Lob.Q-Q GBs	Lob.Q-F GBs
V 26	Tonalite S: 140°85°SW L: 130°32°SE	XX	130°	Sx	\	XXX	XX	\
Z 93	Tonalite S: 090°80S L: 095°25°SE	XX	110°	Sx (weak)	Sx	\	\	\
DSL70	Granite S: 140°90° L: 140°12°SE	\	\	Sx	Sx	X	X	\
DSL71	Alkaligranite S: 125°90° L: 120°30°SE	XX	105°	\	Dx	\	X	\
DSL 107	Aplite S:0150°80°SW L: 150°25°SE	XX	90°, 115°	\	Sx	\	X	\
F2								
SSL26.1B	Tonalite S: 135°80°NE L: 140°27°SE	X	55°, 115°	\	\	XX	X	\
Z 31A	Alkaligranite S: 130°90° L: 130°35°SE	\	135°, 140°	Sx (weak)	\	X	X	\
DSL72	Granodiorite S: 140°52°NE L: 130°10°SE	\	135°	Sx	Sx	XX	XX	X
DSL81	Granodiorite S: 135°82°NE L: 135°42°SE	\	135°	Sx (?)	Sx	XX	XX	\
DSL88	Tonalite S: 120°60°NE L: 130°18°SE	X	105°, 125°	\	\	XX	XXX	\
F3								
SSL 27.1B	Alkaligranite S: 135°80°NE L: 140°27°SE	\	110°, 130°	\	Sx	XX	X	XX
Z72.3	Granite (I-type) S: 180°55°E L: 180°33°S	\	145°	Sx	\	XXX	XXX	X
DSL 80	Granodiorite S: 145°86°SW L: 140°45°SE	XX	40°, 140°	Sx (weak)	Sx	X	XXX	XXX

Tab. 5: summary of microstructural features of samples investigated for LPO. “X” symbols indicate the frequency of the occurrence of a certain microstructural feature (i.e. quartz subgrain boundaries), as approximately estimated in a relative range (from zero, indicated with “\”) to three.

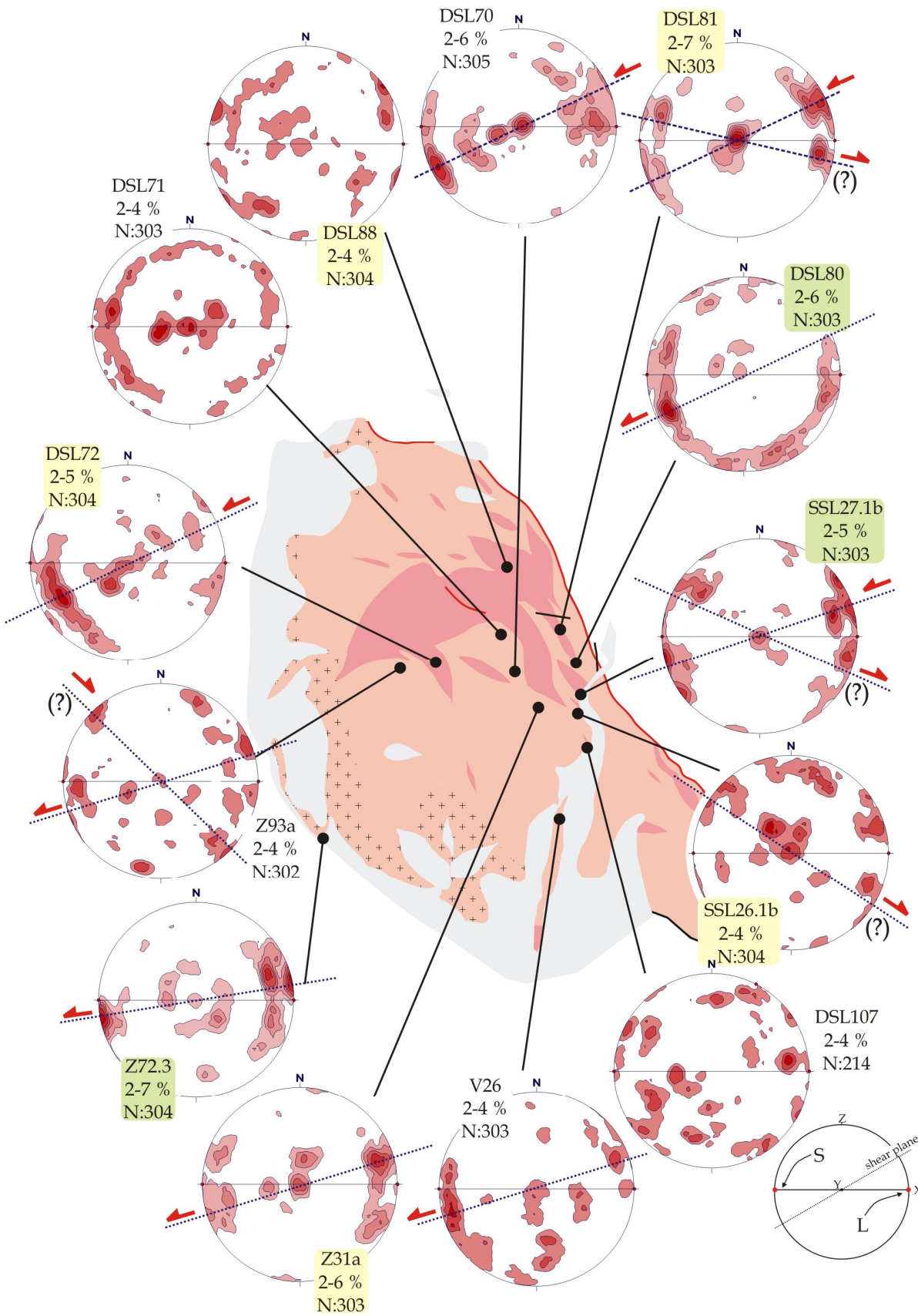


Fig. 3.33: map summarizing quartz c-axis fabric from samples with magmatic fabric. Different label backdrops indicate different fabric. White: F₁ fabric; yellow: F₂ fabric; green: F₃ fabric. Where possible, the shear plane (dotted line) and the inferred shear sense (half arrow) are indicated. For each equal area (lower hemisphere, 1% of search area) stereographic projection, the labels are (from the top): sample name, contour interval, number of measurements.

3.2.3 Dominant shear sense during magmatic to submagmatic flow

The imbrication (or tiling) of elongate magmatic crystals is a common indication of magmatic flow (Den Tex, 1969), since the role of compaction in the development of a shape preferred orientation is thought to be very weak during magmatic flow (Higgins, 1991). This is true, however, only if the considered crystals are not internally deformed. Under these conditions, magmatic tiling implies sufficient freedom for crystals to rotate as rigid particles and impinge without undergoing widespread plastic deformation. This type of flow requires high viscosity contrast between rigid particles and matrix. Thus, tiling effect is expected to occur during magmatic flow, i.e. at melt fraction above ~0.4 even if, at low strain rate, magmatic fabric can be preserved down to melt fraction of ~0.1 (Rosenberg, 2001). In the experiments of Arbaret et al. (1996), magmatic tiling occurs at melt fraction up to ~0.6. Paterson et al. (1998) observed, however, that magmatic fabric developed at melt fraction above ~0.4-0.5 is unlikely preserved in the final rock fabric. Consequently, these latter values likely represent the uppermost limit for tiling preservation. Tiling is mainly influenced by particle aspect ratio and by the imposed shear strain (Fernandez & Laporte, 1991). Besides an evidence of magmatic flow, tiling structures can be used as kinematic indicators during non-coaxial magmatic flow (Fig. 3.34; Nicolas, 1992). In this regard, Blumenfeld & Bouchez (1988) showed that ~30% of the analyzed pairs of crystals provided the reverse shear sense (probably because of a combination of rotation and relative translation of crystals). Thus, Mulchrone et al. (2005) suggested that tiling structure represent a reliable shear sense indicator only if a sufficiently large number of observations (>60) are provided for each shear sense determination. In our case, the outcrop condition for the GC does not provide such a large number of observations. Thus in order to obtain a statistically valid shear sense indication, the orientation of euhedral feldspar grains was systematically measured both at the outcrops (3 measured outcrops, I-type coarse-grained granitoids) and in thin section (12 samples from microgranitoids), in several pluton domains (Fig. 3.37). The observations were carried out in sections normal to the magmatic foliation and parallel to the magmatic lineation. In case of non-coaxial flow, the resulting spatial distribution of feldspar grains may exhibit a monoclinic symmetry. In analogy with non-coaxial solid-state flow, distinct subfabrics develop, where the main peak will indicate the foliation plane (assumed as the finite flattening plane, Blumenfeld & Bouchez, 1988). The occurrence of subfabrics is also due to the different rotation rate of particles with different aspect ratios (Fernandez et al., 1983). This "obliquity criterion" was applied by Blumenfeld & Bouchez, 1988) to granitic veins sheared in the magmatic state during pluton emplacement. Moreover, the obtained shear sense is reliable only for moderate strain values. This is because, for high strain values ($\gamma > \sim 5$), particles with moderate aspect ratio ($n=2-3$) tend to depart from the shear plane, providing the wrong shear sense (Blumenfeld & Bouchez, 1988). Taking these restrictions, four samples of the present study exhibit nearly orthorhombic symmetry: they are useless to determine the dominant sense of shear (Fig.3.37). In the other eleven samples, the long axis of feldspars grains exhibits an asymmetrical and bimodal pattern: the main maximum is parallel to the local trend of magmatic foliation, and a smaller maximum (or few smaller maxima) forms an angle of 10-40° with the main orientation. Here, the monoclinic symmetry indicates sinistral sense of shear in 9/11 of samples (i.e. 60% of the total analyzed samples).

Another suitable tool to deduce the dominant shear sense during (late-) magmatic flow is provided by the statistical orientation of submagmatic microfractures (Fig. 3.36; Bouchez et al., 1992). These authors reported that 63% of fracture traces are oriented at 50-80° to the foliation plane, but are nearly normal to the orientation of fractured grains (Fig. 3.36). Consequently, the geometrical coherence between the shear sense indicated by statistical feldspar orientation and those indicated by submagmatic fractures could suggest that stress field is not modified during the transition from magmatic state to submagmatic state (Bouchez et al., 1992). During this work, three samples were analyzed for both feldspars and microfractures statistical orientation. All the measured microfractures satisfied the microstructural constrains proposed by Bouchez et al (1992), as described in section 3.2.3.2. As described by Bouchez et al. (1992), a clear connection between the orientation of feldspars and microfractures is evident in the analyzed samples. In sample SSL27.2b, where feldspar orientations exhibits a nearly orthorhombic symmetry, the fracture traces are mainly normal to the foliation plane. In contrast, where feldspar orientations display a monoclinic symmetry (samples SSL27.1b and DSL80), an angle of ~10-30° between the foliation normal and the mean fracture trace orientation occurred. Moreover, the clustering of feldspar orientations is directly comparable with that of fracture orientation. The inferred dominant shear sense is also corroborated by the comparison between feldspar orientation, submagmatic microfractures and the external monoclinic symmetry provided by the quartz fabric. Because these fabrics developed through distinct processes (i.e. magmatic flow for tiling; oriented grain growth and/or dislocation creep for Qtz fabric), these different methods independently provide indications on the dominant shear sense during magmatic flow (in the broad sense). These methods never provide incongruous shear sense. However, some mismatch occurs as, in the same sample, feldspar orientation may exhibit orthorhombic symmetry, whereas quartz LPO fabric exhibits a clear monoclinic symmetry, suggesting sinistral shear sense (this is the case of sample Z72.3). In addition, also the opposite is found (i.e. sample z93: monoclinic symmetry in the feldspar orientation, but orthorhombic symmetry in quartz LPO fabric). Despite these limits, concomitant sinistral shear sense is provided by five samples, which are representative of the different magmatic fabric (F₁ to F₃, see Tab.1). In contrast, no samples indicate unambiguous dextral shear sense.



Fig. 3.34 (left): the tiling of crystals during non-coaxial magmatic flow; slightly modified after Blumenfeld & Bouchez (1988). **Fig. 3.35** (centre): bimodal feldspar orientation in a magmatically foliated leucogranite, suggesting dominant sinistral shear sense during non-coaxial magmatic flow (outcrop along *Tavignano Valley*. Feldspar orientation from this outcrop is not included in Fig.3.37). **Fig. 3.36** (right): geometrical relationship between statistical orientation of feldspars and submagmatic microfractures. "P_{fract}" indicates the mean orientation of fractured feldspar grains. From Bouchez et al. (1992).

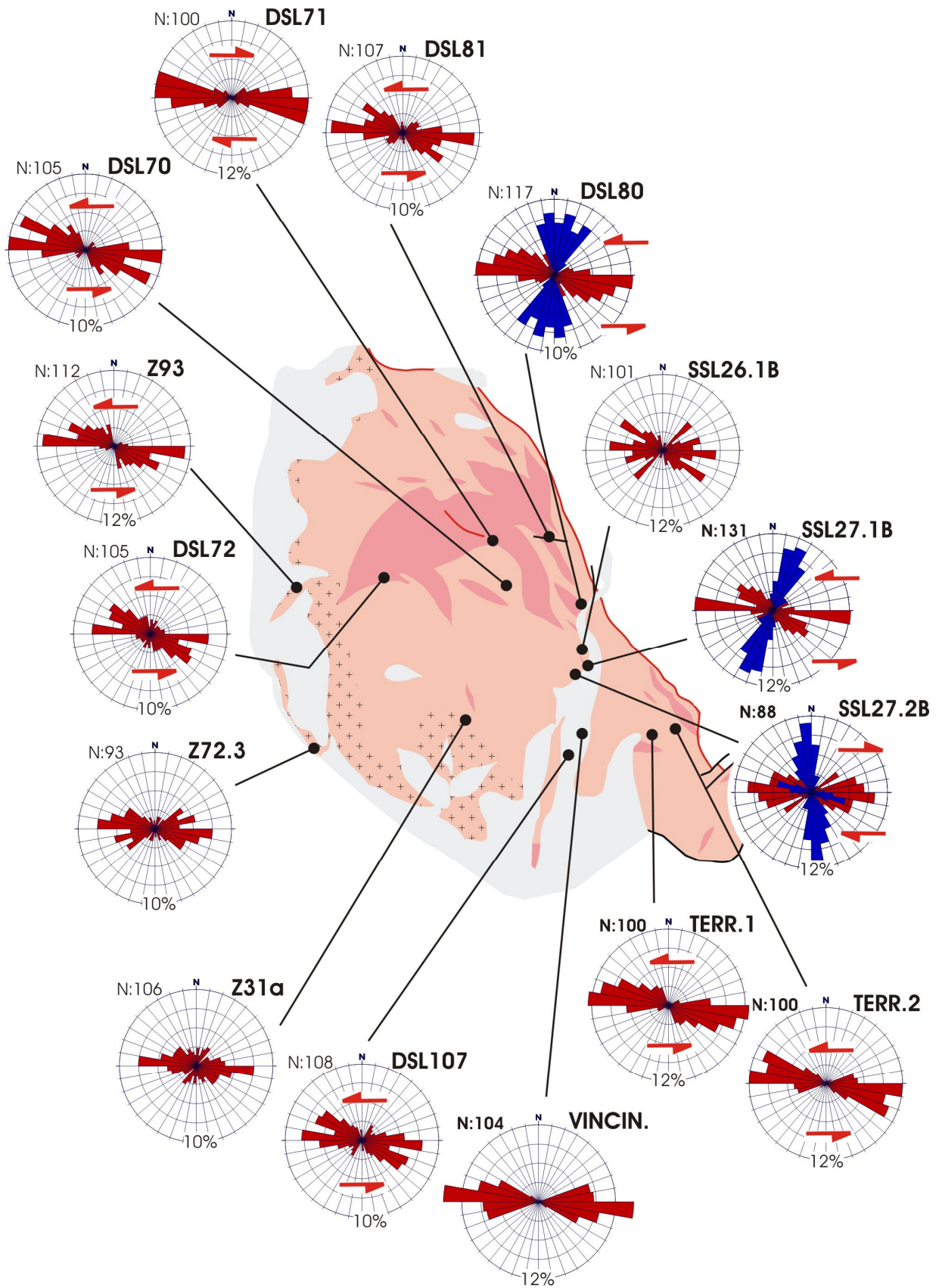


Fig. 3.37: rose diagrams showing the statistical orientation of feldspars long axes (red branches), and submagmatic microfractures (blue branches) as measured both on the outcrop and in thin section. Each branch is 10° in width. Branch's length is indicated (in percentage) along the outermost ring. In order to facilitate the comparison between different samples, the main maxima are plotted along the E-W direction.

3.3 Solid-state fabric

3.3.1 Introduction

Evidences of pre-Alpine solid-state flow are mainly detected along the preserved NE pluton margin. The solid-state overprint is visible in all the previously described rocks, with the exception of ultramafic rocks. The thickness of the “mylonitic rim” is about 100-200mt, with strain intensity that gradually increases outward (i.e. against the roof of MC). From the inner part of the pluton towards the mylonitic rim, no clear discordant solid-state overprint is visible at outcrop scale. Instead, solid-state fabric gradually and concordantly superimposed (sub-) magmatic fabric without any visible crosscutting relations. On the solid-state foliation, a prominent stretching lineation is defined by elongate trails of quartz, feldspars and mica aggregates. This solid-state lineation roughly exhibits the same orientation of magmatic lineation (Fig.3.11).

After Berthé et al. (1979) and Simpson (1984) the term “S-tectonite” is used here for homogeneously and moderately deformed granitoids, showing non-penetrative and isolated C planes (Fig.3.38a). The term S-C tectonite refers to heterogeneously deformed mylonites, where shear strain is progressively localized into penetrative C shear bands (Fig. 3.38b and c). Finally, the term “C’ tectonite” (Fig. 3.38d) is used here for a strongly anisotropic mylonite, displaying parallelized S and C planes, “transected” by penetrative C’ shear bands (Passchier, 1991b). Furthermore, the geometrical definitions proposed by Blenkinsop & Treloar (1995) are adopted here, where α and β define the S-C and the C-C’ angles, respectively (Fig. 3.39). This purely descriptive classification is useful on the outcrop and thin section scales; moreover, it reflects the progressive strain accumulation during bulk heterogeneous simple shear (Passchier & Trouw, 1996).

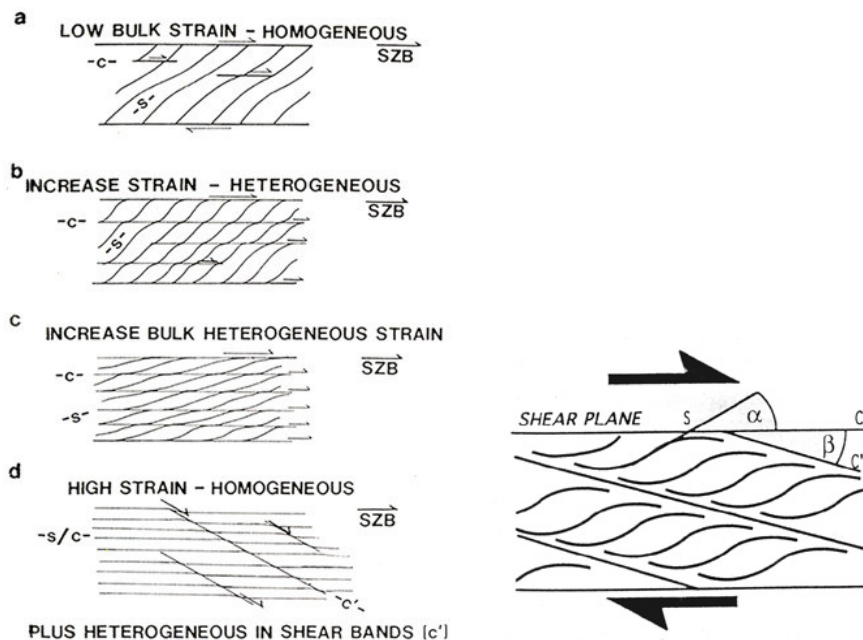


Fig. 3.38 (left): different types of foliation in shear zones, after Simpson (1984). **Fig. 3.39** (right): schematic sketch of composite planar fabric in a tectonite, with the definition of angles α and β . After Blenkinsop & Treloar (1995).



Fig. 3.40 (left): orthogneiss deriving from coarse-grained leucocratic granodiorite. Partly parallelized S and C surfaces and sporadic C' shear bands define sinistral shear sense (see sketch at upper left). "Mylonitic" rim at contact between GC and MC, west from Mount Tomboni. **Fig. 3.41** (right): view of the median portion of the sheared quartz vein injected into Ms-bearing microtonalite. This mylonite crops out ~500mt westward from *Cima Incalcinata*, representing one of the rare examples of pre-Alpine shear zones developed in the inner part of the pluton.

3.3.2 The main solid-state fabric

Within the main solid-state foliation, three end-member microfabric-types can be distinguished. Field relations and microstructures suggest that a gradual transition between these main fabric types occurs, interpretable as subsequent stages of strain localization during progressive deformation. The generalized sinistral shear sense, detectable at outcrop scale (e.g. Fig. 3.40 and 3.41), is confirmed at microscale in all the investigated samples.

3.3.2.1 *S* tectonite

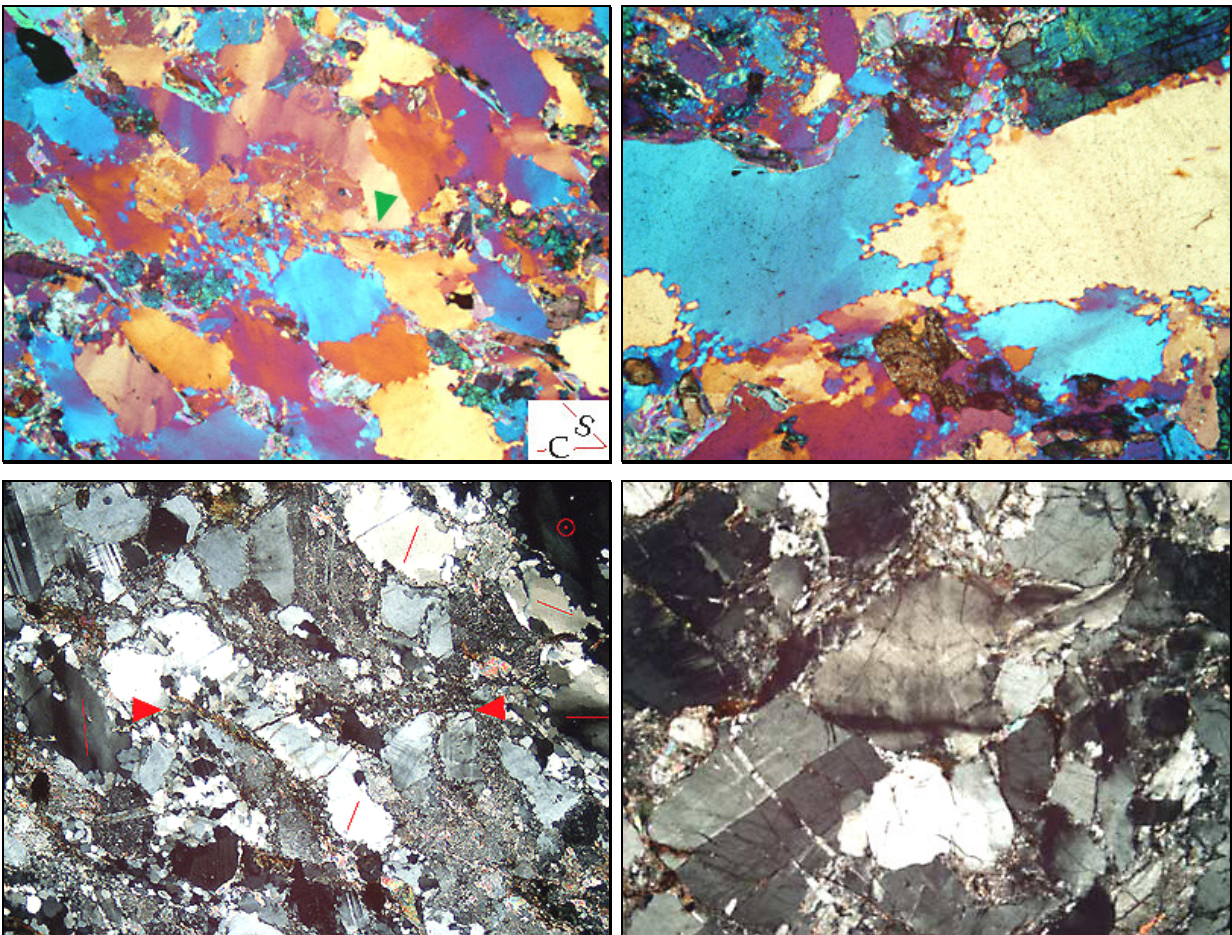
This rock type crops out in the inner, low-strain portion of the "mylonitic rim". At naked eye, the less deformed rocks show a magmatic-looking fabric. However, thin sections indicate the occurrence of a superimposed solid-state fabric. The whole fabric is marked by a rather homogeneous solid-state foliation (S planes), locally "transected" by discontinuous, discrete C planes (Fig.3.42). S surfaces are marked by the alignment of subhedral feldspars, moderately elongate and homogeneously flattened Qtz porphyroclasts and deformed mica flakes (Fig.3.44). Local Qtz recrystallization may occur at the periphery of magmatic Qtz grains, developing a thin and discontinuous mantle of polygonal grains (Fig.3.42 and 3.43). Moreover, quartz new grains tend to develop thin trails aligned along sporadic C planes (green arrowhead in Fig.3.42), together with fine-grained recrystallized quartz, epidote and mica. These recrystallized quartz aggregates are very different from those developed during submagmatic flow, as will be discussed below (section 3.3.6). Within feldspar-rich domains (Fig. 3.45), S and C surfaces are less clearly defined, and the microstructure seems, as a whole, more "disorganized". Non-interconnected micaceous films tend to develop along two main orientations, i.e. parallel to the main foliation and at 40-50° from it (along the sporadic C shear bands), defining an incipient S-C fabric. C planes are short (~500μ to ~5mm in length) and very discontinuous at this stage, but its orientation is rather homogeneous.

As a whole, the deformation is markedly heterogeneous, owing to the high competence contrast between quartz and feldspars. Here, weaker Quartz porphyroclasts are

heterogeneously deformed, being isolated in the load-bearing framework (Handy, 1990) represented by “rigid” feldspar porphyroclasts. The recrystallized quartz is commonly ~10-20% at this stage.

Feldspars recorded widespread brittle deformation (i.e. microfaulting and microboudinage), especially where two or more feldspar grain are into direct contact. Feldspar microfractures are mainly oriented at high to moderate angle (45-70°) from the foliation plane (Fig. 3.45). They are filled by fine-grained aggregates mainly made up of Ms, Bt, Ep and Qtz, being well discernible from submagmatic microfractures.

It is worth noting that, at this stage, the total strain visible at thin section scale is probably rather small. The observed feldspar alignment (along S planes) is likely partly inherited from (sub-) magmatic fabric, but Qtz and mica recrystallization suggest that the former main anisotropy was reworked at moderate angle under solid-state conditions.



Some examples of incipient deformation along the inner (low-strain) part of the “mylonitic rim”. **Fig. 3.42** (upper left): moderately deformed two-mica leucogranite, showing a nearly homogeneous S fabric transected by sharp and discontinuous C shear bands (green arrowhead; sample DSL99; crossed polars, gypsum plate inserted; base of photo: 4mm). **Fig. 3.43** (upper right): detail of Qtz-Qtz grain boundaries showing marginal recrystallization along S foliation plane (crossed polars, gypsum plate inserted; base of photo: 1.8mm). **Fig. 3.44** (lower left): two-mica microgranite (foliation trace from lower right to upper left); Qtz porphyroclasts exhibit incipient core and mantle microstructure; they are moderately flattened along S surfaces. Arrowheads indicate one of the sporadic C planes. The trace of the c-axis in some Qtz porphyroclasts is also indicated (crossed polars; base of photo: 3mm). **Fig. 3.45** (lower right): moderate deformation in feldspar-rich domains, marked by the onset of heterogeneous deformation, which is plastic in Qtz, mainly brittle in feldspars. Note the tail of Qtz porphyroclast squeezed between two “rigid” Kfs porphyroclasts (crossed polars; base of photo: 4mm).

3.3.2.2 *S-C tectonite*

Toward the pluton margin, the described S tectonites grade into S-C tectonites. With respect to the S tectonite, C planes are increasingly interconnected, and more closely spaced, representing penetrative structures. When observed on C foliation surfaces, the intersection between S and C planes is nearly orthogonal to the stretching lineation. In the more deformed rocks, discontinuous C' planes may locally occur. At the light microscope scale, quartz and feldspar microstructures are comparable with those of the S tectonites, but the accumulated strain is distinctly larger. Two end member microstructures can be defined.

(a) Moderately deformed S-C tectonite

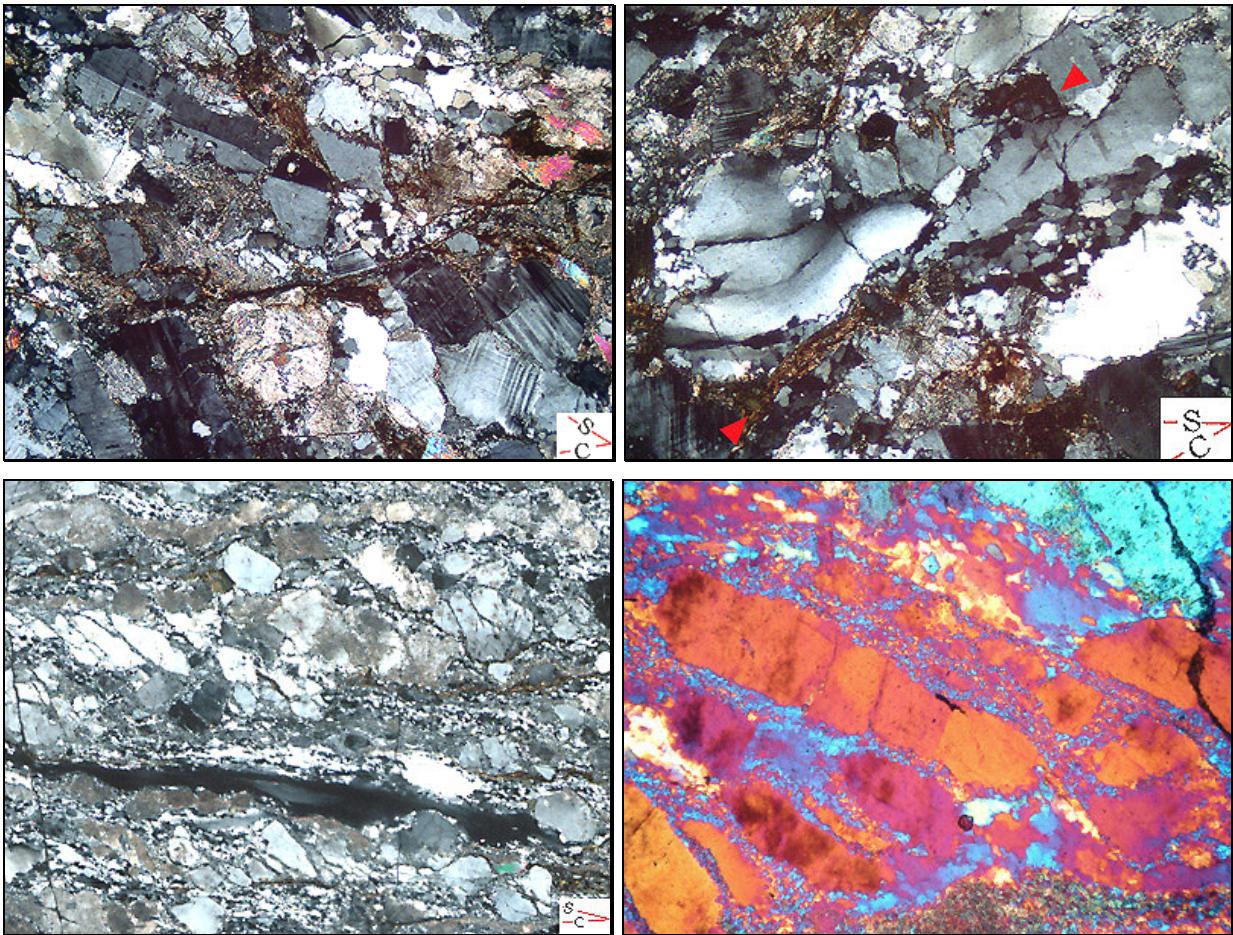
In the less deformed samples, some elements from the former "magmatic framework" are detectable. S surfaces are still partly highlighted by tabular feldspars (Fig. 3.46), which are progressively reduced in grain size owing to widespread brittle deformation and recrystallization. C shear planes tend to coalesce, becoming a penetrative subfabric ($\alpha \sim 30\text{--}40^\circ$; see Fig. 3.39 for definitions). Fig. 3.47 shows a detail of a C plane (marked by recrystallized biotite and quartz, red arrowheads) sharply transecting the more homogeneous S surfaces. Here, is well visible the strong bending of the quartz ribbon grain, exhibiting prismatic SGBs. At this stage, the contrasting nature of continuous vs. discontinuous deformation along S and C planes (Berthé et al. 1979) is well detectable. Around quartz ribbon grains, mantles of recrystallized grains become progressively wider as the strain increases. Quartz commonly develops lenticular aggregates with aspect ratio up to $\sim 5:1$, made up by polygonal grains of nearly equal size ("foam texture"), which likely derive from complete replacement of former ribbon grains. Quartz recrystallization also occurs along C planes, where new grains are often smaller than those developed along foliation planes. This is in agreement with the idea that C and C' shear bands develop close to the direction of maximum shear strain rate (Platt & Vissers, 1980). The systematic grain size discrepancy between S and C planes in mylonites with S-C fabric was described by Krohe (1990). As in the previous stage, feldspar is mainly deformed by brittle processes, but the amount of fine-grained recrystallized material is slightly greater with respect to the S tectonites. Mantles of fine-grained ($5\text{--}20\mu$) albite and Kfs newgrains become progressively more continuous; recrystallized material starts to develop along microfaults also (Fig. 3.49; see also Fig. 3.66 for a closer view on a microfault transecting a Kfs porphyroclast).

(b) Highly deformed S-C tectonite

With increasing deformation, a sensible decrease in α angle occurs at this stage ($\alpha \sim 10\text{--}20^\circ$), being commonly associated with an increase C planes density. The progressive rotation of S planes toward C surfaces reflects the rotation of the XY ("flattening") plane toward the shear plane, as expected during non-coaxial deformation (Ramsay, 1980). The angles α and β are also influenced by the parent rock. This is particularly true in the case of deformed porphyritic granitoids, where S surfaces are mainly defined by long side of feldspar clasts, causing an increase in α angle ("megacrystic type" in Blenkinsop & Treloar, 1995). In our case, however, most of the studied samples likely derive from

parent rocks (microgranitoids) with a relatively homogeneous grain size. Thus, angles α and β are inferred to be mainly strain-dependent.

Recrystallized Qtz is about 40-50% in the moderately deformed S-C tectonite (i.e. sample DSL83, Fig. 3.46 and 3.47), reaching ~70-80% in the more deformed domains (i.e. sample DSL84, Fig.3.48). The marked increase in the proportion of recrystallized quartz coincides with the onset of widespread feldspar recrystallization (Fig. 3.49). Sporadic quartz porphyroclasts locally escaped from complete recrystallization, appearing as isolated single ribbon grains with aspect ratio up to~12:1 (Fig. 3.48).



Moderately to highly deformed S-C tectonites. **Fig. 3.46** (upper left): moderately deformed S-C tectonite. Note the fragmented but still subhedral feldspars, which commonly develop patchy microcline twinning (i.e. lower right side). Sharp C planes are marked by recrystallized Bt (crossed polars; base of photo: 4mm). **Fig. 3.47** (upper right): example of sharp C sinistral shear band truncating the more homogeneously deformed S surface. Note the deflection of S planes along the C shear plane (crossed polars; base of photo: 3.3mm). **Fig. 3.48** (lower left): enlarged micrograph from highly deformed S-C tectonite, showing the contrasting deformation behaviour between Qtz and feldspars. Note the small α angle ($\alpha \sim 20^\circ$) compared to low-strain rocks (crossed polars, base of photo: 1.1cm). **Fig. 3.49** (lower right): Detail from the central portion of a feldspar-rich domain, showing fragmented and recrystallized Kfs porphyroclast, which exhibit strong patchy undulose extinction and serrate grain boundaries toward newgrains in the mantles. Note the strong LPO of Kfs-Ab newgrains (crossed polars; gypsum plate inserted; base of photo: 1.8mm).

3.3.2.3 *C'* tectonite

C' tectonites are mainly sampled close to the contact with the Mafic Complex (i.e. ~1-10mt). These rocks exhibit dramatic grain size reduction; they are characterized by small α angle ($\alpha \sim 0-10^\circ$) and β angles of $\sim 15-30^\circ$. With respect to S-C tectonite, quartz is completely recrystallized (commonly no porphyroclasts occur), and the proportion of recrystallized feldspar is commonly greater than 50%. According to the traditional classification, *C'* tectonites are classifiable as mylonites displaying mm- to cm-thick ultramylonite domains. The latter are strongly foliated, displaying monomineralic quartz layers alternating with polymineralic layers made up of completely recrystallized feldspars and quartz (Fig.3.53).

In contrast to S and C surfaces, *C'* shear bands are commonly discontinuous; they are few mm to few cm long and inhomogeneously spaced at both hand sample and thin section scale, being closely spaced ($\sim 1-3\text{mm}$) within homogeneously layered domains.

Figs. 3.50 and 3.51 illustrate typical structural features of *C'* tectonite (polished hand sample and thin section from DSL77b; $\sim 5\text{mt}$ from the contact with the roof of MC). Here, quartz occurs as monomineralic (commonly 1-2cm-long) ribbons made up of fine-grained polygonal grains with uniform grain size (30-60 μ).

Ribbon-forming grains are slightly elongate, defining a shape fabric oblique ($\sim 30-40^\circ$) with respect to the ribbon outline (which approximately coincides with both S and C planes). Oblique foliation (indicated by the blue line in Fig.3.52) typically develops during non-coaxial flow, where its orientation reflects the last increments of the deformation history (Ree, 1991). In contrast, distinctive quartz fabric domains (Pauli et al., 1996) commonly define elongate lenses at low angle ($\sim 10-20^\circ$) from C planes. Fabric domains are detectable as groups of adjacent recrystallized grains showing comparable lattice orientation, likely deriving from complete replacement of former ribbon grains. In Fig.3.52, they are detectable as groups of neighbour grains exhibiting similar grey tonalities, where their mean orientation is indicated by the yellow line. The unambiguous identification of quartz fabric domains is obviously easier by using the gypsum plate and the U-stage. Stipp et al. (2002) described that distinct quartz fabric domains start to develop near the upper limit of SGR recrystallization regime, namely at temperature around 500°C .

For the reasons described above, distinct quartz fabric domains are inferred to provide a good approximation of the XY plane of the finite strain ellipsoid, whereas the oblique foliation indicates the approximate orientation of the XY plane of the last increments of deformation. Thus, defining α' as the angle between C planes and the oblique foliation, the relation $\alpha' > \alpha$ is generally expected to occur for high strain values achieved by non-coaxial flow. These geometrical relations are shown in Fig.3.52, where the measured α and α' are $\sim 15^\circ$ and $\sim 30^\circ$, respectively. Analogous geometrical relations between quartz fabric domains and oblique foliation were described by Lister & Snoke (1984).

Both synthetic and antithetic microfaults developed in feldspars. In the upper portion of Fig. 3.51, several fragments of a former single plagioclase porphyroclast (pale yellow; the identity of single fragments was checked by the gypsum plate) were displaced by a network of en-echelon synthetic microfaults, producing long fragment trails aligned along C planes, connected by thin trails of albite newgrains. Analogous microstructure occurs in K-feldspar porphyroclast (e.g. above plagioclase trails in Fig.3.51).

Fig. 3.53 shows a detail from the nearly ultramylonitic domain in the sheared Ms-bearing microgranite. These domains are characterized by an evident layered microstructure, made up of monomineralic quartz ribbons (grain size: $\sim 50\text{-}70\mu$) alternating with finer-grained K-feldspar- albite-quartz layers (grain size: $\sim 5\text{-}15\mu$).

Few examples of subsolidus shear zones occur in the inner part of the pluton, where three main $\sim 10\text{mt}$ -thick mylonites were mapped (Fig.3.11) and sampled. The geometry of these shear zones is broadly comparable with those of the main solid-state fabric developed along the eastern pluton margin. The best exposed example crops out $\sim 500\text{mt}$ westward from Cima Incalcinata (Fig.3.11). This mylonite nucleated along the boundary between 1mt -thick quartz vein and host two-mica microtonalite (Fig.3.41). Microstructures and quartz LPO from these “internal” C' tectonite (Fig.3.54 and 3.55) are comparable to those detected in the high-strain domains along the pluton margin.

The relationships between “internal” shear zones and the main solid-state fabric along the pluton margin will be discussed in chapter five.

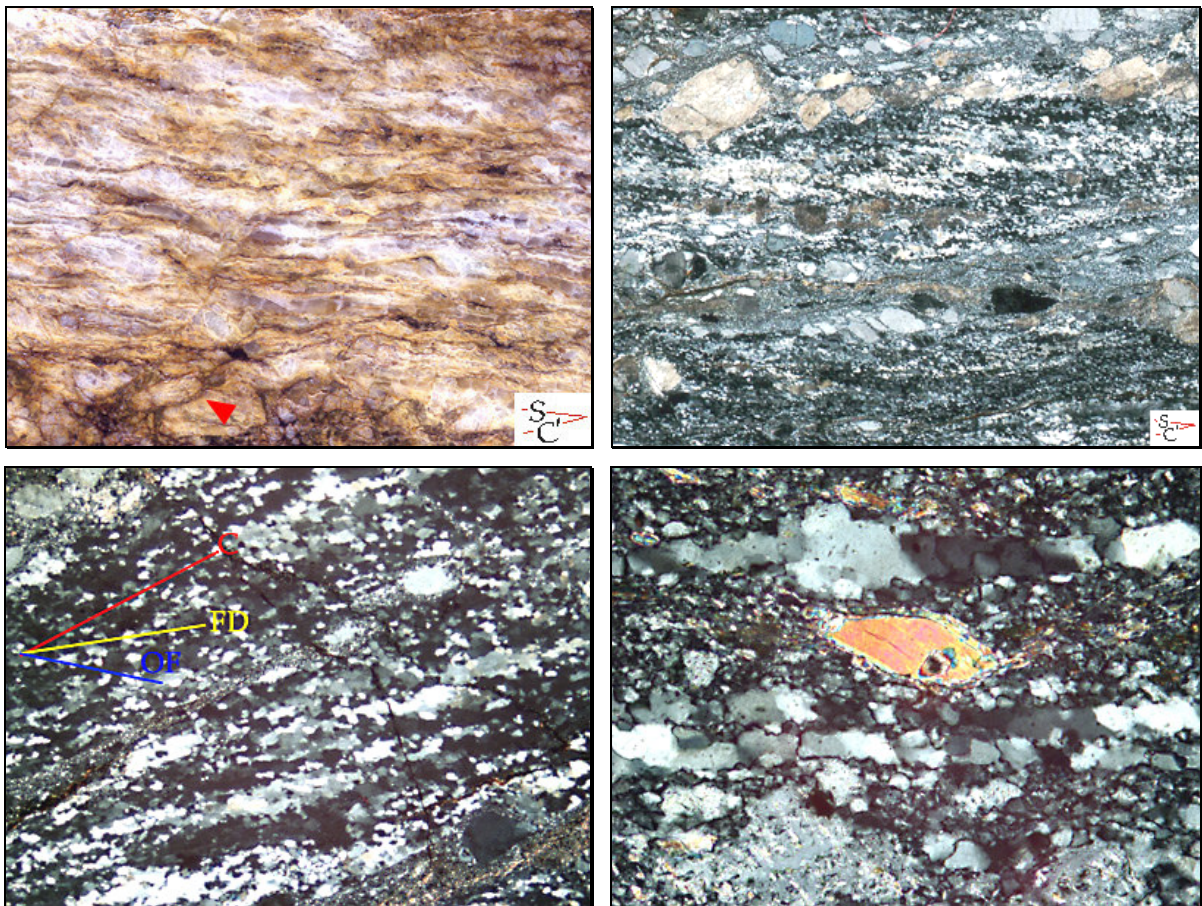


Fig. 3.50 (upper left): typical mesoscopic features of C' tectonite, at the magmatic contact between Bt-granodiorite and coarse-grained tonalite (bottom). Note the synthetic microfault in the coarse Pl clast (red arrowhead; polished hand sample from DSL77b; base of photo: 5cm). **Fig. 3.51** (upper right): enlarged micrograph from sample DSL77b showing the typical microstructure of C' tectonites. Note the en-echelon array of Pl porphyroclasts, aligned along C planes (crossed polars; base of photo: 0.93cm). **Fig. 3.52** (lower left): a closer view of a nearly monomineralic Qtz ribbon, showing the geometrical relations between different subfabrics. C planes are highlighted by elongate trails of recrystallized feldspars (red lines), whereas blue and yellow lines indicate the oblique foliation (OF) and fabric domains (FD), respectively (crossed polars; base of photo: 3.2mm). **Fig. 3.53** (lower right): detail from C' tectonite (sample z87) showing the layered microfabric made up of totally recrystallized quartz and feldspars monomineralic layers. Sporadic mica fish and C' shear bands help to define the prevailing sinistral shear sense (crossed polars; base of photo: 0.7mm).

3.3.3 Quartz LPO

Quartz LPO has been measured in 10 samples from each solid-state deformation stage previously described. Where possible, quartz fabrics have been investigated in both porphyroclasts and recrystallized grains. The progressive fabric evolution is shown by the schematic cross-section from the low-strain domains in the inner part of the “mylonitic rim” outward, i.e. toward the contact with the roof of the Mafic Complex.

3.3.3.1 *Evolution of quartz fabric through the “mylonitic rim”*

Low-strain S tectonites (sample DLS99, Fig.3.42 and 3.43) exhibits partly discontinuous type I crossed girdle (in the sense of Lister, 1977), with two main maxima, close to the Y-axis and in intermediate position. The girdle makes an angle of 70° with both the S and the C planes. If analyzed in rocks of external asymmetry with respect to the shear plane, the girdle should provide dextral shear sense, hence opposite to the overall sinistral shear sense suggested by microstructural criteria. Analogous results were shown by Berthé et al. (1979) and by Krohe (1990). At this stage, C planes represent a non-penetrative subfabric, and most of the quartz fabric was likely achieved by non-coaxial deformation along foliation planes. With respect to the reference frame provided by the S planes, the asymmetric fabric skeleton is slightly inclined toward the overall sinistral shear sense.

In sample DSL83 (Fig.3.46 and 3.47; moderately deformed S-C tectonite), both porphyroclasts and recrystallized grains exhibit a less-continuous pattern. Recrystallized grains exhibit a prominent maximum near Y position, and some secondary maxima around the foliation poles. The latter become dominant in porphyroclasts. In both cases, some other sub-maxima in intermediate position cluster around a plane at high angle from C planes, possibly identifying a type I crossed girdle (Fig.3.56). Respect to the shear plane, the fabric skeleton of neoblasts is inclined against the overall sinistral shear sense, whereas the fabric skeleton from porphyroclasts is orthogonal from C surfaces (Fig.3.56). In both cases, the orientation of the fabric skeleton respect to prominent S planes and the internal monoclinic symmetry fit the overall sinistral shear sense.

Sample DSL12 corresponds to the stage of the onset of fully coalescence between C planes, which represent the main subfabric. Here, the noticeable decrease in the grain size of the recrystallized quartz (likely as an effect of the increased strain rate along C planes) is accompanied by a clear reduction of α angle (from ~40° to ~25°).

Quartz fabrics from both porphyroclasts and recrystallized grains exhibit a nearly continuous girdle, which is transitional between type I crossed girdle and single girdle (Fig.3.56). At this stage, the longest arm of the girdle is consistently rotated toward the overall shear sense, making an angle of ~65-70° with the shear plane. This external monoclinic symmetry characterizes domains where non-coaxial deformation along shear planes is prevailing on the more homogeneous deformation along foliation planes (Krohe, 1990).

Sample DSL84 is a S-C tectonite characterized by small α angles (~10-15°) and the occurrence of sporadic C' shear bands (Fig.3.48 and 3.49). From this stage few porphyroclasts are locally preserved, and the quartz fabric exhibits a prominent single girdle character, which also typify the fabric of C' tectonite. The fabric skeleton is normal to C planes in sample SL84, whereas in C' tectonite stage (samples Z87, DSL39 and

DSL77b) it is slightly rotated sympathetically with the overall shear sense, making an angle of $\sim 75\text{-}80^\circ$ from C planes (Fig.3.56). The first appearance of C' shear bands corresponds with a steepening of the single girdle. As C' shear bands are thought to develop rather late during the activity of shear zones, relict domains could passively rotate antithetically respect to the overall shear sense, in the manner proposed by Passchier (1991b). In this way the shear zone is stretched parallel to its boundaries; this kind of shear zones are generally associated to large-scale extension terrains (i.e. Basin and Range province).

3.3.3.2 *Interpretation of the quartz fabric*

As a whole, the quartz fabric through the "mylonitic rim" exhibits a transition from Type I crossed girdle (which characterizes low-strain domains) to single girdle in the highly strained domains. Such a transition has been described by many workers; Schmid & Casey (1986) suggested that this transition might represent an increasing rotational component in the strain path. In alternative, a similar evolution is expected with increasing strain during simple shear (Garcia Celma, 1983). The latter interpretation fits the evolution of field relations and microstructures described in this paper. In all the analyzed samples, neither prominent nor secondary maxima around the stretching lineation occur. Thus, the described fabrics are interpretable in rocks of dominant slip along the $\langle a \rangle$ direction, which operated on basal, rhombohedral and prismatic planes.

(a) *Porphyroclasts*

Quartz porphyroclasts aspect ratios range from $\sim 1:2$ (in the inner, low strain domains; e.g. sample DSL99, Fig.3.42 to 3.44) up to $\sim 10:1$ at the transition between S-C and C' tectonite (Fig.3.48), where quartz porphyroclasts are nearly totally recrystallized. Quartz ribbon grains commonly show strong internal deformation, frequently displaying prism-parallel SGBs and undulose extinction.

The fabric of porphyroclasts in the low-strain (inner) domain is characterized by type I (partly discontinuous) asymmetric crossed girdle, showing the highest concentration of c-axis around the foliation poles. The internal monoclinic symmetry is in agreement with the overall sinistral shear sense (Fig.3.56). Such a fabric suggests that basal, rhombohedral and prismatic slip along the $\langle a \rangle$ direction likely cooperated in the deformation of quartz porphyroclasts, producing ribbon grains. The observed Y maximum was unlikely inherited from (sub) magmatic stage (Fig.3.33), since no X maxima occur here. The LPO of quartz porphyroclasts from "internal" mylonite (sample DSL73.3; 3.55) do not differs from those deriving from the pluton margin.

(b) *Recrystallized grains*

Clear maxima in Y and intermediate position are prevailing in all the analyzed samples. This suggests that the activity of the $\langle a \rangle$ slip along the basal (0001) slip system played a subordinate role at any stage of solid-state flow. Instead, $\langle a \rangle$ slip along rhombohedral and prismatic planes was prevailing. Samples z87 and DSL73.3 (both C' tectonites) partly differ from the general trend, exhibiting a very strong maximum around Y position and secondary maxima around the foliation poles, without intermediate peaks. The observed slightly different pattern might be related to the occurrence of domainal fabric, which is described to persist up to high finite strains (Pauli et al, 1996). On the other hand, no

herringbone microstructure (Garcia Celma, 1982) is generally visible in our case. Another possible explanation could be that this mylonite experienced a polyphase retrograde evolution. In this case, the essential of the fabric could be developed (during a first “step”) by active slip along prismatic plane alone, in the field of dominance GBM for quartz. This early fabric could be partially overprinted during the retrograde evolution, producing the observed fine-grained ($\sim 30\text{-}50\mu$) foam texture in quartz, associated (in the pole figure) with the secondary maxima close to the foliation poles).

The fabric is progressively strengthened with increasing strain, as predicted by Lister & Hobbs (1980); the increase of fabric intensity seems rather abrupt, around the transition between S-C and C’ tectonite (Fig.3.56). Krohe (1990) measured separately the quartz fabric within S and C domains; the author reported that in the c-axis pattern “C domains” tends to exhibits a single Y maximum, whereas “S domains” are characterized by single to crossed girdle pattern.

Stipp et al. (2002) described that the abrupt change from single girdle to distinct Y maxima (which is interpreted to represent the transition from multiple to single slip system) coincides with the switch in the dominant recrystallization mechanism, from SGR to GBM (i.e. around $\sim 500^\circ\text{C}$). This is explained in the way that, owing to the limited mobility of grain boundaries in the SGR regime, more than one independent slip system is needed in order to satisfy strain compatibility. The interpretation proposed by Stipp et al. (2002) fits with the quartz pattern discussed in this paper, where the evolution of the main microfabric across the “mylonitic rim” took place entirely in the field of SGR for quartz (section 3.3.6.1). Thus, the progressive strengthening toward Y-axis can be viewed in the sense of dominant simple shear along both S and C planes, where the subordinate slip activity along rhombohedral and basal planes help to adjust the local strain compatibility. The measured opening angles cluster around $40\text{-}50^\circ$ in all the analyzed samples (Tab.3), providing a temperature range of $\sim 400^\circ\pm 50^\circ\text{C}$ (Kruhl, 1998).

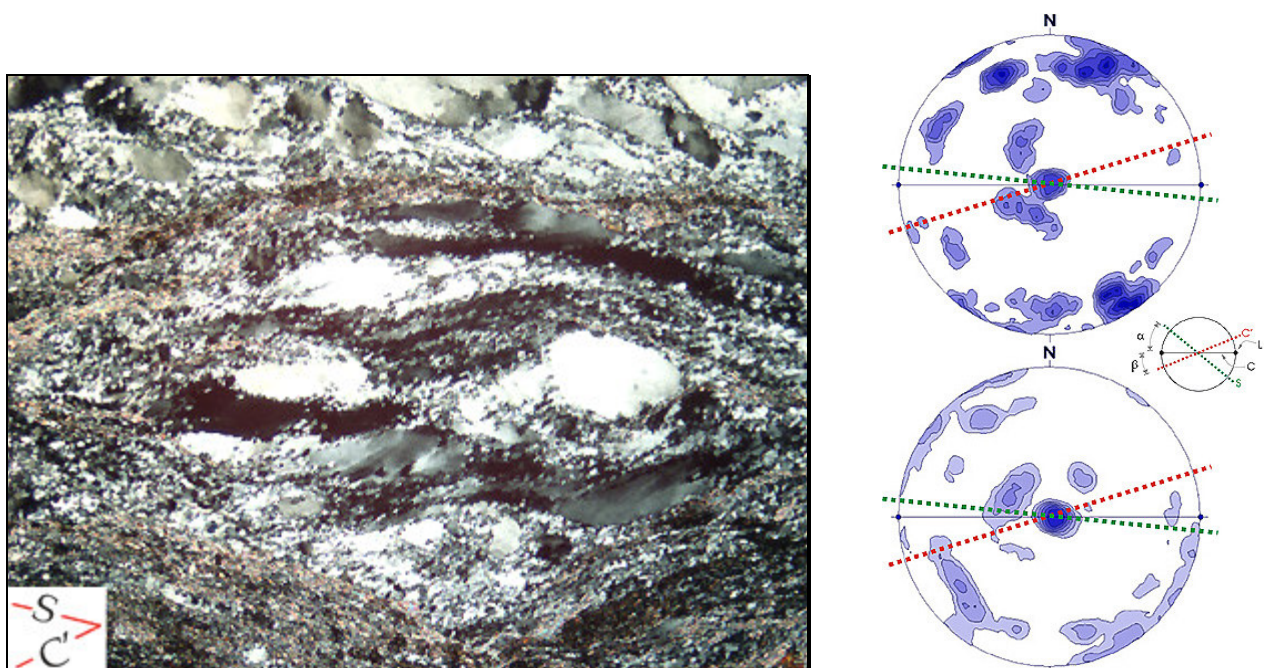


Fig. 3.54 (left): microstructure from sheared quartz vein shown in Fig.3.41. **Fig. 3.55** (right): quartz LPO from the “internal” mylonite shown in Fig.3.82 and 83 (sample DSL73.3). Left: LPO from porphyroclasts [N= 175. Contours: 2-8% (1% of search area)]. Right: LPO from recrystallized grains [N= 302. Contours: 2-8% (1% of search area)]. Lower hemisphere projection in both cases.

Tab. 6: summary of the main microstructural features in the representative tectonites belonging to the “mylonitic rim” and analyzed for quartz LPO.

Sample	Fabric type	parent rock	a	β	opening angle
DSL99	S	leucogranite	\	\	50°
DSL83n	S-C	leucogranite	40-45°	\	40°
DSL83c	S-C	leucogranite	40-45°	\	40-45°
DSL84	S-C	granodiorite	9-15°	25-28°	45°
DSL 12n	S-C	leucogranite	25-30°	\	40-45°
DSI 12c	S-C	leucogranite	25-30°	\	40°
DSL39	C'	granodiorite	\	20-25°	\
DSL77	C'	leucogranite	5-10°	20-25°	\
z 87	C'	tonalite-leucogr. contact	\	15-22°	\
DSL 733n	C'	Qtz-vein	\	15-20°	75°
DSL733c	C'	Qtz-vein	\	15-20°	50°
z 86	C' (HT)	leucogranite			\
DSL92	S-C (HT)	porphyritic leucogr.	20-25°	\	80°

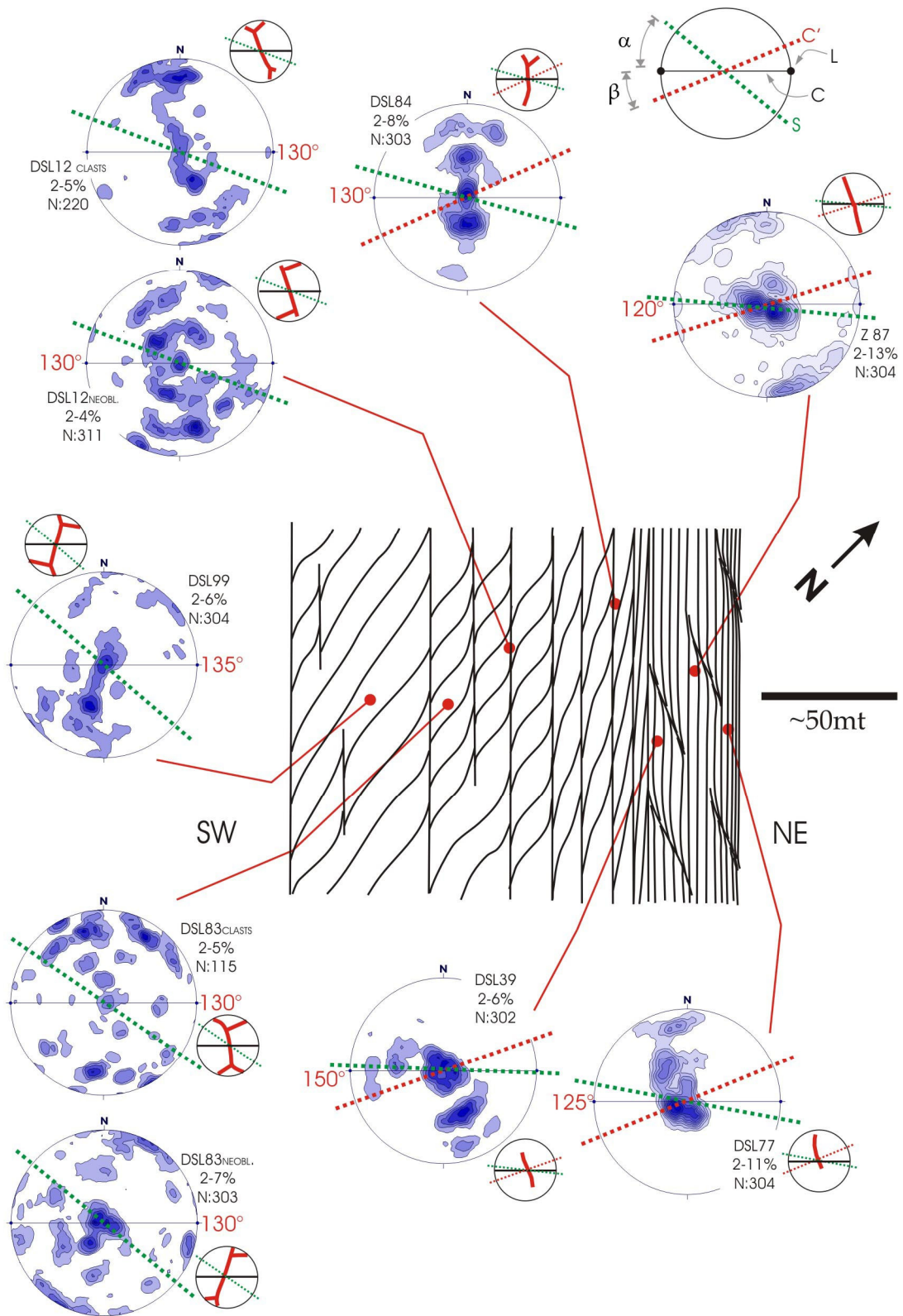


Fig. 3.56: schematic cross-section through the "mylonitic rim", showing the fabric evolution from low-strain S tectonite toward high-strain C' tectonite at the pluton margin. For each pole figure, the fabric skeleton is proposed in the smaller diagram, emphasizing the geometrical relations between Qtz fabric, S, C and C' subfabrics. The local orientation of C plane is provided (red values). C-axis orientation refers to recrystallized grains (if not otherwise indicated).

3.3.4 Relicts of high-temperature solid-state fabric

Microstructures described in section 3.3.2 belong to the *main* solid-state foliation, largely preserved along the NE pluton margin. This foliation locally contains some metric to sub-metric domains where an older fabric is preserved. The two representative examples shown here came from porphyritic granite from the northernmost part of the pluton margin (i.e. near *Pietroso* locality; sample DSL92; Fig.3.57) and from granite pegmatite intruded into Ms-bearing microtonalite, from the surroundings of *Cima Incalcinata* (sample z86). The geometry of mesoscopic structures is comparable to those described for the main solid-state fabric.

The northernmost sample is a S-C tectonite ($\alpha \sim 40^\circ$) deriving from porphyritic leucogranite (Fig.3.7 and 3.40). Quartz porphyroclasts are sporadically preserved within pressure shadows of larger feldspar porphyroclasts (Fig.3. 57b).

Here, quartz clasts commonly exhibit chessboard SGB pattern and coarse-grained (0.2-1mm) recrystallized grains (Fig. 3.57c), displaying coarsely sutured grain boundaries with squared outline (mosaic-like aggregates, Fig. 3.57c and 3.57d), and dissection microstructure (Urai et al., 1986).

The hypothesis that quartz chessboard pattern was inherited from submagmatic stage cannot be completely ruled out (compare Fig.3.57D with Figs.3.15 and 3.17). Nevertheless, the c-axis of both quartz porphyroclasts and recrystallized grains (in the strain shadow domains) point consistently toward the (solid-state) stretching lineation (pole figure in Fig.3.57), suggesting that these microstructures are in equilibrium with this solid-state foliation. The quartz fabric from the complete thin section exhibits a strong maximum near the Y-axis and some secondary maxima clustering around the stretching lineation. As a whole, this kind of quartz fabric is qualitatively analogous to those developed during magmatic to submagmatic flow. Feldspar porphyroclasts recorded only minor brittle deformation, at least at light microscope scale. These localized brittle features likely developed rather late in the evolution of this S-C tectonite. Instead, K-feldspar exhibits incipient recrystallization and sweeping undulose extinction, suggesting the occurrence of deformation in the dislocation creep regime (Tullis & Yund, 1987).

Larger K-feldspar porphyroclasts exhibit a peculiar microstructure. They are partially to totally replaced by coarse-grained aggregates (Fig.3. 57e and 3.57f), where Kfs-Kfs grain boundaries are moderately to strongly lobate, and are locally highlighted by thin trails of recrystallized Ab and Kfs grains. Aggregate-forming grains exhibit large grain size (i.e. up to 1-2mm) and widespread sweeping undulose extinction. The progressive misorientation of some large portion of porphyroclasts is visible in Fig.3.57e. This process may lead to complete replacement of the former grain (Fig.3.57f). Aggregate-forming grains show irregular and lobate outlines, which in most cases are unlikely crystallographically controlled.

This microstructure displays some striking similarities with those described by Hanmer (1982). The latter author proposed that these coarse-grained aggregates developed by ductile shearing on pre-existing growth boundaries. For the coarse-grained "replacing grains" Hanmer (1982) used the term "subgrains" in the *sensu lato*: they are not true subgrains, because they are not bounded by arrays of dislocations; on the other hand, they are not fragments, because they are thought to develop by ductile rather than brittle

shearing. In the case study reported by Hanmer (1982) these microstructures developed during syndeformational cooling of a syntectonic granite, at temperature around 500-600°C. In our case, the boundaries separating coarse “subgrains” (*sensu lato*) are partially replaced by strain-induced myrmekites (yellow arrowheads in Fig.3.57f), suggesting that grain boundary adjustment took place at relatively high temperature ($T > \sim 500^\circ$).

The high-temperature microstructures discovered in sample DSL92 are preserved within mm- to cm-scale low-strain domains (i.e. in strain shadow positions respect to centimetric feldspar clasts). In contrast, the mylonitic matrix recorded dramatic grain size reduction (mainly along C shear bands, Fig.3.57f), displaying microstructures that progressively evolve toward those typical of the main solid-state fabric (section 3.2). This inhomogeneous deformation is indicative of the retrograde character of this mylonite and, more in general, it documents the progressive syndeformational cooling of the pluton margin. The preservation of feldspar microstructures as those shown in Fig. 3.57 were likely allowed by the increased quartz-feldspar strength contrast due to progressive cooling, involving strain localization into finer-grained (and quartz-rich) matrix.

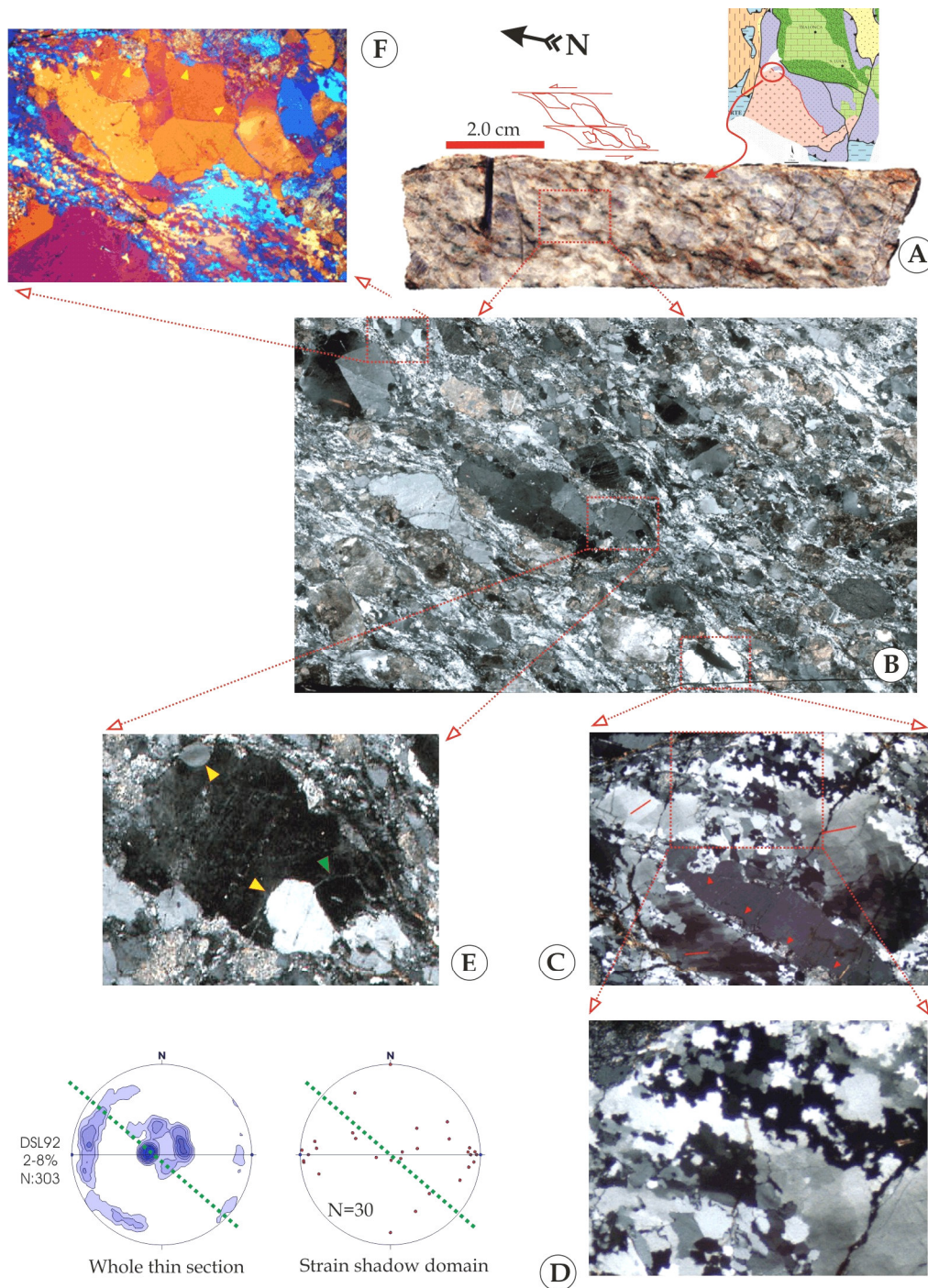


Fig. 3.57: synthetic sketch summarizing meso-, microstructures and c-axis fabric from sample DSL92. [A] Polished hand sample showing the S-C geometry developed at depends of porphyritic leucogranite. [B] Enlarged micrograph emphasizing the strain partitioning between “hard” feldspar porphyroclasts and weak quartz. Dramatic grain size reduction mainly occurs along sub-horizontal C shear planes (crossed polars; base of photo: 4.2 cm). [C] Detail of a strain shadow area near coarse Pl clast, showing chessboard pattern and GBM recrystallization in Qtz. Red lines indicate the c-axis trace of Qtz porphyroclasts (crossed polars; base of photo: 4mm). [D] Detail from (C) to show mosaic-like Qtz aggregate around Qtz clast (crossed polars; base of photo: 1.6mm). [E] Stage of incipient development of coarse Kfs monomineralic aggregate. “Subgrains” (sensu lato) with small and high misorientation angles are shown (green and yellow arrowheads, respectively; crossed polars; base of photo: 4mm). [F]: Stage of complete replacement of former porphyroclast. Yellow arrowheads point to strain-induced myrmekite (crossed polars; gypsum plate inserted; base of photo: 4mm).

Sample z86 (Fig. 3.58 to 3.61) comes from mylonitic gneiss belonging to a lensoid-shaped domain, which is enclosed into finer-grained S-C tectonites (section 3.3.2.2). This medium- to coarse-grained lens (sheared pegmatite) crops out few tens of meters from the contact with the Mafic Complex. At grain scale, microstructures resemble those described for adjacent leucogranitoids belonging to DGS (chapter two). Quartz occurs as 0.5-2mm-thick polycrystalline ribbons (Fig. 3.59 and 3.61), displaying an internal, oblique foliation developed at $\sim 30\text{-}40^\circ$ from the ribbon margins. Ribbon-forming grains exhibit irregular outlines, wide range in grain size ($\sim 100\text{-}1000\mu$) and are coarsely to finely serrate. Prism-parallel SGBs are locally observed.

Feldspars porphyroclasts lack any evidence of brittle deformation, commonly showing sweeping undulose extinction and lobate grain boundaries. Optically visible subgrains (grain size: $\sim 50\text{-}100\mu$) occur near the periphery of porphyroclasts (Fig.3.60), providing the gradual transition toward the mantle of recrystallized grains (grain size $\sim 20\text{-}100\mu$). In plagioclase, recrystallized grains display a composition comparable with that of the host (oligoclase, as estimated by conventional optical methods). Strain-induced myrmekites are rather common along Kfs crystal faces at low angle with the mylonitic foliation. Muscovite is completely recrystallized, developing thin folia made up of fine-grained aggregates. Sample z86 exhibit strong quartz LPO, where most of c-axes cluster around Y-axis; monoclinic symmetry of S-C fabric, oblique quartz foliation, σ -type and δ -type mantled porphyroclasts (i.e. feldspars) suggest that sinistral shear sense is prevailing in both the described samples.

The micrograph shown in Fig.3.61 offers the opportunity to discuss (under a purely qualitative viewpoint) the importance of local variation in quartz LPO caused by non-quartz material (feldspars, in our case). In sample Z86, plagioclase and K-feldspar occur as rounded porphyroclasts (diameter: $\sim 1\text{-}5\text{mm}$). Away from these porphyroclasts, ribbon-forming grains exhibit strong LPO, where the c-axes are mostly oriented around Y-axis (i.e. normal to the view plane in Fig.3.61). In contrast, most of the c axes from the quartz grains in the surroundings of the Kfs porphyroclast are contained in the XZ plane, or they are moderately inclined respect to it (i.e. $<20^\circ$; in Fig.3.61, the c-axis trace of these grains is indicated by red lines). This phenomenon was quantitatively studied by Lister & Price (1978); the authors demonstrated that, at grain-scale, different regions of a mylonitized granitoid exhibit different quartz LPO in function of the position respect to the more competent feldspar porphyroclasts. Obviously, these strain heterogeneities are somewhat proportional to the grain size of the "rigid" clasts; moreover, they are markedly increased by a decrease in the deformation temperature. In our case, grain scale strain heterogeneities are likely negligible in the striped gneiss at the base of the mafic complex. In contrast, this effect on quartz LPO were likely significant in the "megacrystic" meta-leucogranites within the roof of MC (DG suite), and in some medium to coarse-grained tectonites belonging to the "mylonitic rim" of the GC (e.g. sample DSL92, Fig.3.57). In sample z86, despite the local occurrence of scattered c-axis orientation (Fig.3.61), the observed strong LPO (Fig.3.58) suggest that grain-scale strain heterogeneities were negligible at the scale of the whole thin section.

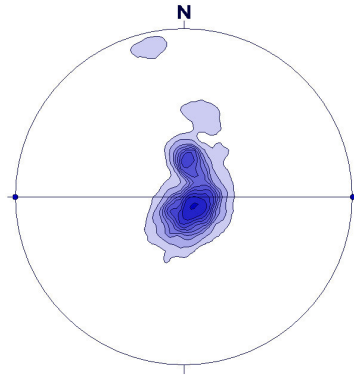


Fig. 3.58: pole Figure of the quartz fabric from sample z86. N= 304. Lower hemisphere projection; contours: 2-14% (1% of search area).

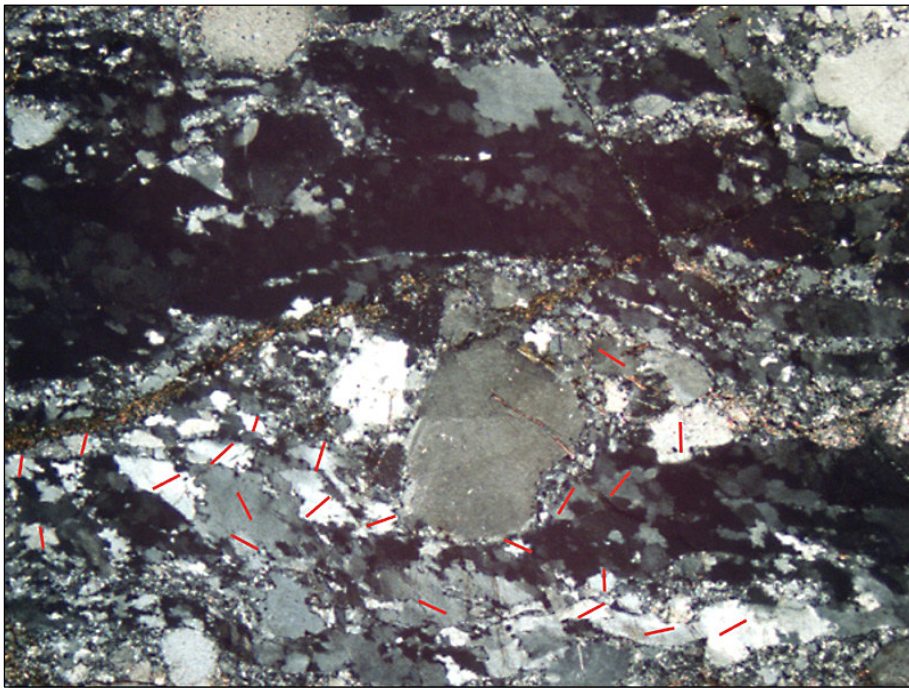
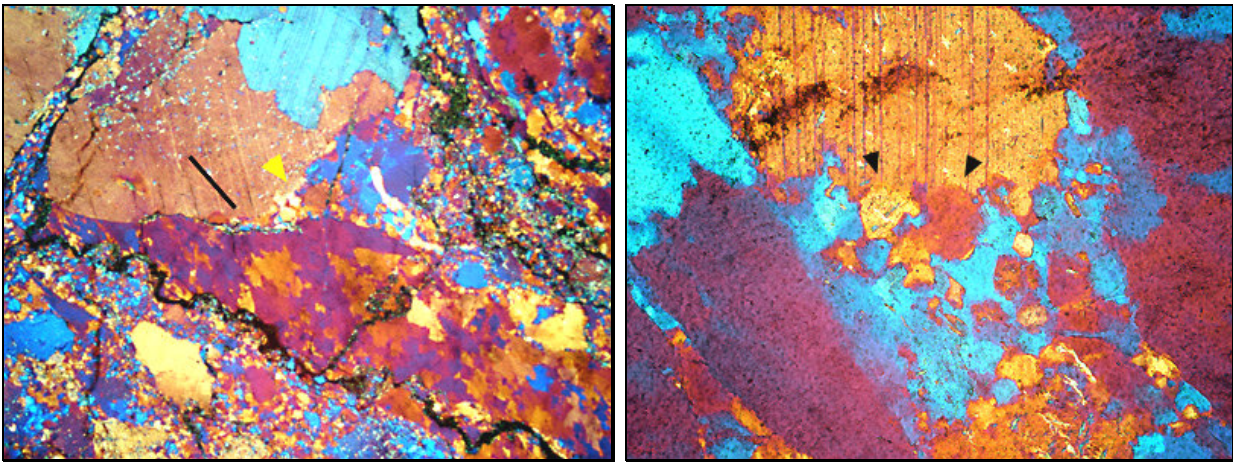


Fig. 3.59 (upper left): Qtz ribbon wrapping around a composite porphyroblast composed by two deeply sutured Pl grains. Black line indicates the trace of the Qtz oblique foliation (crossed polars; gypsum plate inserted; base of photo: 4mm). **Fig. 3.60** (upper right): detail of a Pl porphyroblast mantled by sutured recrystallized grains and subgrains near the porphyroblast margins (black arrowheads; crossed polars; gypsum plate inserted; base of photo: 0.7mm). **Fig. 3.61** (lower centre): enlarged micrograph showing an overview on high-temperature microfabric from sample z86. Note the strong Qtz LPO (from black to dark grey), in contrast

with the scattered C-axis orientation around the large Kfs porphyroblast. Further explanations in the text (crossed polars; base of photo: 4mm).

3.3.5 Pre-Alpine low-temperature solid-state fabric

As described for the MC (section 2.1.7.4), some evidences of pre-Alpine low-temperature shear zones are detected also in GC. The example shown here comes from the 1cm-thick ultramylonite (developed from a porphyritic, Hbl-bearing, granodiorite, Fig.3.6) sampled near the NE pluton margin, around *Pietroso* locality. This thin mylonite (Fig.3.62) is oriented N110°60°NE, where the associated stretching lineation dips ~30° toward SE.

Within the median part of the ultramylonite, syn-mylonitic isoclinal folds are highlighted by the strongly deformed polycrystalline quartz ribbons (Fig.3.63). Ribbon-forming grains are very fine-grained, displaying a rather homogeneous grain-size (5-20 μ). Observations with the gypsum plate suggest that the ultramylonite is characterized by strong quartz LPO (Fig.3.63). As qualitatively observed under the light microscope, most of the c-axis from this central domain lies in the XZ planes, mainly clustering around the foliation poles. This suggests that basal <a> slip was dominant during shearing. These quartz microstructures will be discussed in the next section.

The ultramylonitic matrix is mainly composed by albite, epidote, chlorite and sericite. Feldspar porphyroclasts mainly experienced brittle deformation, even if a thin mantle of albite newgrains is locally developed around K-feldspar porphyroclasts. The sinistral shear sense is provided by the asymmetric folds, σ and δ type mantled porphyroclasts, and by the occurrence of sporadic C' shear bands.

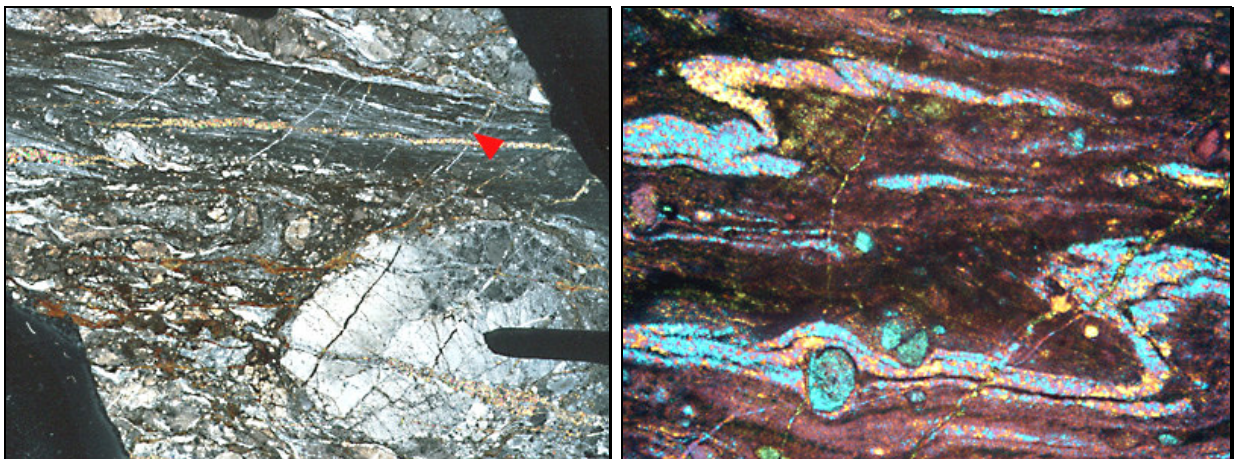


Fig. 3.62 (left): overview on the low-temperature ultramylonite, which likely nucleated along the boundary of the coarse Kfs porphyroclast. The median part of the shear zone is transected by epidote veins. Red arrowhead indicates the mylonitic folds shown in Fig.3.63 (sample DSL95a; crossed polars; base of photo: 2cm). **Fig. 3.63** (right): detail from the central part of the ultramylonite, to show the strong Qtz LPO in the folded Qtz ribbons ((crossed polars; gypsum plate inserted; base of photo: 0.7mm).

3.3.6 Some remarks on quartz and feldspars microstructures

This section provides some additional remarks about some quartz and feldspar microstructures acquired during solid-state flow.

3.3.6.1 Quartz

(a) *The main solid-state fabric*

Different stages of quartz recrystallization are detectable across the “mylonitic rim”. In the low-strain domains, quartz porphyroclasts are surrounded by a mantle of recrystallized grains, which display homogeneous grain size (50-100 μ), nearly polygonal outlines, and commonly lack any evidence of intracrystalline deformation features. Toward the grain margins, nearly polygonal and equidimensional subgrains (~50-100 μ in size) provide the gradual transition toward the newgrains. Polygonal subgrains occur also in the interior of porphyroclasts (Fig.3.64). These microstructures suggest quartz recrystallization is mainly achieved through progressive misorientation of subgrains. With increasing deformation, former porphyroclasts are progressively replaced by nearly polygonal quartz aggregate (“foam texture”, Fig.3.65). Within some low-strain domains, quartz aggregates display more irregular (lobate) grain boundaries and a wider range of grain size (~50-150 μ), suggesting that some contribution of grain-boundary-migration recrystallization (GBM) likely occurred during the early stages of the development of the main solid-state fabric. Thus, the preserved main microfabric along the “mylonitic rim” likely started to develop at temperature around ~500° (near the transition between SGR and GBM, Hirth & Tullis, 1992; Stipp et al., 2002), whereas the progressive localization in the high-strain domains might reflect a progressive increase in strain rates, accompanied by gradual cooling.

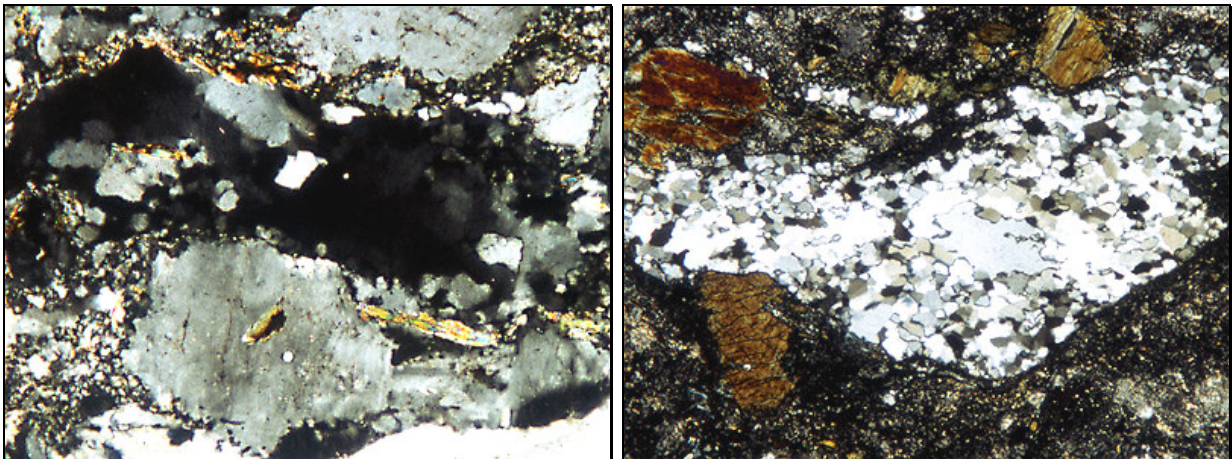


Fig. 3.64 (left): detail of a quartz ribbon grain aligned in the S foliation plane, where newgrains generated by progressive misorientation of nearly polygonal subgrains (crossed polars; base of photo: 2mm). **Fig. 3.65** (right): D₃ mylonite in quartz-diorite from DG suite at contact with GC (Pietroso locality). The process of SGR led to nearly total replacement of former quartz porphyroclast. Here, some remnants of the host grain are still detectable in the central part of the aggregate (crossed polars; base of photo: 4mm).

(b) High-temperature solid-state fabric

In both the examples shown in section 3.3.4, quartz recrystallization was mainly achieved in the GBM field, as suggested by both microstructures and quartz LPO. However, some conspicuous differences exist between the two examples. In sample DSL92, quartz porphyroclasts exhibit chessboard SGB pattern (Fig.3.57c), indicating that part of the evolution of this tectonite (likely the older part) developed in the high-quartz field (Kruhl, 1996). Taking into account that the minimum pressure of the GC emplacement is around 4Kbar (chapter IV), a minimum temperature of $\sim 670^\circ$ can be proposed for the development of the described microstructures. On the other hand, the occurrence of recrystallized quartz displaying mosaic-like aggregates (Fig.3.57d), suggest that quartz recrystallization occurred at temperature close to the granite solidus (Gapais & Barbarin, 1986). These microstructures are in agreement with the observed quartz LPO, showing some evidence of [c]-slip activation (pole figure in Fig.3.57). These quartz features are comparable to those typical to the GBM II field as defined by Stipp et al. (2002). Thus, of the older part of the shearing history preserved in sample DSL92 likely occurred during (or immediately after) the complete crystallization of the pluton margin.

In sample z86, quartz microstructures are slightly different. In fact, neither evidences of chessboard pattern, nor indications of prismatic [c]-slip activation are visible in this sample. Instead, the observed strong Y maximum (in the quartz LPO, Fig.3.58) typifies the GBM I field of Stipp et al. (2002), which, at about 4kbar, is restricted in the $\sim 550-670^\circ$ temperature range. Thus, the quartz microstructures preserved in sample z86 could testify a transitional deformation stage between those represented by near solidus temperatures (sample DSL92) and those typical of the main solid-state fabric.

(c) Low-temperature solid-state fabric

Quartz microstructures in sample DSL95a (Fig.3.62 and 3.63) provide evidences of further cooling (or higher strain rates) with respect to the main solid-state fabric. In fact, the quartz grain size is $\sim 5-10\mu$ in the centre of the ultramylonite (Fig.3.63), whereas it is $\sim 20\mu$ along the shear zone boundaries. Here, microstructures in the locally preserved quartz porphyroclasts suggest that SGR is still the prevailing recrystallization mechanism. The observed quartz grain size and the extreme shear localization suggest that this shear zone likely developed in a transitional field between SGR and bulging recrystallization (BLG; Urai et al., 1986), namely at temperature close to 400°C or even less. Taking into account the observed fully plastic behaviour of quartz porphyroclasts, in this case the lower temperature limit could be placed at about 350°C .

3.3.6.2 Feldspars

(a) The main solid-state fabric

Within the main solid-state fabric, both plagioclase and K-feldspar porphyroclasts experienced dramatic grain size reduction, through both brittle fragmentation and recrystallization (Fig. 3.48 and 3.49). Kfs porphyroclasts exhibit patchy undulatory extinction (Fig. 3.49), suggesting the occurrence of widespread catalysis at sites of dislocation tangles (Tullis & Yund, 1987). Fragmented feldspar clasts were progressively rounded because of syntectonic recrystallization (Fig. 3.49), but they were not stretched, as slightly misoriented adjacent fragments may be virtually matched (i.e. see K-feldspar

fragments in Fig. 3.48). The margins of feldspar porphyroclasts are finely serrate. In K-feldspar, microstructures resembling subgrains are optically detectable (black arrowhead in Fig. 3.66). However, the occurrence of irregularly shaped subgrains (yellow arrowhead in Fig. 3.66) and the observed limited feldspar ductility (as revealed by microscopic cataclastic flow and patchy undulatory extinction) suggests that they likely represent sites of submicroscopic lattice failure rather than true subgrains (Tullis & Yund, 1987).

Within the mantles of fine-grained feldspar aggregates, the uniform grain size, the strong LPO, the polygonal outline and the convex shape against the host grain suggest that we are actually dealing with syntectonic recrystallized grains, rather than annealed fragments (Tullis & Yund, 1987). Here, feldspar newgrains are commonly small (2-15 μ , e.g. Fig. 3.49), showing nearly equidimensional shape. Newgrains are mainly made up of albite (surrounding plagioclase porphyroclasts) and albite +K-feldspar (around Kfs porphyroclasts). The occurrence of high-angle boundary migration in feldspars is testified by the commonly serrate grain boundaries. The very gradational transition zone at the porphyroclast margins (in both Kfs and plagioclase, Fig.3.66 and 3.67, respectively) might suggest that, within the main solid-state fabric, a large contribute of bulging recrystallization (Fitzgerald & Stünitz, 1993) can be supposed. The “classical” nucleation-and-growth mechanism (Tullis & Yund, 1991) likely dominates at lower temperature (section 3.3.5), where feldspar newgrains are represented by albite.

The observed strong LPO of feldspar newgrains (as qualitatively checked with the gypsum plate; Fig. 3.49) suggest that the contribution of grain boundary sliding (e.g. Boullier & Gueguen, 1975; Fitzgerald and Stünitz, 1993) was likely limited (or absent) in the moderately deformed domains. Instead, the very weak LPO in the fine-grained (~1-10 μ) aggregate of nearly equidimensional grains of albite, K-feldspar and quartz (Fig.3.52 and 3.54), might suggests that grain-sensitive granular flow (perhaps partly driven by chemical disequilibrium in feldspars, Stünitz & Fitzgerald, 1993) played a role in the deformation, at least in the ultramylonite domains. As a whole, feldspar microstructures indicate that the main foliation along the “mylonitic rim” developed in the ~400-500°C temperature range (as summarized by Passchier & Trouw, 1996).

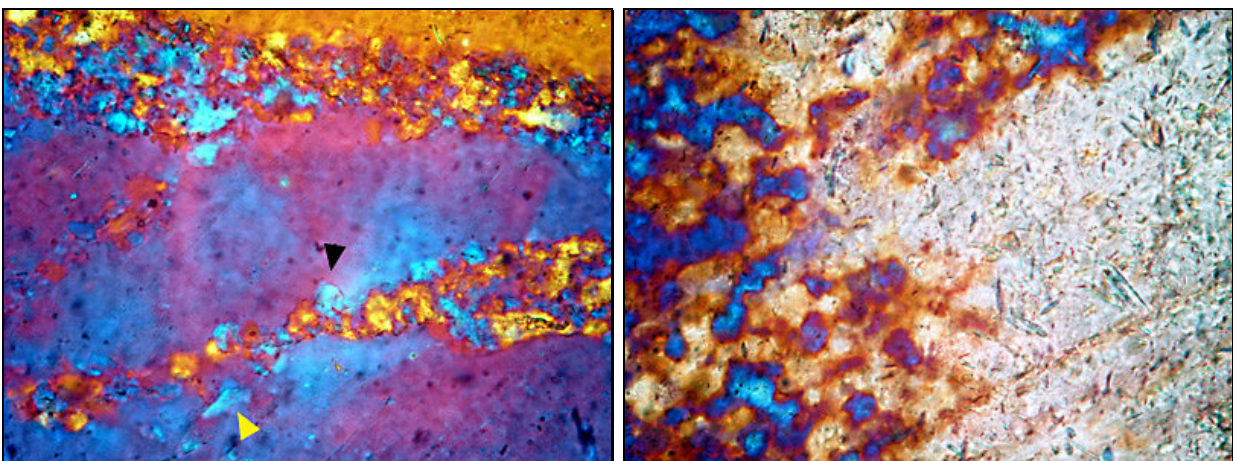


Fig. 3.66 (upper left): detail of a micro-scale shear zone transecting the core of Kfs porphyroclast. Well-rounded SGBs (black arrowhead), but also irregularly shaped SGBs (yellow arrowhead) are associated with patchy undulatory extinction (crossed polars; gypsum plate inserted; base of photo: 250 μ). **Fig. 3.67** (upper right): gradational boundary between Pl porphyroclast and recrystallized grains in the mantle (crossed polars; gypsum plate inserted; base of photo: 250 μ).

(b) High-temperature solid-state fabric.

The peculiar feldspar microstructures from sample DSL92 have been already described in section 3.3.4. The deformation features in sample Z86 do not differ substantially from those described in the case of meta-leucogranites belonging to the roof of the Mafic Complex (chapter II). In sample z86, recrystallized grains are relatively coarse-grained in both K-feldspar and plagioclase (Fig.3.60) and lobate grain boundaries are very common within the recrystallized aggregates. Moreover, in the periphery of porphyroclasts, some subgrains with comparable grain size of recrystallized grains are commonly detectable. These observations suggest that subgrain rotation might contribute to recrystallization (i.e. in the recovery-accommodated dislocation creep regime; Tullis & Yund, 1985). The minimum temperature for subgrain formation in feldspars is $\sim 550^{\circ}\text{C}$ (Pryer, 1993), whereas SGR recrystallization should become dominant at $T > \sim 650^{\circ}$ (Yund & Tullis, 1991; Rosenberg & Stünitz, 2003). Furthermore, the switch toward dominant SGR might be partly related to strain increase (Ji & Mainprice, 1990).

The coarse suturing between plagioclase porphyroclasts (Fig.3.59) could testify the occurrence of deformation at very high temperature, in the crystal mush or during the early stage of solid-state deformation (see the striking similarities with Fig.3 in Kruhl, 2005).

3.4 The effect of superposed quartz fabrics: comparison with other case studies

As described previously, the quartz fabric developed along the “mylonitic rim” is superimposed on an earlier fabric inherited from the late-magmatic history. This kind of polyphase fabric evolution is described by several authors. Simpson (1980) studied the example of Maggia nappe (Central Alps) where the pre-Alpine fabric exhibits some maxima around the X position. Simpson (1980) shown that the shearing due to Alpine-age mylonitization produced a single girdle fabric at high angle from the foliation, where the pre-existing fabric was nearly erased also in the domains affected by weak superimposed shearing. These results fits with the data exposed here, as the low-strain samples from the inner part of the “mylonitic rim” show that no magmatic fabric survived the solid-state overprint, even in the low-strain domains. Analogous sequence of superposed fabric related to distinct tectonic events is reported by Cavalcanti de Araújo et al. (2003).

In our case, however, more interesting are such cases where superimposed fabric occurred during progressive deformation within a single tectonic event, such as pluton emplacement and subsequent (syndeformational) cooling. At this regard, Blumenfeld et al. (1986) studied a thrust pile in Hercynian Vosges, which range from migmatites to granite. The preserved fabric exhibits a gradual transition from fabric developed by magmatic flow (in the nappe core), toward fabric developed under solid-state conditions (near the thrust sole). Kinematic analysis demonstrates that the whole fabric progressively developed within a single tectonic event. Blumenfeld et al. (1986) identified three main microstructural classes (defining magmatic, submagmatic and solid-state microfabric). These classes are broadly comparable with F_1 , F_2 - F_3 and the solid-state fabric described

here (respectively). From magmatic to solid-state stage the microstructural evolution proposed by Blumenfeld et al. (1986) document a fabric transition from dominant prismatic [c] slip to dominant prismatic <a> slip, which is very similar to those described here. As described by Simpson (1980) no high-temperature fabric outlived the solid-state overprint in the Hercynian Vosges granite-migmatite thrust pile. According to Blumenfeld et al. (1986), small increments of finite strain under conditions suitable for dominant <a> slip are enough to replace the former high-temperature fabric. This observation may explain why clear [c] slip fabrics are uncommon in nature.

Analogous geological framework is proposed by Gapais & Barbarin (1986), in the case Hermitage granite, which is considered as a syntectonic pluton emplaced along an active transcurrent shear zone. The authors shown that the [c] - <a> fabric transition occurred in coincidence with the transition in quartz recrystallization mechanism, from dominant GBM to dominant SGR. Such a transition is macroscopically reflected by a switch from homogeneous foliated granite to S-C orthogneiss along the pluton margin. According to Gapais & Barbarin (1986), this evolution should be typical of granitic bodies emplaced at mid crustal levels (i.e. under amphibolite-facies conditions), where the rapid cooling along the pluton margin and the high strain rates imposed by an active shear zone involves a sharp transition from "stable" to "unstable" flow. According to what exposed in this chapter, the S. Lucia granitic complex exhibits several striking similarities with the case study described by Gapais & Barbarin (1986). A further discussion on this topic will be proposed in chapter V.

4 MINERAL CHEMISTRY AND GEOCHRONOLOGY

This chapter shows the results from preliminary geochronological and mineral-chemistry investigations. In the first part, the representative electron microprobe analyses are shown, together with the obtained structural formulas. The second part deals with P-T estimation, based on some commonly used geothermobarometers. Additional sections are dedicated to the whole-rock chemical analysis from undeformed dolerite veins (which intruded Mafic Complex) and geochronological investigations on Ms-bearing pegmatite (Granitic Complex).

Mineral chemistry data

Mineral analyses were carried out with the assistance of A. Montanini at Dipartimento di Scienze della Terra of Università di Parma using a JEOL-6400 electron microprobe equipped with LINK-ISIS energy-dispersive microanalytic system. Operating conditions were accelerating voltage of 15 kV and probe current of 0.25 nA, a spot diameter of 1-2 μ and counting time of 100 s. Both natural minerals and synthetic compounds were used as standards.

4.1.2 Mineral chemistry from S. Lucia basement; introduction

In this section, mineral chemistry data obtained from several terms of S. Lucia basement are shown. Mineral chemistry investigations were performed with some detail by Libourel (1985), but only in the lower portion of Mafic Complex (Units I and II, Grt-bearing gneisses). During this work, one sample from garnet-bearing gneisses has been analyzed, in order to check the data from Libourel (1985), with the assistance of recent thermobarometrical methods (e.g. TWEEQU, Berman, 1991). Moreover, some granitoid samples from granite-diorite suite (DGS) and from adjacent Granitic Complex (GC) has been investigated, in order to estimate the P/T condition which were prevailing during emplacement.

4.1.3 The lower part of MC: Grt-bearing gneisses

The selected sample was collected from a boulder around Pedimaio locality (see sample map for location), where pre-Alpine assemblages within metasedimentary rocks are locally well preserved (Libourel, 1985). Sample Zx is a mylonitic gneiss (embedded within Unit II) containing garnet, orthopyroxene and plagioclase porphyroclasts, in a matrix of syntectonically recrystallized Opx^{II}, Pl^{II}, Bt and Qtz. Microfabric from this sample are comparable to those described in chapter II: garnet is weakly-deformed, whereas Opx porphyroclasts show evidences of plastic deformation (i.e. sweeping undulose extinction, development of ribbon grains) and core-and-mantle microstructure. Plagioclase is nearly completely recrystallized, developing granoblastic aggregates with a mean grain size of ~100 μ . Quartz develops polycrystalline ribbons (comparable to type 3 ribbons of Boullier & Bouchez, 1978), chessboard SGB pattern locally occurs in few ribbon-forming grains.

This sample is comparable with the “paragneisses with primary Opx” as described in Libourel (1985).

Biotite

All the analyzed biotite derives from the syntectonic D₂ assemblage, from the tails around Opx and Grt porphyroclasts. According to Libourel, the occurrence of biotite marks the onset of retrograde hydration, under granulite facies conditions. This is in agreement with the occurrence of Opx^{II} (together with Bt) in the mantle surrounding Opx^I porphyroclasts.

Orthopyroxene

Opx porphyroclasts (Opx^I) and recrystallized grains (Opx^{II}) have been analyzed in sample Zx. In both cases, the composition clusters around En₅₅, being analogous to what reported by Libourel (1985) for the paragneisses with primary Opx.

Plagioclase

Plagioclase porphyroclasts are rather calcic in composition, exhibiting anorthite contents between An₅₀ and An₅₅. Plagioclase recrystallized grains exhibit analogous composition (tab.4.3). No compositional zoning occurs in the investigated sample. Plagioclases analyzed by Libourel (1985) show analogous composition (for terms with primary Opx) whereas, within Grt-bearing gneisses with secondary Opx, plagioclase composition clusters around An₃₅. According to the author, the higher An content in the first group of gneisses could be related to higher Ca contents in the whole-rock composition.

Garnet

The analyzed garnet porphyroclasts represent the remnants (together with Opx^I) of D₁ assemblage. These garnets are relatively rich in almandine (~58-63%) and pyrope (~27-30%), displaying low spessartine contents (~2%). As a whole, the data from this work are in agreement with those from Libourel (1985), indicating that the main difference between paragneisses with primary and secondary Opx is represented by the grossularia content, which is higher in the former type (Fig.4.1). The same trend is detectable from cores to rims of the garnets analyzed here (Fig.4.1). This mineral also exhibits a chemical zonation respect to Fe content (which increases toward the rim, tab.4.4).

Tab. 4-1: composition of biotite from the synkinematic matrix of sample Zx.

Complex Sample point	MC II Zx 5a	MC II Zx 7a	MC II Zx 7b
SiO ₂	36,86	36,19	36,20
TiO ₂	6,73	5,72	5,60
Al ₂ O ₃	14,35	14,86	14,61
Cr ₂ O ₃	0,06	0,29	0,09
Fe ₂ O ₃	0,00	0,00	0,00
FeO	14,43	16,00	15,76
MnO	0,21	0,15	0,29
MgO	12,29	12,66	12,29
CaO	0,02	0,06	0,00
Na ₂ O	0,00	0,00	0,00
K ₂ O	10,18	9,96	10,05
Li ₂ O	0,00	0,00	0,00
Rb ₂ O	0,00	0,00	0,00
SrO	0,00	0,00	0,00
Cs ₂ O	0,00	0,00	0,00
BaO	0,00	0,00	0,00
F ⁻	1,93	1,59	1,64
Cl ⁻	0,22	0,12	0,14
Total	96,42	96,90	95,95
	26,93	28,81	28,34
Si	2,71	2,67	2,70
Ti	0,37	0,32	0,31
Al	1,24	1,29	1,28
Cr	0,00	0,02	0,01
Fe ³⁺	0,00	0,00	0,00
Fe ²⁺	0,89	0,99	0,98
Mn	0,01	0,01	0,02
Mg	1,35	1,39	1,37
Ca	0,00	0,01	0,00
Na	0,00	0,00	0,00
K	0,96	0,94	0,96
Li	0,00	0,00	0,00
Rb	0,00	0,00	0,00
Sr	0,00	0,00	0,00
Cs	0,00	0,00	0,00
Ba	0,00	0,00	0,00
F ⁻	0,45	0,37	0,39
Cl ⁻	0,03	0,02	0,02
total	8,01	8,02	8,02

Tab. 4-2: chemical composition and structural formulas from orthopyroxene in sample Zx

Complex Sample point	MC II Zx 5d	MC II Zx 7a	MC II Zx 7b	MC II Zx 8a	MC II Zx 8b	MC II Zx 8c	MC II Zx 5a	MC II Zx 5b	MC II Zx 7c	MC II Zx 5c	MC II Zx 7d
	Opx I	Opx I	Opx I	Opx I	Opx II						
SiO ₂	50,04	50,06	50,91	50,14	50,52	50,70	49,54	50,16	50,30	49,93	49,47
TiO ₂	0,00	0,00	0,00	0,14	0,00	0,00	0,24	0,00	0,42	0,00	0,29
Al ₂ O ₃	2,74	2,94	3,43	2,50	2,70	3,37	2,86	3,33	2,90	2,99	3,09
Cr ₂ O ₃	0,00	0,28	0,00	0,02	0,00	0,24	0,31	0,00	0,06	0,00	0,00
FeO	28,49	28,22	27,66	28,62	28,76	28,00	27,44	27,53	27,11	28,38	26,45
MnO	0,65	0,37	0,56	0,74	0,55	0,50	0,41	0,44	0,76	0,41	0,41
MgO	18,36	18,18	18,41	17,45	17,73	17,77	17,38	17,68	18,04	18,03	18,16
CaO	0,24	0,53	0,26	0,30	0,25	0,27	0,13	0,29	0,31	0,14	0,14
Na ₂ O	0,00	0,00	0,00	0,00	0,00	0,00	0,00	0,00	0,00	0,00	0,00
Total	100,52	100,58	101,23	99,91	100,51	100,85	98,31	99,43	99,90	99,88	98,01
numbers of cations on the basis of 6 oxygens											
Si	1,901	1,901	1,916	1,927	1,926	1,922	1,928	1,926	1,923	1,910	1,921
Al ^{IV}	0,099	0,099	0,084	0,073	0,074	0,078	0,072	0,074	0,077	0,090	0,079
Al ^{VI}	0,024	0,033	0,068	0,040	0,047	0,073	0,059	0,077	0,053	0,045	0,062
Fe ²⁺	0,831	0,838	0,855	0,895	0,890	0,888	0,893	0,884	0,867	0,863	0,859
Mg	1,040	1,029	1,033	1,000	1,008	1,004	1,008	1,012	1,028	1,028	1,051
Mn	0,021	0,012	0,018	0,024	0,018	0,016	0,014	0,014	0,025	0,013	0,013
Ti	0,000	0,000	0,000	0,004	0,000	0,000	0,007	0,000	0,012	0,000	0,008
Cr	0,000	0,008	0,000	0,001	0,000	0,007	0,010	0,000	0,002	0,000	0,000
Ca	0,010	0,022	0,010	0,012	0,010	0,011	0,005	0,012	0,013	0,006	0,006
Na	0,000	0,000	0,000	0,000	0,000	0,000	0,000	0,000	0,000	0,000	0,000
Wo	0,52	1,14	0,55	0,65	0,54	0,58	0,28	0,63	0,67	0,30	0,30
En	55,31	54,48	54,42	52,43	52,81	52,77	52,88	53,04	53,90	54,21	54,87
Fs	44,17	44,38	45,03	46,92	46,66	46,65	46,84	46,33	45,44	45,49	44,83

Tab. 4-3: chemical composition and structural formula of plagioclase from sample Zx.

Complex Sample point	MC II Zx 5a PI II	MC II Zx 7a PI I	MC II Zx 8a PI I	MC II Zx 8b PI I
SiO ₂	55,10	54,70	53,35	54,43
TiO ₂	0,00	0,00	0,00	0,00
Al ₂ O ₃	28,19	28,15	26,00	26,52
Cr ₂ O ₃	0,00	0,06	0,14	0,18
Fe ₂ O ₃	0,00	0,00	0,00	0,00
FeO	0,20	0,00	0,78	0,11
MnO	0,00	0,12	0,12	0,00
MgO	0,03	0,18	0,00	0,00
CaO	10,92	10,61	13,17	12,92
Na ₂ O	5,53	5,16	5,21	5,29
K ₂ O	0,49	0,48	0,28	0,11
Li ₂ O	0,00	0,00	0,00	0,00
Rb ₂ O	0,00	0,00	0,00	0,00
SrO	0,00	0,00	0,00	0,00
Cs ₂ O	0,00	0,00	0,00	0,00
BaO	0,00	0,00	0,00	0,00
Total	100,46	99,46	99,05	99,56
numbers of cations on the basis of 8 oxygens				
Si	2,48	2,48	2,47	2,49
Ti	0,00	0,00	0,00	0,00
Al	1,50	1,51	1,42	1,43
Cr	0,00	0,00	0,01	0,01
Fe ³⁺	0,00	0,00	0,00	0,00
Fe ²⁺	0,01	0,00	0,03	0,00
Mn	0,00	0,01	0,01	0,00
Mg	0,00	0,01	0,00	0,00
Ca	0,53	0,52	0,65	0,63
Na	0,48	0,45	0,47	0,47
K	0,03	0,03	0,02	0,01
Li	0,00	0,00	0,00	0,00
Rb	0,00	0,00	0,00	0,00
Sr	0,00	0,00	0,00	0,00
Cs	0,00	0,00	0,00	0,00
Ba	0,00	0,00	0,00	0,00
Total	5,03	5,01	5,06	5,03
Anorthite	50,30	50,85	55,72	56,89
Albite	46,10	44,75	39,89	42,15
Orthoclase	2,69	2,74	1,41	0,58

complex	MC II Zx 5° core	MC II Zx 5b core	MC II Zx 5c int	MC II Zx 8° core	MC II Zx 8b int	MC II Zx 5d rim	MC II Zx 5e rim	MC II Zx 8c rim
SiO ₂	39,12	38,73	38,71	39,17	38,92	38,55	38,73	38,79
TiO ₂	0,07	0,14	0,00	0,00	0,00	0,00	0,00	0,00
Al ₂ O ₃	21,38	21,83	21,76	21,50	22,25	21,46	21,93	22,57
Cr ₂ O ₃	0,00	0,03	0,00	0,00	0,04	0,15	0,01	0,00
Fe ₂ O ₃	1,05	0,00	0,28	0,80	0,00	0,17	0,26	0,00
FeO	27,13	27,38	28,19	27,01	28,30	28,87	28,89	28,32
MnO	1,32	1,12	1,56	1,12	1,32	1,72	1,66	1,44
MgO	7,42	7,28	6,96	7,48	7,14	6,81	7,59	7,64
CaO	3,78	3,50	3,25	3,46	3,52	1,93	1,92	1,94
Na ₂ O	0,00	0,00	0,00	0,00	0,00	0,00	0,00	0,00
Total	101,28	100,01	100,72	100,54	101,49	99,66	100,99	100,70
numbers of cations on the basis of 12 oxygens								
Si	3,00	3,00	3,00	3,02	2,99	3,02	2,99	2,99
Ti	0,00	0,01	0,00	0,00	0,00	0,00	0,00	0,00
Al	1,94	2,00	1,99	1,95	2,01	1,98	2,00	2,05
Cr	0,00	0,00	0,00	0,00	0,00	0,01	0,00	0,00
Fe ³⁺	0,06	0,00	0,02	0,05	0,00	0,01	0,02	0,00
Fe ²⁺	1,74	1,78	1,83	1,74	1,82	1,89	1,87	1,82
Mn	0,09	0,07	0,10	0,07	0,09	0,11	0,11	0,09
Mg	0,85	0,84	0,80	0,86	0,82	0,80	0,87	0,88
Ca	0,31	0,29	0,27	0,29	0,29	0,16	0,16	0,16
Na	0,00	0,00	0,00	0,00	0,00	0,00	0,00	0,00
Total	7,99	7,99	8,00	7,98	8,01	7,98	8,01	7,99
Pyrope	28,42	28,23	26,80	29,04	27,35	26,84	29,21	29,68
Almandine	58,30	59,55	60,91	58,83	60,81	63,84	62,38	61,72
Grossular	7,36	9,66	8,17	7,30	9,56	4,49	4,53	5,42
Spessartine	2,87	2,47	3,29	2,47	2,16	3,85	3,10	3,18
Uvarovite	0,00	0,09	0,00	0,00	0,12	0,47	0,03	0,00
Andradite	3,05	0,00	0,83	2,35	0,01	0,50	0,75	0,00

Tab. 4-4: composition and structural formula of garnet from sample Zx.

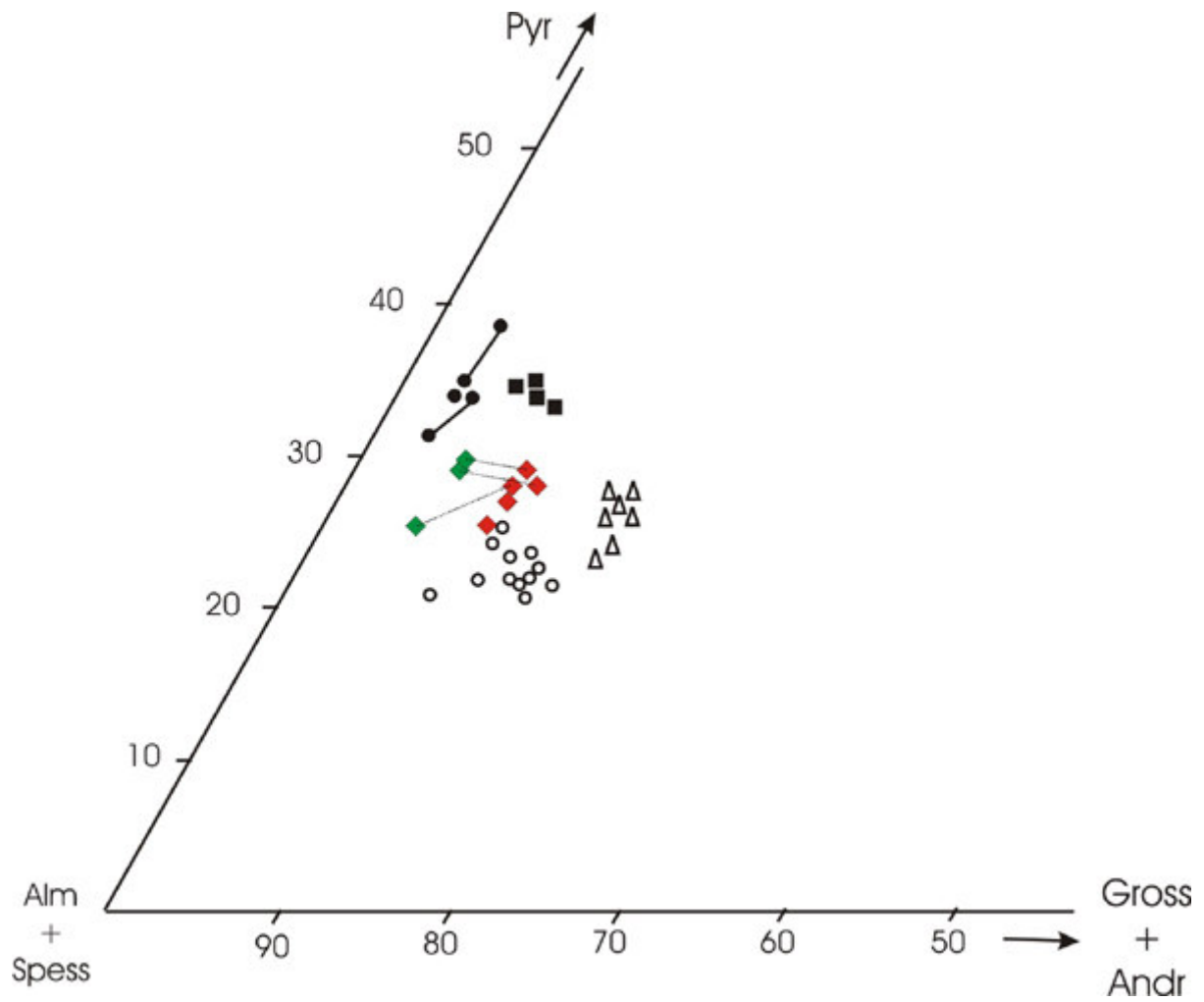


Fig. 4.1: garnet composition from sample Zx. Red diamonds: core; green diamonds: rim. Black symbols are from Libourel (1985). Triangles: Grt from layered gabbros; empty circles: Grt at the interfaces gabbro-paragneisses; full circles: Grt from Opx-free paragneisses; squares: Grt from paragneisses with primary Opx. Slightly modified after Libourel (1985).

Hbl-bearing granitoids from DGS and GC

Mineral chemistry investigations have been carried on in various granitoids from the roof of mafic complex (DG suite), and from Granitic Complex. The main purpose of this group of analysis is the estimation of P-T conditions that were prevailing during granitoids emplacement. Thus, during this work the analysis were focussed on mineral phases of magmatic origin. As the "Al in Hbl" (Hammarstrom & Zen, 1986) barometer has been used, amphibole represents the most investigated mineral phases. All the Hbl-bearing investigated samples display nearly tonalitic composition. In order to facilitate the comparison of different chemical analyses, Hbl-bearing granitoids from both DGS and GS are treated together.

Amphibole

The composition of amphiboles from different samples is graphically shown in Fig.4.5 to 4.9, where the SiO₂ content is plotted against Na₂O, TiO₂, Mg#, MnO, CaO, Al₂O₃. Hornblende commonly does not show clear compositional zoning from core to rim. The compositions of amphibole were normalized to 13 cations, because this procedure provides the best estimation of Fe²⁺ and Fe³⁺ (Cosca et al., 1991).

complex	DGS z200 1a	DGS z200 1b	DGS z200 1c	DGS z200 1d	DGS z200 5a	DGS z200 2b	DGS SSL2 1a(*)	DGS SSL2 b (*)	DGS SSL2 4a	DGS SSL2 6a	DGS SSL2 6b	DGS SSL2 6c	DGS SSL2 1a
SiO ₂	43,86	42,68	46,38	45,07	43,22	42,29	42,50	40,93	40,37	42,17	41,73	41,59	42,19
Al ₂ O ₃	9,76	11,11	8,09	8,61	11,35	11,05	10,23	11,42	11,37	10,91	11,17	11,51	11,23
TiO ₂	1,22	1,42	1,15	1,18	1,79	1,71	2,21	1,94	1,76	2,17	1,77	1,64	1,46
MgO	11,66	10,48	12,34	11,34	10,31	10,20	6,96	7,10	5,90	7,87	7,38	8,41	7,62
FeO	15,61	16,97	15,47	16,06	17,20	16,81	20,46	20,09	23,00	19,77	20,73	19,66	20,71
MnO	0,35	0,48	0,37	0,53	0,42	0,38	0,32	0,27	0,72	0,22	0,18	0,23	0,79
CaO	11,14	11,22	11,51	11,28	11,22	11,21	11,35	10,77	11,43	11,39	11,47	11,46	11,30
Na ₂ O	1,13	1,06	0,51	0,59	1,28	1,17	0,98	1,13	1,14	0,89	1,04	1,06	0,99
K ₂ O	1,11	1,22	0,79	0,81	1,36	1,34	1,89	2,13	1,94	2,05	1,98	1,82	1,29
Total	95,84	96,64	96,61	95,47	98,15	96,16	96,90	95,78	97,63	97,44	97,45	97,38	97,58
Numbers of cations on the basis of 23 oxygens													
Si	6,55	6,37	6,84	6,75	6,38	6,38	6,58	6,38	6,27	6,44	6,40	6,32	6,39
Al ^{IV}	1,45	1,63	1,16	1,25	1,62	1,62	1,42	1,63	1,73	1,56	1,60	1,68	1,61
AlTot	1,72	1,96	1,41	1,52	1,98	1,96	1,87	2,10	2,08	1,96	2,02	2,06	2,00
Al ^{VI}	0,27	0,33	0,24	0,27	0,36	0,34	0,45	0,47	0,35	0,41	0,42	0,38	0,39
Ti	0,14	0,16	0,13	0,13	0,20	0,19	0,26	0,23	0,21	0,25	0,20	0,19	0,17
Fe ³⁺	0,80	0,85	0,66	0,73	0,69	0,67	0,03	0,34	0,44	0,27	0,30	0,53	0,68
Mg	2,60	2,33	2,71	2,53	2,27	2,29	1,61	1,65	1,37	1,79	1,69	1,91	1,72
Fe ²⁺	1,15	1,27	1,25	1,29	1,43	1,45	2,62	2,28	2,54	2,26	2,37	1,97	1,94
Mn	0,04	0,06	0,05	0,07	0,05	0,05	0,04	0,04	0,10	0,03	0,02	0,03	0,10
Ca	1,78	1,80	1,82	1,81	1,78	1,81	1,88	1,80	1,90	1,86	1,89	1,87	1,83
Na M4	0,22	0,21	0,15	0,17	0,23	0,19	0,12	0,20	0,10	0,14	0,11	0,13	0,17
NaTot	0,33	0,31	0,15	0,17	0,37	0,34	0,29	0,34	0,34	0,26	0,31	0,31	0,29
Na-A	0,11	0,10	0,00	0,00	0,14	0,15	0,18	0,14	0,24	0,13	0,20	0,18	0,12
K	0,21	0,23	0,15	0,16	0,26	0,26	0,37	0,42	0,38	0,40	0,39	0,35	0,25
Sum-A	0,32	0,33	0,15	0,16	0,40	0,41	0,55	0,56	0,63	0,53	0,58	0,53	0,37
Fe/(Fe+Mg)	0,31	0,35	0,31	0,34	0,39	0,39	0,62	0,58	0,65	0,56	0,58	0,51	0,53

Tab. 4-5: Representative electron microprobe analyses of amphibole from granitoids in this study. (*) is for analyses on amphibole rims.

complex sample point	DGS Z4 1b (*)	DGS Z4 1c	DGS Z4 1d (*)	DGS Z4 2a	DGS Z4 2b	DGS Z4 2c (*)	DGS Z4 4a	DGS Z4 4b	DGS Z4 4c (*)	DGS z4 1e	DGS z4 1f	DGS z4 1g	DGS z79b 2a
Actinolite													
SiO ₂	42,90	43,07	45,50	41,99	41,59	43,92	53,40	44,45	43,81	41,29	41,73	41,03	42,61
Al ₂ O ₃	10,63	9,20	9,20	12,11	12,21	10,49	2,49	9,91	10,25	12,05	12,38	12,56	10,49
TiO ₂	1,62	1,34	0,59	0,96	0,67	0,65	0,08	0,97	1,03	1,42	0,71	0,94	2,19
MgO	8,26	8,65	9,70	7,86	7,58	8,84	15,49	9,26	9,54	7,64	7,73	7,65	8,06
FeO	20,40	20,32	19,89	20,15	20,52	20,17	13,13	19,83	18,99	20,86	19,57	20,59	19,12
MnO	0,81	0,80	0,84	0,70	0,58	0,57	0,50	0,68	0,80	0,73	0,65	0,81	0,27
CaO	11,71	11,89	11,60	11,45	11,61	11,53	12,11	11,63	11,30	11,56	11,60	11,40	10,82
Na ₂ O	0,96	0,88	0,98	1,11	0,85	0,89	0,00	0,93	1,19	1,02	0,92	0,87	1,83
K ₂ O	1,28	1,25	0,84	1,44	1,33	1,19	0,28	1,19	1,13	1,55	1,49	1,64	1,50
Total	98,57	97,40	99,14	97,77	96,94	98,25	97,48	98,85	98,04	98,12	96,78	97,49	96,89
Numbers of cations on the basis of 23 oxygens													
Si	6,43	6,55	6,68	6,34	6,33	6,54	7,71	6,58	6,51	6,24	6,36	6,21	6,53
Al ^{IV}	1,57	1,45	1,32	1,66	1,67	1,46	0,29	1,42	1,49	1,76	1,64	1,79	1,47
AlTot	1,88	1,65	1,59	2,15	2,19	1,84	0,42	1,73	1,80	2,15	2,22	2,24	1,89
Al ^{VI}	0,31	0,20	0,27	0,49	0,52	0,38	0,14	0,31	0,31	0,39	0,58	0,46	0,42
Ti	0,18	0,15	0,07	0,11	0,08	0,07	0,01	0,11	0,12	0,16	0,08	0,11	0,25
Fe ³⁺	0,61	0,57	0,84	0,65	0,71	0,77	0,08	0,72	0,79	0,71	0,54	0,85	0,16
Mg	1,85	1,96	2,12	1,77	1,72	1,96	3,34	2,04	2,11	1,72	1,76	1,73	1,84
Fe ²⁺	1,95	2,02	1,60	1,89	1,91	1,74	1,50	1,74	1,57	1,93	1,95	1,76	2,29
Mn	0,10	0,10	0,10	0,09	0,08	0,07	0,06	0,09	0,10	0,09	0,08	0,10	0,04
Ca	1,88	1,94	1,82	1,85	1,89	1,84	1,87	1,84	1,80	1,87	1,89	1,85	1,78
Na M4	0,12	0,06	0,18	0,15	0,11	0,16	0,00	0,16	0,20	0,13	0,11	0,15	0,22
NaTot	0,28	0,26	0,28	0,33	0,25	0,26	0,00	0,27	0,34	0,30	0,27	0,26	0,54
Na-A	0,16	0,20	0,10	0,18	0,14	0,10	0,00	0,11	0,14	0,17	0,17	0,11	0,32
K	0,25	0,24	0,16	0,28	0,26	0,23	0,05	0,23	0,21	0,30	0,29	0,32	0,29
Sum-A	0,41	0,44	0,26	0,45	0,40	0,32	0,05	0,34	0,36	0,47	0,46	0,42	0,61
Fe/(Fe+Mg)	0,51	0,51	0,43	0,52	0,53	0,47	0,31	0,46	0,43	0,53	0,53	0,50	0,55

Tab.4.5 (cont.)

complex sample point	DGS z79b 2b	DGS z79b 4a (*)	DGS z79b 3a	DGS z79b 3b	DGS z79b 5a	DGS z79b 5b	GC z73 1a	GC z73 1b	GC z73 1c (*)	GC z73 6a	GC z73 2a	GC z73 2b	GC z73 1d
SiO ₂	42,65	42,19	41,56	43,72	41,46	44,53	42,09	42,15	42,06	42,98	41,72	43,30	42,74
Al ₂ O ₃	10,71	10,96	10,29	11,15	10,62	10,85	10,59	10,98	10,42	9,77	10,26	9,11	10,52
TiO ₂	2,19	1,89	2,02	2,22	1,98	1,75	1,18	1,34	1,06	1,37	1,55	1,41	1,09
MgO	7,96	8,00	7,98	8,77	8,25	9,14	8,02	8,38	8,12	8,62	8,53	8,65	7,70
FeO	18,91	19,21	18,76	18,07	19,69	18,55	20,16	20,48	21,53	20,27	20,45	20,76	20,91
MnO	0,52	0,47	0,39	0,45	0,45	0,34	0,58	0,45	0,50	0,67	0,59	0,61	0,59
CaO	10,97	11,13	10,67	10,90	10,74	11,68	11,51	11,39	11,59	11,40	11,13	11,39	11,34
Na ₂ O	1,82	1,85	1,65	1,32	1,16	1,01	1,08	1,17	0,95	1,22	1,12	1,05	0,90
K ₂ O	1,80	1,72	1,49	1,62	1,46	1,60	1,43	1,50	1,48	1,37	1,31	1,34	1,47
Total	97,53	97,42	94,81	98,22	95,81	99,45	96,64	97,84	97,71	97,67	96,66	97,62	97,26
Numbers of cations on the basis of 23 oxygens													
Si	6,52	6,46	6,50	6,53	6,37	6,57	6,46	6,36	6,38	6,51	6,36	6,56	6,50
Al ^{IV}	1,48	1,54	1,50	1,47	1,63	1,43	1,55	1,64	1,62	1,50	1,64	1,45	1,50
Al ^{Tot}	1,93	1,98	1,90	1,96	1,92	1,89	1,91	1,95	1,86	1,74	1,84	1,63	1,89
Al ^{VI}	0,45	0,44	0,40	0,49	0,29	0,46	0,37	0,32	0,25	0,25	0,20	0,18	0,39
Ti	0,25	0,22	0,24	0,25	0,23	0,19	0,14	0,15	0,12	0,16	0,18	0,16	0,13
Fe ³⁺	0,04	0,13	0,26	0,31	0,71	0,29	0,52	0,70	0,80	0,62	0,86	0,68	0,61
Mg	1,81	1,83	1,86	1,95	1,89	2,01	1,83	1,89	1,84	1,95	1,94	1,95	1,75
Fe ²⁺	2,37	2,33	2,20	1,94	1,82	2,00	2,07	1,89	1,94	1,95	1,74	1,95	2,06
Mn	0,07	0,06	0,05	0,06	0,06	0,04	0,08	0,06	0,06	0,09	0,08	0,08	0,08
Ca	1,80	1,83	1,79	1,74	1,77	1,85	1,89	1,84	1,88	1,85	1,82	1,85	1,85
Na M4	0,20	0,17	0,21	0,26	0,23	0,15	0,11	0,16	0,12	0,15	0,18	0,15	0,15
Na ^{Tot}	0,54	0,55	0,50	0,38	0,35	0,29	0,32	0,34	0,28	0,36	0,33	0,31	0,27
Na-A	0,34	0,38	0,29	0,13	0,11	0,14	0,21	0,19	0,16	0,21	0,15	0,16	0,12
K	0,35	0,34	0,30	0,31	0,29	0,30	0,28	0,29	0,29	0,27	0,26	0,26	0,29
Sum-A	0,69	0,71	0,59	0,43	0,40	0,44	0,49	0,47	0,45	0,47	0,40	0,41	0,40
Fe/(Fe+Mg)	0,57	0,56	0,54	0,50	0,49	0,50	0,53	0,50	0,51	0,50	0,47	0,50	0,54

Tab.4.5

(cont.)

Complex sample point	GC z73 7a	GC z73 7b	GC z73 8a	GC z73 8b (*)	GC z73 8c	GC z73 8d	GC z73 8e (*)	GC z73 8f
SiO ₂	41,96	40,91	42,75	41,93	42,04	41,81	42,46	42,70
Al ₂ O ₃	10,92	10,85	9,33	10,51	10,06	10,31	10,72	9,38
TiO ₂	1,41	1,46	1,49	1,26	1,20	1,43	1,31	1,53
MgO	8,01	8,40	8,99	7,97	8,27	8,08	7,74	8,40
FeO	21,12	21,42	19,88	20,57	20,25	20,90	20,46	19,93
MnO	0,63	0,89	0,57	0,43	0,58	0,70	0,56	0,83
CaO	11,29	11,11	11,68	11,65	11,58	11,36	11,29	11,12
Na ₂ O	1,16	1,02	1,21	1,23	1,17	1,10	1,04	1,20
K ₂ O	1,58	1,53	1,29	1,47	1,35	1,43	1,42	1,21
Total	98,08	97,59	97,19	97,02	96,50	97,12	97,00	96,30

Numbers of cations on the basis of 23 oxygens

Si	6,34	6,19	6,51	6,44	6,46	6,38	6,48	6,55
Al ^{IV}	1,66	1,82	1,49	1,57	1,54	1,62	1,52	1,45
Al ^{Tot}	1,95	1,93	1,67	1,90	1,82	1,86	1,93	1,70
Al ^{VI}	0,29	0,12	0,18	0,34	0,29	0,24	0,41	0,24
Ti	0,16	0,17	0,17	0,15	0,14	0,16	0,15	0,18
Fe ³⁺	0,75	1,17	0,55	0,45	0,54	0,73	0,54	0,61
Mg	1,80	1,89	2,04	1,82	1,90	1,84	1,76	1,92
Fe ²⁺	1,92	1,54	1,99	2,19	2,06	1,94	2,07	1,94
Mn	0,08	0,11	0,07	0,06	0,08	0,09	0,07	0,11
Ca	1,83	1,80	1,91	1,92	1,91	1,86	1,85	1,83
Na M4	0,17	0,20	0,10	0,09	0,09	0,14	0,15	0,17
Na ^{Tot}	0,34	0,30	0,36	0,37	0,35	0,33	0,31	0,36
Na-A	0,17	0,10	0,26	0,28	0,26	0,18	0,15	0,18
K	0,31	0,30	0,25	0,29	0,27	0,28	0,28	0,24
Sum-A	0,47	0,39	0,51	0,57	0,52	0,46	0,43	0,42
Fe/(Fe+Mg)	0,52	0,45	0,49	0,55	0,52	0,51	0,54	0,50

Tab.4.5 (cont.)

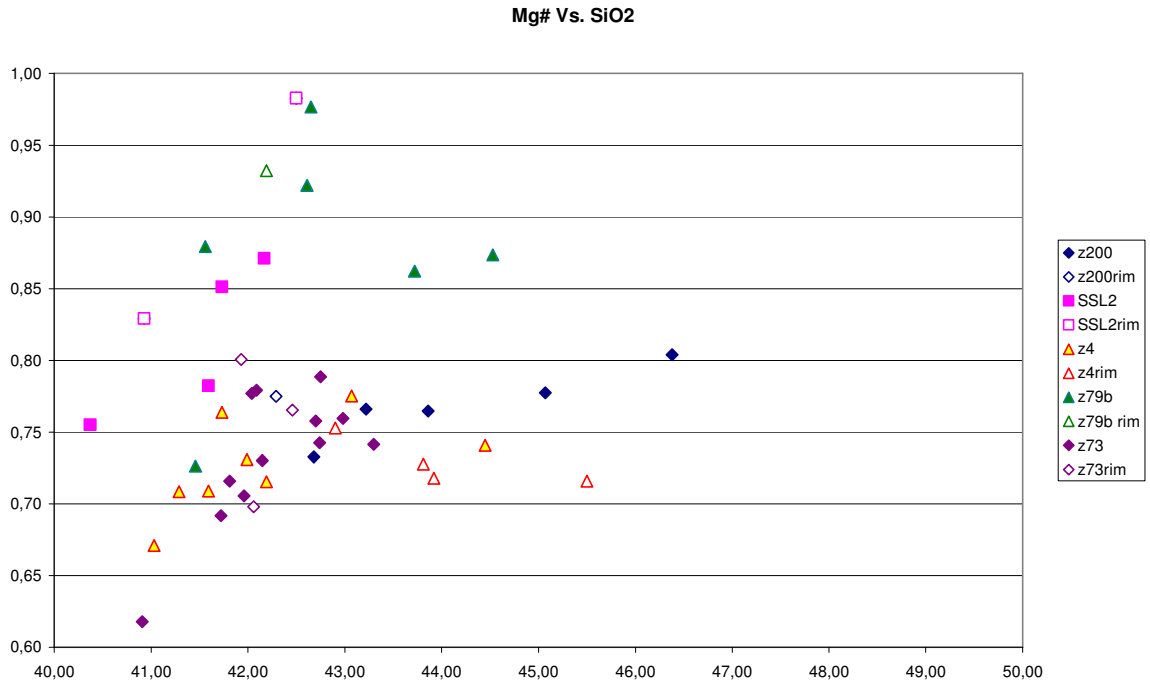


Fig. 4.4: SiO₂ vs. Mg# [MgO/(MgO+FeO)] contents from the Hbl-bearing investigated samples.

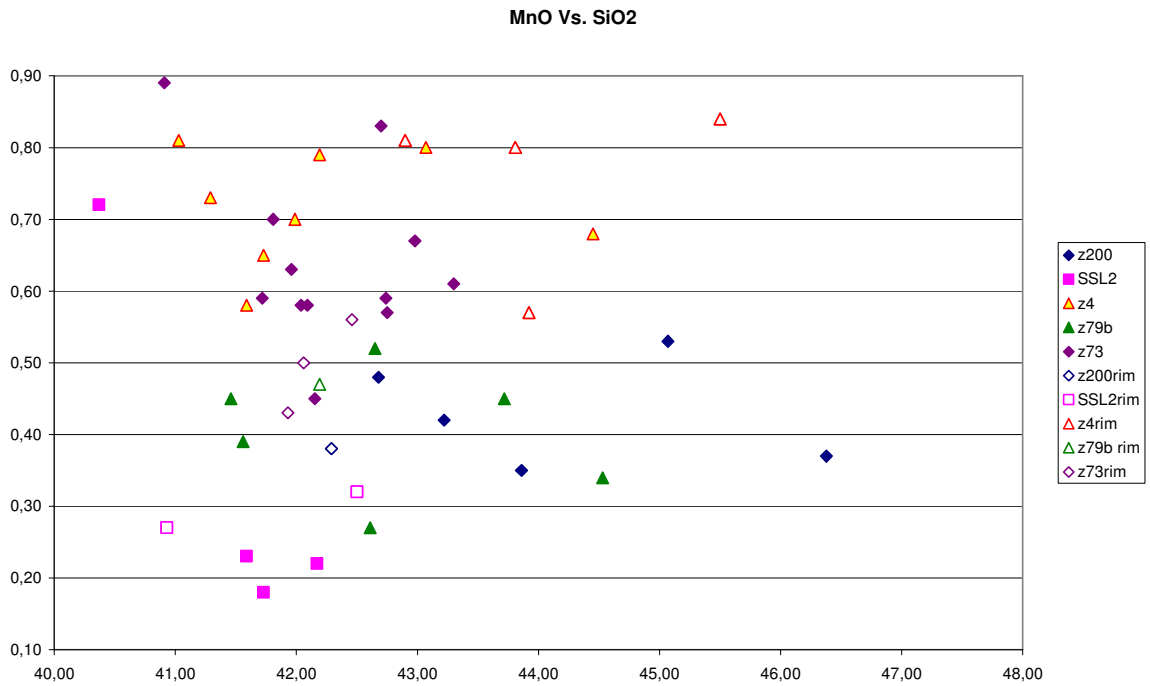


Fig. 4.5: SiO₂ vs. MnO contents from the Hbl-bearing investigated samples.

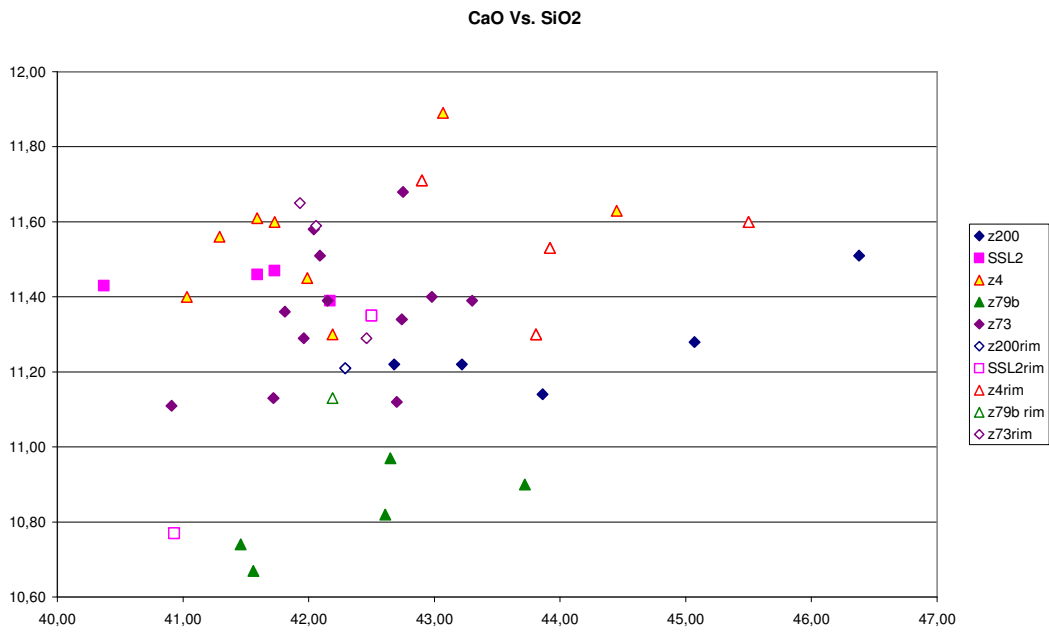


Fig. 4.6: SiO₂ vs. CaO contents from the Hbl-bearing investigated samples.

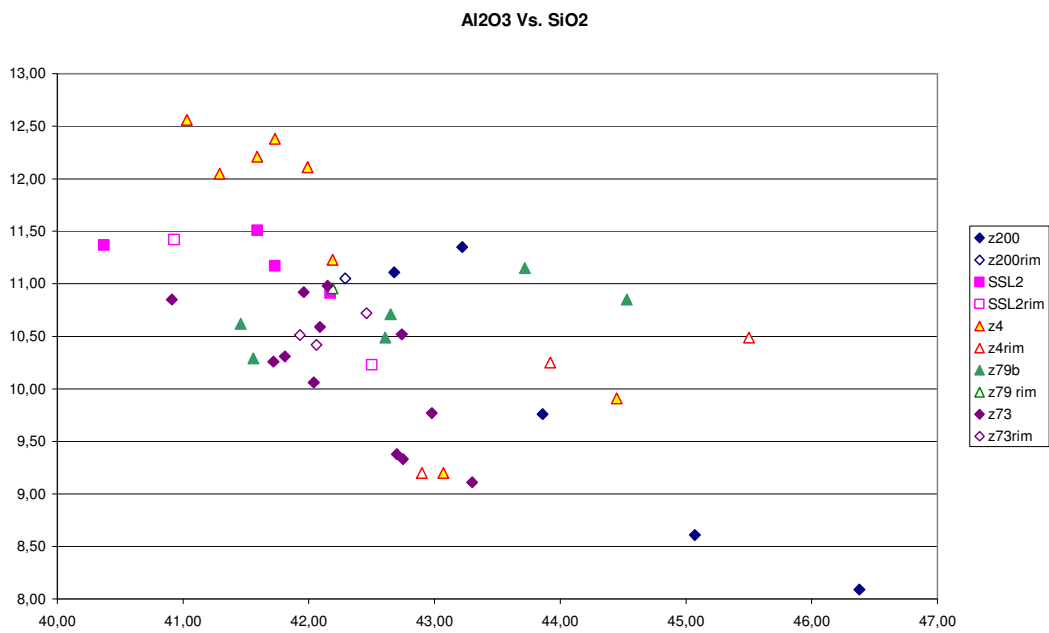


Fig. 4.7: SiO₂ vs. Al₂O₃ contents from the Hbl-bearing investigated samples.

Plagioclase

Tab. 4-6: Representative electron microprobe analyses of plagioclase from granitoids in this study. (*) is for analyses from plagioclase rims.

complex sample point	DGS z200 5a	DGS z200 5b	DGS z200 2a	DGS SSL2 1a	DGS SSL2 1b	DGS SSL2 2a	DGS SSL2 2b(*)	DGS SSL2 4a	DGS SSL2 4b	DGS SSL2 5a	DGS SSL2 5b	DGS SSL2 6a	DGS SSL2 6b
SiO ₂	65,20	61,99	57,69	58,46	58,69	57,39	58,43	57,79	59,73	58,20	57,73	56,07	58,45
TiO ₂	0,00	0,00	0,00	0,00	0,00	0,01	0,07	0,05	0,00	0,04	0,00	0,10	0,07
Al ₂ O ₃	20,81	21,04	25,52	24,81	24,43	25,21	26,09	25,94	22,36	25,41	25,92	23,37	25,77
Cr ₂ O ₃	0,00	0,00	0,00	0,17	0,01	0,07	0,07	0,01	0,05	0,00	0,05	0,00	0,08
Fe ₂ O ₃	0,00	0,00	0,00	0,00	0,00	0,00	0,00	0,00	0,00	0,00	0,00	0,00	0,00
FeO	0,02	0,98	0,21	0,42	0,03	0,08	0,00	0,25	1,14	0,38	0,08	6,19	0,00
MnO	0,00	0,25	0,00	0,00	0,00	0,14	0,23	0,06	0,10	0,00	0,00	0,28	0,00
MgO	0,26	0,55	0,00	0,19	0,17	0,17	0,01	0,12	0,00	0,00	0,00	0,40	0,00
CaO	2,10	5,85	8,22	7,55	7,98	7,95	7,92	7,83	6,62	8,12	8,28	6,87	7,52
Na ₂ O	10,35	8,47	6,35	6,25	6,29	6,97	7,17	6,72	8,08	6,58	6,83	5,43	6,88
K ₂ O	0,18	0,20	0,55	1,48	0,56	0,49	0,48	0,41	0,10	0,35	0,39	0,63	0,46
Li ₂ O	0,00	0,00	0,00	0,00	0,00	0,00	0,00	0,00	0,00	0,00	0,00	0,00	0,00
Rb ₂ O	0,00	0,00	0,00	0,00	0,00	0,00	0,00	0,00	0,00	0,00	0,00	0,00	0,00
SrO	0,00	0,00	0,00	0,00	0,00	0,00	0,00	0,00	0,00	0,00	0,00	0,00	0,00
Cs ₂ O	0,00	0,00	0,00	0,00	0,00	0,00	0,00	0,00	0,00	0,00	0,00	0,00	0,00
BaO	0,00	0,00	0,00	0,00	0,00	0,00	0,00	0,00	0,00	0,00	0,00	0,00	0,00
Total	98,92	99,33	98,54	99,33	98,16	98,48	100,47	99,18	98,18	99,08	99,28	99,34	99,23
numbers of cations on the basis of 8 oxygens													
Si	2,90	2,79	2,62	2,65	2,67	2,62	2,61	2,61	2,73	2,63	2,61	2,60	2,63
Ti	0,00	0,00	0,00	0,00	0,00	0,00	0,00	0,00	0,00	0,00	0,00	0,00	0,00
Al	1,09	1,12	1,37	1,32	1,31	1,36	1,37	1,38	1,20	1,35	1,38	1,28	1,37
Cr	0,00	0,00	0,00	0,01	0,00	0,00	0,00	0,00	0,00	0,00	0,00	0,00	0,00
Fe ³⁺	0,00	0,00	0,00	0,00	0,00	0,00	0,00	0,00	0,00	0,00	0,00	0,00	0,00
Fe ²⁺	0,00	0,04	0,01	0,02	0,00	0,00	0,00	0,01	0,04	0,01	0,00	0,24	0,00
Mn	0,00	0,01	0,00	0,00	0,00	0,01	0,01	0,00	0,00	0,00	0,00	0,01	0,00
Mg	0,02	0,04	0,00	0,01	0,01	0,01	0,00	0,01	0,00	0,00	0,00	0,03	0,00
Ca	0,10	0,28	0,40	0,37	0,39	0,39	0,38	0,38	0,32	0,39	0,40	0,34	0,36
Na	0,89	0,74	0,56	0,55	0,56	0,62	0,62	0,59	0,72	0,58	0,60	0,49	0,60
K	0,01	0,01	0,03	0,09	0,03	0,03	0,03	0,02	0,01	0,02	0,02	0,04	0,03
Li	0,00	0,00	0,00	0,00	0,00	0,00	0,00	0,00	0,00	0,00	0,00	0,00	0,00
Rb	0,00	0,00	0,00	0,00	0,00	0,00	0,00	0,00	0,00	0,00	0,00	0,00	0,00
Sr	0,00	0,00	0,00	0,00	0,00	0,00	0,00	0,00	0,00	0,00	0,00	0,00	0,00
Cs	0,00	0,00	0,00	0,00	0,00	0,00	0,00	0,00	0,00	0,00	0,00	0,00	0,00
Ba	0,00	0,00	0,00	0,00	0,00	0,00	0,00	0,00	0,00	0,00	0,00	0,00	0,00
Total	5,01	5,03	4,99	5,01	4,97	5,03	5,02	5,00	5,03	4,99	5,01	5,02	4,99
Anorthite	9,80	25,28	40,04	35,59	39,33	36,88	36,56	37,48	29,65	39,15	39,12	29,80	36,65
Albite	87,43	66,23	55,97	53,31	56,10	58,51	59,90	58,22	65,48	57,41	58,39	42,62	60,68
Orthoclase	1,00	1,03	3,19	8,31	3,29	2,71	2,64	2,34	0,53	2,01	2,19	3,25	2,67

Tab.4.6 (cont.)

complex sample point	DGS z4 2a(*)	DGS z4 3a	DGS z4 5a	DGS z4 6a(*)	DGS z4 1a	DGS z4 1b(*)	DGS z4 1c	DGS z79b 4a	DGS z79b 5a
SiO ₂	60,40	60,20	60,00	60,45	60,36	59,80	59,98	59,80	60,25
TiO ₂	0,07	0,11	0,05	0,14	0,12	0,02	0,00	0,04	0,00
Al ₂ O ₃	25,72	25,69	25,24	24,90	24,56	24,99	25,00	24,94	25,14
Cr ₂ O ₃	0,00	0,00	0,00	0,00	0,00	0,00	0,00	0,00	0,00
Fe ₂ O ₃	0,00	0,00	0,00	0,00	0,00	0,00	0,00	0,00	0,00
FeO	0,31	0,11	0,00	0,45	0,08	0,17	0,46	0,11	0,14
MnO	0,00	0,00	0,00	0,06	0,03	0,00	0,00	0,04	0,01
MgO	0,04	0,13	0,32	0,03	0,10	0,03	0,08	0,00	0,00
CaO	7,37	7,56	7,05	7,35	7,15	7,01	7,96	6,89	7,20
Na ₂ O	7,43	7,51	7,86	7,71	7,81	7,69	7,70	7,77	7,85
K ₂ O	0,07	0,10	0,00	0,00	0,17	0,15	0,16	0,30	0,36
Li ₂ O	0,00	0,00	0,00	0,00	0,00	0,00	0,00	0,00	0,00
Rb ₂ O	0,00	0,00	0,00	0,00	0,00	0,00	0,00	0,00	0,00
SrO	0,00	0,00	0,00	0,00	0,00	0,00	0,00	0,00	0,00
Cs ₂ O	0,00	0,00	0,00	0,00	0,00	0,00	0,00	0,00	0,00
BaO	0,00	0,00	0,00	0,00	0,00	0,00	0,00	0,00	0,00
Total	101,41	101,41	100,52	101,09	100,38	99,86	101,34	99,89	100,95
Numbers of cations on the basis of 8 oxygens									
Si	2,66	2,65	2,66	2,67	2,68	2,67	2,66	2,67	2,67
Ti	0,00	0,00	0,00	0,01	0,00	0,00	0,00	0,00	0,00
Al	1,33	1,33	1,32	1,30	1,29	1,32	1,30	1,31	1,31
Cr	0,00	0,00	0,00	0,00	0,00	0,00	0,00	0,00	0,00
Fe ³⁺	0,00	0,00	0,00	0,00	0,00	0,00	0,00	0,00	0,00
Fe ²⁺	0,01	0,00	0,00	0,02	0,00	0,01	0,02	0,00	0,01
Mn	0,00	0,00	0,00	0,00	0,00	0,00	0,00	0,00	0,00
Mg	0,00	0,01	0,02	0,00	0,01	0,00	0,01	0,00	0,00
Ca	0,35	0,36	0,34	0,35	0,34	0,34	0,38	0,33	0,34
Na	0,63	0,64	0,67	0,66	0,67	0,67	0,66	0,67	0,67
K	0,00	0,01	0,00	0,00	0,01	0,01	0,01	0,02	0,02
Li	0,00	0,00	0,00	0,00	0,00	0,00	0,00	0,00	0,00
Rb	0,00	0,00	0,00	0,00	0,00	0,00	0,00	0,00	0,00
Sr	0,00	0,00	0,00	0,00	0,00	0,00	0,00	0,00	0,00
Cs	0,00	0,00	0,00	0,00	0,00	0,00	0,00	0,00	0,00
Ba	0,00	0,00	0,00	0,00	0,00	0,00	0,00	0,00	0,00
Total	4,99	5,00	5,02	5,01	5,01	5,01	5,03	5,01	5,02
Anorthite	34,77	35,10	32,46	33,80	32,93	32,94	35,29	32,16	32,80
Albite	63,43	63,10	65,49	64,17	65,10	65,40	61,78	65,63	64,71
Orthoclase	0,39	0,55	0,00	0,00	0,93	0,84	0,84	1,67	1,95

Tab.4.6 (cont.)

complex sample point	GC z73 2a	GC z73 2b	GC z73 2c	GC z73 6a	GC z73 6b	GC z73 6c	GC z73 7a	GC z73 9a	GC z73 9b
SiO ₂	60,35	58,06	58,53	65,08	59,44	59,99	63,36	57,33	58,08
TiO ₂	0,00	0,08	0,22	0,00	0,00	0,14	0,00	0,22	0,08
Al ₂ O ₃	24,19	25,56	22,02	22,48	24,39	24,80	22,65	22,02	25,56
Cr ₂ O ₃	0,00	0,00	0,00	0,00	0,00	0,00	0,00	0,00	0,00
Fe ₂ O ₃	0,00	0,00	0,00	0,00	0,00	0,00	0,00	0,00	0,00
FeO	0,05	0,16	2,37	0,00	0,57	0,24	0,06	2,37	0,16
MnO	0,01	0,07	0,07	0,09	0,00	0,10	0,00	0,07	0,07
MgO	0,00	0,00	0,14	0,25	0,12	0,09	0,34	0,14	0,00
CaO	7,09	7,40	8,84	3,16	6,77	5,39	3,92	8,84	7,40
Na ₂ O	7,63	7,57	7,82	9,61	8,19	7,66	9,21	7,52	7,57
K ₂ O	0,14	0,06	0,60	0,25	0,97	1,24	0,25	0,60	0,06
Li ₂ O	0,00	0,00	0,00	0,00	0,00	0,00	0,00	0,00	0,00
Rb ₂ O	0,00	0,00	0,00	0,00	0,00	0,00	0,00	0,00	0,00
SrO	0,00	0,00	0,00	0,00	0,00	0,00	0,00	0,00	0,00
Cs ₂ O	0,00	0,00	0,00	0,00	0,00	0,00	0,00	0,00	0,00
BaO	0,00	0,00	0,00	0,00	0,00	0,00	0,00	0,00	0,00
Total	99,46	98,96	100,61	100,92	100,45	99,65	99,79	99,11	98,98
numbers of cations on the basis of 8 oxygens									
Si	2,70	2,63	2,66	2,84	2,66	2,69	2,81	2,65	2,63
Ti	0,00	0,00	0,01	0,00	0,00	0,01	0,00	0,01	0,00
Al	1,28	1,36	1,18	1,16	1,29	1,31	1,18	1,20	1,36
Cr	0,00	0,00	0,00	0,00	0,00	0,00	0,00	0,00	0,00
Fe ³⁺	0,00	0,00	0,00	0,00	0,00	0,00	0,00	0,00	0,00
Fe ²⁺	0,00	0,01	0,09	0,00	0,02	0,01	0,00	0,09	0,01
Mn	0,00	0,00	0,00	0,00	0,00	0,00	0,00	0,00	0,00
Mg	0,00	0,00	0,01	0,02	0,01	0,01	0,02	0,01	0,00
Ca	0,34	0,36	0,43	0,15	0,33	0,26	0,19	0,44	0,36
Na	0,66	0,66	0,69	0,81	0,71	0,67	0,79	0,67	0,66
K	0,01	0,00	0,04	0,01	0,06	0,07	0,01	0,04	0,00
Li	0,00	0,00	0,00	0,00	0,00	0,00	0,00	0,00	0,00
Rb	0,00	0,00	0,00	0,00	0,00	0,00	0,00	0,00	0,00
Sr	0,00	0,00	0,00	0,00	0,00	0,00	0,00	0,00	0,00
Cs	0,00	0,00	0,00	0,00	0,00	0,00	0,00	0,00	0,00
Ba	0,00	0,00	0,00	0,00	0,00	0,00	0,00	0,00	0,00
Total	4,99	5,02	5,10	4,99	5,08	5,02	5,01	5,10	5,02
Anorthite	33,58	34,66	34,26	14,86	28,98	25,52	18,31	34,99	34,66
Albite	65,40	64,16	54,84	81,77	63,45	65,63	77,87	53,87	64,16
Orthoclase	0,79	0,33	2,77	1,40	4,94	6,99	1,39	2,83	0,33

Biotite

Tab. 4-7: Representative electron microprobe analyses and structural formula of biotite from granitoids in this study.

complex sample point	DGS z4 2a	DGS z4 4a	DGS z4 6a	DGS z79b 3a	DGS z79b 3b	DGS z79b 4a	DGS z79b 5a	DGS z79b 6a
SiO ₂	34,29	36,30	35,62	36,31	36,00	36,40	36,31	36,53
TiO ₂	2,30	4,28	3,00	5,68	6,26	5,73	5,77	5,65
Al ₂ O ₃	16,33	14,78	15,64	14,66	14,58	14,40	13,87	15,17
Cr ₂ O ₃	0,00	0,00	0,00	0,06	0,00	0,00	0,00	0,00
Fe ₂ O ₃	0,00	0,00	0,00	0,00	0,00	0,00	0,00	0,00
FeO	24,65	20,55	21,70	20,70	19,56	19,15	20,89	20,34
MnO	0,31	0,59	0,31	0,37	0,27	0,22	0,25	0,22
MgO	10,52	9,77	9,80	9,23	10,12	9,96	9,28	8,98
CaO	0,12	0,06	0,22	0,14	0,00	0,03	0,02	9,40
Na ₂ O	0,00	0,00	0,18	0,55	0,37	0,04	0,08	0,21
K ₂ O	6,16	9,97	8,60	9,72	10,06	10,08	9,80	9,40
Li ₂ O	0,00	0,00	0,00	0,00	0,00	0,00	0,00	0,00
Rb ₂ O	0,00	0,00	0,00	0,00	0,00	0,00	0,00	0,00
SrO	0,00	0,00	0,00	0,00	0,00	0,00	0,00	0,00
Cs ₂ O	0,00	0,00	0,00	0,00	0,00	0,00	0,00	0,00
BaO	0,00	0,00	0,00	0,00	0,00	0,00	0,00	0,00
F ⁻	0,00	0,00	0,00	0,00	0,00	0,00	0,00	0,00
Cl ⁻	0,00	0,00	0,00	0,19	0,13	0,16	0,00	0,00
Total	94,68	96,30	95,07	97,57	97,32	96,13	96,27	105,90
Numbers of cations on the basis of 11 oxygens								
Si	2,67	2,78	2,75	2,74	2,72	2,77	2,78	2,59
Ti	0,13	0,25	0,17	0,32	0,36	0,33	0,33	0,30
Al	1,50	1,33	1,43	1,31	1,30	1,29	1,25	1,27
Cr	0,00	0,00	0,00	0,00	0,00	0,00	0,00	0,00
Fe ³⁺	0,00	0,00	0,00	0,00	0,00	0,00	0,00	0,00
Fe ²⁺	1,60	1,31	1,40	1,31	1,24	1,22	1,34	1,21
Mn	0,02	0,04	0,02	0,02	0,02	0,01	0,02	0,01
Mg	1,22	1,11	1,13	1,04	1,14	1,13	1,06	0,95
Ca	0,01	0,01	0,02	0,01	0,00	0,00	0,00	0,71
Na	0,00	0,00	0,03	0,08	0,05	0,01	0,01	0,03
K	0,61	0,97	0,85	0,94	0,97	0,98	0,96	0,85
Li	0,00	0,00	0,00	0,00	0,00	0,00	0,00	0,00
Rb	0,00	0,00	0,00	0,00	0,00	0,00	0,00	0,00
Sr	0,00	0,00	0,00	0,00	0,00	0,00	0,00	0,00
Cs	0,00	0,00	0,00	0,00	0,00	0,00	0,00	0,00
Ba	0,00	0,00	0,00	0,00	0,00	0,00	0,00	0,00
F ⁻	0,00	0,00	0,00	0,00	0,00	0,00	0,00	0,00
Cl ⁻	0,00	0,00	0,00	0,02	0,02	0,02	0,00	0,00
Total	7,76	7,80	7,80	7,80	7,80	7,76	7,75	7,92

Tab. 4-8: (cont.)

complex sample point	DGS SSL2 4a	DGS SSL2 5a	DGS SSL2 6a	DGS SSL2 6b	DGS SSL2 6c
SiO ₂	35,69	35,26	35,67	35,56	35,69
TiO ₂	5,47	5,21	5,33	5,16	4,96
Al ₂ O ₃	13,44	14,25	13,49	14,04	14,24
Cr ₂ O ₃	0,14	0,09	0,00	0,08	0,00
Fe ₂ O ₃	0,00	0,00	0,00	0,00	0,00
FeO	22,38	22,35	21,47	21,40	21,57
MnO	0,19	0,08	0,00	0,20	0,34
MgO	8,25	9,35	9,16	9,39	9,68
CaO	0,00	0,00	0,00	0,04	0,10
Na ₂ O	0,00	0,07	0,00	0,00	0,00
K ₂ O	9,72	10,10	9,53	10,04	9,97
Li ₂ O	0,00	0,00	0,00	0,00	0,00
Rb ₂ O	0,00	0,00	0,00	0,00	0,00
SrO	0,00	0,00	0,00	0,00	0,00
Cs ₂ O	0,00	0,00	0,00	0,00	0,00
BaO	0,00	0,00	0,00	0,00	0,00
F	1,33	1,38	2,08	0,87	1,21
Cl	0,21	0,14	0,22	0,13	0,18
Total	96,21	97,67	96,03	96,51	97,39
Numbers of cations on the basis of 11 oxygens					
Si	2,74	2,67	2,72	2,72	2,70
Ti	0,32	0,30	0,31	0,30	0,28
Al	1,22	1,27	1,21	1,27	1,27
Cr	0,01	0,01	0,00	0,01	0,00
Fe ³⁺	0,00	0,00	0,00	0,00	0,00
Fe ²⁺	1,44	1,42	1,37	1,37	1,37
Mn	0,01	0,01	0,00	0,01	0,02
Mg	0,95	1,06	1,04	1,07	1,09
Ca	0,00	0,00	0,00	0,00	0,01
Na	0,00	0,01	0,00	0,00	0,00
K	0,95	0,98	0,93	0,98	0,96
Li	0,00	0,00	0,00	0,00	0,00
Rb	0,00	0,00	0,00	0,00	0,00
Sr	0,00	0,00	0,00	0,00	0,00
Cs	0,00	0,00	0,00	0,00	0,00
Ba	0,00	0,00	0,00	0,00	0,00
F ⁻	0,32	0,33	0,50	0,21	0,29
Cl ⁻	0,03	0,02	0,03	0,02	0,02
Total	7,981	8,060	8,099	7,951	8,018

Pyroxenes

Tab. 4-9: Representative electron microprobe analyses and structural formula of biotite from granitoids in this study.

complex	DGS	DGS	DGS	DGS	DGS	DGS
sample	z200	z200	z79b	SSL2	SSL2	SSL2
point	1a	4a	2a	2a	3a	3c (*)
SiO ₂	51,70	52,00	51,24	50,80	50,18	50,10
TiO ₂	0,09	0,03	0,18	0,00	0,00	0,00
Al ₂ O ₃	1,60	1,01	1,16	0,70	0,00	0,65
Cr ₂ O ₃	0,00	0,00	0,00	0,15	0,19	0,05
Fe ₂ O ₃	0,00	0,00	0,00	0,00	0,00	0,00
FeO	10,78	10,76	13,49	32,42	33,53	33,68
MnO	0,77	0,46	0,73	1,13	0,94	1,06
MgO	12,41	13,00	10,70	13,79	13,70	13,60
CaO	21,69	21,67	20,94	0,69	1,01	0,64
Na ₂ O	0,00	0,00	0,76	0,00	0,00	0,00
Total	99,04	98,93	99,20	99,68	99,55	99,78
numbers of cations on the basis of 8 oxygens						
Si	1,97	1,98	1,96	2,00	2,00	1,99
Al ^{IV}	0,03	0,02	0,04	0,00	0,00	0,02
Al ^{VI}	0,04	0,02	0,01	0,03	0,00	0,02
Fe ²⁺	0,34	0,34	0,36	1,07	1,12	1,12
Fe ³⁺	0,00	0,00	0,07	0,00	0,00	0,00
Mg	0,70	0,74	0,61	0,81	0,81	0,80
Mn	0,03	0,02	0,02	0,04	0,03	0,04
Ti	0,00	0,00	0,01	0,00	0,00	0,00
Cr	0,00	0,00	0,00	0,01	0,01	0,00
Ca	0,88	0,88	0,86	0,03	0,04	0,03
Na	0,00	0,00	0,06	0,00	0,00	0,00
Wo	45,00	45,00	46,93	1,53	2,18	1,40
En	36,00	37,00	33,36	42,47	41,22	41,27
Fs	17,00	17,00	19,71	56,01	56,60	57,33

Ms-bearing granitoids

Mineral chemistry from two-mica microgranite and from Ms-bearing pegmatite has been investigated. As discussed in section 4.2, these terms exhibit the suitable assemblage to use the well-known phengite barometer (Velde, 1965).

White mica and biotite

Tab. 4-10: Representative electron microprobe analyses and structural formula of magmatic muscovite from granitoids in this study.

complex sample point	GC SSL26 7a	GC SSL26 7b	GC SSL26 9a	GC SSL26 9b	GC SSL26 9c	GC SSL22 a1	GC SSL22 a2	GC SSL22 a3	GC SSL22 a4	GC SSL22 a5	GC SSL22 a6	GC SSL22 a7
SiO ₂	47,07	46,20	45,96	46,07	46,54	47,62	46,76	46,20	46,95	46,40	48,25	47,26
TiO ₂	1,64	1,56	0,68	0,44	1,00	0,23	0,00	0,02	0,12	0,14	0,32	0,00
Al ₂ O ₃	29,62	29,30	30,58	30,37	30,88	33,37	33,94	33,89	33,69	33,09	34,52	34,60
Cr ₂ O ₃	0,00	0,09	0,07	0,11	0,00	0,00	0,00	0,00	0,00	0,00	0,00	0,00
Fe ₂ O ₃	0,00	0,00	0,00	0,00	0,00	0,00	0,00	0,00	0,00	0,00	0,00	0,00
FeO	4,44	4,28	4,11	4,98	4,05	5,19	4,53	4,24	4,24	5,04	4,86	4,28
MnO	0,06	0,22	0,00	0,22	0,07	0,04	0,00	0,00	0,00	0,02	0,00	0,14
MgO	1,34	1,61	1,30	1,38	1,32	0,23	0,09	0,08	0,18	0,17	0,09	0,00
CaO	0,16	0,17	0,00	0,00	0,00	0,02	0,00	0,00	0,12	0,06	0,03	0,00
Na ₂ O	0,09	0,19	0,34	0,28	0,05	0,58	0,93	0,81	0,80	0,57	0,51	0,92
K ₂ O	11,54	11,83	11,51	11,00	11,23	10,60	10,27	10,21	11,21	11,06	8,92	10,09
Li ₂ O	0,00	0,00	0,00	0,00	0,00	0,00	0,00	0,00	0,00	0,00	0,00	0,00
Rb ₂ O	0,00	0,00	0,00	0,00	0,00	0,00	0,00	0,00	0,00	0,00	0,00	0,00
SrO	0,00	0,00	0,00	0,00	0,00	0,00	0,00	0,00	0,00	0,00	0,00	0,00
Cs ₂ O	0,00	0,00	0,00	0,00	0,00	0,00	0,00	0,00	0,00	0,00	0,00	0,00
BaO	0,00	0,00	0,00	0,00	0,00	0,00	0,00	0,00	0,00	0,00	0,00	0,00
F	1,19	0,97	1,97	1,27	0,10	0,00	0,00	0,00	0,00	0,00	0,00	0,00
Cl	0,06	0,02	0,00	0,00	0,00	0,00	0,00	0,00	0,00	0,00	0,00	0,00
Total	96,70	96,03	95,69	95,59	95,20	97,88	96,52	95,45	97,31	96,55	97,50	97,29
Numbers of cations on the basis of 8 oxygens												
Si	3,15	3,13	3,10	3,12	3,16	3,14	3,12	3,11	3,12	3,12	3,15	3,12
Ti	0,08	0,08	0,03	0,02	0,05	0,01	0,00	0,00	0,01	0,01	0,02	0,00
Al	2,34	2,34	2,43	2,43	2,47	2,60	2,67	2,69	2,64	2,62	2,66	2,69
Cr	0,00	0,01	0,00	0,01	0,00	0,00	0,00	0,00	0,00	0,00	0,00	0,00
Fe ³⁺	0,00	0,00	0,00	0,00	0,00	0,00	0,00	0,00	0,00	0,00	0,00	0,00
Fe ²⁺	0,25	0,24	0,23	0,28	0,23	0,29	0,25	0,24	0,24	0,28	0,27	0,24
Mn	0,00	0,01	0,00	0,01	0,00	0,00	0,00	0,00	0,00	0,00	0,00	0,01
Mg	0,13	0,16	0,13	0,14	0,13	0,02	0,01	0,01	0,02	0,02	0,01	0,00
Ca	0,01	0,01	0,00	0,00	0,00	0,00	0,00	0,00	0,01	0,00	0,00	0,00
Na	0,01	0,03	0,04	0,04	0,01	0,07	0,12	0,11	0,10	0,07	0,07	0,12
K	0,99	1,02	0,99	0,95	0,97	0,89	0,87	0,88	0,95	0,95	0,74	0,85
Li	0,00	0,00	0,00	0,00	0,00	0,00	0,00	0,00	0,00	0,00	0,00	0,00
Rb	0,00	0,00	0,00	0,00	0,00	0,00	0,00	0,00	0,00	0,00	0,00	0,00
Sr	0,00	0,00	0,00	0,00	0,00	0,00	0,00	0,00	0,00	0,00	0,00	0,00
Cs	0,00	0,00	0,00	0,00	0,00	0,00	0,00	0,00	0,00	0,00	0,00	0,00
Ba	0,00	0,00	0,00	0,00	0,00	0,00	0,00	0,00	0,00	0,00	0,00	0,00
F-	0,25	0,21	0,42	0,27	0,02	0,00	0,00	0,00	0,00	0,00	0,00	0,00
Cl-	0,01	0,00	0,00	0,00	0,00	0,00	0,00	0,00	0,00	0,00	0,00	0,00
Total	7,23	7,25	7,38	7,27	7,05	7,03	7,04	7,03	7,08	7,08	6,91	7,02

Tab.4.11 (cont.)

complex sample point	GC SSL22 a1	GC SSL22 a2	GC SSL22 a3	GC SSL22 a4	GC SSL22 a5	GC SSL22 a6	GC SSL22 a7
SiO ₂	47,62	46,76	46,20	46,95	46,40	48,25	47,26
TiO ₂	0,23	0,00	0,02	0,12	0,14	0,32	0,00
Al ₂ O ₃	33,37	33,94	33,89	33,69	33,09	34,52	34,60
Cr ₂ O ₃	0,00	0,00	0,00	0,00	0,00	0,00	0,00
Fe ₂ O ₃	0,00	0,00	0,00	0,00	0,00	0,00	0,00
FeO	5,19	4,53	4,24	4,24	5,04	4,86	4,28
MnO	0,04	0,00	0,00	0,00	0,02	0,00	0,14
MgO	0,23	0,09	0,08	0,18	0,17	0,09	0,00
CaO	0,02	0,00	0,00	0,12	0,06	0,03	0,00
Na ₂ O	0,58	0,93	0,81	0,80	0,57	0,51	0,92
K ₂ O	10,60	10,27	10,21	11,21	11,06	8,92	10,09
Li ₂ O	0,00	0,00	0,00	0,00	0,00	0,00	0,00
Rb ₂ O	0,00	0,00	0,00	0,00	0,00	0,00	0,00
SrO	0,00	0,00	0,00	0,00	0,00	0,00	0,00
Cs ₂ O	0,00	0,00	0,00	0,00	0,00	0,00	0,00
BaO	0,00	0,00	0,00	0,00	0,00	0,00	0,00
F	0,00	0,00	0,00	0,00	0,00	0,00	0,00
Cl	0,00	0,00	0,00	0,00	0,00	0,00	0,00
Total	97,88	96,52	95,45	97,31	96,55	97,50	97,29
Numbers of cations on the basis of 8 oxygens							
Si	3,14	3,12	3,11	3,12	3,12	3,15	3,12
Ti	0,01	0,00	0,00	0,01	0,01	0,02	0,00
Al	2,60	2,67	2,69	2,64	2,62	2,66	2,69
Cr	0,00	0,00	0,00	0,00	0,00	0,00	0,00
Fe ³⁺	0,00	0,00	0,00	0,00	0,00	0,00	0,00
Fe ²⁺	0,29	0,25	0,24	0,24	0,28	0,27	0,24
Mn	0,00	0,00	0,00	0,00	0,00	0,00	0,01
Mg	0,02	0,01	0,01	0,02	0,02	0,01	0,00
Ca	0,00	0,00	0,00	0,01	0,00	0,00	0,00
Na	0,07	0,12	0,11	0,10	0,07	0,07	0,12
K	0,89	0,87	0,88	0,95	0,95	0,74	0,85
Li	0,00	0,00	0,00	0,00	0,00	0,00	0,00
Rb	0,00	0,00	0,00	0,00	0,00	0,00	0,00
Sr	0,00	0,00	0,00	0,00	0,00	0,00	0,00
Cs	0,00	0,00	0,00	0,00	0,00	0,00	0,00
Ba	0,00	0,00	0,00	0,00	0,00	0,00	0,00
F-	0,00	0,00	0,00	0,00	0,00	0,00	0,00
Cl-	0,00	0,00	0,00	0,00	0,00	0,00	0,00
Total	7,03	7,04	7,03	7,08	7,08	6,91	7,02

Tab. 4-11: Representative electron microprobe analyses and structural formula of magmatic biotite from Ms-bearing granite in this study.

complex sample point	GC SSL26 4a	GC SSL26 4b	GC SSL26 7a
SiO ₂	35,03	36,04	36,11
TiO ₂	2,31	2,00	2,74
Al ₂ O ₃	17,58	18,27	17,68
Cr ₂ O ₃	0,00	0,00	0,00
Fe ₂ O ₃	0,00	0,00	0,00
FeO	20,18	19,90	21,74
MnO	0,33	0,40	0,56
MgO	7,74	7,82	9,38
CaO	0,16	0,04	0,13
Na ₂ O	0,00	0,24	0,00
K ₂ O	9,33	9,79	7,60
Li ₂ O	0,00	0,00	0,00
Rb ₂ O	0,00	0,00	0,00
SrO	0,00	0,00	0,00
Cs ₂ O	0,00	0,00	0,00
BaO	0,00	0,00	0,00
F	0,00	0,00	0,54
Cl	0,00	0,00	0,00
Total	92,66	94,50	96,25
numbers of cations on the basis of 8 oxygens			
Si	2,76	2,78	2,72
Ti	0,14	0,12	0,16
Al	1,64	1,66	1,57
Cr	0,00	0,00	0,00
Fe ³⁺	0,00	0,00	0,00
Fe ²⁺	1,33	1,28	1,37
Mn	0,02	0,03	0,04
Mg	0,91	0,90	1,05
Ca	0,01	0,00	0,01
Na	0,00	0,04	0,00
K	0,94	0,96	0,73
Li	0,00	0,00	0,00
Rb	0,00	0,00	0,00
Sr	0,00	0,00	0,00
Cs	0,00	0,00	0,00
Ba	0,00	0,00	0,00
F-	0,00	0,00	0,13
Cl-	0,00	0,00	0,00
Total	7,75	7,77	7,77

Feldspars

Tab. 4-12: Representative electron microprobe analyses and structural formula of magmatic feldspars from Ms-bearing granitoids in this study.

complex sample point	GC SSL26 4a	GC SSL26 5a	GC SSL26 7a	GC SSL26 2a	GC SSL22 1a	GC SSL22 2a
SiO ₂	59,51	62,08	63,80	65,23	66,40	66,60
TiO ₂	0,01	0,00	0,00	0,17	0,00	0,02
Al ₂ O ₃	25,05	24,81	23,15	18,50	20,67	21,11
Cr ₂ O ₃	0,00	0,00	0,00	0,00	0,00	0,00
Fe ₂ O ₃	0,00	0,00	0,00	0,00	0,00	0,00
FeO	0,17	0,00	0,18	0,00	0,01	0,00
MnO	0,11	0,02	0,00	0,00	0,04	0,00
MgO	0,05	0,07	0,36	0,00	0,07	0,00
CaO	7,12	5,79	5,39	0,10	0,69	1,32
Na ₂ O	7,44	8,51	8,78	0,28	11,27	10,66
K ₂ O	0,13	0,22	0,18	16,17	0,20	0,08
Li ₂ O	0,00	0,00	0,00	0,00	0,00	0,00
Rb ₂ O	0,00	0,00	0,00	0,00	0,00	0,00
SrO	0,00	0,00	0,00	0,00	0,00	0,00
Cs ₂ O	0,00	0,00	0,00	0,00	0,00	0,00
BaO	0,00	0,00	0,00	0,00	0,00	0,00
Total	99,59	101,50	101,84	100,45	99,35	99,79
numbers of cations on the basis of 8 oxygens						
Si	2,67	2,72	2,78	3,00	2,93	2,92
Ti	0,00	0,00	0,00	0,01	0,00	0,00
Al	1,32	1,28	1,19	1,00	1,08	1,09
Cr	0,00	0,00	0,00	0,00	0,00	0,00
Fe ³⁺	0,00	0,00	0,00	0,00	0,00	0,00
Fe ²⁺	0,01	0,00	0,01	0,00	0,00	0,00
Mn	0,00	0,00	0,00	0,00	0,00	0,00
Mg	0,00	0,01	0,02	0,00	0,01	0,00
Ca	0,34	0,27	0,25	0,01	0,03	0,06
Na	0,65	0,72	0,74	0,03	0,96	0,91
K	0,01	0,01	0,01	0,95	0,01	0,00
Li	0,00	0,00	0,00	0,00	0,00	0,00
Rb	0,00	0,00	0,00	0,00	0,00	0,00
Sr	0,00	0,00	0,00	0,00	0,00	0,00
Cs	0,00	0,00	0,00	0,00	0,00	0,00
Ba	0,00	0,00	0,00	0,00	0,00	0,00
Total	5,00	5,01	5,00	4,98	5,02	4,99
Anorthite	33,86	26,85	24,35	0,50	3,22	6,38
Albite	64,03	71,41	71,78	2,55	95,04	93,16
Orthoclase	0,74	1,21	0,97	96,95	1,11	0,46

Pressure and temperature estimations

4.2.1 “Peak” conditions in Grt-bearing gneisses

P-T estimation for D₁ and D₂ phases from Libourel (1985) are summarized in tab.4.14, where the adopted thermobarometers are also indicated. During this work, the calibrations of Newton & Perkins (1982) and Bohlen et al. (1983), which were utilized by Libourel (1985), were applied on D₁ assemblage, providing pressure estimations of 7.6±0.6Kb and 8.7±1Kb, respectively. The thermometer Grt-Opx (Lal, 1993) provided a temperature of 801±50°C. Regarding D₂ assemblage, in absence of cordierite, only the thermometer Opx-Bt has been applied; the calibration of Sengupta et al. (1990) provided a temperature of 588±50°C.

Besides these “traditional” thermobarometers, the software TWEEQU (Berman, 1991) version 2.02 has been used. This program calculates all possible equilibria in a given mineral assemblage. The internally consistent thermodynamic dataset is that of Berman (1988). End members proportions and activities were calculated with TWEEQU v2.02. On the basis of the assemblage Grt-Pl-Opx-Qtz, the obtained P-T values are calculated with the intersection function, which is available within the TWEEQU suite.

The results from the application of TWEEQU software on D₁ assemblage are shown in tab.4.15. On the basis on the adopted quartz polymorph, TWEEQU provides two possible P-T windows. In our case, the common occurrence of chessboard SGB pattern, joined with quartz LPO fabric displaying strong X-maxima, suggests that D₂, synkinematic assemblage developed in the high-quartz field. Taking into account that D₂ assemblage has a retrograde character (respect to D₁ “peak” conditions; Libourel, 1985), we can assume that D₁ assemblage developed in the high-quartz field also. Using this microstructural constrain, P-T estimations provided by TWEEQU software are well in agreement with those obtained from previous calibrations (compare tab.4.14 and 4.15).

Opx porphyroclasts exhibit biotite inclusions, indicating that pyroxene (Opx^I) likely derived from fluid-absent partial melting of biotite. The appearance of Opx at the expense of biotite marks the transition from amphibolite- to granulite facies conditions (Bucker & Frey, 2003, pag. 236). According to these authors, the minimum temperature for this reaction is ~750°-800°C. The temperature range for this metamorphic reaction is also evidenced by the summary compiled by Nair & Chacko (2002). However, as pointed out by these authors, in several experimental studies the lower temperature boundary for this reaction (at a pressure of ~7Kb) is shifted toward higher temperature (between ~840° and ~950°). The experimentally derived *Opx-in* curve of Vielzeuf & Montel (1994) is adopted here, because these authors used a natural metagreywake that can be comparable with the studied sample Zx. In the 6.5-8.1 Kbar range (Tab.4.15), this *Opx-in* curve imposes an upper temperature limit of ~850°C (Fig.4.9).

Tab. 4-13: table summarizing P-T estimation from Libourel (1985) applied on D₁ and D₂ assemblages.

phase	assemblage	P [Kb]	barometer	calibration	T [°C]	thermometer	calibration
D ₁	Grt-Opx-Pl-Qtz±Kfs	7±1	Grt-Opx-Pl-Qtz	Newton & Perkins (1982) Bohlen et al. (1983) Wells (1979)	800–850°	Grt-Bt	Indares & Martignole (1985)
D ₂	Opx-Crd-Bt-Qtz	4,5-6	Grt-Opx-Pl-Qtz	Newton & Perkins (1982) Bohlen et al. (1983) Wells (1979)	~750–800°	Grt-Crd; Grt-Bt	Thompson (1976) Holdaway & Lee (1977)

Tab. 4-14: table summarizing P-T estimation from Grt-Opx-Pl-Qtz D₁ assemblage (sample Zx, this work), as provided by TWEEQU software.

D ₁ assemblage	α - quartz	β - Qtz
P [Kb]	6,3 ± 1,1	7,3 ± 0,8
T [°C]	576 ± 21	824 ± 119

4.2.2 Estimation of P-T conditions for the emplacements of Hbl-bearing granitoids (DGS and GC).

The “Al-in-Hbl” barometer is based on the assumption that, in granitoids containing [Qtz-Kfs-Pl-Bt-Hbl-Ttn-Fe/Ti oxide], the Al content in hornblende increases with pressure. After the empirical calibrations of Zen (1986) and Hollister et al. (1987), this barometer has been improved through subsequent experimental calibrations performed by Johnson & Rutherford (1989) and Schmidt (1992). More recently, Anderson & Smith (1995) pointed out that the Al-in-Hbl barometer is strongly temperature-dependent; moreover, others intensive parameters, such as f_{O_2} , might markedly affect the pressure estimations. Thus, these authors proposed a revisited version of the expression for the barometer, incorporating the effect of temperature. The expression (which) is:

$$P (\pm 0.6\text{Kbar}) = (4,76\text{Al}) - 3,01 - \left\{ \frac{[T (\text{°C}) - 675]}{85} \right\} \{ (0,530\text{Al}) + (0,005294[T (\text{°C}) - 675]) \}$$

Moreover, these authors documented that this barometer fails by yielding elevated pressures for low- f_{O_2} plutons with iron-rich hornblende.

The calibration from Anderson & Smith (1995) was adopted in this work, but only where the Fe/(Fe+Mg) ratios for hornblende (see tab.4.5) are in the range ~0.40–0.65, indicating high f_{O_2} . Furthermore, only plagioclase showing An content in the range An₂₅-An₃₅ are used here, because higher anorthite content can markedly increase the Al content in Hbl, independently of pressure (Anderson & Smith, 1995).

Owing to widespread feldspar alteration, no samples with the suitable assemblage described above were obtained. All the selected granitoids display tonalitic composition (namely where Kfs occurs, Hbl is commonly absent). Although Anderson & Smith (1995) documented that the absence of Kfs and Ttn does not produce any detectable error in the calculated pressure, pressure estimations obtained from tonalites are maximum values (Anderson, 1996). The edenite-richterite calibration of the Hbl-Pl thermometer (Holland & Blundy, 1994) was adopted here, in order to estimate the temperature of tonalite

crystallization. This calibration is considered the most reliable for mid- to lower crustal intrusions (Anderson, 1996). Pressure and temperature estimations, provided by hornblende and plagioclase crystals with appropriate composition, are summarized in tab.4.16.

4.2.3 Estimation of P-T conditions for the emplacements of Ms-bearing granitoids (GC)

Two-mica microgranite and Ms-bearing pegmatite from Granitic Complex has been investigated in order to obtain P-T estimation for the emplacement of S-type granitoid suite.

Plagioclase-muscovite thermometer (Green & Usdansky, 1986) was used; this thermometer is related to the compositions of coexisting plagioclase and muscovite, being based on the Na-K exchange between these mineral phases. This thermometer is suitable for pelitic metasedimentary rocks and peraluminous granitoids that crystallized at temperature of 415-725°C and pressure of 2.5-13Kbar (Green & Usdansky, 1986).

This thermometer is moderately temperature-dependent; thus assuming (for the whole granitic Complex, tab.4.16) a pressure of emplacement of 5.5Kbar, Pl-Ms thermometer provides a temperature of ~708°C, which is appropriate for Ms-bearing leucogranites. This value was obtained by using mean compositions of coexisting plagioclase and muscovite crystals. The application of this thermometer on Ms-bearing pegmatite (sample SSL22) provides a temperature of ~500°C.

The phengite barometer (Velde, 1965) has been used in order to estimate the pressure of emplacement. This barometer is based on the celadonite content in phengite (coexisting with Qtz, Kfs and Bt), which is mainly dependent on pressure. However, phengite barometer is markedly temperature-dependent and it is very sensitive to (even small) analytical errors in Si pfu determinations (Anderson, 1996). The recent calibrations of Massonne & Szpurka (1997) and Simpson et al. (2000) have been used here. The older calibration provides a slightly higher pressure (6.0Kbar vs. 5.5Kbar, Tab.4.16). Taking into account that microstructures and quartz LPO from two-mica microgranitoids indicate without ambiguity that the submagmatic fabric and the high-temperature solid-state fabric developed in the high-quartz field (sections 3.2 and 3.3), the calibration of Simpson et al. (2000) likely provides the best estimation for the emplacement of Ms-bearing suite.

Both two-mica microgranite and Ms-bearing pegmatite display an average Si content of 3.13 apfu (atoms per formula units). Nevertheless, the different Pl-Ms solidus temperature generates a sensible discrepancy in the resulting pressure of emplacement (tab.4.16). Moreover, the absence of biotite in the pegmatite implies that the phengite composition provide (in this case) minimum pressure estimation.

On the other hand, additional constraints about the pressure of emplacement are provided by the primary magmatic assemblage. In fact, magmatic muscovite in granite has a lower stability limit of ~4Kbar (Chatterjee & Johannes, 1974; Anderson & Rowley; 1981).

Tab. 4-15: table summarizing the estimations of P-T conditions for the emplacement of tonalites, from DG suite (i.e. the roof of MC) and from GC. The different calibrations of phengite barometer are indicated as follows; (*): Simpson et al. (2000); (**): Massonne & Szpurka (1997). Temperature estimations were obtained by Hbl-Pl (Holland & Blundy, 1994) and Pl-Ms (Green & Usdansky, 1986).

complex	sample	assemblage	P ($\pm 0,6$ Kb)	T (± 40 °C)	point	
DGS	z200	Cpx-Hbl-Bt-Pl-Qtz	5,4	735	5b	core
DGS	SSL2	Cpx-Opx-Hbl-Bt-Pl-Qtz	5,4	735	4	core
DGS	z4	Hbl-Bt-Pl-Qtz	5,8	720	1a	core
DGS			5,2	724	1b	rim
DGS	z79b	Cpx-Hbl-Bt-Pl-Qtz	5,3	745	4	rim
DGS			4,9	750	5	core
GC	z73	Hbl-Bt-Ep-Pl-Qtz	4,7	770	2a	core
GC			4,9	750	2b	core
GC			4,9	740	6	rim
complex	sample	assemblage	P	T		
GC	SSL26.1a	Bt-Ms-Ep-Pl-Kfs-Qtz	5.5 (*)	693		
GC	SSL26.1a		6.0 (**)			
GC	SSL22	Ms-Pl-Kfs-Qtz	2.7 (*)	498		
GC	SSL22		3.0 (**)			

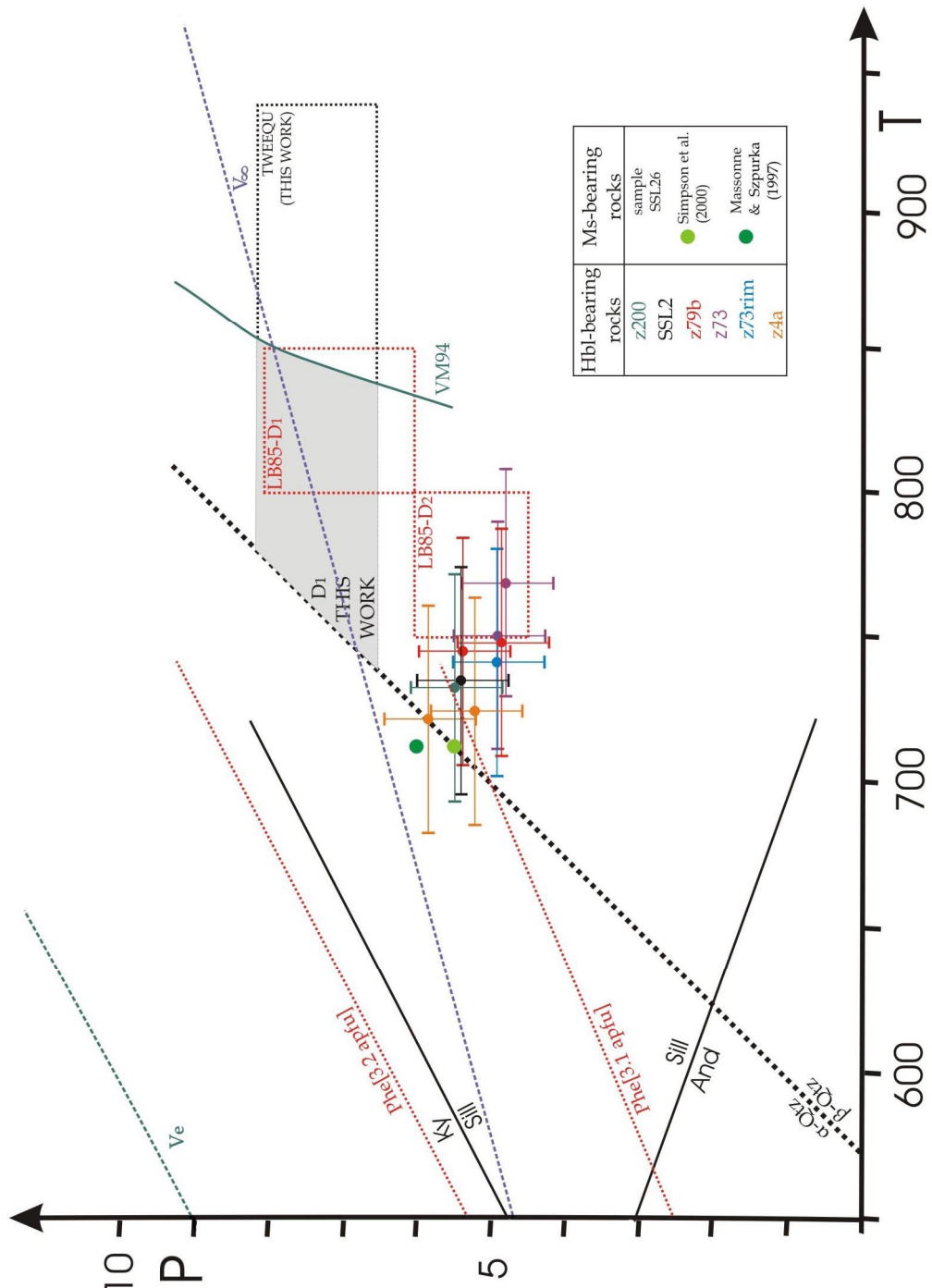


Fig. 4.8: P-T conditions for the emplacement of granitoids (DG suite and GC) and for D₁ and D₂ phases in the lower part of MC. Low to high quartz boundary after Gross & Van Heege (1973). Al₂SiO₅ after Holdaway (1971). The reaction curves for phengite → Qtz + K-feldspar + phlogopite + H₂O (Massonne & Szpurka, 1997) are reported for Si=3.1 and Si=3.2. LB85-D₁ and LB85-D₂ are from Libourel (1985). The line “VM94” represents the *Opx-in* curve, after Vielzeuf & Montel (1994). The undisturbed geotherm (V_e) and the maximally relaxed geotherm (V_∞) for reasonable heat supply after thrusting is after Thompson & England (1984). See discussion in chapter V.

4.3 Geochemical investigation on dolerite dykes (MC)

The high-temperature (pre-Alpine) foliation in Mafic Complex is transacted by dm-wide dolerite dykes, displaying ~1 cm-thick chilled margins. In contrast with the various mylonitized veins described in chapter II (which share the main solid-state fabric with the surrounding metagabbros and Grt-bearing gneisses), dolerite veins are completely undeformed at grain scale. Here, the primary subvolcanic texture (displaying a weak magmatic foliation) is marked by the assemblage containing nearly idiomorphic phenocrysts (0.5-2mm long) of brown hornblende, clinopyroxene and plagioclase. Analogous mafic dykes were found by Caby and Jacob (2000) in the SE portion of the nappe.

Mafic veins postdate the emplacement of Units I & II (i.e. 286 ± 1 Ma; Paquette et al., 2003), and predate the deposition of Lower Senonian sedimentary cover (Chapter I). Even if absolute dating on dolerite dykes are lacking, some constraints are provided by geochemical data. The sample selected for geochemical investigations was collected within S. Lucia Valley, in the surroundings of *Capo A l'Olive* locality; here, the dolerite vein is intruded in mylonitized melagabbro (Unit I, see chapter II).

The REE pattern (red line in Fig. 4.9) is nearly flat, showing a moderate LREE enrichment, being broadly comparable with the trace element compositions of ophiolitic basalts from Northern Apennine (black lines in Fig. 4.9; see also Marroni et al., 2002). REE abundances are ~20 times chondritic, where no evident fractionation occurs between LREE and HREE. Incompatible trace elements reveal normal to transitional MORB affinity for the ophiolitic basalts (Vannucci et al., 1993).

In contrast, Permian to Triassic dolerite dykes of Hercynian Corsica exhibit markedly different patterns, defined by decreasing trends from medium REE toward HREE. Here, LREE abundances are up to 60 times chondritic, whereas HREE abundances cluster around ~5-20 times chondritic (Cabanis et al., 1990; Marroni et al., 2001). These Permo-Triassic mafic dykes are regarded as transitional to tholeiitic within-plate basalts, injected during continental crust thinning, after the final stage of Hercynian orogenesis (Cabanis et al., 1990).

In conclusion, the strong geochemical analogies with the ophiolitic basalts suggest that dolerite dykes injected into gabbro-derived granulites can be regarded as MOR basalt with scarce depletion in LREE. Thus, data presented in this section suggest that these intrusions may represent a witness of the Jurassic magmatism related to Tethyan oceanization. This hypothesis is consistent with the 183 and 175 Ma thermal pulses recorded by granulite facies metasediments (Rossi et al., 2005), which indicate that during Jurassic times the S. Lucia basement was located within the thinned continental margin prior to oceanization.

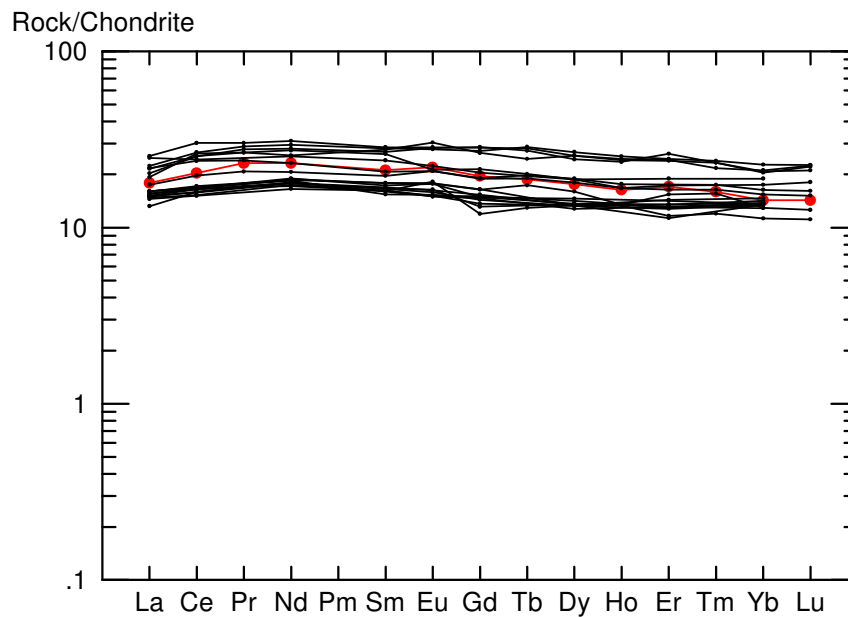


Fig. 4.9: Chondrite-normalized REE patterns of dolerite dyke from S. Lucia basement (red) and of basaltic rocks from the Northern Apennine ophiolites (black; External Ligurian Units; unpublished data from A. Montanini). Normalizing values after Eversen et al. (1978).

4.4 Geochronology

As previous geochronological investigations from authors were focussed on Mafic Complex, no age data concerning Granitic Complex are available from the literature. In the Mafic Complex, granulite-facies metasedimentary septa recorded a major anatectic event at 285.6 ± 1.0 (U-Pb dissolution method on zircon, Paquette et al., 2003). In addition, the detailed ion-microprobe U-Pb zircon dating carried out by Rossi et al. (2005) reveals that these paragneisses (which are representative of the late-Hercynian lower crust) recorded a long-lived history of thermal events, from the Variscan orogeny (~ 350 Ma) to the main Tethyan rifting and subsequent oceanization (~ 160 Ma).

During this work, $^{40}\text{Ar}/^{39}\text{Ar}$ method was applied to magmatic muscovite from a granitoid pegmatite (sample SSL22, see sample map for location). The analyses were performed at Nevada Isotope Geochronology Laboratory (University of Nevada Las Vegas). Details of the sample and analytical procedures are reported in the appendix section.

The age spectrum is discordant, with an initial age of ~ 215 Ma, followed by steadily rising ages to ~ 278 Ma at $\sim 80\%$ gas released, and slightly lower ages for the final two steps. There is no plateau age or isochron defined by these data; however, the form of the age spectrum does not indicate that excess argon is present. The total gas age (equivalent to a K/Ar age) is 258.1 ± 1.3 Ma. A possible interpretation is that the age at ~ 278 Ma may represent the cooling age after emplacement of the Granitic Complex. This interpretation is consistent with the emplacement age (300-310Ma) proposed by Rossi (1993).

The initial step at ~215 Ma (Fig.4.10), suggest that Granitic Complex has undergone a resetting event around the Triassic-Jurassic boundary. This age is broadly in agreement with the 195 ± 9 Ma plagioclase-whole-rock-garnet isochron from granulite-facies metasediments (Rossi et al., 2005). According to these authors, this age could be related to crustal thinning in a regional setting dominated by widespread extension (“onset of pre-Tethyan rifting”).

The lack of resetting events of Alpine age suggests that the maximum temperature during Alpine metamorphism was $\leq 400^\circ$. This is in agreement with the temperature estimates ($T \sim 300$ - 350°C) obtained on the basis on microstructures and quartz LPO from the main tectonic foliation in the Tomboni Conglomerate (section 1.4.2).

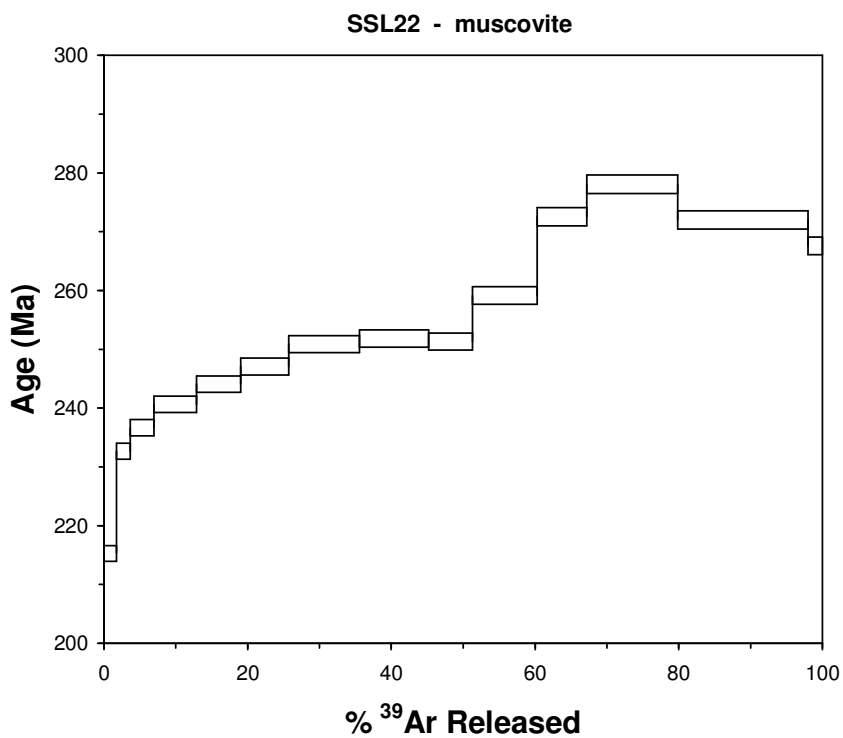


Fig. 4.10: muscovite Ar/Ar age spectrum from Ms-bearing pegmatite (sample SSL22).

enter data				cumulative			option	calc plateau age				spectrum plot		
step	Age	1s.d.	anal. Err.	% ³⁹ Ar	³⁹ Ar	frac. ³⁹ Ar	step	% ³⁹ Ar	Age	anal. Err.	step	% ³⁹ Ar	Age	1s.d.
1	215,31	1,32	0,76211	1,741	1,7	0,02	1	1,741	215,31	0,76211	1	1,741	215,31	1,32
2	232,68	1,38	0,747766	1,922	3,7	0,04	2	3,663	232,68	0,747766	2	3,663	232,68	1,38
3	236,67	1,38	0,700211	3,339	7,0	0,07	3	7,001	236,67	0,700211	3	7,001	236,67	1,38
4	240,62	1,39	0,688121	5,901	12,9	0,13	4	12,9	240,62	0,688121	4	12,9	240,62	1,39
5	244,09	1,40	0,677721	6,141	19,0	0,19	5	19,04	244,09	0,677721	5	19,04	244,09	1,40
6	247,07	1,41	0,685888	6,689	25,7	0,26	6	25,73	247,07	0,685888	6	25,73	247,07	1,41
7	250,90	1,44	0,700847	9,83	35,6	0,36	7	35,56	250,90	0,700847	7	35,56	250,90	1,44
8	251,86	1,45	0,726828	9,622	45,2	0,45	8	45,18	251,86	0,726828	8	45,18	251,86	1,45
9	251,30	1,42	0,667712	6,1	51,3	0,51	9	51,28	251,30	0,667712	9	51,28	251,30	1,42
10	259,13	1,47	0,696496	9,017	60,3	0,60	10	60,3	259,13	0,696496	10	60,3	259,13	1,47
11	272,54	1,55	0,738585	6,864	67,2	0,67	11	67,16	272,54	0,738585	11	67,16	272,54	1,55
12	278,05	1,57	0,738053	12,66	79,8	0,80	12	79,82	278,05	0,738053	12	79,82	278,05	1,57
13	271,98	1,54	0,729074	18,21	98,0	0,98	13	98,04	271,98	0,729074	13	98,04	271,98	1,54
14	267,56	1,51	0,706706	1,964	100,0	1,00	14	100	267,56	0,706706	14	100	267,56	1,51

5 SYNTHESIS, DISCUSSION AND TECTONIC INTERPRETATION

This section provides a synthesis of pertinent geological data, in order to summarize the pre-Alpine evolution of S. Lucia basement, and to compare the evolution of this “slice” of late-Hercynian lower crust with some analogous (and roughly coeval) lower crustal sections preserved in the Alps-Northern Apennines domain.

5.1 The age of deformation through the S. Lucia deep crustal section

5.1.1 Mafic Complex

The “peak” conditions during granulite-facies metamorphism in metasedimentary country rocks are dated at $286\pm 1\text{Ma}$ (Paquette et al., 2003). This metamorphic episode was likely induced by the emplacement of gabbroic magma, now testified by metagabbros of Units I & II (Paquette et al., 2003). As summarized by Bohlen & Mezger (1989), most of the now exposed granulite terranes were thermally equilibrated at moderate depth (i.e. ~20-30 Km), where their evolution is consistent with episodic metamorphic events caused by magmatic underplating. This concept is particularly reliable for most of the post-Hercynian (~280Ma) granulite facies terranes now exposed in the Alps (e.g. Ivrea, Sesia and Malenco Zones), where “peak” metamorphic conditions were acquired later than orogenic crustal thickening, in a context of high geothermal gradient and extensional tectonic setting (Wickham & Oxburgh, 1986; Brodie & Rutter, 1987). These late-Paleozoic granulite-facies terranes are distinct from orogenic Variscan granulites belonging to the high-pressure belt, extending from Sardinia to the Alps, through Corsica (i.e. Solenzara, Libourel & Vielzeuf, 1988). This belt is related to Variscan subduction, collision, and crustal thickening (age $>350\text{Ma}$, Giacomini et al., 2005 and references therein).

In the S. Lucia section, two diorite samples from Unit III (displaying isotropic to mylonitic microfabric) provided an emplacement age of $\sim 280\pm 2\text{Ma}$ (Paquette et al., 2003). As field relations and microstructures suggest that most of rock types in Unit III are roughly coeval (i.e. submagmatic fabric commonly overprint igneous contact, section 2.1.7.1), this emplacement age can be extended to the whole DGS. The fact that the post-emplacement metamorphic evolution of DGS probably did not reach granulite facies conditions (section 2.1.7.3) is consistent with the temperature discrepancy between dioritic to granitic magma ($T\sim 700\text{-}750^\circ\text{C}$, chapter IV) and gabbroic magmas from Units I & II ($900\text{-}1050^\circ\text{C}$, Libourel, 1985). We can infer that the emplacement age of DGS ($\sim 280\text{Ma}$) is reasonably close to the age of D_2 shear event (and D_2 assemblages) in the whole MC. This is suggested by several lines of evidences:

- (i) Pressure conditions prevailing during emplacement of DGS ($\sim 5.0\text{-}5.5\text{Kbar}$, chapter IV) correspond to those dominant during D_2 shearing in Units I & II ($4.5\text{-}6\text{Kb}$; $750\text{-}800^\circ\text{C}$; Libourel, 1985; see also P-T diagram in Fig.4.8);
- (ii) In the DGS, the preserved transition from submagmatic to high-temperature solid-state flow strongly suggests that D_2 shearing occurred immediately after (and possibly during the latest stages of) pluton crystallization (e.g. see discussion on quartz LPO in section 2.1.7.3; see also Fig.5.4).

- (iii) There are some evidences that some melt was (at least locally) present during and after the development of S_2 foliation (e.g. undeformed gabbroic melt crystallizing within boudin necks, or sealing small faults; section 2.1.5) testifying the occurrence of synmagmatic deformation in Units I & II. Analogous structures, described in the lower part of the Ivrea Zone, were interpreted in a similar way (Quick et al., 1992).

This assumption is consistent with the rates of pluton crystallization, as discussed by Paterson & Tobisch (1992). Crystallization and cooling rates depends on several factors (e.g. pluton size and shape, depth of emplacement, exhumation rates, initial temperature of the melt, country rocks temperature, etc.), being commonly between few yrs to few Ma. However, Paterson & Tobisch (1992) summarized that, for most of moderately sized plutons emplaced at mid crustal levels, the time needed for the transition from magmatic to submagmatic and HT solid-state flow is likely ~ 0.25 Ma. This is because to the rapid viscosity change (in a narrow temperature range) during crystallization. Analogous conclusions (a maximum crystallization time of $\sim 10^5$ yrs for plutons emplaced at mid crustal level) were reported by Karlstrom et al. (1993).

The gradual transition and the homogeneous kinematic framework between D_2 and most of D_3 shear zones is evidenced by field relations, microstructures and quartz LPO (section 2.1.7.4). These data suggest that the moderate-temperature D_3 overprint occurred in a geologically short time span.

On the other hand, D_3 overprint is spatially related to the development of the main solid-state fabric along the “mylonitic rim” of GC; this analogy includes also microstructures (i.e. compare section 2.1.7.4 with 3.3.2.3 and 3.3.6) and quartz LPO fabric (compare section 2.1.7.4b with 3.3.3).

Zircon crystals from Grt-bearing septa, embedded within the gabbro-derived granulites, recorded some additional (older) thermal events in the ~ 350 - 300 Ma-time span, which are broadly comparable with the late- to post-Hercynian magmatic activity in Corsica (Rossi et al., 2005) and in the whole Variscan chain (Bonin et al., 1998). However, within the Grt-bearing gneisses, neither meso- nor microstructures predating the intrusion of the gabbroic sequence seem preserved (Libourel, 1985; this work, chapter II). In these rocks, the main fabric was acquired synchronously with the main fabric in the surrounding metagabbros, as testified by geometrical arguments (this work, chapter II), by comparable P-T evolution (Libourel, 1985) and by geochronological data (Paquette et al., 2003).

Zircon crystals recorded also some important thermal events at ~ 240 and ~ 175 Ma, which are likely related to the onset of pre-Tethyan rifting (Rossi et al., 2005). These thermal pulses were likely connected to the emplacement of MORB-type dolerite dykes. The emplacement of subvolcanic veins could be broadly contemporaneous with the development of pre-Alpine cataclasites (section 1.3), which were related to the final stages of basement exhumation.

5.1.2 Granitic Complex

The age of emplacement and deformation of GC is poorly constrained by direct geochronological data, as the only available radiometric age is represented by the ~ 278 Ma Ar/Ar cooling age from Ms-bearing pegmatite (chapter IV). However, some temporal constraints are provided by overprinting relations with the adjacent DGS. In fact, from the

previous section we can conclude that the main solid-state fabric along the “mylonitic rim” developed broadly synchronously with S_3 foliation in DGS, i.e. likely ~1-2Ma (or less, Paterson & Tobisch, 1992) after the emplacement of the DGS.

In general, it may be difficult to establish whether a solid-state overprint (even concordant with pre-existing magmatic fabric) occurred without significant temporal gap. However, the nearly continuous transition from submagmatic flow toward high-temperature and moderate-temperature solid-state flow (sections 3.3.2 to 3.3.4) is corroborated by quartz LPO, by the invariable orientation of the lineation, and by the persistence of sinistral shear sense.

To summarize, geochronological data provide some important constrains for the evolution of the S. Lucia section: the ~286-280 Ma time span is characterized (in the MC) by a close interplay between gabbroic to granitic magmatic activity, granulite-facies metamorphism and submagmatic to high-temperature solid-state deformation. Despite some analytical uncertainty (section 4.4), the ~278 Ma cooling age from GC suggests that a rather rapid cooling of the whole section (down to ~400°C, i.e. the closure temperature of Ar/Ar system in muscovite) occurred after the high-temperature stages. At ~175 Ma the S. Lucia basement was likely close to the surface, and was intruded by dolerite dykes with MORB affinity. Further investigations should be focused on the emplacement age of GC, as the timing of this igneous crystallization could provide some additional constraints about the temporal relations between MC and GC.

5.2 The restoration of Permian geometries

The consistent orientation of the mesoscopic fabric shown by all rock units represents a striking feature of the whole S. Lucia deep crustal section (Fig.5.1). The analogy concerns the attitude of both foliation and lineation, acquired during (sub-) magmatic and solid-state flow. This idea, qualitatively proposed by Caby & Jacob (2000), is testified by the large number of measurements systematically collected during this work (~800 and ~500 data for foliation and lineation, respectively). Moreover, the generalized sinistral shear sense characterizes any solid-state fabric (S_2 foliation in MC, mylonitic foliation along the “mylonitic rim” in GC), but it was likely prevailing during (sub-) magmatic flow within GC (section 3.2.3). The dominant shear sense during magmatic (and sub-magmatic) flow is much less constrained in the DGS (see discussion in chapter III, section 3.2.3), despite the local occurrence of S-C fabric might suggest that sinistral shearing was prevailing during magmatic stage also (section 2.1.7.2). Finally, the sporadic retrograde shear zones in Units I & II (which preferentially nucleated within Bt-rich, “restite” layers) are mostly not kinematically separable from the main fabric.

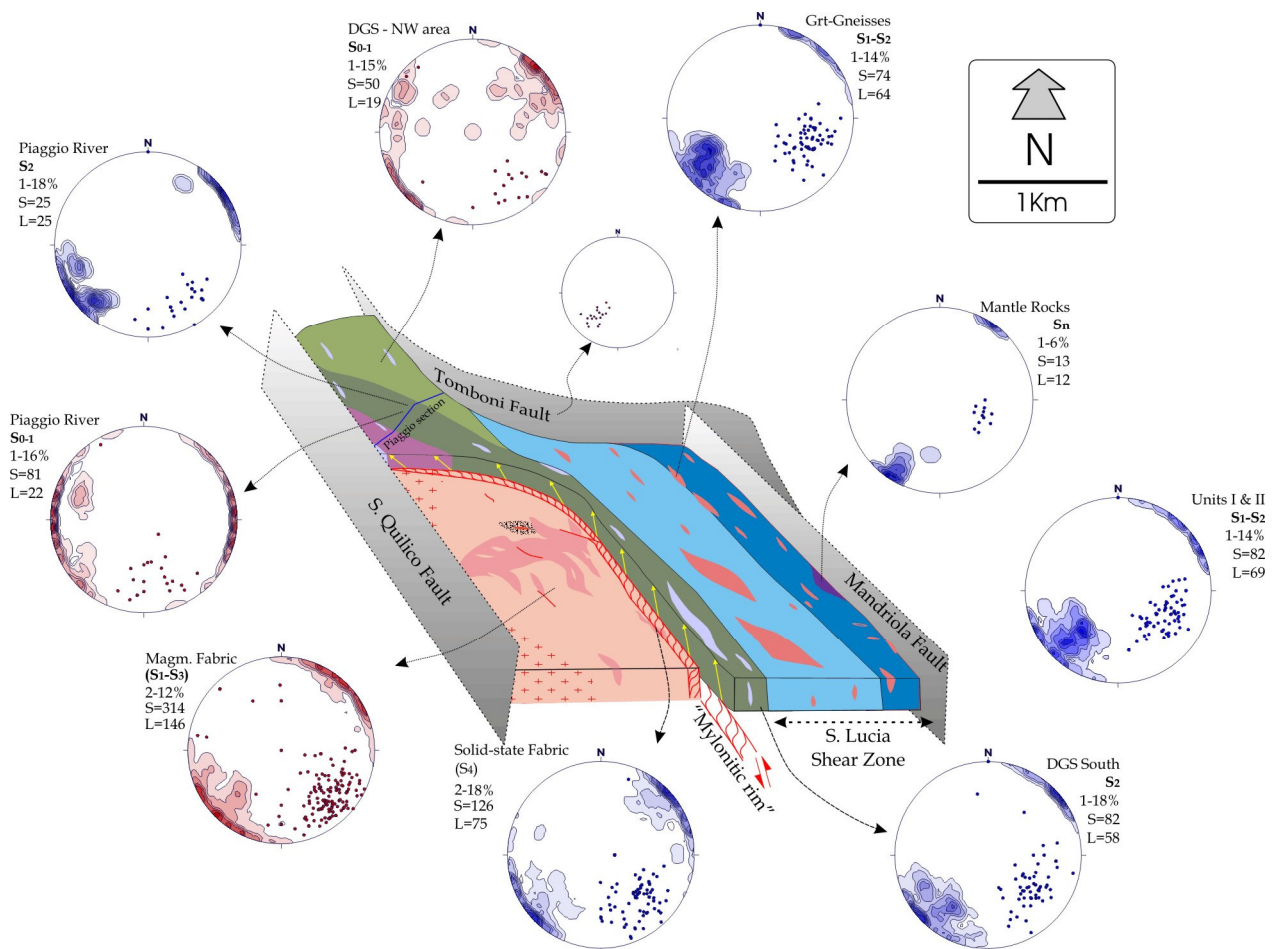


Fig. 5.1: tectonic block diagram of the western portion of S. Lucia basement. Lower hemisphere, equal area plots summarize the orientation of foliation poles and lineation for (sub-) magmatic (red pole figures) and solid-state fabric (blue pole figures). The poles of S_2 mylonitic foliation along the (Alpine) Tomboni Fault are also indicated.

Caby & Jacob (2000) proposed that the present-day sub-vertical geometry of the Mafic Complex represent a primary (i.e. Permian) feature, related to the opening of a Red Sea-type rift. According to this model, the diapiric ascent of mantle slices drove the emplacement of layered gabbros on sub-vertical planes. This viewpoint is based on the assumption that, in the western portion of the nappe, primary geometrical relations between basement and cover are preserved (showing sub-horizontal boundary).

As partly discussed in the previous chapters, this model has some problems:

- (i) The main structural evolution in the basement developed around 280Ma (Caby & Jacob, 2000; Paquette et al., 2003; this work), whereas the deposition of sedimentary cover occurred around "Middle" Cretaceous (i.e. ~100Ma, Durand Delga, 1984). Thus, no geological record is preserved concerning the kinematic evolution of S. Lucia basement in the ~280-100Ma-time span;
- (ii) The suggestion of a largely preserved sedimentary contact as geometrical reference contradicts several generations of field investigations (i.e. Ritsema, 1952; Rieuf, 1980; Du Chaffaut, 1980; Rossi et al., 1994), even in the restrict sector examined by Caby & Jacob (2000), in the S. Lucia Valley (this work, section 1.4).
- (iii) The sedimentation of Tomboni Conglomerate likely occurred in a context of tilted basement blocks (Fig.4 in Durand Delga, 1984). Thus, during the deposition of

Tomboni Conglomerate, the Cretaceous erosion surface was not necessarily sub-horizontal;

- (iv) The sector examined by Caby & Jacob (2000) is characterized by an E-W trending, Km-scale, F_2 (Alpine) recumbent fold, which cause the steepening of the basement-cover boundary (Fig.106 in Rieuf, 1980). Thus, in the area between mount Tomboni and S. Lucia Valley, this boundary is inclined $\sim 40-60^\circ$ toward NE (“Tomboni Fault” in Fig.5.1 and 5.2b).

In order to verify the qualitative model proposed by Caby & Jacob (2000), the attempt of restoration of pre-Alpine geometries in the basement by using the basement-cover boundary is proposed in Fig. 5.2. Here, the orientation of rotational axis ($310^\circ/00^\circ$) corresponds to the mean strike of basement-cover boundary in the sector between mount Tomboni and S. Lucia Valley (Fig.5.1). The rotational angle (50°) and the counterclockwise rotational sense (looking NW) are those needed to restore the basement-cover surface to the horizontal position (Fig.5.1 and 5.2). In the equal area net, the position of the mean lineation (before and after rotation) and the restored mean foliation planes are reported for the each unit of the S. Lucia section. In the rotated coordinates, the mean foliation planes are moderately dipping (i.e. $\sim 20-40^\circ$) toward NE, and the mean lineations are gently dipping eastward. Taking into account that sinistral shear sense is prevailing in the present-day coordinates (Fig.5.2b), the restored geometries implies a “top to west” transport (i.e. thrusting) of MC respect to GC (Fig.5.2c).

In summary, the analytical restoration proposed in Fig.5.2 demonstrates that the model proposed by Caby & Jacob (2000) is not consistent with field relations and with the other lines of geological evidences. In the absence of any external geometrical reference, a reliable Permian orientation could be achieved by careful thermobarometric estimation, systematically collected from coeval assemblages along the complete section (i.e. $\sim 5\text{Km}$). Analogous investigations were performed by Henk et al. (1997) and by Demarchi et al. (1998). As also discussed in the next section (5.3.1), other indications concerning the original orientation of the S. Lucia section are suggested by several lines of evidences. Lardeaux & Spalla (1991) documented that the late-Paleozoic evolution of lower crustal rocks from Sesia Zone (which is interpreted as an analogous of the Ivrea Zone, Dal Piaz et al., 1972) exceeds the high geothermal gradient for maximally relaxed geotherm (Thompson & England, 1984). This gradient is also plotted in Fig.4.8 and 5.3, highlighting the comparable intermediate- to low-P and high-T character of the S. Lucia granulites. This high geothermal gradient is not consistent with thickening processes, being proper for extensional tectonics (Lardeaux & Spalla, 1991 and references therein). Analogous results were obtained by Gardien et al (1994) for the pre-Alpine evolution of lower crustal rocks from Valpelline area (Western Alps). Moreover, thermal models for pervasively ductile lower crust (McKenzie, 1978) predict that all points of thinned crustal sections undergo cooling during crustal-scale stretching. In contrast, crustal thickening causes upward migration of isotherms, involving regional metamorphism (England & Thompson, 1984). On the other hand, the widespread lower Permian extensional tectonics has been largely documented in the Hercynian chain, as will be discussed in the next section.

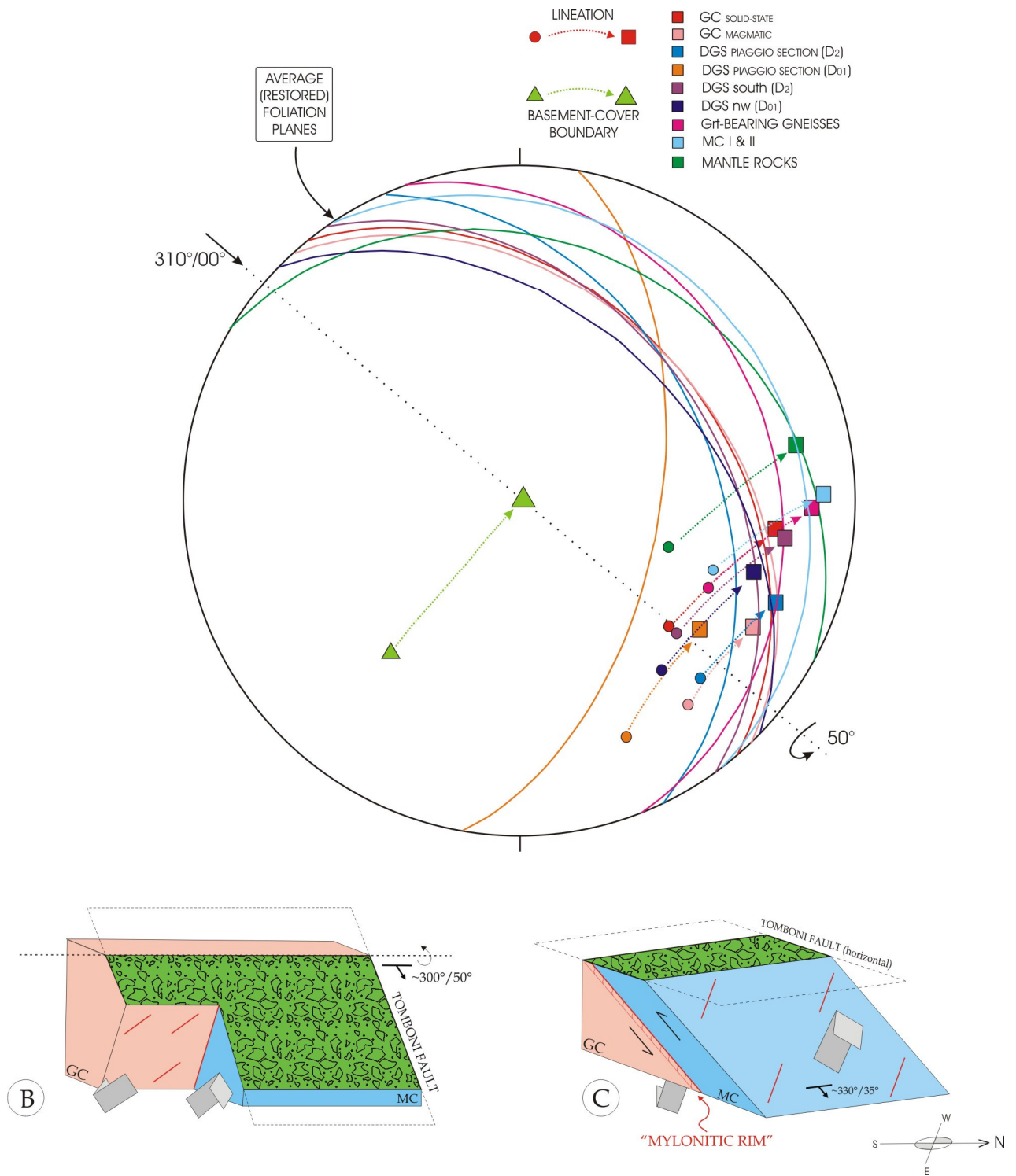


Fig. 5.2: [A] equal area net (lower hemisphere projection) showing the main fabric elements from the S. Lucia deep crustal section. [B]: Block diagram showing the present-day geometrical relations between pre-Alpine basement and Tomboni Fault, which represent the boundary with Cretaceous cover. [C]: hypothetical restoration of geometrical framework at "Middle" Cretaceous. Further explanations in the text.

5.3 Tectonic interpretation

5.3.1 The S. Lucia section in the Late Paleozoic regional framework

During the late Paleozoic (i.e. ~300-250Ma), the Variscan domain was characterized by an intense basic and acid magmatic activity, which is interpreted to reflect the combination of lithospheric thinning and asthenosphere upwelling (Piccardo et al., 1992; Quick et al., 1992) or the late-orogenic collapse of the fold belt (Lardeaux et al., 1994). Magmatic underplating caused widespread granulite-facies metamorphism into an already thinned mid to lower crust (Voshage et al., 1990). Moreover, this period is characterised by an active extensional (Bonin et al., 1998) or transtensional tectonic regime (Arthaud & Matte, 1977; Zingg et al., 1990). In the Alpine region, the close relationship between Permian LP-HT granulite-facies metamorphism and ductile normal shear zones is reported by several authors (e.g. Brodie & Rutter, 1987; Malavieille et al., 1990; Rutter et al., 1993; Trommsdorff et al., 1993; Hermann & Müntener, 1996; Marroni et al., 1998; Ledru et al., 2001).

In Corsica, the 305-270 time-span was characterized by intense magmatic activity in a dominant extensional setting (Paquette et al., 2003; Rossi et al., 2005). As an example, the metamorphic evolution of the Zicavo basement (Thévoux-Chabuel et al., 1995) testifies that extensional shearing was active during the emplacement of the calc-alkaline granitoid suite (300-280Ma, Paquette et al., 2003). In northern Sardinia, the age of the post-collisional extensional tectonic (constrained by emplacement ages, metamorphic ages and sedimentary data) occurred in the ~310-270 Ma time span (Carmignani et al., 2001). During the same period, in the Axial Zone of Sardinia, HT/LP assemblages overprinted the Barrovian amphibolite-facies assemblages (Elter et al., 1999 and references therein). According to Carmignani et al. (1993), the late Carboniferous-Early Permian extension in the Axial Zone likely started by magmatic underplating, and subsequently propagated toward the external zones by normal and strike-slip shear zones.

It is commonly thought that the large-scale compositional banding in the present-day deep continental crustal might be sub-horizontal. This is mainly suggested by the information provided by crustal reflection studies, indicating that the present-day lower crust is mostly characterized by near horizontal, flat-lying markers (e.g. Smithson et al., 1986). Moreover, in regions affected by extension, some gently dipping reflectors, transecting the lower crust and the upper mantle, are interpreted as low-angle, lithosphere-scale detachment faults (Beach, 1986). These observations fit the synthetic reflection data of Fountain (1986), applied on the Ivrea and Strona-Ceneri Zones. Furthermore, as summarized by Brodie & Rutter (1987) and by Snoke et al. (1999), the lower part of the Ivrea section (characterized by interlamination of meta-igneous mafic rocks and metasediments) exhibit the appropriate properties of high-reflectivity (namely high velocity contrasts) to reproduce the results obtained by the present-day seismic surveys (e.g. ECORS, etc.). Moreover, thermobarometric studies (Henk et al., 1997; Demarchi et al., 1998) suggest that the present-day steep structure (at least in the central and southern portions of the Ivrea Zone) derives from ~90° tilting of a pre-existing low-angle structure. The Tertiary steepening of planar structures of the Ivrea Zone (related to the Neogene movements along the Insubric Line) is also deduced by several lines of regional geology, as summarized by Schmid et al. (1987).

In the case of S. Lucia deep crustal section, the occurrence of a thick (i.e. at least 1 Km-wide) granulite-facies shear zone, indicates that strain in the lower crust was homogeneously distributed on a large scale (Coward, 1984). The non-coaxial character of the deformation and the invariable sinistral shear sense, generalized along the whole section, recalls the models of uniform-sense, crustal-scale normal shear zones (Wernicke, 1984). After Handy & Zingg (1991), the strike-slip Permian tectonics in the Alpine region was characterized (at shallow crustal levels) by high-angle discrete faults, which were connected with gently dipping to sub-horizontal, wide shear zones at lower crustal levels (Fig.5.6A). Thus, in analogy with that proposed for the Permian evolution of the Ivrea Zone (Quick et al., 1992; Snoke et al., 1999), for the Malenco Zone (Trommsdorff et al., 1993) and for granulitic rocks from Northern Apennines (Marroni et al., 1998), here we can envisage that the granulite-facies shear zone represents a segment of a low-angle, Km-scale deep crustal detachment fault (the “*S. Lucia shear zone*”; Fig.5.6B). In analogy with the compositional zoning in the Ivrea zone, mantle rocks and melagabbros are located at the base of the MC (now located at East, and bounded by the Mandriola Fault of Alpine age), whereas the more differentiated rocks are located near the roof (DGS, Fig.5.6C). The same is valid for GC, where coarse tonalites are replaced westward by the more evolved leucogranites (i.e. compare Fig.5.1 and 5.6C). Moreover, this model fits the findings of Pin (1989), who suggested that the compositional zoning in MC is related to the emplacement of anastomosing sills, incorporating septa of country rocks in a lower crustal setting (Fig.5.6A). Analogous emplacement model was proposed for the Ivrea Zone also (Rutter et al., 1993). However, in the absence of precise geometrical and kinematic references, the choice of a low-angle tectonic framework remains questionable.

The unroofing by lateral displacement (i.e. along low-angle shear zones) is probably one of the most convincing models to justify the fast adiabatic decompression of the former granulite-facies assemblages (i.e. ~2 Kbar in ~6 Ma, at ~700-800°C, chapter IV and section 5.1; see also Fig. 5.3). This high-temperature evolution was followed by a rather rapid cooling, as suggested by syndeformational microstructures preserved along the “mylonitic rim” of GC, indicating that deformation continued (likely without any significant temporal gap) down to ~400°C. The geothermal gradient for maximally relaxed geotherm (Thompson & England, 1984) provides pressure estimation of ~3.5-4.0 Kbar, suggesting that the Early Permian exhumation of the S. Lucia section ended at the base of the upper crust (~10 Km).

Some lower temperature shear zones (likely developed in the 350-400°C temperature range; sections 2.1.7.4 and 3.3.5), kinematically coherent with higher temperature mylonites, might represent further late-Paleozoic syndeformational cooling or, in alternative, could be regarded as distinct and localized Mesozoic reactivations, possibly related to the final stages of basement exhumation (during Jurassic?).

5.3.2 Geodynamic implications for the Tethyan rifting

In the Alpine region, the occurrence of granulite-facies rocks along passive continental margins is commonly used as an evidence to support the rifting model of asymmetric extension by low-angle detachment fault. This lithosphere-scale normal shear zone, which was likely active during Middle to Late Jurassic, should be responsible of the exhumation

of the lower crust and the subcontinental margin at the lower (Adria) plate margin (Lemoine et al., 1987; Vissers et al., 1991). Consistently, most of the lower crustal slices from the Alps-Northern Apennines systems are generally referred to the Adria continental margin, respect to the Jurassic Western Tethys. Although the paleogeographic origin of S. Lucia nappe is still poorly constrained (e.g. Caby & Jacob, 2000), this unit is commonly referred to the European margin, respect to the Mesozoic Western Tethys (e.g. Durand Delga, 1984; Rossi et al., 2005). Thus, the occurrence of granulite-facies rocks along the European continental margin apparently contradicts the model of asymmetric “low-angle” Jurassic rifting.

However, in the Alpine region several lines of evidence suggest that the Permian extension and Jurassic rifting represent two distinct and largely unrelated tectonic events (Zingg et al., 1990; Hermann & Müntener, 1996). For example, Permian extension in Malenco Zone was followed by isobaric cooling, whereas exhumation occurred well later, through Jurassic isothermal decompression (Fig. 5.3; Müntener et al., 2000). In contrast, granulites from Sesia Lanzo, Valpelline and S. Lucia zones experienced nearly isothermal decompression during Permian times (Lardeaux & Spalla, 1991; Gardien et al., 1994; Libourel, 1985; this work), which was likely unrelated to the later opening of the Tethyan Ocean. In other words, these Permian granulites were already at upper crustal levels before the Jurassic rifting. Along the Galicia margin (which is often considered as a present-day equivalent of the Jurassic Adria margin) zircon fission track ages document that granulitic rocks were already incorporated into the upper crust during Permian, i.e. ~150 Ma before the rifting phase that led to the opening of the Northern Atlantic Ocean (Fügenschuh et al, 1998).

In conclusion, even if several types of data indicate that Permian granulites are more or less intimately associated with ophiolitic rocks at the ocean continent transition (e.g. Marroni et al., 1998; Rossi et al., 2005; this work), the occurrence of granulite-facies rocks alone cannot be taken as an indication of syn-rift exhumation of lower crust along the continental margin. On the other hand, the occurrence of granulites along the Upper plate (i.e. European) margin does not contradict the model of asymmetric Jurassic detachment fault, which is also supported by sedimentological and structural data (e.g. Eberli, 1988; Froitzheim & Manatschal, 1996).

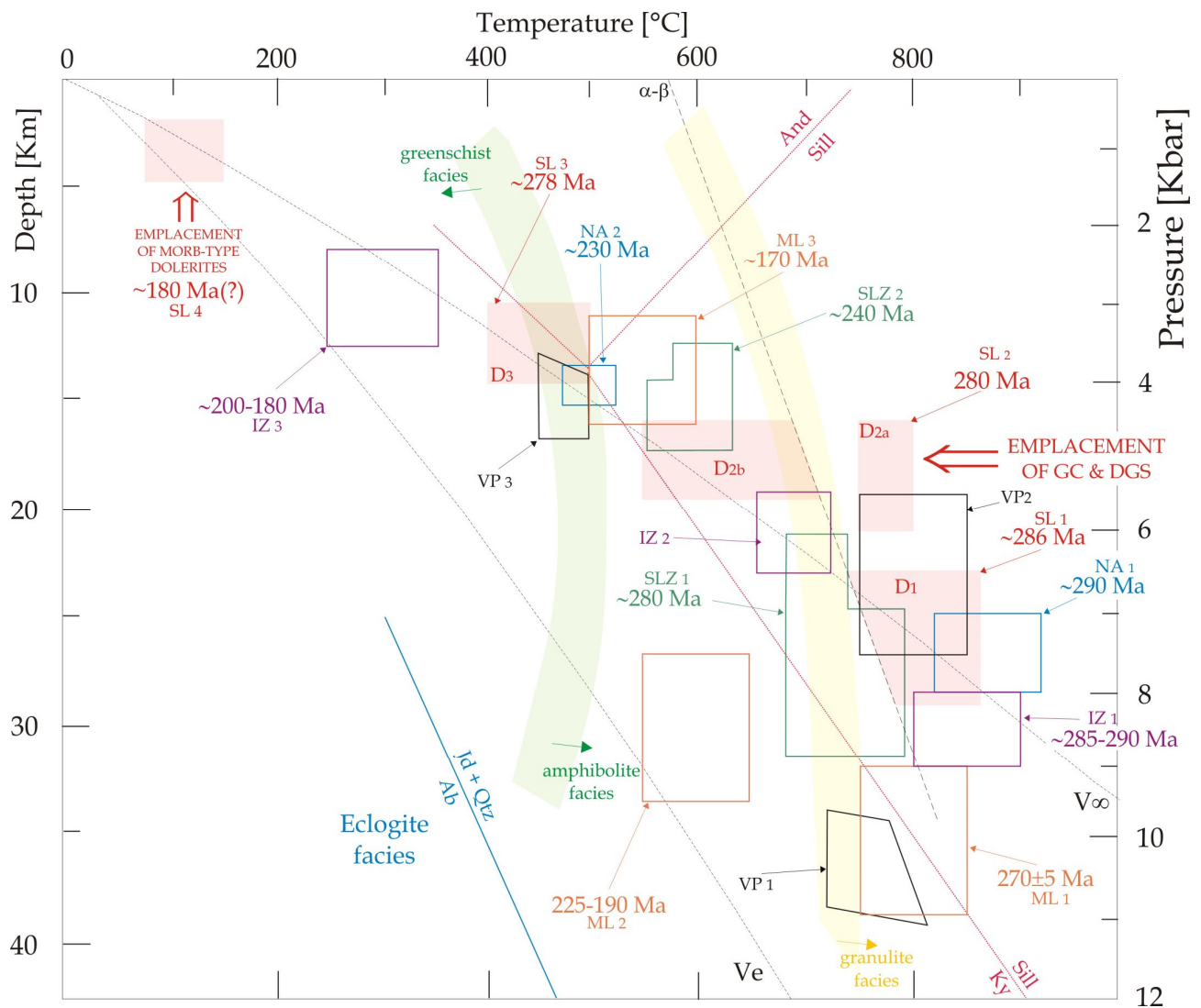


Fig. 5.3: correlation of P-T-t path of some Late-Hercynian lower crustal section from Alps-Northern Apennines system. [IZ₁] Ivrea Zone, after Quick et al. (2003). [IZ₂] after Henk et al. (1997); [IZ₃] Pogallo Zone, after Handy (1987). [ML] Malenco Zone, after Müntener et al. (2000). [NA] Northern Apennines, after Marroni et al. (1998). [SL]: S. Lucia, after Libourel (1985) and this work. [SLZ] Sesia Lanzo Zone, after Lardeaux & Spalla (1991). [VP] Valpelline Zone, after Gardien et al. (1994). Granulite, amphibolite and eclogite facies domains after Spear (1993). Al₂SiO₅ stability fields after Holdaway (1971). α-β: low- to high-quartz boundary after Gross & Van Heege (1973). The undisturbed geotherm (Ve) and the maximally relaxed geotherm (V_∞) for reasonable heat supply after thrusting is after Thompson & England (1984).

5.4 The emplacement of granitoid bodies along the shear zone

Melt pathways through the crust may be influenced by the strong mechanical anisotropy represented by pre-existing shear zones ("*melt channelling*", see review in Rosenberg, 2004) or, in contrast, the presence of melt may promote the nucleation of shear zones ("*melt-enhanced deformation*", Hollister & Crawford, 1996). A close interplay between these end member processes is probably common in several geological settings (e.g. Brown, 1994; Brown & Solar, 1998a). Moreover, shear zones also play an important role in providing the space necessary for magma emplacement (e.g. Hutton, 1988a and 1988b).

In our case, despite the original regional framework is lacking (owing to the nappe situation), the 1Km-wide S. Lucia shear zone can be regarded as representative of large scale, Early Permian regional deformation. The older history of this shear zone occurred at deep crustal levels, as testified by D_1 assemblages recorded only by Units I & II of MC ($P \sim 7.3 \pm 0.8$ Kbar, chapter IV; see also Libourel, 1985). Here, primary features within gabbroic rocks were severely overprinted by granulite facies solid-state overprint, whereas syntectonic features are only sporadically preserved (section 2.1.5). DGS were intruded along the S. Lucia shear zone, during its retrograde evolution (i.e. ~ 5 Ma after the granulite facies metamorphic peak). Moreover, GC was emplaced at the same crustal level and approximately at the same time of DGS (section 5.1). Of course, GC could have been detached from its original wallrock during solid-state deformation (testified by the "mylonitic rim" preserved along the NE margin). Nevertheless, because of the strong homogeneity of fabric orientation respect to MC (Fig. 5.1), we can infer that GC was emplaced under the same stress field testified by the S. Lucia shear zone. In summary, we are dealing with two different and composite granitoid complexes, which were likely intruded along (or at margins of) a large-scale shear zone. For the reasons explained previously, here we infer that granitoid plutons emplaced along a low-angle detachment fault (Fig.5.6B). However, the discussion proposed here on the relationships between magmatism and deformation is largely independent from the actual Permian orientation of the S. Lucia section.

Plutons inferred to have been emplaced during regional deformation commonly exhibit elongate shapes. They display high aspect ratio and long axis parallel to the shear zone margins, and/or parallel to the structural trend in the host rocks (Paterson et al., 1989). Cleavage triple points commonly occur near the ends of the plutons (within "strain shadow" respect to the trend of regional foliation; Paterson & Tobisch, 1988). Moreover, synkinematic porphyroblasts commonly developed within the pluton aureole (Vernon, 2004). Obviously, all these criteria are not suitable in the case of S. Lucia section.

On the other hand, the pattern of (sub-) magmatic fabric in both DGS and GC exhibits some striking similarities with the "folded to rectilinear" end-member type of magmatic fabric patterns described in Paterson et al. (1998). This fabric type is typical of plutons that are compositionally heterogeneous over short distances; in these cases, the magmatic lineation is usually well developed, and magmatic structures commonly overprint igneous contacts. Moreover, these plutons commonly contain magmatic folds, showing the same geometrical arrangement of similar structures in host rocks. Because these granitoid bodies commonly exhibit complete coupling with country rocks (respect to both foliation and lineation), the fabric pattern is inferred to reflect strain of magma caused by

regional deformation. In contrast, the contribution of internal processes to fabric development is considered negligible or subordinate (Paterson et al., 1998).

By definition, in plutons emplaced during regional deformation, the (sub-) magmatic fabric is overprinted by solid-state fabric (Paterson et al., 1989). In these cases, several generations of subsequent superimposed fabrics should be preserved, testifying the transition from magmatic flow toward high-temperature and moderate temperature solid-state flow (i.e. during syndeformational crystallization and cooling). However, several case studies demonstrate that this general assumption is often unverified in syntectonic plutons (e.g. Spanner & Kruhl, 2002).

The preservation of submagmatic features and the structural style of the subsequent solid-state overprint depend on several factors (e.g. see discussion in Miller & Paterson, 1994). At shallow crustal levels, pluton emplacement and crystallization processes are commonly much faster than regional deformation events, which usually span over several tens of Ma (Paterson & Tobisch, 1992). Consequently, syntectonic features are unlikely preserved in these cases. In contrast, at deep crustal levels, owing to the slower cooling rates, synmagmatic deformation features are largely overprinted by subsequent solid-state deformation. Thus, syntectonic structures can be better preserved in pluton emplaced along a shear zone, at mid crustal levels, where strain rates likely approach the rates of magmatic processes (Paterson & Tobisch, 1992).

Tribe & D'Lemos (1996) pointed out that the dominant solid-state imprint observed in syntectonic plutons likely develops at a temperature equivalent to the ambient temperature of the host rocks at the time of emplacement. In our case, the pressure of emplacement for DGS and GC is ~5 Kbar (chapter IV); by adopting the high geothermal gradient (V_{∞}) from Thompson & England (1984), which is appropriate for P-T evolution (from D₁ to D₂ phases) of MC (Fig.5.3), we can infer that the maximum country-rocks temperature (at the time of emplacement) was around 500-550°C. Gapais (1989) reported that this temperature range corresponds to a major microstructural and rheological boundary (the "*semibrittle-ductile transition*"; see also Voll, 1976). Analogous results were obtained by using paleopiezometry along a crustal section (the "*greenschist-amphibolite facies rheological boundary*"; Zulauf, 2001). As discussed in section 3.3.6, in quartzofeldspathic rocks, this transition coincides with the most important switch in quartz and feldspars behaviour (Stipp et al., 2002; Tullis & Yund, 1987). Briefly, below ~500-550°C, the high strength contrast between these phases involves extreme grain refinement, strain localization and development of shear bands (e.g. Simpson, 1985). Above this limit, the strength contrast between quartz and feldspars is markedly reduced, allowing the development of more homogeneous and pervasive fabrics (Gapais, 1989). Thus, across the rheological boundary, the most remarkable changes are in feldspars (e.g. Tullis & Yund, 1987).

In our case, both complexes exhibit a nearly complete continuum of down-temperature deformation. Furthermore, because the two adjacent granitoid complexes were emplaced under the same regional stress field, they likely experienced comparable strain and cooling rates. Therefore, one should expect analogous structural style between GC and DGS.

However, a closer observation on the spatial distribution of the different generations of structures indicates that the two complexes display different sensitivity in recording

subsequent superimposed fabrics. In fact, the subsolidus evolution of GC mainly developed in the ~400-500°C temperature range (section 3.3.2). Consistently with the muscovite cooling age, these observations suggest that after (or during the latest stages of) pluton crystallization, the temperature of pluton margins fell reasonably quickly toward that of the ambient country rocks. In contrast, within the DGS, the solid-state overprint mainly developed in the ~550-700°C temperature range (section 2.1.7.3).

Moreover, also the spatial distribution of the solid-state is markedly different. Within GC, the solid-state fabric is strictly confined along the NE pluton margin. In contrast, within DGS two main structural domains are detectable (see Fig.5.6C): in the NW sector, ~100m-spaced D₂ shear zones anastomosing around “low strain” domains, where submagmatic features are preserved. In contrast, in the SE portion of DGS, D₂ shear zones are much more closely spaced, and submagmatic features are less frequently preserved. In both domains, the sporadic D₃ overprint mainly took place along mechanical discontinuities, such as aplite veins and along the boundary with GC.

The cause of this evident discrepancy in structural style might be related to bulk composition of the adjacent plutons. In fact, GC is dominated by quartz/mica-rich leucogranites whereas, within DGS, intermediate compositions (i.e. Hbl-rich Qtz-diorite to tonalite) are largely prevailing. The compositional control of deformation is inferred to play a fundamental role in the deformation behaviour during both submagmatic and solid-state flow, as emphasized by Vernon & Flood (1988) and by Paterson et al. (1989).

Submagmatic features are more easily preserved in rocks with compositions far from the minima in granite system (Bouchez et al., 1992), such as tonalites and Qtz-diorites. This is in agreement with what observed within the S. Lucia granitoids, where submagmatic features are more commonly preserved within melanocratic granitoids of DGS.

The strong alignment of tabular Hbl and Pl grains, acquired by coarse-grained melanocratic granitoids during magmatic to sub-magmatic flow (e.g. Fig.2.58) was pervasively overprinted during high-temperature D₂ shearing, which was active during progressive cooling down to ~550°C (Fig.5.4). Because feldspar is dominant within intermediate granitoids (i.e. > ~50% in Qtz-diorite), during subsequent further cooling (transition to D₃ phase) dramatic strain hardening occurred, promoting strain partitioning into adjacent weaker domains, represented by leucogranitoid-dominated “mylonitic rim”. The strain partitioning along the GC-DGS boundary was likely enhanced by the contrasting grain size in the “starting material” (i.e. coarse-grained Qtz-diorite vs. two-mica microgranite). The sporadic preservation of high-temperature mylonitic microfabric in GC (section 3.3.4) was possibly allowed by the coarse grain size of the protholith (i.e. porphyritic leucogranite and Ms-bearing pegmatite).

MC	Inferred type of flow	Age	P-T conditions	Quartz LPO fabric	Quartz regime	Feldspars regime	Key microstructures in quartzfeldspathic rocks	Mafic rocks
Units I & II	D ₁	286 ± 1 Ma (+)	P = 7.3 ± 0.8 Kbar T = 800 ± 50°C (x) ----- P = 4.5 - 6.0 Kbar (x)	(Domainal Fabric) ~100°	GBM II (β-Qtz) ----- GBM II (β-Qtz) ↓ GBM I (α-Qtz)	SGR (GBM?) ----- SGR	Striped gneiss Qtz Pl 250μ	Fig.2.20 Opx → Opx' → Pl 100μ Opx → Bt+Qtz (metapelites) Opx → Hbl+Qtz (metagabbros)
	D _{2a}	~280 Ma	T = 750 - 800°C (x) ↓ ~ 550 - 680°C	~90°	GBM II (β-Qtz)	Q-F diffusion creep ----- cataclasis	Qtz Kfs 250μ	Hbl Bt 1mm [Fig.2.58]
Unit III (DCS)	D _{2a}	~280 Ma	P = 5.4 ± 1 Kbar T ≥ ~ 680 - 800°C	~100°	GBM II (β-Qtz) → GBM I (α-Qtz)	SGR	250μ	Opx → Hbl+Qtz
	D _{2b}	~280 Ma	T ~ 550 - 680°C	~85°	SGR	Nucleation & growth ----- BLG ----- Cataclasis	500 μ	Hbl → Act
D ₃	moderate to LT solid-state	~278 Ma	T ~ 400 - 550°C ↓ T ~ 350 - 400°C	~35° → ~30°	BLG		Qtz	

Fig. 5.4: summary of the available data for Mafic Complex, collected from geochronology, mineral chemistry and microstructural investigations. Data from this work except: (+) Paquette et al., 2003 and (x) Libourel, 1985.

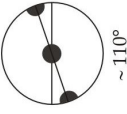
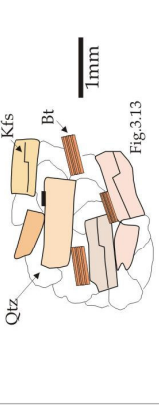
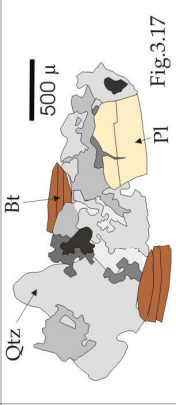
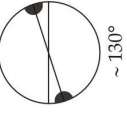
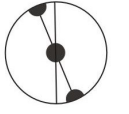
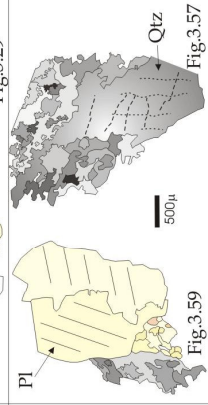
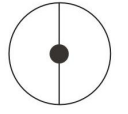
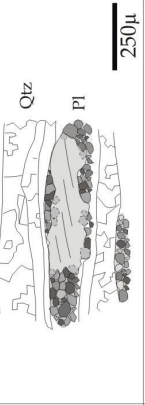
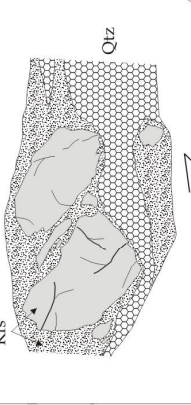
GC	Inferred flow type	Age	P-T conditions	Quartz LPO fabric (with mean opening angle)	Quartz regime	Feldspars regime	Key Microstructures quartzofeldspathic rocks
D1	magmatic	> ~278 Ma	P = 5.0 ± 1 Kbar T ~ 680 - 750° C	 ~110°	oriented grain growth	magmatic flow	 Fig. 3.13
D2	sub-magmatic		T ~ 680 - 750° C	 ~125°	GBM II (β-Qtz)	magmatic flow ----- cataclasis	 Fig. 3.17
D3	sub-magmatic ↓ flow at low melt fraction (?)		T ~ 680 - 750° C	 ~130°	GBM II (β-Qtz)	Q-F diffusion creep ----- cataclasis ----- SGR	 Fig. 3.28
D4a	HT solid state		T ~ 680 - 750° C	 ~80°	GBM II (β-Qtz)	Q-F diffusion creep (?) ----- SGR	 Fig. 3.29
D4b	HT solid state		T ~ 550 - 680° C	 ~45°	GBM I (α-Qtz)	SGR	 Fig. 3.57
D4c	moderate to LT solid-state	~ 278 Ma	T ~ 350 - 550° C		SGR	Nucleation & growth ----- BLG ----- Cataclasis	

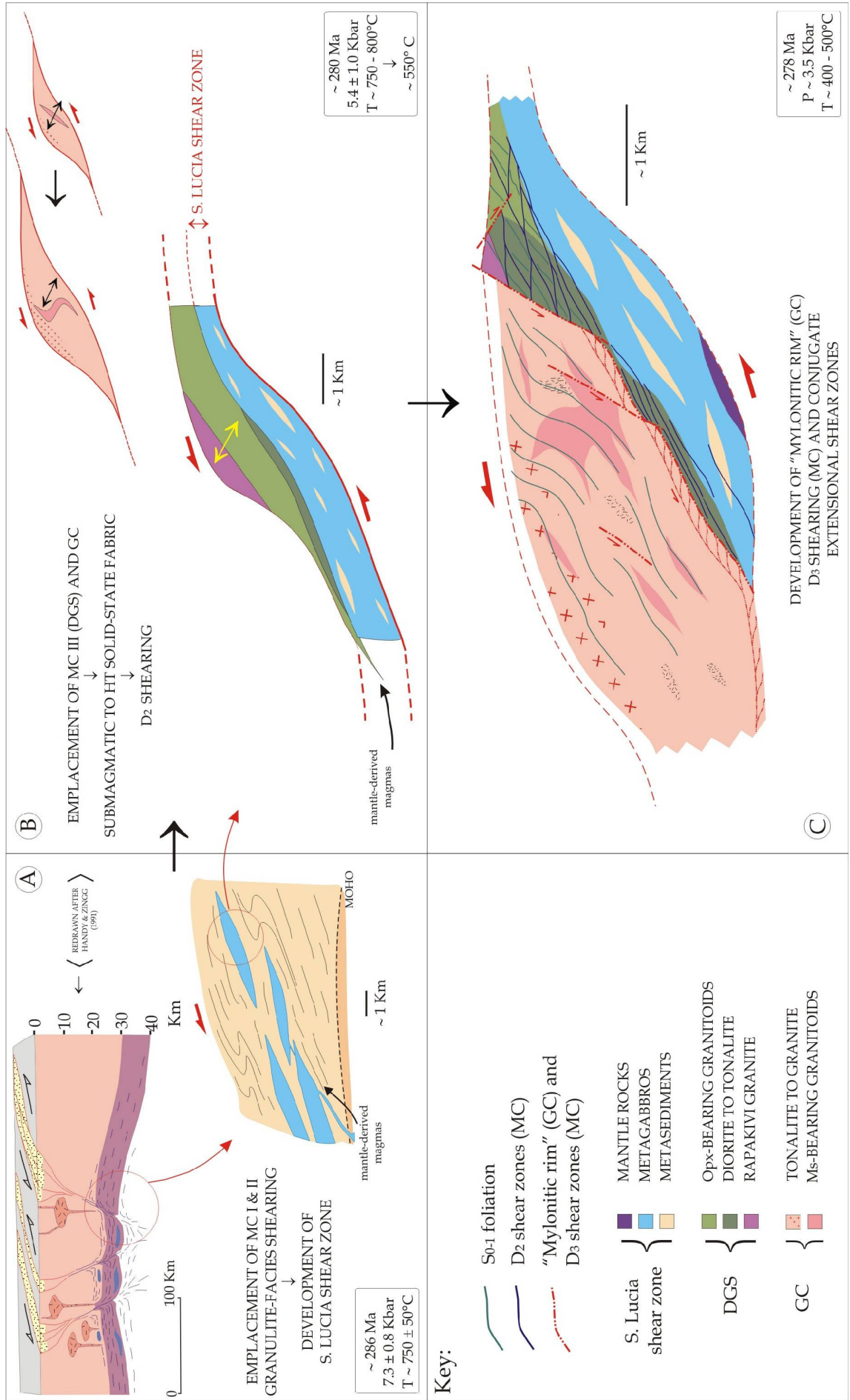
Fig. 5.5: summary of the available data for Granitic Complex, collected from geochronology, mineral chemistry and microstructural investigations. Data from this work.

5.4.1 Some inferences concerning the emplacement model

The comprehension of the geological processes driving the emplacement of plutons is a prerequisite to solve the “space problem” related to the intrusion of mantle-derived magmas into the crust. The distinction between forceful (i.e. space created by magma pushing) and passive (tectonically-driven) emplacement emphasized by Hutton (1988a) seems an excessive simplification, as several processes may operate at different levels through the same pluton (Paterson & Fowler, 1993; Rosenberg et al., 1995).

Little information can be obtained in the case of S. Lucia granitoid plutons, mainly because three-dimensional shape of the plutons at the time of emplacement is largely unknown. On the other hand, from the observed structural pattern and the relations with the S. Lucia shear zone, we can speculate that both DGS and GC might be emplaced along dilatational jogs along the S. Lucia shear zone. In particular, this model could explain the intrusion of the two-mica microgranitoid suite into coarse tonalite to granite suite (Fig.5.6B & C). This model was proposed for the Strontian granite (Hutton, 1988a and 1988b) and for the Mortagne granite (Guinebertau et al., 1987). Hutton et al. (1990) suggested that Proterozoic rapakivi granite from Greenland intruded as large sheets along low-angle, extensional shear zones, which display “ramp and flat” geometry. Despite magma supply rates are commonly much higher than the rate of cavities opening (Paterson & Fowler, 1993), other processes such as magma buoyancy, high strain rates and deformation of wall rocks (e.g. in our case, simple shear plus flattening in the 1Km-wide shear zone) might helped to provide the space for the final emplacement.

Fig. 5.6 (next page): schematic reconstruction of the late-Hercynian evolution of the S. Lucia basement



5.5 Conclusions

The deep crustal section preserved within the S. Lucia basement provides new additional data concerning the behaviour of the middle to lower crust during late-orogenic lithospheric thinning combined with asthenosphere upwelling. While the transtensional tectonic activity was prevailing at shallow crustal levels, the deep continental crust was characterized by a close interplay between magmatic underplating, granulite-facies metamorphism and low-angle detachment faults (Handy & Zingg, 1991; see also Fig.5.6a). Following this geological framework, the S. Lucia section testifies that extensional shearing started in the lower crust (i.e. ~25 Km), where rapid exhumation were achieved by nearly adiabatic decompression, associated with the emplacement of two different granitoid plutons. Microstructures and quartz LPO fabric document that both plutons preserve evidences of a nearly continuum down-temperature deformation, acquired during emplacement and subsequent syndeformational cooling. Quartz C-axis analysis within the granites shows that they experienced progressive left-lateral shearing from magmatic to solid-state conditions under decreasing temperatures. This fact, in addition to microstructural arguments, indicates syntectonic emplacement of these plutons respect to the S. Lucia shear zone. However, the bulk composition of the plutons likely played a fundamental role in the structural evolution, influencing structural style and spatial distribution of the solid-state overprint. In both cases, the pattern of magmatic and solid-state fabrics was strongly controlled by the stress field imposed by the S. Lucia shear zone. The observed structural style suggests that both DGS and GC likely accommodated large strains through magmatic to submagmatic flow. The occurrence of magmas along the shear zone may have promoted strain partitioning within the melt-rich areas, allowing the exhumation and the preservation of granulite-facies rocks.

The syn-rift exhumation of the S. Lucia basement is suggested by the occurrence of MORB-type dolerites and Middle Jurassic thermal anomaly. However, although the P-T-t evolution of the S. Lucia section is only partly constrained, several lines of evidence suggest that the Permian granulites had already been incorporated into the upper crust prior to the Mesozoic.

Acknowledgments

Many thanks to G. Molli and J.H. Kruhl for stimulating discussions and encouragement during fieldwork and microstructural investigations. They have introduced me to the modern concepts of the Structural Geology. Special thanks to J.H. Kruhl, who has provided his precious automatic U-stage (assisted by the Futron™ software). This instrument facilitates the quartz LPO investigations. Moreover, I am grateful to J.H. Kruhl, G. Andries, M. Peternell, V. Ruttner and S. Volland for their hospitality and for all the technical and logistic facilities during my prolonged stay at TUM (Technische Universität München).

G. Saviozzi is thanked for the excellent thin sections. P. Elter is thanked for the recurrent discussions, which have improved my understanding of the regional geology of the Alpine area. R. Tribuzio and A. Montanini provided a great help for field and microstructural petrology, especially during the first part of my work. Moreover, additional thanks to A. Montanini and the technicians of the Earth Sc. Dept from Parma University, who have provided a great assistance during microprobe investigations and additional thin section preparations. Many thanks to my friend R. Braga, who has provided a great support for thermobarometrical elaborations with the TWEEQU software.

Many thanks to S. Sinigoi for the interesting discussions in the field, in the S. Lucia area and in the Ivrea zone. Thanks to F.M. Elter for the fruitful discussions on the Hercynian orogeny and for the two excursions in the Axial Zone of Sardinia. This work has benefited from many open and stimulating discussions with the participants in the "Corsica Excursion 2005"; I would like to thank, beside the others, M.F. De Bitencourt, S. Büttner, R.H. Vernon, D. Zanoni and R. Weinberg.

Detailed and constructive reviews from C. Rosenberg and J.H. Kruhl have significantly improved the quality of this paper. M. Marroni has partially provided the financial support for the 3rd year of my PhD thesis.

Finally, special thanks to Viola, Gianna, Veronica, Vanna, Pino, Dora, Giulio and the other friends: over the past few years, they have provided love, food, wine and other facilities, which have considerably improved the quality of my life.

REFERENCES

- A. Du Chaffaut S, 1980. Les Unités Alpine a la marge orientale du massif cristalline corse. Thèse Doct. Etat, Paris, 247 p.
- A. Du Chaffaut S, Saliot P, 1979. La région de Corte: secteur clé pour la compréhension du métamorphisme alpin en Corse. Bull. Soc. Géol. Fr. **21** (7), n°2: 149-154.
- Anderson JL, 1996. Status of thermo barometry in granitic batholiths. Transaction of the Royal Society of Edinburgh: Earth Sciences **87**: 125-138.
- Anderson JL, Rowley MC, 1981. Synkinematic intrusion of two-mica and associated metaluminous granitoids, Whipple Mountains, California. Canadian Mineralogist **19**: 83-101.
- Arthaud F, Matte P, 1977. Détermination de la position initiale de la Corse et de Sardaigne à la fin de l'orogénèse hercynienne grâce aux marquer ante-mésozoïques. Bull. Soc. Geol. Fr. **7**: 833-840.
- Arzi AA, 1978. Critical phenomena in partially melted rocks. Tectonophysics **44**: 173-184.
- Ashworth, JR, 1985. Migmatites, Blackie, Glasgow.
- Bambauer HU, Bernotat WH, 1982. The microcline-sanidine transformation isograd in metamorphic regions. I. composition and structural state of alkali feldspar from granitoid rocks of two N-S traverses across the Aar massif and Gotthard "massif", Swiss Alps. Schweizerische mineralogische und Petrographische Mitteilungen **62**: 185-230.
- Bard JP, 1980. Microtexture des roches magmatiques et métamorphiques. Masson, Paris, New York, Barcelona, Milan.
- Baudelot S, Durand Delga M, Mirouse R, Perret MF, Taugourdeau-Lants J, 1981. Le Dévonien de Galeria en Corse septentrionale, sa datation et sa mise en place dans le cadre de la Méditerranée occidentale. C.R. Acad. Sci. Paris **292** :347-354.
- Beach A, 1986. A deep seismic reflection profile across the northern North Sea. Nature **323**: 53-55.
- Becker A, 1995. Quartz pressure solution: influence of crystallographic orientation. Journal of Structural Geology **17**: 1395-1405.
- Bell TH, Johnson SE, 1989. The role of deformation partitioning in the deformation and recrystallization of plagioclase and K-feldspar in the Woodroffe Thrust mylonite zone, central Australia. Journal of metamorphic Geology **7**: 151-168.

- Berger A, Stünitz H, 1996. Deformation mechanisms and reactions of hornblende: examples from the Bergell tonalite (Central Alps). *Tectonophysics* **140**: 297-305.
- Berman RG, 1991. Thermobarometry using multiequilibrium calculations: a new technique with petrologic applications. *Canadian Mineralogist* **29**: 833-855.
- Berman, RG, 1988. Internally-consistent thermodynamic data for stoichiometric minerals in the system Na₂O-K₂O-CaO-MgO-FeO-Fe₂O₃-Al₂O₃-SiO₂-TiO₂-H₂O-CO₂. *Journal of Petrology* **29**: 445-522.
- Berthé D, Choukroune P, Jegouzo P, 1979. Orthogneiss, mylonite and non coaxial deformation of granite: the example of the South Armorican Shear Zone. *Tectonophysics* **1**: 31-42.
- Bézert P, Caby R, 1989. La déformation progressive de l'Éocène de la région de Corte: nouvelles données pétrostructurales et conséquences pour le tectogénèse alpine en Corse. *C.R. Acad. Sci. Paris* **309**: 95-101.
- Blenkinsop TG, Treloar PJ, 1995. Geometry, classification and kinematics of S-C and S-C' fabrics in the Mushandike area, Zimbabwe. *Journal of Structural Geology* **17**: 397-408.
- Blumenfeld P, Bouchez JL, 1988. Shear criteria in granite and migmatite deformed in the magmatic and solid states. *Journal of Structural Geology* **10**: 361-372.
- Blumenfeld P, Mainprice D, Bouchez JL, 1986. C-slip in quartz from subsolidus deformed granite. *Tectonophysics* **127**: 97-115.
- Bohlen SR, Wall, V J, Boettcher AL, 1983. Experimental investigation and application to garnet granulite equilibria. *Contributions to Mineralogy and Petrology* **83**: 52-61.
- Bohlen SR, Mezger- K, 1989. Origin of granulite terranes and the formation of the lowermost continental crust. *Science* **244**: 326-329.
- Bonin B, Azzouni-Sekkal A, Bussy F, Ferrag S, 1998. Alkalicalcic and alkaline post-orogenic (PO) granite magmatism: petrologic constraints and geodynamic settings. *Lithos* **45**: 45- 70.
- Boullier AM, Bouchez, JL, 1978. Le quartz en rubans dans les mylonites. *Bull. Soc. Geol. Fr.* **20**: 253-262.
- Boullier AM, Gueguen Y, 1975. SP-mylonites: origin of some mylonites by superplastic flow. *Contrib. Mineral. Petrol.* **50**: 93-104.
- Brandon, AD, Creaser, RA, Chacko, T, 1996. Constraints on rates of granitic magma transport from epidote dissolution kinetics. *Science* **271**: 1845-1848.

- Brodie KH, Rutter E, 1985. On the relationship between deformation and metamorphism, with special reference to the behaviour of basic rocks. In: A.B. Thompson, D.C. Rubie (Editors), *Metamorphic reactions: kinetics, texture and deformation*. Adv. Phys. Geochem. **4**: 138-179.
- Brodie KH, Rutter E, 1987. Deep crustal extensional faulting in the Ivrea Zone of Northern Italy. *Tectonophysics* **140**: 193-212.
- Brown M, 1994. The generation, segregation, ascent and emplacement of granite magma: the migmatite-to-crustally-derived granite connection in thickened orogens. *Earth Science Review* **36**: 83-130.
- Brown M, Solar G, 1998a. Shear-zone systems and melts: feedback relations and self-organization in orogenic belts. *Journal of Structural Geology* **20**: 211-227.
- Bucker K, Frey M, 2003. *Petrogenesis of metamorphic rocks*, seventh edition. Springer, Berlin, Heidelberg, New York.
- Burg JP, 1986. Quartz shape fabric variations and c-axis fabrics in a ribbon-mylonite: arguments for an oscillating foliation. *Journal of Structural Geology* **8**: 132-131.
- Cabanis B, Cochemé JJ, Vellutini PJ, Joron JL, Treuil M, 1990. Post-collisional Permian Volcanism in northwestern Corsica: an assessment based on mineralogy and trace element geochemistry. *J. Volca. Geother. Res.* **44**: 51-67.
- Caby R, Jacob C, 2000. La transition croute-manteau dans la nappe de Santa-Lucia-di-Mercurio (Corse Alpine): les racines d'un rift Permien. *Géologie de la France* **1**: 21-34.
- Caby R, Kienast JR, Harris L, Guiraud M, 1984. Les klippen de socle ante-Alpin du Cap Corse: arguments pétrogénétiques et structuraux pour un origine Sud-Alpine. In: Harris LB, *déformations et déplacements dans la chaîne alpine: l'exemple des Schistes lustrés du Cap Corse*. Thèse Doct 3^e cycle, Un. Rennes, 307pp.
- Carmignani L, Carosi R, Di Pisa A, Elter FM, Gattiglio M, Musumeci G, Oggiano G, Pertusati PC, 1993. Post-collisional extensional tectonics in the Hercynian belt of Sardinia (Italy). In: *Late orogenic extension in mountains belts*. International meeting BRGM-SGF, Montpellier, 36-37.
- Carmignani L, Rossi P, 1999. *Carta geologica e strutturale della Sardegna e della Corsica*. Servizio Geologico d'Italia.
- Carmignani L, Oggiano G, Barca S, Conti P, Salvadori I, Eltrudis A, Funedda A, Pasci S, 2001. *Memorie descrittive della Carta Geologica d'Italia*. 2001. Volume LX. *Geologia della Sardegna*. Note illustrative della Carta Geologica della Sardegna a scala 1:200000. Istituto Poligrafico e Zecca dello Stato.

- Caron JM, 1977. Lithostratigraphie et tectonique des Schistes lustrés dans les Alpes méridionales et en Corse orientale. Thèse Etat, Strasbourg. Sci. Géol., mém. n°48, 333p.
- Caron JM, 1994. Metamorphism and deformation in Alpine Corsica. Schweizerische Mineralogische und Petrographische Mitteilungen **74**: 105-114.
- Castro A, 1986. Structural pattern and ascent model in the Central Extremadura batholith, Hercynian belt, Spain. Journal of Structural Geology **8**: 633-645.
- Cavalcanti de Araújo MN, Alves da Silva FC, Jardim de Sá EF, Holcombe RJ, Vasconcelos PM, 2003. Microstructural evolution of the Seridó Belt, NE Brazil: the effect of two tectonic events on development of c-axis preferred orientation in quartz. Journal of Structural Geology **25**: 2089-2107.
- Chatterjee ND, Johannes W, 1974. Thermal stability and standard thermodynamic properties of synthetic 2M1 muscovite $KAl_2AlSi_3O_{10}(OH)_2$. Contributions to Mineralogy and Petrology **49**: 89-114.
- Cocherie A, Rossi P, Fouillac AM, Vidal P, 1994. Crust and mantle contributions to granite genesis—an example from the Variscan batholith of Corsica, France, studied by trace element and Nd-Sr-O isotope systematics. Chemical Geology **115**: 173– 211.
- Cocherie A, Rossi Ph, Fanning CM, Guerrot C, 2005. Comparative use of TIMS and SHRIMP for U-Pb zircon dating of A type granites and mafic tholeiitic layered complexes and dykes from the Corsican Batholith (France). Lithos **82**: 185– 219.
- Cosca MA, Essene EJ, Bowman JR, 1991. Complete chemical analyses of metamorphic hornblendes. Implications for normalizations, calculated H_2O activities and thermobarometry. Contributions to Mineralogy and Petrology **108**: 472-484.
- Coward MP, 1984. Major shear zones in the Precambrian crust: examples from NW Scotland and southern Africa and their significance. In Kröner A & Greiling R (Eds.). Precambrian Tectonics Illustrated. Schweitzerbart, Stuttgart: 207-235.
- Culshaw NG, Fyson WK, 1984. Quartz ribbon in high grade granite gneiss: modification of dynamically formed quartz c-axis preferred orientation by oriented grain growth. Journal of Structural Geology **6**: 6631-668.
- Dallan L, Nardi R, 1984. Ipotesi sulla evoluzione dei domini “liguri” della Corsica nel quadro della paleogeografia e della paleotettonica delle unità alpine. Boll. Soc. Geol. It. **103**: 515-527.
- Dal Piaz GV, Hunziker JC, Martinotti G, 1972. La zona Sesia Lanzo e l’evoluzione tettonico-metamorfica delle Alpi Nord-occidentali interne. Memorie della Società Geologica Italiana **11**: 433-460.

- Daniel JM, Jolivet L, Goffe B, Poinssot C, 1996. Crustal-scale strain partitioning: footwall deformation below the Alpine Oligo-Miocene detachment of Corsica. *Journal of Structural Geology* **18**: 41-59.
- Dell'Angelo LN, Tullis J, 1988. Experimental deformation of partially melted granitic aggregates. *Journal of Metamorphic Geology* **6**: 495-515.
- Demarchi G, Quick JE, Sinigoi S, Mayer A, 1998. Pressure gradient and original orientation of a lower-crustal intrusion in the Ivrea-Verbanò Zone, northern Italy. *Journal of Geology* **106**: 609-622.
- Den Brok B, 1996. The effect of crystallographic orientation on pressure solution in quartzite. *Journal of Structural Geology* **18**: 859-860.
- Den Brok B, Kruhl JH, 1996. Ductility of garnet as an indicator of extremely high temperature deformation: discussion. *Journal of Structural Geology* **18**: 1369-1373.
- Den Tex E, 1969. Origin of ultramafic rocks, their tectonic setting and history: a contribution to the discussion of the paper: "the origin of ultramafic and ultrabasic rocks" by PJ Wyllie. *Tectonophysics* **7**: 457-488.
- Didier J, Barbarin B, 1991. The different types of enclaves in granites - nomenclature. In: *Developments in Petrology*, Didier J, Barbarin B (Eds.). *Granites and their enclaves*. Elsevier, Amsterdam.
- Drury MR, Urai JL, 1990. Deformation-related recrystallization processes. *Tectonophysics* **172**: 235-253.
- Durand Delga M 1978. Corse. Guides géol. Rég., Masson édit., 208p.
- Durand Delga M 1984. Principaux traits de la Corse Alpine et corrélations avec les Alpes Ligures. *Mem. Soc. Geol. It.* **28**: 285-329.
- Eberli GP, 1988. The evolution of the southern continental margin of the Jurassic Tethys Ocean as recorded in the Allgäu Formation of the Austroalpine nappes of Graubünden (Switzerland). *Eclogae geol. Helv.* **81**: 175-214.
- Egal E, 1992. Structures and tectonic evolution of the external zone of Alpine Corsica. *Journal of Structural Geology* **14**: 1215-1228.
- Egal E, Caron JM, 1988. Tectonique polyphasée dans l'Eocène autochtone à la bordure ouest de la nappe de Balagne (Corse). *Bull. Soc. Géol. France* **8**: 315-321.
- Eggleton & Buseck, 1980. The orthoclase-microcline inversion: an high-resolution TEM study and strain analysis. *Contributions to Mineralogy and Petrology* **74**: 123-133.
- Elter FM, Faure M, Ghezzi C, Corsi B, 1999. Late Hercynian shear zones in northeastern Sardinia (Italy). *Géologie de la France* **2**: 3-16.

- England PC, Thompson AB, 1984. Pressure-temperature-time paths of regional metamorphism. I. Heat transfer during the evolution of regions of thickened continental crust. *Journal of Petrology* **25**: 894-928.
- Etchecopar A, 1977. A plane kinematic model of progressive deformation in a polycrystalline aggregate. *Tectonophysics* **39**: 121-139.
- Evensen , Hamilton PJ, O'Nions RK, 1978. Rare-earth abundances in chondritic meteorites. *Geochim. Cosmochim. Acta* **42**: 1199-1212.
- Fernandez A, Feybesse JL, Mezure JF, 1983. Theoretical and experimental study of fabrics developed by different shaped markers in two-dimensional simple shear. *Bull. Soc. Géol. Fr.* **25**: 319-326.
- Fernandez A, Laporte D, 1991. Significance of low symmetry fabric in magmatic rocks. *Journal of Structural Geology* **13**: 337-347.
- Ferré EC, 1989b. Les gneiss à cordiérite-grenat-orthoamphibole de Topiti : témoin possible d'un socle métamorphique Protérozoïque en Corse occidentale. *C.R. Acad. Sci. Paris* **309**: 893-898.
- Ferre´ EC, Leake BE, 2001. Geodynamic significance of early orogenic high-K crustal and mantle melts: example of the Corsica Batholith. *Lithos* **59**: 47-67.
- Ferry JM, Spear FS, 1978. Experimental calibration of the partitioning of Fe and Mg between garnet and biotite. *Contributions to Mineralogy and Petrology* **66**: 113-117.
- Feuten F, Robin P-YF, Stephens R, 1991. A model for the development of a domainal quartz c-axis fabric in a coarse-grained gneiss. *Journal of Structural Geology* **13**: 1111-1124.
- Fitzgerald JD, Stünitz H, 1993. Deformation of granitoids at low metamorphic grade. I: reactions and grain size reduction. *Tectonophysics* **221**: 269-297.
- Foster DA, Miller CF, Harrison TM, Hoisch TD, 1992. ⁴⁰Ar/³⁹Ar thermochronology and thermobarometry of metamorphism, plutonism and tectonic denudation in the Old Woman Mountains area, California. *Geological Society of America Bulletin* **104**: 176-191.
- Fountain DM, 1986. Implications of deep crustal evolution for seismic reflection interpretation. In Baranzagi M, Brown L (Eds) *Reflection seismology: the continental crust*. Am Geophys Union Geodynamics Series **14**: 1-8.
- Frost BR, Frost CD, Hulsebosch TP, Swapp SM, 2000. Origin of the charnockite of the Louis Lake batholith, Wind River Range, Wyoming. *Journal of petrology* **41**: 1759-1776.

- Fügenschuh B, Froitzheim N, Boillot G, 1998. Cooling history of granulite samples from the ocean-continent transition of the Galicia margin: implication for rifting. *Terra Nova* **10**: 96-100.
- Gapais D and Barbarin B, 1986. Quartz fabric transition in a cooling syntectonic granite (Hermitage Massif, France). *Tectonophysics* **125**: 357-370.
- Gapais D, 1989. Shear structures within deformed granites: mechanical and thermal indicators. *Geology* **17**: 1144-1147.
- Garcia Celma A, 1982. Domainal and fabric heterogeneities in the Cap de Creus quartz mylonites. *Journal of Structural Geology* **4**: 443-455.
- Garcia Celma A, 1983. C-axis and shape fabric in quartz mylonites of Cap de Creus (Spain); their properties and development. PhD thesis, Utrecht University.
- Gardien V, Reusser E, Marquer D, 1994. Pre-Alpine metamorphic evolution of the gneisses from the Valpelline series (Western Alps, Italy). *Schweizerische mineralogische und Petrographische Mitteilungen* **74**: 489-502.
- Ghezzo C, Ricci CA, Orsini JB, 1990. Le magmatisme paléozoïque (500-250Ma) dans le segment varisque Corso-Sarde. Réunion extraordinaire des sociétés géologiques de France et d'Italie. Livre guide d'excursion. Siena, 1990.
- Giacomini F, Bomparola RM, Ghezzo C, 2005. Petrology and geochronology of metabasites with eclogite facies relics from NE Sardinia: constraints for the Palaeozoic evolution of Southern Europe. *Lithos* **82**: 221- 248.
- Gleason GC, Tullis J, Heidelbach F, 1993. The role of dynamic recrystallization in the development of lattice preferred orientations in experimentally deformed quartz aggregates. *Journal of Structural Geology* **15**: 1145-1168.
- GLOM ("gruppo di lavoro sulle ofioliti mediterranee"), 1977. I complessi ofiolitici e le unità cristalline della Corsica alpina. *Ofioliti* **2**: 265-324.
- Gower RJW, Simpson C, 1992. Phase boundary mobility in naturally deformed, high-grade quartzofeldspathic rocks: evidence for diffusional creep. *Journal of Structural Geology* **14**: 301-314.
- Green NL, Usdansky SI, 1986. Toward a practical plagioclase-muscovite thermometer. *American mineralogist* **71**: 1109-1117.
- Gross AFK, Van Heege GPT, 1973. The high-low quartz transition up to 10 Kb pressure. *Journal of geology* **81**: 717-724.
- Guinebertau B, Bouchez JL, Vignerresse JL, 1987. The Mortagne granite pluton (France) emplaced by pull-apart along a shear zone: structural and gravimetric arguments and regional implications. *Geological Society of America Bulletin* **99**: 763-770.

- Hammarstrom JM, Zen E, 1986. Aluminium in hornblende: an empirical igneous geobarometer. *Am. Mineral* **71**: 1297-1313.
- Handy M, 1987. The structure, age and kinematics of the Pogallo Fault Zone; Southern Alps, northwestern Italy. *Eclogae geol. Helv.* **80**: 593-632.
- Handy M, Zingg A, 1991. The tectonic and rheological evolution of an attenuated cross section of the continental crust; Ivrea crustal section, Southern Alps, northwestern Italy and southern Switzerland. *Geological Society of America Bulletin* **103**: 236-253.
- Handy M, 1990. The solid-state flow of polymineralic rocks. *Journal of Geophysical Research* **95**: 8647-8661.
- Hanmer SK, 1982. Microstructure and geochemistry of plagioclase and microcline in naturally deformed granite. *Journal of Structural Geology* **4**: 197-213.
- Henk A, Franz L, Teufel S, Oncken O, 1997. Magmatic underplating, extension, and crustal reequilibration. Insights from a cross-section through the Ivrea Zone and Strona-Ceneri Zone, northern Italy. *Journal of Geology* **105**: 367-377.
- Hermann J, Müntener O, 1996. Extension-related structures in the Malenco-Margna system: implications for the paleogeography and consequences for rifting and Alpine tectonics. *Schweizerische Mineralogische und Petrographische Mitteilungen* **76**: 501-519.
- Hibbard MJ, Watters RJ, 1985. Fracturing and diking in incompletely crystallized granitic plutons. *Lithos* **18**: 1-12.
- Hibbard MJ, 1987. Deformation of incompletely crystallized magma system: granitic gneisses and their tectonic implications. *Journal of Geology* **95**: 543-561.
- Higgins M, 1991. The origin of laminated and massive anorthosite, Sept Iles layered intrusion, Quebec, Canada. *Contribution to mineralogy and petrology* **106**: 340-354.
- Hirth G, Tullis J, 1992. Dislocation creep regimes in quartz aggregates. *Journal of Structural Geology* **14**: 145-159.
- Holdaway MJ, 1971. Stability of andalousite and the aluminium silicate phase diagram. *American Journal of Science* **271**: 97-131.
- Holland T, Blundy J, 1994. Non-ideal interactions in calcic amphiboles and their bearing on amphibole-plagioclase thermometry. *Contributions to Mineralogy and Petrology* **116**: 433-447.
- Holland TH, 1900. The charnockite series, a group of Archean hypersthene rocks in peninsular India. *Memoirs of the Geological Survey of India* **28**: 119-249.

- Hollister LS, Crawford ML, 1986. Melt-enhanced deformation: a major tectonic process. *Geology* **14**: 558-561.
- Hollister LS, Grissom GC, Stowell HH, Sisson VB, 1988. Confirmation of the empirical calibration of Al in hornblende with pressure of solidification of calc-alkaline plutons. *Am. Mineral* **72**: 231-239.
- Hutton HW, 1988a. Granite emplacement mechanisms and tectonic controls: inferences from deformation studies. *Transactions of the Royal Society of Edinburgh: Earth Science* **79**: 245-255.
- Hutton HW, 1988b. Igneous emplacement in a shear zone termination: the biotite granite at Strontian, Scotland. *Bull. Soc. Geol. Am.* **100**: 1392-1399.
- Hutton HW, Dempster TJ, Brown PE, Becker SD, 1990. A new mechanism of granite emplacement: intrusion in active extensional shear zone. *Nature* **343**: 452-455.
- Ildefonse B, Mancktelow NS, 1993. Deformation around rigid particles: the influence of slip at the particle-matrix interface. *Tectonophysics* **221**: 345-359.
- Jessell MW, 1987. Grain-boundary migration microstructure in a naturally deformed quartzite. *Journal of Structural Geology* **9**: 1007-1014.
- Ji S, Mainprice D, 1990. Recrystallization and fabric development in plagioclase. *Journal of Geology* **98**: 65-79.
- Johnson MC, Rutherford MJ, 1989. Experimental calibration of aluminium-in-hornblende geobarometers with application to Long Valley caldera (California) volcanic rocks. *Geology* **17**: 837-841.
- Karlstrom KE, Miller CF, Kingsbury JA, Wooden JL, 1993. Pluton emplacement along an active ductile thrust zone, Piute Mountains, Southeastern California: interaction between deformational and solidification processes. *Geological Society of America Bulletin* **105**: 213-230.
- Kleinschrodt R, McGrew A, 2000. Garnet plasticity in the lower continental crust: implications for deformation mechanisms based on microstructures and SEM-electron channeling pattern analysis. *Journal of Structural Geology* **22**: 795-809.
- Knipe RJ, 1989. Deformation mechanisms - recognition from natural tectonites. *Journal of Structural Geology* **11**: 127-146.
- Knipe RJ, Law RD, 1987. The influence of crystallographic orientation and grain boundary migration on microstructural and textural evolution in an S-C mylonite. *Tectonophysics* **135**: 155-169.
- Knipe RJ, Rutter EH, 1990. Deformation mechanisms, rheology and tectonics. *Geological Society of London, Special Publication* **54**, 535pp.

- Kretz R, 1983. Symbols for rock-forming minerals. *American Mineralogist* **68**: 277-279.
- Krohe A, 1990. Local variations in quartz [c]-axis orientations in non-coaxial regimes and their significance for the mechanics of S-C fabrics. *Journal of Structural Geology* **12**: 995-1004.
- Kruhl JH, 1996. Prism and basal-plane parallel subgrain boundaries in quartz: a microstructural geothermobarometer. *Journal of Metamorphic Geology* **14**: 581-589.
- Kruhl JH, 1998. Prism and basal-plane parallel subgrain boundaries in quartz: a microstructural geothermobarometer. Discussion. *Journal of Metamorphic Geology* **16**: 141-146.
- Kruhl JH, 2001. Crystallographic control on the development of foam textures in quartz, plagioclase and analogue materials. *Int. J. Earth Sciences* **90**: 104-117.
- Kruhl JH, 2005. Development of microfabrics in sheared crystallizing magmas. In: sheared magma in nature and experiment: bridging the brittle and ductile fields. A conference in honour of RH Vernon. Abstract book.
- Kruhl JH, Peternell M, 2002. The equilibration of high-angle grain boundaries in dynamically recrystallized quartz: the effect of crystallography and temperature. *Journal of Structural Geology* **24**: 1125-1137.
- Kruse R, Stünitz H, 1999. Deformation mechanisms and phase distribution in mafic high-temperature mylonites from the Jotun nappe, southern Norway. *Tectonophysics* **303**: 223-249.
- Lacassin R, Mattauer M, 1985. Kilometre scale sheath fold at Mattmark and implications for transport direction in the Alps. *Nature* **315**: 739-742.
- Lacombe O, Jolivet L, 2005. Structural and kinematic relationships between Corsica and the Pyrenees-Provence domain at the time of the Pyrenean orogeny. *Tectonics* **24**: 1-20.
- Lafrance B, John BE, Scoates JS, 1995. Syn-emplacement recrystallization and deformation microstructures in the Poe Mountain anorthosite, Wyoming. *Contribution to Mineralogy and Petrology* **122**: 431-440.
- Lafrance B, Vernon RH, 1993. Mass transfer and microfracturing in gabbroic mylonites of the Guadalupe igneous complex, California. In: Boland JN, Fitz Gerald JD (Eds.), *defects and processes in the solid state: Geoscience Applications*. Elsevier, Amsterdam: 151-167.
- Lahondère D, 1988. Le métamorphisme éclogitique dans les orthogneiss et les metabasites ophiolitiques de la région de Farinole. *Bull. Soc. Géol. France* **4** : 579-585.

- Lal RK, 1993. Internally consistent recalibrations of mineral equilibria for geothermobarometry involving garnet-orthopyroxene-plagioclase-quartz assemblage and their application to the South Indian granulites. *Journal of Metamorphic Geology* **11**: 855-866.
- Laporte D, Orsini JB, Fernandez A, 1991. Le complexe d'Ile-Rousse, Balagne, Corse du Nord-Ouest: pétrologie et cadre de mise en place des granitoïdes magnésio-potassiques. *Géologie de la France* **4**: 15-30.
- Lardeaux JM, Spalla MI, 1991. From granulites to eclogites in the Sesia zone (Italian Western Alps): a record of the opening and closure of the Piedmont ocean. *Journal of Metamorphic Geology* **9**: 35-59.
- Lardeaux JM, Menot RP, Orsini JB, Rossi P, Naud G, Libourel G, 1994. Corsica and Sardinia. In: Keppie, JD (Ed.), *Pre-Mesozoic Terranes in France and Correlative Areas*. Springer Verlag: 468- 479.
- Law RD, Schmid SM, Wheeler J, 1990. Simple shear deformation and quartz crystallographic fabric: a possible natural example from the Torrindon area of NW Scotland. *Journal of Structural Geology* **12**: 29-45.
- Ledru P, Courrioux G, Dallain C, Lardeaux JM, Montel JM, Vanderhaeghe O, Vitel G, 2001. The Velay dome (French Massif Central): melt generation and granite emplacement during orogenic evolution. *Tectonophysics* **342**: 207- 237.
- Le Maitre RW, Bateman P, Dudek A, Keller J, Lameyre J, Le Bas MJ, Sabine PA, Schmid R, Sorensen H, Streckeisen A, Woolley A, Zanettin B, 1989. *A classification of igneous rocks and glossary of terms*. London, Blackwell.
- Libourel G, 1985. Le complexe de Santa Lucia di Mercurio (Corse). Thèse Doct., Toulouse, 405 p.
- Libourel G, 1988a. Le complexe de Santa Lucia di Mercurio (Corse): un nouveau jalon de la base de la croûte varisque en méditerranée occidentale. *C.R. Acad. Sci. Fr., Paris* **307**: 1067-1073.
- Libourel G, 1988b. Le complexe de Santa Lucia di Mercurio (Corse): un équivalent possible des complexes de la zone d'Ivrée. *C.R. Acad. Sci. Fr., Paris* **307**: 1225-1230.
- Libourel G, Vielzeuf D, 1988. Isobaric cooling at high pressure: examples of Corsican high pressure granulites. *Terra cognita* **8**: 268.
- Lisle RJ 1985. The effect of composition and strain on quartz -fabric intensity in pebbles from a deformed conglomerate. *Geol. Rdsch* **74**: 657-663.
- Lister GS, Dornsiepen UF, 1982. Fabric transition in the Saxony granulite terrain. *Journal of Structural Geology* **4**: 81-92.

- Lister GS, 1977. Discussion: crossed girdle c-axis fabric in quartzites plastically deformed by plane strain and progressive simple shear. *Tectonophysics* **39**: 51-54.
- Lister GS, Hobbs BE, 1980. The simulation of fabric development during plastic deformation and its application to quartzite: the influence of deformation history. *Journal of Structural Geology* **2**: 355-371.
- Lister GS, Price GP, 1978. Fabric development in a quartz-feldspar mylonite. *Tectonophysics* **49**: 37-78.
- Lister GS, Snoke AW, 1984. S-C mylonites. *Journal of Structural Geology* **6**: 617-638.
- Loubières, 1979. Etude du socle métamorphique anté-hercynien en Corse. Dipl. Etudes Approfondies. Univ. Montpellier.
- Mainprice DH, Bouchez JL, Blumenfeld P, Tubia JM, 1986. Dominant c slip in naturally deformed quartz: implications for dramatic plastic softening at high temperature. *Geology* **14**: 819-822.
- Malavieille J, Guihot P, Costa S, Lardeaux JM, Gardien V, 1990. Collapse of the thickened Variscan crust in the French Massif Central: Mont Pilat extensional shear zone and St. Etienne Late Carboniferous basin. *Tectonophysics* **177**: 139-149.
- Malavieille J, Chemenda A, Larroque C, 1998. Evolutionary model for alpine Corsica: mechanism for ophiolite emplacement and exhumation of high-pressure rocks. *Terranova* **10** : 317-322.
- Malusky H, 1977. Application de la méthode $^{40}\text{Ar}/^{39}\text{Ar}$ aux minéraux des roches cristallines perturbées par des événements thermiques en Corse. *Bull. Soc. Geol. Fr.* **7**: 849-855.
- Malusky H, Mattauer M, Matte P, 1973. Sur la présence de décrochements alpins en Corse. *C.R. Acad. Sc. Paris* **276**: 709-712.
- Marre J, 1986. The structural analysis of granitic rocks. Elsevier, Amsterdam.
- Marroni M, Molli G, Montanini A, Tribuzio R, 1998. The association of continental crust rocks with ophiolites in the Northern Apennines (Italy): implications for the continent-ocean transition in the Western Tethys. *Tectonophysics* **292**: 43- 66.
- Marroni M, Pandolfi L, Saccani E, 2001. Mafic rocks from the sedimentary breccias associated to the Balagne ophiolitic nappe (Northern Corsica): geochemical features and geological implications. *Ophioliti* **26**: 433-444.
- Marroni M, Molli G, Montanini A, Ottria G, Pandolfi L, Tribuzio R, 2002. The external Ligurian units (Northern Apennine, Italy): from rifting to convergence of a fossil ocean-continent transition zone. *Ophioliti* **27**: 119-131.

- Martelat JE, Schulmann K, Lardeaux JM, Nicollet C, Cardon H, 1999. Granulite microfabric and deformation mechanisms in southern Madagascar. *Journal of Structural Geology* **21**: 671-687.
- Massonne HJ, Szpurska Z, 1997. Thermodynamic properties of white micas on the basis of high-pressure experiments in the system K_2O - MgO - Al_2O_3 - SiO_2 - H_2O . *Lithos* **41**: 229-250.
- Mattauer M, Proust F, 1975. Données nouvelles sur l'évolution structurale de la Corse alpine. *C. R. Acad. Sci. Paris* **281**: 1681-1685.
- Mawer CK, Williams PF, 1991. Progressive folding and foliation development in a sheared coticule-bearing phyllite. *Journal of Structural Geology* **13**: 539-557.
- McKenzie D, 1978. Some remarks on the development of sedimentary basins. *Earth Planetary Science Letters* **40**: 25-32.
- McLaren AC, Pryer LL, 2001. Microstructural investigations of the interaction and interdependence of cataclastic and plastic mechanisms in feldspar crystals deformed in the semi-brittle field. *Tectonophysics* **335**: 1-15.
- Ménot RP Orsini JB, 1990. Evolution du socle ante-Stéfanien de Corse: événements magmatiques et métamorphiques. *Schweiz. Mineral. Petrogr. Mitt* **70**: 35-53.
- Miller RB, Paterson SR, 1994. The transition from magmatic to high-temperature solid-state deformation: implications from the Mount Stuart batholith, Washington. *Journal of Structural Geology* **16**: 853-865.
- Molli G, Tribuzio R, 2004. Shear zones and metamorphic signature of subducted continental crust as tracers of the evolution of the Corsica/Northern Apennine orogenic system. *Geol. Soc. London, Spec. Publ.* **224**: 321-335.
- Moore AC, 1970. Descriptive terminology for the textures of rocks in granulite facies terrains. *Lithos* **3**: 123-127.
- Mulchrone KF, Grogan S, De P, 2005. The relationship between magmatic tiling, fluid flow and crystal fraction. *Journal of Structural Geology* **27**: 179-197.
- Müntener O, Hermann J, Trommsdorff V, 2000. Cooling history and exhumation of lower-crustal granulite and upper mantle (Malenco, Eastern Central Alps). *Journal of Petrology* **41**: 175-200.
- Nair R, Chacko T, 1992. Fluid-absent melting in high-grade semi-pelites: P-T constrains on orthopyroxene formation and implications for granulite genesis. *Journal of petrology* **43**: 2121-2142.
- Naney, MT, 1983. Phase equilibria of rock-forming ferromagnesian silicates in granitic systems. *Am. J. Sci.* **283**: 993-1033.

- Newton RC, Perkins D III, 1982. Thermodynamic calibration of geobarometers based on the assemblage garnet-plagioclase-orthopyroxene (clinopyroxene)-quartz. *American Mineralogist* **67**: 203-222.
- Nicolas A, 1992. Kinematics of magmatic rocks with special reference to gabbros. *Journal of Petrology* **33**: 891-915.
- Nicolas A, Ildefonse B, 1996. Flow mechanism and viscosity in basaltic magma chambers. *Geophysical Research Letters* **23**: 2013-2016.
- Nicolas A, Poirier JP, 1976. Crystalline plasticity and solid-state flow in metamorphic rocks. John Wiley & Sons, London 444pp.
- Nyman MW, Law RD, Smelik EA, 1992. Cataclastic deformation for the development of core and mantle structure in amphibole. *Geology* **20**: 455-458.
- Ohnenstetter M, Rossi P, 1985. Découverte d'une paléochambre magmatique exceptionnelle dans le massif du Tenda, Corse hercynienne. *C.R. Acad. Sci. Paris* **300**: 853-858.
- Orsini JB, Michon G, Laporte D, Vellutini P, Fumey-Humbert F, Conchon O, Gauthier A, 1987. Carte géologique de la France (1/50 000), feuille Calvi (1105). Orléans BRGM Notice, 57 pp.
- Palagi P, Laporte D, Lardeaux JM, Ménot RP, Orsini JB, 1985. Identification d'un complexe leptyno-amphibolique au sein des « gneiss de Belgodere » (Corse occidentale. *C.R. Acad. Sci. Paris* **301** :1047-1052.
- Pandey P, Rawat RS, Jowhar TN, 2004. Structural state transformation in alkali feldspar: evidence for post-crystallization deformation from Proterozoic granite, Kumaun Himalaya (India). *Journal of Asian Earth Sciences* **18**: 1-10.
- Paquette JL, Menot RP, Pin C, Orsini JP, 2003. Episodic and short-lived granitic pulses in a post-collisional setting: evidence from precise U-Pb zircon dating through a crustal cross-section in Corsica. *Chemical Geology* **14148**: 1-20.
- Park Y, Means WD, 1996. Direct observation of deformation processes in crystal mushes. *Journal of Structural Geology* **18**: 847-858.
- Passchier CW, 1991b. Geometric constraints on the development of shear bands in rocks. *Geol. Mijnb.* **70**: 203-211.
- Passchier CW, Myers JS, Kroner A, 1990b. Field geology of high-grade gneiss terrains. Springer, Berlin Heidelberg New York.
- Passchier CW, Trouw RAJ, 1996. *Microtectonics*. Springer, Berlin/ Heidelberg / New York.

- Paterson SR, Fowler Jr. TK, 1993. Re-examining pluton emplacement processes. *Journal of Structural Geology* **15**: 191-206.
- Paterson SR, Fowler Jr. TK, Schmidt KL, Yoshinobu AS, Yuan ES, Miller RB, 1998. Interpreting magmatic fabric patterns in plutons. *Lithos* **44**: 53-82.
- Paterson SR, Pignotta GS, Vernon RH, 2004. The significance of microgranitoid enclave shapes and orientation. *Journal of Structural Geology* **26**: 1465-1481.
- Paterson SR, Tobisch OT, 1988. Using pluton ages to date regional deformations: problems with the commonly used criteria. *Geology* **16**: 1108-1111.
- Paterson SR, Tobisch OT, 1992. Rates of processes in magmatic arcs: implications for the timing and nature of pluton emplacement and wall rock deformation. *Journal of Structural Geology* **14**: 291-300.
- Paterson SR, Vernon RH, Tobisch OT, 1989. A review of criteria for the identifications of magmatic and tectonic foliations in granitoids. *Journal of Structural Geology* **11**: 349-363.
- Pauli C, Schmid SM, Panozzo Heilbronner R, 1996. Fabric domains in quartz mylonites: localized three-dimensional analysis of microstructure and texture. *Journal of Structural Geology* **18**: 1183-1203.
- Pèquignot G, Potdevin JL, 1984. Métamorphisme et tectonique dans les Schistes Lustrés l'Est de Corte (Corse). Thèse 3^o cycle, Univ. Claude-Bernard (Lyon), 3 vol., 245 p.
- Piccardo GB, Rampone E, Vannucci R, 1990. Upper mantle evolution during continental rifting and ocean formation: evidences from peridotite bodies of the western Alpine-northern Apennine system. *Mémoires de la Société Géologique de France* **156**: 323-333.
- Piccardo GB, Rampone E, Vannucci R, 1992. Ligurian peridotites and ophiolites: from rift to ocean formation in the Jurassic Ligure-Piemontese basin. *Acta Vulc.* **2**: 313-325.
- Pin C, 1989. Essai sur la chronologie et l'évolution géodynamique de la chaîne Hercynienne d'Europe. Thèse Doct. Etat, Clermont-Ferrand.
- Platt JP, Vissers RLM, 1980. Extensional structures in anisotropic rocks. *Journal of Structural Geology* **2**: 397-410.
- Poirier JP, 1985. Creep of crystals: high-temperature deformation processes in metals, ceramics and minerals. Cambridge Univ. press, Cambridge.
- Poldervaart A, Hess HH, 1951. Pyroxenes in the crystallization of basaltic magmas. *Journal of Geology* **59**: 472-489.

- Pryer L, 1993. Microstructures in feldspars from a major crustal thrust zone: the Greenville front, Ontario, Canada. *Journal of Structural Geology* **15**: 21-36.
- Quick J, Sinigoi S, Negrini L, Demarchi G, Mayer A, 1992. Synmagmatic deformation in the underplated igneous complex of the Ivrea-Verbano Zone. *Geology* **20**: 613-616.
- Quick J, Sinigoi S, Meyer A, 1994. Emplacement dynamics of a large mafic intrusion in the lower crust, Ivrea-Verbano Zone, northern Italy. *Journal of Geophysical Research* **99**: 559-573.
- Quick J, Sinigoi S, Snoke AW, Kalakay TJ, Mayer A, Peressini G, 2003. Geologic map of the Southern Ivrea-Verbano Zone, Northwestern Italy. U.S. Geological Survey; Geologic Investigations Series Map I-2776.
- Ramsay JG, 1980. Shear zone geometry : a review. *Journal of Structural Geology* **2**: 83-89.
- Ree JH, 1991. An experimental steady-state foliation. *Journal of Structural Geology* **13**: 1001-1011.
- Rieuf M, 1980. Etude stratigraphique et structurale des unités au nord est de Corte (Corse). Thèse 3^e cycle, Toulouse, 211p.
- Ritsema L, (1952). Géologie de la région de Corte (Corse). Thèse Amsterdam n°196, 110 pp.
- Rosenberg CL, Berger A, Schmid SM, 1995. Observations from the floor of a granitoid pluton: inferences on the driving force of final emplacement. *Geology* **23**: 443-446.
- Rosenberg CL, Berger A, 2001. Syntectonic melt pathways in granitic gneisses, and melt-induced transition in deformation mechanisms. *Phys. Chem. Earth* **26**: 287-293.
- Rosenberg CL, Stünitz H, 2003. Deformation and recrystallization of plagioclase along a temperature gradient: an example from the Bergell tonalite. *Journal of Structural Geology* **25**: 389-408.
- Rosenberg, CL, 2001. Deformation of partially molten granite: a review and comparison of experimental and natural case studies. *Int. J. Earth Sciences* **90**: 60-76.
- Rosenberg, CL, Handy M, 2000. Syntectonic melt pathways during simple shearing of a partially molten rock analogue (Norcamphor-Benzamide). *Journal of Geophysical Research* **105**: 3135-3149.
- Rosenberg, CL, 2004. Shear zones and magma ascent: a model based on a review of the Tertiary magmatism in the Alps. *Tectonics* **23**: 1-21.
- Rosenberg, CL, Handy M, 2005. Experimental deformation of partially melted granite revisited: implications for the continental crust. *Journal of Metamorphic Geology* **23**: 19-28.

- Rossi P et al., 1994. Carte géol. France (1\50000), feuille Corte (1110), Orléans: BRGM. Notice explicative par P. Rossi et al. (1994), 150pp.
- Rossi P, 1986. Organisation et genèse d'un grand batholite orogénique: le batholite calco-alcalin de la Corse. Thèse Doct. d'Etat, Un. de Toulouse. Doc. BRGM n° 107, 292p.
- Rossi P, 1993. La corse varisque. In: Congrès international de l'APBG. Corte, France, 1993.
- Rossi P, Calvez JY, Cocherie A, 1988. Age varisque précoce du plutonisme magnésio-potassique en Corse occidentale: conséquences géodynamiques. C.R. Acad. Sci. Paris **307** :1541-1547.
- Rossi P, Cocherie A, 1991. Genesis of a Variscan Batholith. The Corsica-Sardinia batholith. Field, petrological and mineralogical evidence. In: R. Freeman, M. Huch and S. Mueiler (Eds.). The European geotraverse. Tectonophysics **195**: 319-346.
- Rossi P, Cocherie A, Fanning CM, Deloule E, 2005. Variscan to Eo-Alpine events recorded in European lower-crust zircons sampled from the French Massif Central and Corsica, France. Lithos in press.
- Rutter EH, Brodie KH, Evans PJ, 1993. Structural geometry, lower crustal magmatic underplating and lithospheric stretching in the Ivrea-Verbano zone, northern Italy. Journal of Structural Geology **15**: 647-662.
- Rutter EH, Neumann DHK, 1995. Experimental deformation of partially molten Westerly granite under fluid-absent conditions, with implications for the extraction of granite magmas. Journal of Geophysical Research **100**: 15697-15715.
- Schmid SM, 1982. Microfabric studies as indicators of deformation mechanisms and flow laws operative in mountain building. In: Hsu KJ (Ed) mountain building processes. Academic press. London, pp 95-110.
- Schmid SM, Casey M, 1986. Complete fabric analysis of some commonly observed quartz c-axis patterns. Geophysical monograph **36**: 263-286.
- Schmid SM, Casey M, Starkey J 1981. An illustration of the advantages of a complete texture analysis described by the orientation distribution function (ODF) using quartz pole figure data. Tectonophysics **78**: 101-117.
- Schmid SM, Zingg A, Handy M, 1987. The kinematics of movements along the Insubric Line and the emplacement of the Ivrea Zone. Tectonophysics **135**: 47-66.
- Schmidt MW, 1992. Amphibole composition in tonalite as a function of pressure: an experimental calibration of Al in Hbl barometer. Contributions to Mineralogy and Petrology **110**: 304-310.

- Schmidt MW, Thompson AB, 1996. Epidote in calc-alkaline magmas: an experimental study of stability, phase relationships, and the role of epidote in magmatic evolution. *Am. Mineralogist* **81**: 462-474.
- Sengupta P, Dasgupta S, Bhattacharya PK, Mukherjee M, 1990. An orthopyroxene-biotite geothermometer and its application in crustal granulites and mantle-derived rocks. *J. Metamorphic Geology* **8**: 191-198.
- Sial AN, Toselli AJ, Saavedra J, Parada MA, Ferreira VP, 1999. Emplacement, petrological and magnetic susceptibility characteristics of diverse magmatic epidote-bearing granitoid rocks in Brazil, Argentina and Chile. *Lithos* **46**: 367-392.
- Simi P, 1980. Précis de géographie Humaine, économique et régionale de la Corse. Soc Sci. Hist. et nat. Corse, n°11.
- Simpson C, 1980. Oblique girdle orientation patterns of quartz c-axes from a shear zone in the basement core of the Maggia Nappe Ticino, Switzerland. *Journal of Structural Geology* **2**: 243-247.
- Simpson C, 1984. Borrego Springs-Santa Rosa mylonite zone: a late-Cretaceous west-directed thrust in southern California. *Geology* **12**: 8-11.
- Simpson C, 1985. Deformation of granitic rocks across the brittle-ductile transition. *Journal of Structural Geology* **7**: 503-511.
- Simpson C, Wintsch RP, 1989. Evidence for deformation-induced K-feldspar replacement by myrmekite. *Journal of Metamorphic Geology* **7**: 261-275.
- Simpson C, Wintsch RP, 1989. Evidence for deformation-induced K-feldspar replacement by myrmekite. *Journal of Metamorphic Geology* **7**: 261-275.
- Simpson GDH, Thompson AB, Connolly JAD, 2000. Phase relations, singularities and thermobarometry of metamorphic assemblages containing phengite, chlorite, biotite, K-feldspar, quartz and H₂O. *Contribution to mineralogy and petrology* **139**: 555-569.
- Sinigoï S, Quick JE, Mazzucchelli G, Negrini L, Rivalenti G, 1994. Chemical evolution of a large mafic intrusion in the lower crust, Ivrea-Verbano zone, northern Italy. *Journal of Geophysical Research* **99**: 21575-21590.
- Smithson SB, Johnson RA, Hurich CA, Fountain DM, 1986. Crustal reflection and crustal structure. In Baranzagi M, Brown L (eds) *Reflection seismology: the continental crust*. Am Geophys Union Geodynamics Series **14**: 21-32.
- Snoke AW, Kalakay TJ, Quick JE, Sinigoï S, 1999. Development of a deep-crustal shear zone in response to syntectonic intrusion of mafic magma into the lower crust, Ivrea-Verbano zone, Italy. *Earth and Planetary Science Letters* **166**: 31-45.

- Spanner BG, Kruhl JH, 2002. Syntectonic granites in thrust and strike slip regimes: the history of the Carmo and Cindacta plutons (southern Brazil). *Journal of South American Earth Sciences* **15**: 431-444.
- Spear FS, 1993. *Metamorphic phase equilibria and pressure-temperature-time paths*. Mineralogical Society of America, Washington, DC.
- Speranza F, Villa IM, Sagnotti L, Florindo F, Cosentino D, Cipollari P, Mattei M, 2002. Age of the Corsica-Sardinia rotation and Ligure-Provencal Basin spreading: new paleomagnetic and Ar/Ar evidence. *Tectonophysics* **223**: 117-147.
- Starkey J Cutforth C, 1978. A demonstration of the interdependence of the degree of quartz preferred orientation and the quartz content of deformed rocks. *Canadian Journal of Earth Sciences* **15**: 841-847.
- Stipp M, Stünitz H, Heilbronner R, Schmid SM 2002. The eastern Tonale fault zone: a "natural laboratory" for crystal plastic deformation of quartz over a temperature range of 250 to 700°C. *Journal of Structural Geology* **24**: 1861-1884.
- Stünitz H, Fitzgerald JD, 1993. Deformation of granitoids at low metamorphic grade. II: granular flow in albite-rich mylonites. *Tectonophysics* **221**: 299-324.
- Suhr G, 1993. Evaluation of upper mantle microstructures in the Table Mountain massif (Bay of island ophiolite). *Journal of Structural Geology* **24**: 1861-1884.
- Takeda YT, Obata M, 2003. Some comments on the rheologically critical melt percentage. *Journal of Structural Geology* **25**: 813-818.
- Thévoux-Chabuel H, Ménot RP, Lardeaux JM, Monnier O, 1995. Évolution tectono-métamorphique polyphasée paléozoïque dans le socle de Zicavo (Corse du Sud) : témoin d'un amincissement post-orogénique. *C.R. Acad. Sci. Paris* **321**: 47-56.
- Thompson AB, England PC, 1984. Pressure-temperature-time paths of regional metamorphism. II. Their inference and interpretation using mineral assemblages in metamorphic rocks. *Journal of Petrology* **24**: 929-955.
- Trepied L, Doukhan JC, Paquet J, 1980. Subgrain boundaries in quartz: theoretical analysis and microscopic observations. *Phys chem. Miner* **5**: 201-218.
- Tribe IR, D'Lemos RS, 1996. Significance in hiatus down-temperature fabric development within syn-tectonic quartz diorite complexes, Channel Island, UK. *Journal of geological Society, London* **153**: 127-138.
- Trommsdorff V, Piccardo GB, Montrasio A, 1993. From magmatism through metamorphism to sea floor emplacement of subcontinental Adria lithosphere during pre-Alpine rifting (Malenco, Italy). *Schweizerische mineralogische und Petrographische Mitteilungen* **73**: 191-203.

- Tsurumi J, Hosonuma H, Kanagawa K, 2003. Strain localization due to a positive feedback of deformation and myrmekite-forming reaction in granite and aplite mylonites along the Hatagawa shear zone of NE Japan. *Journal of Structural Geology* **25**: 557-574.
- Tullis J, Yund RA, 1987. Transition from cataclastic flow to dislocation creep of feldspar: Mechanisms and microstructures. *Geology* **15**: 606-609.
- Tullis J, Yund RA, 1991. Diffusion creep in feldspar aggregates: experimental evidence. *Journal of Structural Geology* **13**: 987-1000.
- Twiss RJ, Moores EM, 1992. *Structural geology*. Freeman and Company, New York.
- Urai JL, Humphreys FJ, 1981. The development of shear zones in polycrystalline camphor. *Tectonophysics* **78**: 677-685.
- Urai JL, Means WD, Lister GS, 1986. Dynamic recrystallization of minerals. In: Hobbs BE, Heard HD (Eds.), *Mineral and rock deformation: Laboratory studies*. Geophysical Monograph **36**: 161-199.
- Vannucci R, Rampone E, Piccardo GB, Ottolini L, Bottazzi P, 1993. Ophiolitic magmatism in the Ligurian Tethys: a ion microprobe study of basaltic clinopyroxenes. *Contributions to Mineralogy and Petrology* **115**: 123-137.
- Van Roermund HLM, 1983. Petrofabric and microstructures of omphacite in a high temperature eclogite from the Swedish Caledonides. *Bull. Minéral* **106**: 709-713.
- Vauchez A, 1980. Ribbon texture and deformation mechanisms in quartz in a mylonitized granite of Great Kabylia (Algeria). *Tectonophysics* **67**: 1-12.
- Velde B, 1965. Phengitic micas: synthesis, stability and natural occurrence. *Am. J. Sci.* **263**: 886-913.
- Vernon RH, 1976. *Metamorphic processes*. Allen and Unwin, London.
- Vernon RH, 1984. Microgranitoid enclaves in granites - globules of hybrid magma quenched in a plutonic environment. *Nature* **309**: 438-439.
- Vernon RH, Flood RH, 1988. Contrasting deformation of S- and I-type granitoids in the Lachlan fold belt, eastern Australia. *Tectonophysics* **147**: 127-143.
- Vernon RH, 2000a. Review of microstructural evidence of magmatic and solid-state flow. *Electronic Geosciences* 5:2.
- Vernon RH, 2004. *A practical guide to rock microstructure*. Cambridge editions.

- Vernon RH, Johnson SE, Melis EA, 2004. Emplacement-related microstructures in the margin of a deformed pluton: the San José tonalite, Baja California, México. *Journal of Structural Geology* **26**: 1867-1884.
- Vernon RH, Etheridge MA, Wall VJ, 1988. Shape and microstructures of microgranitoid enclaves: indicators of magma mingling and flow. *Lithos* **22**: 1-11.
- Veizat R, 1988. Les formations métamorphiques de Zicavo (Corse centrale) et leur signification dans le cadre de l'orogène varisque en Méditerranée. *C.R. Acad. Sci. Paris* **306** :725-729.
- Vissers RLM, Drury MR, Hoogerduijn Straing EH, Van Der Wal D, 1991. Shear zone in the upper mantle: a case study in Alpine lherzolite massif. *Geology* **19**: 990-993.
- Voll G, 1976. Recrystallization of quartz, biotite and feldspars from Erstfeld to the Leventina Nappe, Swiss Alps, and its geological significance. *Schweizerische Mineralogische und Petrographische Mitteilungen* **56**: 641-647.
- Voshage H, Hofmann AW, Mazzucchelli M, Rivalenti G, Sinigoi S, Raczek I, Demarchi G, 1990. Isotopic evidence from the Ivrea Zone for a hybrid lower crust formed by magmatic underplating. *Nature* **347**: 731-736.
- Walker GPL, Skelhorn RR, 1966. Some associations of acid and basic igneous rocks. *Earth Sci. Rev.* **2**: 93-109.
- Warburton J, 1986. The ophiolite-bearing Schistes Lustrés nappe in the Alpine Corsica: a model for the emplacement of ophiolites which have suffered HP-LT metamorphism. In: Evans BW & Brown EH (Eds.) *Blueschists and Eclogites*. Geological Society of America Memoir **164**: 313-331.
- Waters CN, 1990. The Cenozoic tectonic evolution of Alpine Corsica. *Journal of the Geological Society of London* **147**: 811-824.
- White S, 1977. Geological significance of recovery and recrystallization processes in quartz. *Tectonophysics* **39**: 143-170.
- Wickham SM, Oxburgh ER, 1986. A rifted tectonic setting for Hercynian high thermal gradient in the Pyrenees. *Tectonophysics* **129**: 53-69.
- Wilson CJL, 1973. The prograde microfabric in a deformed quartzite sequence, Mount Isa, Australia. *Tectonophysics* **19**: 39-81.
- Wernicke B, 1984. Uniform-sense normal simple shear of the continental lithosphere. *Canadian Journal of Earth Science* **22**: 108-125.
- Yund RA, Tullis J, 1991. Compositional changes of minerals associated with dynamic recrystallization. *Contributions to Mineralogy and Petrology* **108**: 335-346.

- Zarki-Jakni B, Van der Beek P, Poupeau G, Sosson S, 2004. Cenozoic denudation of Corsica in response to Ligurian and Tyrrhenian extension: Results from apatite fission track thermochronology. *Tectonics* **23**: 1-18.
- Zibra I, 2005. Synmagmatic and subsolidus Variscan deformation in a mid-crustal granitoid complex. Evidence from S. Lucia nappe (Alpine Corsica, France). In: sheared magma in nature and experiment: bridging the brittle and ductile fields. A conference in honour of RH Vernon. Abstract book.
- Zingg A, Handy MR, Hunziker JC, Schmid SM, 1990. Tectonometamorphic history of the Ivrea Zone and its relationship to the evolution of the Southern Alps. *Tectonophysics* **182**: 169-192.
- Zulauf G, 2001. Structural style, deformation mechanisms and paleodifferential stress along an exposed crustal section: constraints on the rheology of quartzofeldspathic rocks at supra- and infrastructural levels (Bohemian Massif). *Tectonophysics* **332**: 211-237.